Universitat Autònoma de Barcelona

# IMPROVING THE USE OF RADIUM ISOTOPES AND RADON AS TRACERS OF SUBMARINE GROUNDWATER DISCHARGE

**Marc Diego Feliu**

# IMPROVING THE USE OF RADIUM ISOTOPES AND RADON AS TRACERS OF SUBMARINE GROUNDWATER DISCHARGE

**Marc Diego Feliu**

**Ph.D. in Environmental Science and Technology**

**February 2022**

**SUPERVISORS**

**Dr. Valentí Rodellas Vila**

**Dr. Jordi Garcia Orellana**

**INSTITUT DE CIÈNCIA I TECNOLOGIA AMBIENTALS**

**UNIVERSITAT AUTÒNOMA DE BARCELONA**

This Thesis has been funded by the Agència de Gestió d'Ajuts Universitaris i de Recerca (AGAUR) from the Catalan Government through the grant '*ajuts per a la contractació de personal investigador predoctoral en formació*' (2017FI_B_00365) from the year 2017 to 2021.

The studies developed in this Thesis have also been funded through the financial support of the Marine and Environmental Biogeosciences Research Group (MERS; 2017 SGR-1588) and the following research projects:

- Mixing and dispersion in the transport of energy and solutes (MEDISTRAES I, II, and III; PID2019-110311RB-C21, CGL2016-77122-C2-1-R/2-R, PID2019-110311RB-C21), Spanish government.

- Multidisciplinary study of the coast for the evaluation of strategic groundwater resources and the improvement of coastal ecosystems (TERRA-MAR; ACA210/18/00007), Catalan Water Agency (ACA)

# Agraïments – Acknowledgements

Escriure aquesta tesi ha suposat una carrera de fons durant quatre anys. Quatre anys intensos, plens d'experiències en tots els sentits. Ha implicat una barreja de sensacions, sentiments, canvis, records... indescriptible. Tirant la vista enrere, veig que m'ha permès créixer i madurar com a científic i sobretot, com a persona. Amb la perspectiva de quelcom que està arribant al seu final, penso fermament que res d'això hauria estat possible sense l'equip incondicional que he tingut al meu costat que m'ha animat, esbroncat, rellegit parts d'aquest treball (alguns sense saber ben bé de què anava), escoltat i consolat. Intentar plasmar el meu agraïment pel suport que he rebut en aquest temps en unes poques pàgines es fa complicat, si més no, ho intentaré.

Jordi i Valentí, soc honest quan us dic que no puc haver tingut millors directors de tesi que vosaltres dos. Crec que hi ha persones amb qui sempre estaré en deute, Jordi és evident que tu ets una d'aquestes persones i ho ets perquè si avui en dia puc defensar aquesta tesi és indubtablement gràcies a tu. He de donar-te les gràcies per haver confiat en mi i per haver tingut la paciència infinita que has tingut, però sobretot t'he d'agrair que hagis sigut capaç de transmetre'm la passió que sents per la ciència. Això últim crec que és una virtut que et defineix i que fa que siguis el millor líder que pugui tenir aquest grup de recerca. M'és enllà de la nostra relació professional, per mi ets un amic i en certa manera també has estat com un pare. Sóc incapaç de dir-te aquí com estic de feliç del suport que sempre m'has donat en els moments que ho necessitava, però vull que sàpigues que ho tinc molt present, gràcies.

Valentí, sento una admiració tan profunda per la teva manera de fer ciència que porto els darrers anys de tesi intentant assemblar-me a tu. Ets i has sigut per mi una referència, per la manera que tens d'abordar els reptes científics, per aquesta capacitat inherent d'intentar entendre i de qüestionar-s'ho tot, sincerament penso que ets brillant. És per això que quan l'Aaron ens agrupa als dos dins de la categoria de 'teoricos', per mi és tot un orgull. Estic molt content de ser el teu primer fill acadèmic i desitjo de tot cor que obrin una plaça d'una vegada en aquesta unitat perquè ha de ser per tu!! Això i que puguis complir tots els reptes personals que tens al davant.

Aaron, quina sort haver-te trobat al laboratori mentre preparaves bosses i més bosses de fibres. És cert que en aquell moment no m'imaginava que t'acabaria estimant tant, i és que tens un cor tan gran que no t'hi cap al pit. Ves pensant on vols que fem el postdoc perquè jo no sé viure sense els teus crits i sense la teva energia desbordant. Irene i Júlia, les últimes en arribar, però ja esteu deixant la vostra empremta al laboratori, m'encanteu i no puc estar més feliç de tenir-vos com a amigues. Joan Manuel, ets el pilar d'aquest laboratori i és evident que cap de nosaltres podria fer la seva feina sense tu, gràcies! Ari, ets una crack i t'admiro molt! Estic molt content d'haver sigut el teu 'tamizator',.. Qui m'havia de dir a mi que gràcies a això acabaria fent la tesi aquí. Sarah, en aquests anys t'has comprat un pis, has marxat de postdoc, i t'has casat, però el que mai has fet és venir de campanya amb mi, això no té nom, em deus una i espero que quan siguis rica em convidis a una de les teves!! Carolina, sempre t'agrairé que comptessis amb mi pel projecte de Suècia, visitar els laguitos va ser molt top, i poder-te conèixer millor un gran premi. Laura, me he vuelto un fan de ti en los últimos años, fan de las horas en la biblioteca, de ir de cañas, de tu sentido del humor, de pasear por Collserola i por supuesto de tus microplásticos. Aunque te he echado mucho de menos estos meses, estoy muy contento de que estés feliz y que las cosas salgan bien, t'estimo! Esther, Maxi, Giada, Almu, Muntsa i Viena, heu hagut de marxar d'aquest laboratori per buscar fortuna a altres llocs i hem coincidit poc, vull donar-vos les gràcies pel temps que hem passat junts i per integrar-me quan tot just començava. Als del 'lado oscuro': MdA sigue con el activismo a tope!, Anna ets la Pulsar de la unitat, sempre que ho necessites t'acollirem. Lluís, Carles, i Marcus un plaer haver coincidit amb vosaltres aquests anys.

A tot l'equip de Medistraes, Laura Del Val, Laura Martínez, Tybaud, Andrea, José, Tere, Juanjo, Linda, Jesús, gràcies per haver fet aquest projecte possible. Han sigut moltes hores de campanyes des del 2015 i entre tots heu convertit el que possiblement és el lloc més lleig del litoral català en un lloc molt especial. Albert, tu ets el gran responsable que Medistraes hagi sigut (i continuï sent) un èxit i també que hagi pogut acabar la tesi, mil gràcies, especialment per la paciència que tens amb mi. María te quiero agradecer especialmente toda la ayuda y paciencia que tuviste conmigo cuándo hice el trabajo final de máster, era mi primera experiencia con un trabajo científico y aprendí mucho de ti, muchas gracias.

The Opalines sois los mejores compañeros de viaje! Hemos acumulado muchas horas debajo del sol, muchos piezómetros clavados, unos cuantos lopoyo fresh a tope de mercurio, algún que otro ¡¡¡ESTACIO!!!, cinvirsiciinis cin li i, toboganes, “kitt kitt kitt olivas gazpachas”, un logo, camisetas y hasta banda sonora, así que por favor que esto no pare, o como diría Dani (L) “¡¡Ese radio que no pareee!!”.

Estrangulapof, quatre anys de carrera donen per molts moments i que bonic que ens continuem trobant encara que estiguem tots escampats. Rusiu ets molt gran, no em puc riure més amb tu quan ens veiem. Calba, cada dia més units, m’encantes. Charlie, pot ser que faci molt que no ens veiem y quan ens retrobem sembla que fos ahir. Gisa, tens un magnetisme molt especial, sempre tinc ganes d’estar amb tu. Maria, Marina, Cristian i Jokin, sou un gran descobriment! ¡Bruno eres un hermano y te echo de menos!

Kely, no hi ha persona en aquest planeta que sigui capaç d’entendre’m, de recolzar-me i d’estimar-me com tu ho fas. Em fas sentir a casa i estic infinitament agraït de tots els moments que hem passat junts i de tot el que ens queda per viure.

La persona que soc avui no s’entendria sense amics com tu Isaac. Has fet de mestre, de germà gran i d’amic incondicional. Sempre present, sacrificant-se pels altres, donant tot el que tens, tenir-te al meu costat és un tresor i mai seré capaç d’expressar l’agraïment que sento.

Lena, I think it does not happen frequently that you meet somebody who changes so dramatically the way you perceive the world. You changed my world in so many ways and this is the most beautiful present you could have given me. Sei glücklich, sei stark und vergiss nicht, dass ich dich liebe.

Aquests darrers anys he tingut la gran sort de retrobar-me amb vells amics, de conèixer moltes persones que s’han convertit en imprescindibles per mi i d’estrènyer lligams amb amics de tota la vida. Carrate ets una de les persones més singulars que conec, la teva personalitat és simplement desbordant. No puc estar més content de tenir un amic com tu! Trilla (o hauria de dir cryptotrilla?) tornar-te a trobar 10 anys després ha estat una de les sorpreses més grans d’aquest darrer any, i ara de sobte tenim tants plans per fer junts que necessitarem 10 anys per complir-los tots, m’encanta. Anna, quan vas venir a viure a casa meva amb prou feina ens

coneixíem, després d'un confinament sencer puc dir que m'has guanyat el cor i que ets una persona preciosa. Merche, dels 'martes locos' m'emporto records inoblidables, però sobretot haver-te conegut a tu. Laia, ets una imprescindible i quedar amb tu un cop per setmana per fer un 'mano a mano' i una mica de 'palique', com dius tu, m'ha donat sempre moltes forces, ets un amor. Queralt, crec que ja ho saps, però potser no t'he dit suficient com t'estimo i com m'ho passo de bé amb tu! Nabo, res que et digui s'aproximarà al que signifiques per mi en aquest moment de la meva vida. Ets de les poques persones amb qui puc passar-m'hi hores i hores i no me'n canso mai. Alba, estar a la 'virulé' amb tu ha sigut el millor que em podia passar aquest any. Tens la virtut de fer-me sentir especial i em sento un privilegiat per tenir-te al meu costat. Crec que és fàcil adonar-se que ets una persona extraordinària i dir-te que t'estimo es queda molt curt. Manel, estàs lluny però cada cop que tornes a Barcelona em sento com si mai haguessis marxat. Cardu, Ruben i Fer sou incondicionals, sou indispensables, sou família. No em puc imaginar la meva vida sense vosaltres, de fet, no hi heu faltat mai. Conviure amb vosaltres aquests anys ha significat molt per mi: hem passat penes i hem celebrat moltes victòries i que segueixi així, us estimo!

Laura, iaia, i mama, sou les tres dones de la meva vida. És impossible concebre res del que he fet sense vosaltres, incloent-hi per descomptat aquesta tesi. A vosaltres us vull donar especialment les gràcies per haver-me aguantat en tantes situacions. Joan, sempre que t'hem necessitat hi has estat, sempre atent, gràcies per cuidar-nos a tots. Iaia, ets la columna vertebral d'aquesta família i és colpidor veure la fortalesa que tens i l'amor infinit que ets capaç de transmetre als del teu voltant. Laura, em sento tan orgullós de tu,.. Gràcies per tot, especialment per comprendre'm quan potser et costava fer-ho. Mama, sé que a vegades hagués sigut suficient amb venir a estrènyer-te la mà, o a fer-te una abraçada com has fet tu sempre, però moltes vegades no ho he sabut fer millor. Gràcies per estar amb mi incondicionalment, passi el que passi tu sempre hi ets. T'estimo molt. Papa, m'hauria agradat molt que haguessis estat en un moment tan important de la meva vida, però imagino que a tothom li toca marxar en algun moment. Allí on siguis, aquesta tesi és teva també.

# Table of Contents

## List of Figures

## List of Tables

## List of Manuscripts

The content presented in this Thesis is based on three research articles which are developed in Chapters 4, 5, and 6:

**Chapter 4:**

**Guidelines and Limits for the Quantification of Ra Isotopes and Related Radionuclides with the Radium Delayed Coincidence Counter (RaDeCC)**, **J. Geophys. Res. Ocean.**, 125(4), e2019JC015544, doi:10.1029/2019JC015544, **2020**.
Diego-Feliu, M., Rodellas, V., Alorda-Kleinglass, A., Tamborski, J., Beek, P., Heins, L., Bruach, J. M., Arnold, R. and Garcia-Orellana, J.

**Chapter 5:**

**New perspectives on the use of $^{224}Ra/^{228}Ra$ and $^{222}Rn/^{226}Ra$ activity ratios in groundwater studies**, **J. Hydrol.**, 126043, doi:https://doi.org/10.1016/j.jhydrol.2021.126043, **2021**.
Diego-Feliu, M., Rodellas, V., Saaltink, M. W., Alorda-Kleinglass, A., Goyetche, T., Martínez-Pérez, L., Folch, A. and Garcia-Orellana, J.

**Chapter 6:**

**Extreme precipitation events induce high fluxes of groundwater and associated nutrients to the coastal ocean**, **Hydrol. Earth Syst. Sci. Discuss. [preprint],** https://doi.org/10.5194/hess-2021-594, in review, **2022**.
Diego-Feliu, M., Rodellas, V., Alorda-Kleinglass, A., Saaltink, M., Folch, A. and Garcia-Orellana, J.

Additionally, the candidate has participated and contributed to the manuscripts listed below (submitted and published):

**Published:**

**Remobilization of dissolved metals from a coastal mine tailing deposit driven by groundwater discharge and porewater exchange**, **Sci. Total Environ.**, 688, 1359–1372, doi:10.1016/j.scitotenv.2019.06.224, **2019**.
Alorda-Kleinglass, A., Garcia-Orellana, J., Rodellas, V., Cerdà-Domènech, M., Tovar-Sánchez, A., Diego-Feliu, M., Trezzi, G., Sánchez-Quilez, D., Sanchez-Vidal, A. and Canals, M.

**Submarine karstic springs as a source of nutrients and bioactive trace metals for the oligotrophic Northwest Mediterranean Sea**, **Sci. Total Environ.**, 732, 1–14, doi:10.1016/j.scitotenv.2020.139106, **2020**.
Tamborski, J., van Beek, P., Conan, P., Pujo-Pay, M., Odobel, C., Ghiglione, J. F., Seidel, J. L., Arfib, B., Diego-Feliu, M., Garcia-Orellana, J., Szafran, A. and Souhaut, M.

**Combining fiber optic DTS, cross-hole ERT and time-lapse induction logging to characterize and monitor a coastal aquifer**, **J. Hydrol.**, 588, 125050, doi:https://doi.org/10.1016/j.jhydrol.2020.125050, **2020**.

Folch, A., del Val, L., Luquot, L., Martínez-Pérez, L., Bellmunt, F., Le Lay, H., Rodellas, V., Ferrer, N., Palacios, A., Fernández, S., Marazuela, M. A., Diego-Feliu, M., Pool, M., Goyetche, T., Ledo, J., Pezard, P., Bour, O., Queralt, P., Marcuello, A., Garcia-Orellana, J., Saaltink, M. W., Vázquez-Suñé, E. and Carrera, J.

**The social implications of Submarine Groundwater Discharge from an Ecosystem Services perspective: A systematic review**, **Earth-Science Rev.**, 221, 103742, doi:10.1016/j.earscirev.2021.103742, **2021**.
Alorda-Kleinglass, A., Ruiz-Mallén, I., Diego-Feliu, M., Rodellas, V., Bruach-Menchén, J. M. and Garcia-Orellana, J.

**Radium isotopes as submarine groundwater discharge (SGD) tracers: Review and recommendations**, **Earth-Science Rev.**, 103681, doi:10.1016/j.earscirev.2021.103681, **2021**.
Garcia-Orellana, J., Rodellas, V., Tamborski, J., Diego-Feliu, M., van Beek, P., Weinstein, Y., Charette, M. A., Alorda-Kleinglass, A., Michael, H. A., Stieglitz, T. and Scholten, J.

**A multidisciplinary approach to characterizing coastal alluvial aquifers to improve understanding of seawater intrusion and submarine groundwater discharge**, **J. Hydrol.**, 127510, doi:10.1016/j.jhydrol.2022.127510, **2022**.
Martínez-Pérez, L., Luquot, L., Carrera, J., Angel Marazuela, M., Goyetche, T., Pool, M., Palacios, A., Bellmunt, F., Ledo, J., Ferrer, N., del Val, L., Pezard, P. A., García-Orellana, J., Diego-Feliu, M., Rodellas, V., Saaltink, M. W., Vázquez-Suñé, E. and Folch, A.

**Submitted:**

**Groundwater discharge as a driver of methane emissions from Arctic lakes**, **Submitted to Nat. Commun.**
Olid, C., Rodellas, V., Rocher-Ros, G., Garcia-Orellana, J., Diego-Feliu, M., Alorda-Kleinglass, A., Bastviken, D. and Karlsson, J.

**Using the tidal method for conceptual model identification and hydraulic characterization at the Argentona site**, **Submitted to Hydrogeol. J.**
Goyetche, T., Pool, M., Carrera, J., Diego-Feliu, M., Martinez-Perez, L., Folch, A. and Luquot, L.

# Preface

Natural tracers – any substance present in the environment in small but measurable amounts – are a central tool in many scientific disciplines providing useful information about processes and systems. In hydrology and oceanography, tracers are used to address disparate questions such as how water masses move, how do they mix with each other, or which is their path or provenance. Radioactive tracers, by virtue of its known decay rate, can additionally offer unique opportunities for addressing questions relative to time such as how old water is, how long does it take to travel a certain distance, or what the velocity of a specific process is.

Since the production of knowledge is modulated, limited, and constrained by the available techniques, methods, and instruments which generate dynamic scientific spaces, any significant scientific advance is often accompanied by concurrent technical improvements that articulate new spaces. Likewise, our current knowledge about hydrological and oceanographical systems cannot be understood without the continuous advances made in the measurement and quantification of tracers, or with deeply understanding their distribution and geochemical behavior.

The study of submarine groundwater discharge (SGD), a process that involves the discharge of terrestrial and marine groundwater to the coastal ocean, is no exception of that. Actually, research in SGD has been closely linked to the use of the naturally-occurring radioactive tracers of radium isotopes and radon. Paradoxically, the study of this (almost) invisible macroscopic process (the discharge of groundwater below the sea level) is assessed (or made visible) using invisible tracers such as atoms. This stages a 'problem' of scale, whereby scientists are encouraged, and somehow forced, on the one hand, to understand nanoscopic processes occurring within the pore spaces of sediment grains, where radium and radon are released to groundwater and, on the other hand, to infer the hydrologic, oceanographic, ecologic, and social consequences of groundwater discharge for large-scale environments such as coves, bays, seas, or even the world's oceans.

This Thesis explores the use of radium isotopes and radon as tracers of SGD, from the quantification techniques, through the understanding of their distribution in groundwater systems, to the development of new environmental applications in the areas of coastal hydrology and oceanography. As the water infiltrates and flows through the subsurface from the coastal aquifers to the sea, this Thesis is also a small journey from the sample to the data, from the field to the laboratory, from the system to the model, and from the nanoscopic to the macroscopic world.

# Chapter 1: Introduction

## 1.1. Radium isotopes and radon as hydrological and ocean tracers

Radium (Ra) and radon (Rn) are chemical elements with atomic numbers of 88 and 86, respectively. Radium belongs to the alkaline earth metals group of the periodic table (also known as group II) and it is a product of the decay series of uranium and thorium (Figure **1**.**1**). There are four naturally-occurring Ra isotopes with half-lives ranging from days to millennia ($^{223}$Ra, $T_{1/2}$ = 11.4 d; $^{224}$Ra, $T_{1/2}$ = 3.66 d; $^{226}$Ra $T_{1/2}$ = 1600 y; $^{228}$Ra, $T_{1/2}$ = 5.75 y), which are produced by the decay of their parent Th isotopes ($^{227}$Th, $T_{1/2}$ = 18.7 d; $^{228}$Th, $T_{1/2}$ = 1.9 y; $^{230}$Th, $T_{1/2}$ = 7.5x10$^{4}$ y; $^{232}$Th $T_{1/2}$ = 1.4x10$^{10}$ y, respectively). Radon is a radioactive noble gas which is produced by the decay of its parent Ra. There are three isotopes of Rn, two of them with very short half-lives, known as actinon ($^{219}$Rn, $T_{1/2}$ = 4.0 s) and thoron ($^{220}$Rn, $T_{1/2}$ = 54.6 s), and $^{222}$Rn ($T_{1/2}$ = 3.8 d) which hereinafter will be referred simply as radon.

### 1.1.1. Brief historical overview

#### *1.1.1.1. The concepts of radioactivity, isotopes, and tracers*

The current widespread use of Ra isotopes and Rn for evaluating hydrological processes is the result of one of the most mysterious stories in science history: the discovery of radioactivity (Figure **1**.**2**). The findings that unravel this story exemplify the triumph of observation over reason. Indeed, most of the experimental settings that unveiled this phenomenon were initially intended to answer questions others than the ones they ultimately resolved.

In 1895, experimenting with cathode rays in a Crooke's tube, Dr. Roentgen accidentally noticed the fluorescence of a barium platinocyanide screen, which was placed some distance away from the experimental setting. Since this fluorescence could not be explained by the interaction with cathode rays (their range was on the order of centimeters), Roentgen postulated that a sort of new rays (he called them X-rays) originated when the cathode rays strike the glass of the Crooke's tube caused the fluorescence of the screen (Assumus, 1995). By the end of this same year, Roentgen published his results and included some shadowy pictures (i.e., first radiographies) caused by the interaction of X-rays and matter. These results generated great

interest both for the scientific community and for society, and soon scientists from all over the world started replicating these experiments to find if any other type of radiation could also traverse matter. Shortly afterwards, Henri Becquerel was testing whether phosphorescence light was stopped by opaque objects, or if it consisted of penetrating radiation as the recently discovered X-rays. In his experiments, Becquerel exposed a phosphorescent substance to sunlight and placed it on a photographic plate wrapped in black paper. He found that the substance emitted radiation that could even penetrate thin metals, darkening the photographic plates. Briefly after publishing these results in the *Academie des Sciences de Paris* ("*Sur les radiations invisible émises par les corps phosphorescents*") he developed new photographic plates and discovered that the substance emitted penetrating radiation even if it was not exposed to light (Gasparini, 1984). By "*great good fortune*", Becquerel choose as phosphorescent substance a preparation of uranium and, through this fortunate choice, he discovered that uranium emitted an unknown type of radiation assigned to be a new inherent property of the element (Soddy, 1909).

After Becquerel's discovery many researchers began to investigate whether radioactivity was present not only in U, but also in other elements. Marie Curie, who at that time was studying physics and chemistry at the *Université de Paris*, conducted a systematic examination of different ores and concluded that minerals containing Th also exhibited radioactive properties (Davis, 1924). However, in 1898, shortly before Curie's Thesis was published, Gerhard Schmidt announced and published the same discovery. Marie Curie continued investigating the phenomenon of radioactivity in U-bearing ores, specifically using a mineral known as pitchblende (the same source of U that Becquerel used for his experiments). This mineral was known to contain high contents of U (~50%) and small quantities of lead, copper, bismuth, and barium. When analyzed with her electroscope, Curie found that this ore was several times more radioactive than expected from the percentage of uranium contained in it. She therefore concluded that this higher activity could only be attributed to another (and more radioactive) substance present in the ore (Davis, 1924). In this way, Marie Curie discovered the radioactive elements of polonium (called after her native country) and radium (in allusion to its radioactive properties). Notice that it was not until 1910, twelve years later, when Marie Curie together with

her college André Louis Debierne, separated pitchblende into all its constituents isolating for the first-time pure radium.

The discovery of radon is attributed to Friedrich Ernst Dorn in 1900 when he observed a radioactive substance emanating from radium compounds. However, Ernest Rutherford previously found that "*thorium compounds continuously emit radioactive particles of some kind, which retain their radioactive powers for several minutes*" (Rutherford, 1900), and in 1903 conducting independent experiments Friedrich Giesel and Debierne observed the same kind of emanation from Actinium compounds. The emanations from these compounds were initially named '*Radium emanation', 'Thorium emanation',* and *'Actinium emanation'*, but in 1923 were renamed as Radon ($^{222}$Rn), Thoron ($^{220}$Rn), and Actinon ($^{219}$Rn), respectively (Aston et al., 1923). Although later the isotopes from the same element were numbered instead of independently named (with some exceptions i.e., deuterium and tritium), the names Thoron and Actinon were still in use for some decades (e.g., Giffin et al., 1963).

In the early years of the 20$^{th}$ century, Ernest Rutherford and Frederick Soddy ascribed the phenomenon of radioactive decay to the emission of a particle by an atom of a radioactive element (parent), which spontaneously transformed into a new element (daughter). They also found that this process occurred subsequentially, resulting in a series (decay chain) of unstable atoms decaying into other elements. The study of the decay chains of uranium and thorium led to the discovery of new 'elements' (Soddy, 1923). As an example, for the $^{232}$Th decay chain these elements were initially named as thorium ($^{232}$Th), mesothorium 1 ($^{228}$Ra), mesothorium 2 ($^{228}$Ac), radiothorium ($^{228}$Th), thorium X ($^{224}$Ra), thorium emanation ($^{220}$Rn), etc. Some investigations were conducted to separate these elements by chemical means, but the attempts were unsuccessful for thorium and radiothorium (and mesothorium 1 and thorium X), even if they could be prepared independently by separating their parent elements. This led Frederick Soddy to define, in 1912, the chemically identity of 'elements' as isotopes ('*isos*' – same, '*topes*' – place) since they occupy the same position in the periodic table (Soddy, 1923).

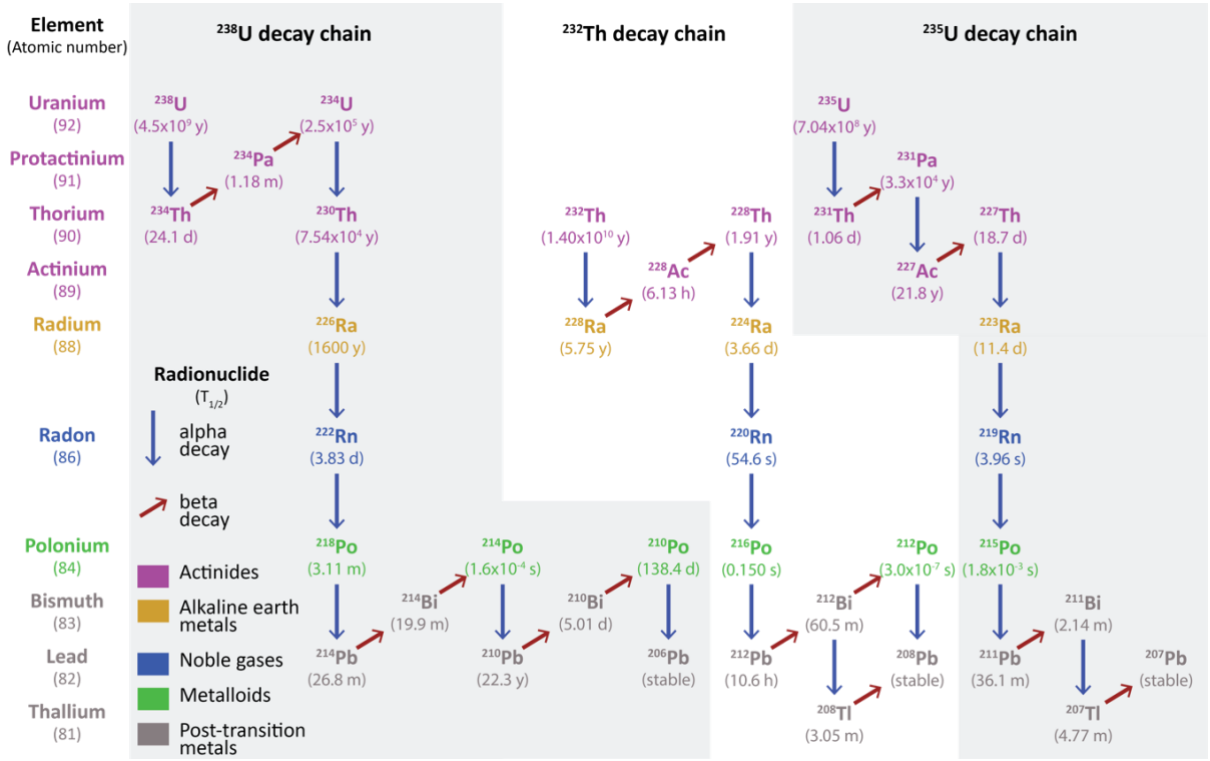


Figure 1.1. Schematic diagram of the uranium ($^{238}$U and $^{235}$U) and thorium ($^{232}$Th) decay series. Gamma emitters are not indicated.

The first uses of radioactive elements as tracers were developed even earlier than the discovery of the term isotope (Horányi, 2004). From 1911 to 1914, George von Hevesy was employed at Rutherford's laboratory with the task of separating a product of the U decay chain, Radium D ($^{210}$Pb), from lead. His efforts were unsuccessful, and "*to make the best of this depressing situation*", Hevesy suggested that since Radium D and led were inseparable, one could use small amounts of Radium D, which can be easily detected by its radioactive properties, as an indicator of lead (Hevesy, 1962). In the following years (1914 to 1926) Hevesy and his co-workers applied radioactive tracer technics to disparate topics (e.g., dissolution velocity of molecular layers, solid-liquid exchange of atoms, radioactive indicators in biology; Hevesy, 1915; Hevesy and Rona, 1914). Since the benchmark works of Roentgen, Becquerel, Curie, Soddy, and Hevesy (among others), radioactive tracers can be considered one of the most important scientific objects that shaped the technology, medicine, and science of the 20$^{th}$ and 21$^{st}$ century (Herran and Roqué, 2009).

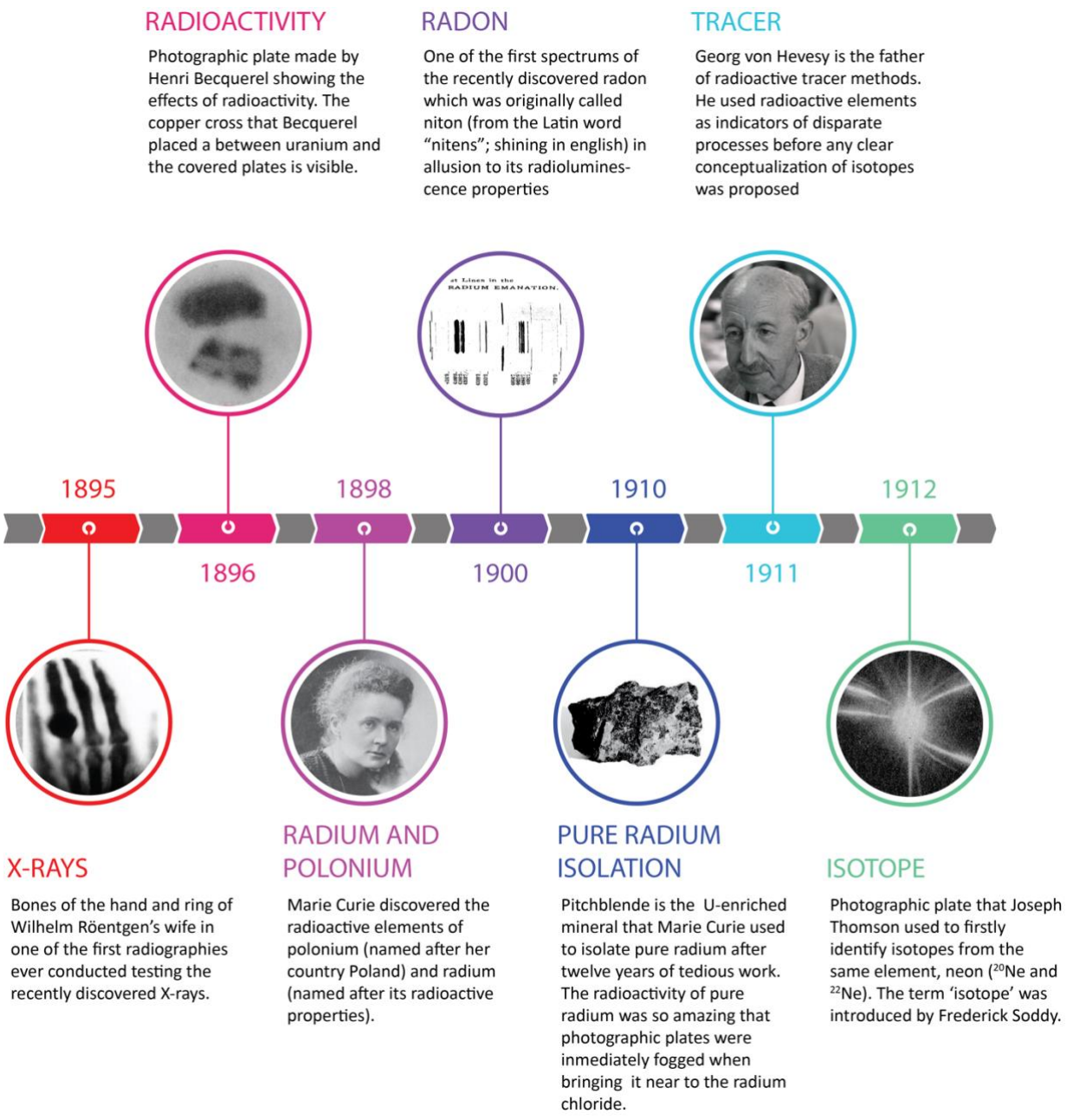


Figure 1.2. Timeline of some important discoveries of the end of 19$^{th}$ century and early 20$^{th}$ century.

#### *1.1.1.2. Radium isotopes and radon as hydrological and oceanic tracers*

The first measurements of Ra and Rn in seawater and marine sediments took place during the early years of the 20$^{th}$ century. Due to the inherent difficulties on collecting and measuring the samples at that time, the first results consisted of scarce measurements that resulted in Ra

activities varying over orders of magnitude among samples and studies (Eve, 1909; Joly, 1908; Mialock, 1915; Satterly, 1911; Strutt, 1906). Joly (1908) and Eve (1909) in their pioneering work found that near-shore samples presented higher activities than those of open seawater. Two decades afterwards, together with a set of studies evaluating the radioactivity of marine sediments (Evans and Kip, 1938; Pettersson, 1930; Piggot, 1932), some authors presented the first $^{226}$Ra and Rn seawater depth profiles, finding an increase in the concentration of both radionuclides with depth (Devaputra et al., 1932; Evans et al., 1938). Simultaneously, tracer techniques involving the use of radionuclides were developed, including those regarding the use of Th and Ra disequilibrium in bottom sediments as a geochronology tool (Kovarik, 1931; Piggot and Urry, 1942). The application of Ra as natural tracer of oceanographical processes was initially introduced by Koczy (1958) and further developed by Koczy and Rosholt (1962), Broecker et al. (1968, 1967), Moore (1969, 1967), an many others (e.g., Blanchard and Oakes, 1965; Li et al., 1977; Li and Chan, 1979; Trier et al., 1972). Simultaneously, several authors started using radon as a tracer for assessing gas exchange rates to the atmosphere, vertical water mixing, and fluxes from ocean sediments to the water column (e.g., Broecker, 1965; Broecker and Kaufman, 1970; Key et al., 1979).

The use of Ra isotopes and Rn was initially limited by the time-consuming available techniques and methods The measurement of $^{226}$Ra was relatively easy since it consisted of quantifying the emanation of its daughter, $^{222}$Rn from a few liters (5 – 10 L) of seawater (e.g., Broecker et al., 1967). In contrast, the analysis of $^{228}$Ra required the collection of large water samples (>> 100 L) and laborious preprocessing methods (Moore, 1969). Four improvements on techniques and instruments permitted the widespread application of these tracers in the forthcoming years: (1) the use of manganese impregnated acrylic fibers which enabled the fast and in situ extraction of radium activities from large volume seawater samples (Moore and Reid, 1973); (2) the widespread availability of high-purity germanium gamma detectors (HPGe), providing relatively fast an precise measurements of long-lived Ra isotopes ($^{226}$Ra and $^{228}$Ra); (3) the fast and precise measurement of short-lived Ra isotopes ($^{223}$Ra and $^{224}$Ra) through the development of delayed coincidence scintillation counters (Giffin et al., 1963; Moore and Arnold,

1996); and (4) the development of low-cost, hand-held equipment to measure $^{222}$Rn in water samples (Burnett and Kim, 2001; Hopke, 1989).

These improvements opened new possibilities and reduced time and costs regarding taking and measuring samples. As a result, many articles about the Ra isotopes and Rn distribution in coastal and open ocean settings were published during the 80s. Elsinger and Moore (1983) published the first study on the distribution of the sort-lived $^{224}$Ra (together with $^{226}$Ra and $^{228}$Ra). Shortly afterwards, two more articles were published using $^{224}$Ra and questioning the sources that this radionuclide may had on the coastal ocean (e.g., bioturbation, bioirrigation, desorption from bottom sediments; Bollinger and Moore, 1984; Levy and Moore, 1985). During this period, there were also significant advances on the application of radon as an ocean tracer, mainly applied for assessing heat and chemical transport from hydrothermal vents (Rosenberg et al., 1988), estimate mixing processes (in the Gulf Stream; Orr et al., 1985), and to study groundwater/surface flow (at Rio Grande de Manati, Puerto Rico; Ellins et al., 1990). It was not until the 90s when researchers recognized that an important source of these radionuclides to the coastal ocean was the discharge of groundwater, which implied in turn that they could be used as tracers of this process (Burnett et al., 1990; Cable et al., 1996a; Rama and Moore, 1996; Veeh et al., 1995).

Henceforth, research on submarine groundwater discharge (SGD) had developed primarily on the basis of the application of Ra isotopes and Rn. Advances in the use of radioactive tracers in SGD studies, including the development of new approaches, conceptual models, and techniques have enabled the quantification of SGD in multiple locations across the globe such as coves, bays, estuaries, and even entire basins or the world's ocean (e.g., Kwon et al., 2014; Peterson et al., 2010; Rodellas et al., 2015). Other applications of these radionuclides include the assessment of groundwater flow dynamics in coastal aquifers (e.g., Condomines et al., 2012; Kiro et al., 2015; Tamborski et al., 2017a), solute fluxes across the sediment-water interface (e.g., Cai et al., 2014; Cook et al., 2018a; Krest and Harvey, 2003), and water ages, residence times and mixing processes in coastal waters (e.g., Knee et al., 2011; Moore and Oliveira, 2008; Wang et al., 2021), among others.

### 1.1.2. Radium isotopes and radon in groundwater

One of the main characteristics that make Ra isotopes and Rn valuable tracers of hydrological and oceanographic studies is that groundwater commonly presents measurable activities of these isotopes. The activities of these radionuclides are governed by their production and decay rates, their geochemical behavior, the characteristic of groundwater flow (e.g., groundwater velocity and transit times) and the behavior of their direct parents (Th and Ra for Ra and Rn, respectively) (Garcia-Orellana et al., 2021; Swarzenski, 2007).

#### *1.1.2.1. Production and decay*

The subsurface production and decay rates of radionuclides control, in part, their activity in groundwater (Figure **1**.**3**). The production rates depend on the decay constant of the target isotope and on the activities of the parent radionuclide dissolved in groundwater and adsorbed on aquifer solids. The activity of dissolved and adsorbed radionuclide together is referred in this manuscript to as the exchangeable radionuclide activity. The radionuclides produced by the $\alpha$-decay of their parent radionuclides, such as Ra isotopes and Rn, are additionally supplied by a process commonly known as $\alpha$-recoil (Sun and Semkow, 1998). This process consists of the mobilization of the daughter radionuclide from the outer mineral lattice (the effective $\alpha$-recoil zone) of the sediment grains to groundwater due to the energy of an $\alpha$-decay (Mehta and Kocar, 2018; Sun and Semkow, 1998). The effective $\alpha$-recoil zone comprises the area of the mineral lattice where an $\alpha$-decay may potentially result in the mobilization of the generated target radionuclide from solid to groundwater (Sun and Semkow, 1998) (Figure **1**.**3**). The supply from $\alpha$-decay to groundwater depends therefore on (1) the activity of the parent radionuclide in sediment grains or solids (hereinafter solid activity), which vary widely depending on the host material (Ivanovich and Harmon, 1992), as well as on (2) the fraction of $\alpha$-decays in sediment grains that effectively recoil in groundwater (Porcelli, 2008). The latest is a function of the grain size, mineralogy, and recoil energy resulting from the $\alpha$-decay (Beck and Cochran, 2013; Sun and Semkow, 1998; Swarzenski, 2007). The greater the specific surface area, the larger the effective $\alpha$-recoil zone and thus the relative amount of parent isotope contained in this zone relative to total aquifer volume (Copenhaver et al., 1992; Porcelli and Swarzenski, 2003). The additional supply through $\alpha$-recoil produces deviations in isotopic ratios in relation to that expected from

the host material. For instance, the groundwater activity ratio in equilibrium of $^{226}Ra/^{228}Ra$ may be up to 1.75 times higher than that of their relative parents ($^{238}U/^{232}Th$) due to the subsequent $\alpha$-decays occurred in the decay chain (3 for $^{226}Ra$ and 1 for $^{228}Ra$). Similarly, activity ratios within radionuclides from the same decay chain (e.g., $^{222}Rn/^{226}Ra$, $^{224}Ra/^{228}Ra$) may present higher equilibrium activity ratios due intermediate $\alpha$-decays (Davidson and Dickson, 1986; Krishnaswami et al., 1982; Swarzenski, 2007). Radium isotopes are generally produced by the decay of Th isotopes contained in the geological matrix (adsorbed or contained in the effective $\alpha$-recoil zone). Production of Ra resulting from dissolved activities of Th is usually negligible since Th is mainly bound to solid phases due to its particle-reactive behavior (Swarzenski, 2007). Contrastingly, radon is produced by the decay of $^{226}Ra$ which can be bound to aquifer solids (solid surfaces or $\alpha$-recoil zone) or dissolved in groundwater. The decay rates of Ra isotopes and Rn in groundwater depend exclusively on their dissolved activities and their decay constants.

#### *1.1.2.2. Geochemical behavior*

Radium distribution in groundwater systems is governed by a set of geochemical processes such as adsorption, desorption, precipitation, and weathering (Figure **1.3**). These processes depend on both the characteristics of the geological matrix (e.g., mineralogy, grain size, cationic exchange capacity; Beck & Cochran, 2013; Krishnaswami et al., 1982; Swarzenski, 2007) and the geochemical signature of groundwater (e.g., pH, Fe and Mn content, ionic strength; Gonneea et al., 2008; Sajih et al., 2014; Webster et al., 1995). The adsorption-desorption of Ra is mainly controlled by the cationic exchange capacity (CEC) of the aquifer solids and the ionic strength of the solution. Sediments with higher CEC are likely to present more adsorption places in the sediment surface that can be potentially occupied by Ra dissolved in groundwater in the form of $Ra^{2+}$ (e.g., Beck and Cochran, 2013; Beneš et al., 1985; Nathwani and Phillips, 1979; Vinson et al., 2009). Conversely, solutions presenting high ionic strength (high concentration of ions; e.g., $Na^{+}$, $K^{+}$, $Ca^{2+}$) may hamper the adsorption of $Ra^{2+}$ due to competition with dissolved cations of the solution, concurrently promoting the desorption of the adsorbed $Ra^{2+}$ due to cationic exchange (e.g., Beck and Cochran, 2013; Gonneea et al., 2013a; Kiro et al., 2012; Webster et al., 1995). As a result, when cationic exchange is the main mechanism for Ra transference between solid and solution, brackish or saline groundwaters are likely to be more enriched in Ra

isotopes relative to fresh groundwaters. The dependency of Ra adsorption-desorption with ionic strength is more significant in coastal aquifers, where intruded saline groundwater mixes with meteoric fresh groundwater. In these environments salinity gradients control adsorption-desorption processes promoting gradients of Ra, which may vary orders of magnitude (Cerdà-Domènech et al., 2017; Cho and Kim, 2016; Gonneea et al., 2008). Other factors relative to the groundwater and sediment geochemistry, such as temperature, oxygen content, pH, and presence of surface-bound Fe or Mn may also play an important role on the adsorption-desorption of Ra (e.g., Beck and Cochran, 2013; Beneš, 1982; Nathwani and Phillips, 1979).

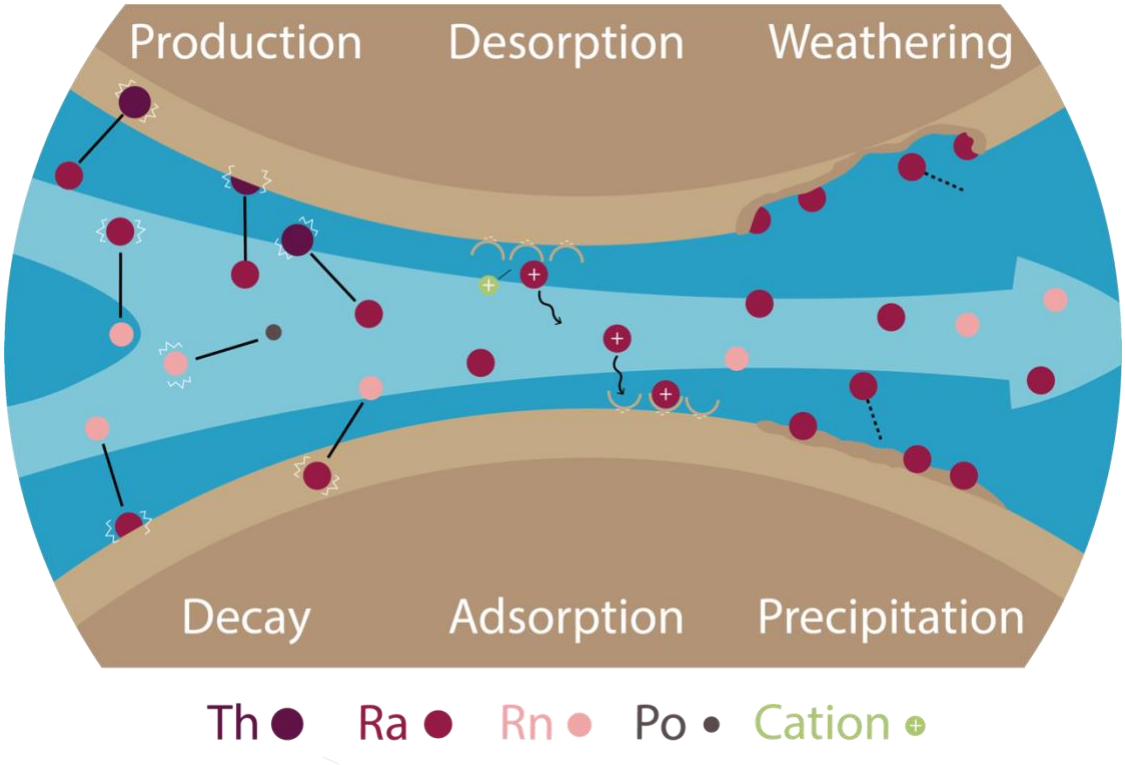


Figure 1.3. Schematic diagram of the mechanisms controlling Ra isotopes and Rn in groundwater. Based on Garcia-Orellana et al. (2021).

Radium isotopes are also removed from groundwater due to mineral precipitation. The removal often occurs via co-precipitation with Fe and Mn hydro(oxides), sulfates (e.g., $Ra(SO_4)$), and carbonates (e.g., $Ra(CO_3)$) due to the low molar activities of Ra in groundwater (Charette and Sholkovitz, 2002). Co-precipitation may occur under high pH (>7) and oxidizing conditions (Gonneea et al., 2008; Kiro et al., 2013, 2012; Krall et al., 2020). Conversely, $Ra^{2+}$ may be released to groundwater due to weathering processes. These processes include chemical dissolution of

the aquifer matrix and breakdown of rocks and minerals resulting from the physical forces derived from the circulation of groundwater through the aquifer. The physiochemistry of groundwater, including temperature, redox potential, pH, and ionic strength, together with the characteristics of aquifer solids (e.g., specific surface area, mineralogy) determine the extent of weathering processes (Chabaux et al., 2008, 2003). For instance, groundwaters with reducing conditions may promote the dissolution of Fe and Mn hydro(oxides), releasing the $Ra^{2+}$ previously adsorbed on the surfaces of hydro(oxides) complexes (Beneš et al., 1984; Gonneea et al., 2013a). However, despite weathering and precipitation may be important for long-lived Ra isotopes ($^{226}Ra$ and $^{228}Ra$), they are assumed to play a minor role in the distribution of short-lived Ra isotopes ($^{223}Ra$ and $^{224}Ra$) due to the long temporal scales of these processes relative to production-decay and adsorption-desorption processes.

Contrastingly, Rn activities are not affected by any chemical processes such as adsorption, desorption, precipitation and weathering due to its unreactive nature. Despite that, Rn is highly influenced by the properties of the geological matrix such as grain size, mineralogy, degree of weathering and by the activities of $^{226}Ra$, which is in turn affected by the above-mentioned processes. Additionally, Rn is also affected by gas exchange in the groundwater-atmosphere interface of unconfined aquifers. This exchange depends on groundwater temperature, salinity, atmospheric pressure, and sediment porosity or rock permeability (Barberio et al., 2018).

#### *1.1.2.3. Groundwater transit times*

The activities of Ra isotopes and Rn in groundwater are also determined by the interaction time between groundwater and aquifer solids. This time, also known in the literature as groundwater transit time, or residence time (e.g., Kiro et al., 2015; Luo and Jiao, 2019; Tamborski et al., 2017a) depends on the driving forces underlying the advective flow as well as on the characteristics of the aquifer matrix. The driving forces of advective flow are disparate (e.g., terrestrial hydraulic gradient, wave pumping), variable in time (e.g., seasonal variations in aquifer level, tidal pumping), and may affect not only the transit times but also the extent of the biogeochemical reactions occurring in the subsurface, including that affecting the mobilization of Ra isotopes and Rn (Santos et al., 2012). The ability of groundwater to circulate through the sediment pores or rock fractures under the effect of a hydraulic gradient, known as aquifer

hydraulic conductivity, is a fundamental parameter regulating the velocity (and transit time) of groundwater. This parameter depends on the characteristics of the aquifer solids such as grain size and intrinsic permeability with values that may vary orders of magnitude depending on the type of sediments (e.g., $10^2$ - $10^3$ m·d$^{-1}$ for gravel, 1 - $10^2$ m d$^{-1}$ for sands, $10^{-3}$ - 1 m d$^{-1}$ for silt, or $10^{-7}$ - $10^{-3}$ m d$^{-1}$ for clay; Shackelford, 2013) or on the type of aquifer (e.g., ~$10^{12}$ m·d$^{-1}$ for karstic or volcanic aquifers or 1 – $10^2$ m d$^{-1}$ for alluvial aquifers; Li et al., 2020; Zhang and Schaap, 2019).

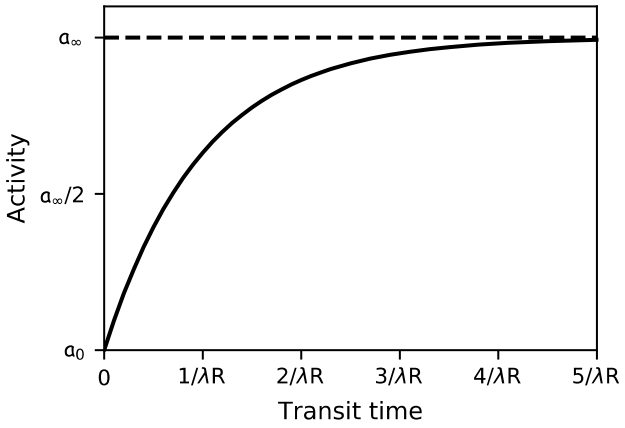


Figure 1.4. Ingrowth of Ra isotopes and Rn in groundwater depending on decay ($\boldsymbol{\lambda}$), retardation (R), and activity of the parent isotope ($\boldsymbol{a}_\infty$). Based on Michael et al. (2011).

Assessing the role of groundwater transit times on the groundwater enrichment rates in Ra isotopes and Rn is challenging due to the complexity of hydrogeological systems (e.g., non-stationary, heterogeneous media, groundwater mixing-reactive zones). However, one of the most common strategies to overcome these complexities is through the development of simple advective transport models of radionuclides (e.g., Cook et al., 2018a; Krest and Harvey, 2003; Michael et al., 2011) (see Section 1.1.2.4). Although the model assumptions hamper the application of these models to real systems, they are instrumental in understanding the main factors controlling the distribution of radionuclides in groundwater systems. The results from these models indicates that groundwater infiltrating into aquifers is enriched in Ra isotopes and Rn at a certain rate, which depends on both the decay constant and the retardation of each specific radionuclide (1/$\lambda$R), until reaching an equilibrium with the activity of the parent isotope ($a_\infty$; Figure **1.4**) (e.g., Kiro et al., 2012; Michael et al., 2011; Tamborski et al., 2017a). The

retardation is defined as the reduction of the average velocity of a solute relative to groundwater velocity due to the solid-solution interaction processes (McKinley and Russell Alexander, 1993). Understanding the role of groundwater transit times on the distribution of Ra isotopes and Rn open up many opportunities regarding the use of these radionuclides as tracers for environmental studies regarding hydrological and oceanographical disciplines such as the discrimination of SGD pathways, the assessment of the tracer concentration in the discharging groundwater, and the determination of ages, velocities and transit times of groundwater (Garcia-Orellana et al., 2021; Kiro et al., 2014; Michael et al., 2011).

#### *1.1.2.4. Transport models of radionuclides in groundwater*

The development of transport models of Ra isotopes and Rn in groundwater have focused the attention of many researchers since the late 70s, when these radionuclides were recognized as important contaminants of soil and groundwater derived from mining activities (International Atomic Energy Agency, 1984). Later on, with the establishment of Ra isotopes and Rn as the most common technique to quantify SGD, transport models were predominantly used for understanding patterns and gradients of these radionuclides in subterranean estuaries (e.g., Krest and Harvey, 2003; Michael et al., 2011; Tamborski et al., 2017a). These advances have been instrumental, on the one hand for constraining the tracer endmember (i.e., Ra isotopes and Rn concentrations in the discharging groundwater) in SGD studies, which is often one of the main uncertainties in Ra or Rn mass balances (Cerdà-Domènech et al., 2017; Cho and Kim, 2016; Cook et al., 2018b), and on the other hand for applying these radionuclides as tracers of hydrogeological processes (e.g., determination of groundwater velocities or ages, assessing the connectivity of the coastal aquifer with the sea, determining ages and velocities of groundwater, differentiating variable spatiotemporal scale processes; Cable and Martin, 2008; Cook et al., 2018a; Kiro et al., 2015).

Transport models should include the different transport mechanisms and all sources and sinks of Ra isotopes and Rn in groundwater. These includes advective and dispersive transport, radioactive production, desorption, and weathering as sources, and radioactive decay, adsorption, and precipitation as sinks. A general equation for radionuclide transport can be written as:

$$\frac{\partial a}{\partial t} = D\frac{\partial^2 a}{\partial x} - v\frac{\partial a}{\partial x} - \lambda R a + \lambda f - \lambda B + \lambda \Gamma \qquad \text{Equation 1.1}$$

where the change in the groundwater activities of a radionuclide ($a$ [Bq m$^{-3}$]) with time (t [s]) depends on the hydrodynamic dispersion coefficient ($D$ [m$^2$ s$^{-1}$]), the groundwater velocity ($v$ [m s$^{-1}$]), the decay constant ($\lambda$ [s$^{-1}$]), the parent radionuclide activity, including the exchangeable and $\alpha$-recoil activity ($f$ [Bq m$^{-3}$]), the distance-dependent activity gradient (where, $x$ [m] is the distance in relation to the recharge point), the retardation factor ($R$ [-]), the rate of co-precipitation ($B$ [Bq m$^{-3}$]), and the rate of weathering ($\Gamma$ [Bq m$^{-3}$]). Notice that since Rn is not affected by retardation, precipitation or weathering, its activity in groundwater only depends on radioactive production and decay, and transport processes. However, in the first cm to m of unconfined aquifers, where groundwater is in contact with air, the evasion of Rn may represent a relevant sink term that needs to be accounted for in Equation 1.1. Radon losses to the atmosphere chiefly depend on groundwater temperature and salinity, atmospheric pressure and sediment porosity or rock permeability (Barberio et al., 2018).

In most of the studies dealing with transport models of Ra isotopes and Rn, Equation 1.1. is often simplified by assuming negligible coprecipitation and weathering ($B = \Gamma = 0$), steady-state conditions ($\partial a/\partial t = 0$), and negligible dispersion relative to advection transport (e.g., Kiro et al., 2013; Krest and Harvey, 2003; Michael et al., 2011; Schmidt et al., 2011; Tamborski et al., 2017a). Based on these assumptions, the solution for Equation 1.1 is commonly expressed as follows (Michael et al., 2011):

$$a(x) = a_\infty + (a_0 - a_\infty)e^{-\frac{\lambda R x}{v}} \qquad \text{Equation 1.2}$$

where $a_0$ [Bq m$^{-3}$] is the activity of the inflowing water and $a_\infty$ is the equilibrium activity which equals the ratio $f/R$. Although these analytical solution may be instrumental for conceptually understanding the distribution of Ra isotopes and Rn in groundwater, the assumptions taken for its derivation may obscure the interpretation of Ra isotopes and Rn activities in systems with

non-stationary conditions (e.g., variable hydrological forcing, tidal fluctuations), mixing of different waters (e.g., subterranean estuaries), variable production rates (e.g., geological heterogeneity) or significant weathering and precipitation processes (e.g., karstic systems).

#### 1.1.2.4.1. Production rates, retardation, and distribution coefficient

One of the main limitations regarding the implementation of transport models of radionuclides is that it does not only rely on the accurate determination of Ra isotopes and Rn activities in groundwater ($a(x)$) and in the inflowing water ($a_0$), which can be easily sampled and measured, but also on the estimation of other model parameters such as the production rate or the retardation factor.

The production rates can be indirectly inferred from measuring the activity of the parent radionuclides (the respective Th isotope for Ra isotopes, and $^{226}$Ra for $^{222}$Rn) in the aquifer. However, this is not straightforward because for properly constraining the production rates, both the exchangeable activity (dissolved and adsorbed) and the $\alpha$-recoil activities (i.e., solid activity that effectively produces the mobilization of the daughter radionuclide from the solid to solution) should be determined. The methods commonly used in the literature are mainly based on the determination of production rates of both processes together, and can be summarized as follows: (1) experimental determination of emanation rates and the content of the parent isotope in the sediment grains (Hussain, 1995; Rama and Moore, 1984; Semkow, 1990); (2) radioactive equilibration experiments (Tamborski et al., 2019); (3) theoretical calculations focused on determining the $\alpha$-recoil supply based on several properties of the host material (e.g., density, surface area; Kigoshi, 1971; Sun and Semkow, 1998); (4) mathematical fitting with advective transport models (Krest and Harvey, 2003), and (5) determination via the recoil rate of $^{222}$Rn (Copenhaver et al., 1992; Krishnaswami et al., 1991, 1982).

The retardation factor is also a key parameter for successfully applying transport models. Since radon is not affected by any chemical reaction, once is released into groundwater it does not interact with solid surfaces, and therefore it is not affected by retardation (i.e., $R = 1$). Conversely, Ra isotopes are affected by many geochemical processes that may contribute to a certain solid-solution distribution (Copenhaver et al., 1993). The retardation factor of Ra can be

determined from *in-situ* measurements (Copenhaver et al., 1992; McKinley and Russell Alexander, 1993) or otherwise estimated from the distribution coefficient of Ra ($K_D$ [$m^3$ $kg^{-1}$]), the aquifer porosity ($\phi$ [-]), and the dry bulk density ($\rho_b$ [kg $m^{-3}$]) of the geology (i.e., $R = 1 + K_D \frac{\rho_b}{\phi}$). The second method implicitly assumes that the main processes controlling the distribution of Ra isotopes are adsorption and desorption. The distribution coefficient is defined as the ratio of solid phase to solute concentrations of radionuclide and the most common techniques for determining $K_D$ are: (1) batch adsorption-desorption experiments (Beck and Cochran, 2013; Rama and Moore, 1996; Tachi et al., 2001; Willett and Bond, 1995); (2) adsorption-desorption modelling (e.g., Copenhaver et al., 1993; Webster et al., 1995); (3) flow-through columns tests (e.g., Meier et al., 2015; Relyea, 1982); and (4) chemical equilibrium calculations (Puigdomenech and Bergstrom, 1995). In appendix A, a compilation of ~250 values for the Ra distribution coefficients have been reviewed from the literature. The values are derived from different experimental settings (e.g., adsorption-desorption experiments, modeling, in situ measurements; Liu et al., 2019; Tachi et al., 2001; Webster et al., 1995), with different sorbents (e.g., marine sediments, organic matter, Mn fibers; Beck and Cochran, 2013; Colbert and Hammond, 2008; Sheppard and Thibault, 1990) and solutions (e.g., synthetic water, groundwater, seawater; Copenhaver et al., 1992; Li and Chan, 1979; Tamamura et al., 2014), and evaluated against different variables (e.g., salinity, pH, CEC; Beck and Cochran, 2013; Beneš et al., 1985; Vandenhove and Van Hees, 2007). Median values for Ra distribution coefficient derived from this compilation for fresh and saline groundwater are 600 L $kg^{-1}$ ($1^{st}$ - $3^{rd}$ quartile; 200 - 1900 L $kg^{-1}$) and 5.0 L $kg^{-1}$ ($1^{st}$ - $3^{rd}$ quartile; 1.5 – 19.0 L $kg^{-1}$), respectively (Figure **1**.**5**).

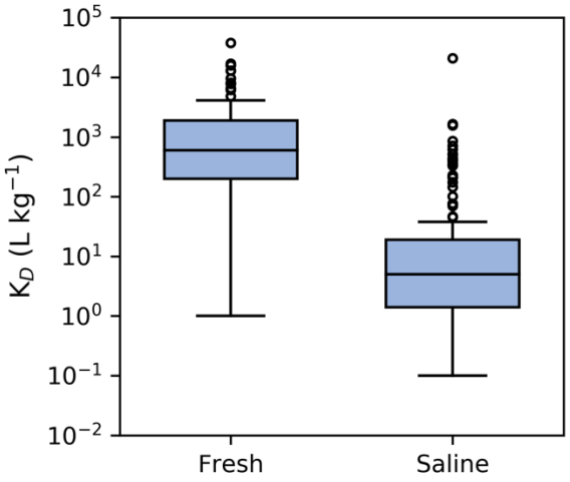


Figure 1.5. Characteristic values for Ra distribution coefficient from a compilation of ~250 values from the literature (Appendix A).

### 1.1.3. Radium isotopes and radon in coastal seawater

The application of any element as a oceanographic tracer requires a proper understanding of the processes modulating its concentration in seawater, thus including the evaluation of all its possible sources and sinks in the water column. Several works have previously described the sources and sinks of Rn and Ra isotopes in coastal seawater (Burnett et al., 2003a, 2003b; Charette et al., 2008; Garcia-Orellana et al., 2021; Moore, 2010; Rama and Moore, 1996; Rodellas et al., 2021; Swarzenski et al., 2007). The main sources of these radionuclides in coastal waters, which may vary its relative significance depending on the sampling locations are: (1) atmospheric inputs, (2) surface water inputs, (3) inputs from sediments, (4) inputs from offshore waters, (5) production in the water column, (6) dissolution of minerals and opal-producing organisms, and (7) SGD inputs, while the major sinks are: (1) atmospheric evasion (only for Rn), (2) decay in the water column, (3) offshore export, (4) chemical precipitation, and (5) biological uptake. Notice that since Rn is a noble gas, source/sink involving chemical reactions (e.g., dissolution, precipitation, biological uptake) should not be considered for this radionuclide. The description, magnitude, and origin of Ra and Rn sources and sinks in coastal waters are summarized in Table **1.1**.

Table 1.1. Description of main sources and sinks of Ra isotopes and Rn in coastal seawater. Values of the relative magnitude as source/sink terms are based on the literature listed below the Table.

| | Processes | Relative magnitude | Description |
|---|---|---|---|
| ***Sources*** | | | |
| **Atmosphere** | Wet and dry deposition | n.a. Rn<br><1% Ra | Dissolved Ra in rainwater and desorption from atmospheric dust. Represents a minor contribution even in large areas affected by atmospheric dust. |
| **Surface waters** | Discharge from Rivers, streams, marshes, channels, outfalls, WWTP | <10% Rn<br>0-10% $^{223,224}$Ra<br>0-40% $^{226,228}$Ra | This source includes dissolved Rn and Ra and desorption of Ra from river- and stream-borne particles and depends on the presence and magnitude of surface inputs, water particle concentration, and type and origin of the particles. |
| **Sediments** | Molecular diffusion, sediment resuspension, diagenesi, bioturbation | 0-90% Rn<br>0-90% $^{223,224}$Ra<br>0-75% $^{226,228}$Ra | Sources from sediment largely depend on sediment characteristics (e.g., grain size, porosity, mineral composition) and the type of process producing these inputs. In most cases, this source can be neglected for long-lived Ra isotopes. Conversely, it may be an important source of Rn and short-lived Ra isotopes. |
| **Offshore waters** | Exhange with offshore waters | negl. Rn<br>negl. $^{223,224}$Ra<br>0-100% $^{226,228}$Ra | Inputs of Ra isotopes and Rn due to mixing between nearshore waters and offshore waters. This term is commonly negligible for short-lived Ra isotopes and Rn since offshore waters are not significantly enriched in these radionuclides. Yet, in absence of any other source, mixing may be significant for long-lived Ra isotopes. |
| **Internal cycling** | Production, biogenic and lithogenic dissolution | <20% Rn<br>negl. Ra | Production is often negligible for Ra isotopes since Th is rapidly scavenged by sinking particles due to its reactivity. Conversely, significant Rn may be produced by its parent $^{226}$Ra content in the water column. Dissolution is often a minor source of Ra isotopes and Rn in coastal waters. |
| **Groundwater** | SGD | 10-100% Rn<br>10-100% $^{223,224}$Ra<br>25-100% $^{226,228}$Ra | SGD, including all its pathways described in Section 1.2.2, is often the primary source of Rn and Ra isotopes to the coastal ocean. |
| ***Sinks*** | | | |
| **Atmosphere** | Evasion | 5-75% Rn<br>n.a. Ra[8-13] | Losses to the atmosphere represent an important sink of radon, especially in shallow water environments. |
| **Offshore waters** | Exhange with offshore waters | 10-100% Rn<br>10-75% $^{223,224}$Ra<br>~100% $^{226}$Ra<br>5-100% $^{228}$Ra | Offshore exchange represents one of the more significant Rn and Ra sinks since nearshore waters are often more enriched than offshore waters. Systems with high dispersing mixing or/and short flushing times are likely to present a higher net export of Ra and Rn to offshore waters. This sink is especially relevant for long-lived Ra isotopes. |
| **Internal cycling** | Decay, chemical precipitation, uptake | 10-100% Rn<br>0-100% $^{223,224}$Ra<br>~0% $^{226}$Ra<br>5-100% $^{228}$Ra | Radioactive decay represents a significant sink for short-lived Ra isotopes and Rn. Conversely, this term may represent a minor sink for long-lived Ra isotopes in coastal areas with short residence times (<100 d). |

negl.: Negligible; n.a.: Not applicable; Reference articles: 1: Rodellas et al. (2015); 2: Moore et al. (2008); 3: Boehm et al. (2004); 4: Boehm et al. (2006); 5: Hwang et al. (2005); 6: Tamborski et al. (2018); 7: Luek and Beck (2014); 8: Su et al. (2014); 9: Crusius et al. (2005); 10: Chanyotha et al. (2014); 11: Burnett and Dulaiova (2003); 12: Dulaiova and Burnett (2006); 13: Swarzenski et al. (2006).

## 1.2. Submarine groundwater discharge

The first evidence on the recognition of groundwater discharging below the sea are very old. Ancient civilizations as the Phoenicians in the Mediterranean Sea or Rapa Nui in Easter Island already used the discharging groundwater as a freshwater resource (Brosnan et al., 2019; Kohout, 1966). Submarine springs are undoubtably the greatest manifestation of groundwater discharge to the ocean. Some of them have been discovered in the course of the last centuries (Fleury et al., 2007), others have a much older discovery and are part of the cultural heritage of some societies. For instance, Greek philosophers and geographers as Aristotle, Pausanias, or Strabo already described tales and legends which mingled their incipient knowledge on submarine springs and hydrological systems with divinity or mortality topics (Clendenon, 2009).

In contrast to what has long been known about groundwater discharge into the ocean, the scientific interest in this process is relatively recent. Some of the first scientific text describing the submarine discharge of groundwater date from the end of the 19$^{th}$ century. Shaler (1894) described in his paper '*Evidences as to Change of Sealevel'* the magnitude of a submarine spring located nearly off Saint Augustine (Florida, USA): "(the spring) *is formed by the discharge of such a volume of water that where it rises through the heavier marine fluid it forms a slight elevation, from which the outsetting stream is so strong that, according to trustworthy reports made to me, a boat has to be rowed with some energy to attain the center of the disk*". Besides preliminary descriptions of these springs in other early research papers (e.g., Matson and Sanford, 1913), the first scientists that effectively intended to assess the discharge of groundwater were hydrologists, who identified this process as a relatively important part of the hydrological cycle (Kohout, 1966; Manheim, 1967). It was not until the end of the 20$^{th}$ century that oceanographers focused on understanding the role that this process may have on the biogeochemical cycles of the coastal ocean (Bokuniewicz, 1980; Cable et al., 1996b; Church, 1996; Johannes, 1980; Lee, 1977; Rama and Moore, 1996; Valiela et al., 1990). Since then, continuous improvement on the techniques used to quantify water and solute fluxes driven by SGD has enabled improving the understanding of this process and better assessing its implications for coastal environments worldwide (Taniguchi et al., 2019). Nowadays, SGD is recognized as a fundamental process regulating the transference of mater from land to ocean, influencing the global budgets of trace elements,

controlling the functioning of coastal ecosystems, and contributing to the well-being of coastal societies (Alorda-Kleinglass et al., 2021; Lecher and Mackey, 2018; Moosdorf and Oehler, 2017; Santos et al., 2021). The increasing number of published articles, and the diverse and interdisciplinary scientific communities currently working with SGD-related topics (e.g., oceanographers, hydrologist, biologists, geochemists) emphasize the existing need for better understanding this (almost) invisible process and its direct implications for the present and future environment and society.

### 1.2.1. Definitions and terminology

The terms and definitions associated with the SGD research have commonly been a source of disagreement for both the SGD community itself and for the "external" communities of hydrogeologist and marine scientist. This is probably due to the interdisciplinary character of these communities, formed by scientist with different backgrounds, conceptions, and ways of thinking. Perhaps, the major source of disagreement has been the definition of submarine groundwater discharge itself. Initially, the term was associated to the "*outflow of water substantially less salty than seawater*" as stated by Manheim (1967) and named submarine discharge of water. Later on, with the involvement of oceanographers, who were mainly interested in the geochemistry of the oceans, the term evolved to include, not only the discharge of meteoric fresh groundwater, but also the flows of circulated seawater through the coastal aquifer, which were also believed to supply many dissolved compounds to the ocean (Bokuniewicz, 1992; Church, 1996; Moore, 1996). At the present day, the definition of SGD continues to be a subject of debate, especially regarding the processes that must be included within the definition, and it should be noted that the term SGD is frequently used for some "external" communities to only refer to the discharge of fresh groundwater. The most inclusive definition of SGD is perhaps the one adopted by Burnett et al. (2003): "*any and all flow of water on continental margins from the seabed to the coastal ocean, regardless of fluid composition or driving force*". Alternatively, Moore (2010) spatially constrained the definition of SGD to "*scale lengths of meters to kilometers*", excluding therefore advective flow processes on the scale of less than 1 m. This arbitrary threshold was convenient for the communities that already had defined these short-scale processes with other terms, such as porewater exchange or benthic

fluxes (King, 2011; Santos et al., 2012). Recently, Taniguchi et al. (2019) revised the definition to include the discharge through insular margins, since islands may have larger discharge rates than those fluxes from continual margins (Moosdorf et al., 2015). The decision on whether adopting the inclusive or restrictive definition of SGD is discretionary and depends on the type of study and the target audience.

The definition of SGD has not been the only source of disagreement between hydrologist and oceanographers. Currently, there is some debate on the terminology that should be adopted in relation to coastal groundwater systems (Duque et al., 2020). Whilst hydrogeologist use the terms coastal aquifer as the domain in "*where continental fresh groundwater and seawater meet*" (Post, 2005), seawater intrusion as the "*landward incursion of seawater*" (Werner et al., 2013), and fresh-salt water mixing zone as the "*transition region that controls regional groundwater flow dynamics and reactive transport processes*" (Abarca and Prabhakar Clement, 2009), oceanographers are more familiarized with the term subterranean estuary, described by Moore (1999) as "*a coastal aquifer where groundwater derived from land drainage measurably dilutes sea water that has invaded the aquifer through a free connection to the sea*". In his disquisition about this topic, Duque et al. (2020) proposed the use of the traditional hydrological concepts (i.e., coastal aquifer, seawater intrusion, fresh-salt water mixing zone) when referring to particular aspects about coastal groundwater systems, whilst using subterranean estuary to refer to the subsurface physical, geochemical, and biological reactions occurring in the reactive zones of coastal aquifers. Again, the decision on whether using the hydrological or oceanographical terms is a discretionary matter.

Other nearly analogous terms that can lead to confusion are benthic flow and porewater exchange, used to describe the exchange of groundwater through the sediment-water interface (i.e., "*rate of flow across the bed of a water body, per unit area of bed*"; King, 2011), or groundwater and porewater used to describe the water contained in the subsurface or in the aquifer pores.

In this dissertation, the most inclusive definition of SGD is adopted (Burnett et al., 2003a; Taniguchi et al., 2019), the terms subterranean estuary and coastal aquifer are used following similar criteria than that proposed by Duque et al. (2020), groundwater and porewater are used

indistinctively, and the term porewater exchange is used to describe the groundwater exchange through sediment-water interface.

### 1.2.2. Driving forces and pathways

The discharge of groundwater to the coastal ocean is governed by a set of driving forces and pathways (Figure **1**.**6**) that likely determine the extent of chemical reactions occurring within the subsurface (Michael et al., 2011; Robinson et al., 2018; Santos et al., 2012). Since different pathways are likely to be differently enriched in nutrients, metals, pollutants, and radionuclides, their biogeochemical implications for the coastal ocean are also likely to differ. Fundamental research has been done in the last years to identify the drivers of advective flows (e.g., Cho et al., 2021; George et al., 2020; Gonneea et al., 2013b; Rodellas et al., 2020) and conceptually describe them (George et al., 2020; Michael et al., 2011; Santos et al., 2012).

Based on the classification made by Garcia-Orellana et al. (2021), the pathways of SGD can be grouped into 5 categories according to their spatiotemporal scale, the groundwater origin, and their driving forces. These pathways are defined as (1) terrestrial groundwater discharge, (2) density-driven seawater circulation, (3) seasonal exchange of seawater, (4) shoreface circulation of seawater, and (5) porewater exchange. The driving forces of advective flow related to each pathway are also indicated below in bold italics and the number in brackets refers to the driving forces shown in Figure **1**.**6**.

1. **Terrestrial groundwater discharge:** meteoric fresh groundwater flow originated from inland recharge and driven by ***terrestrial hydraulic gradients*** (A). This process may occur in the form of submarine springs or through diffusive seepage at the beach face. Despite submarine springs are characteristic of karstic (e.g., Chen et al., 2020; Garcia-Solsona et al., 2010; Tovar-Sánchez et al., 2014) and volcanic (Jeong et al., 2012; Kim and Kim, 2011, 2017) systems, they also may occur in sedimentary basins with high permeabilities and pressure gradients (Santos et al., 2012). Regardless of whether the discharge is diffuse or point-sourced, inflows of meteoric groundwater are specially relevant since it is the only pathway representing a net input of freshwater to the coastal ocean (Luijendijk et al., 2020). The magnitude of this process depends on the terrestrial hydraulic gradient (i.e.,

height of the phreatic level relative to sea level): the higher the hydraulic gradient, the greater the groundwater discharge. Notice however, that for groundwater eventually discharging into the ocean, the aquifer head should be above the sea level, the coastal aquifer should be connected with the sea, and evaporation should not exceed aquifer recharge (Santos et al., 2012). Notice also that the connection between aquifer and sea may occur at the shoreline or further offshore (George et al., 2020).

2. **Density-driven seawater circulation:** flow of seawater associated with ***convection*** (H) driven by thermohaline gradients between originated due to the mixing of terrestrial and marine groundwater in the saltwater wedge of coastal aquifers. The process consists on the natural intrusion of seawater along coastal aquifers and subsequent discharge and it is driven by a combination of forced convection and free or natural convection resulting of fluid density variations (Smith, 2004). The landward extent of the saltwater wedge, and therefore the extent of the seawater recirculation, depends on characteristics of the coastal aquifer (e.g., geometry, saturated thickness) and hydraulic properties (e.g., hydraulic gradient, density gradient) (Kiro et al., 2014; Smith, 2004; Tamborski et al., 2017a).

3. **Seasonal exchange of seawater:** flow of seawater driven by the movement of the freshwater-saltwater interface. Aquifer recharge and sea-level oscillations promotes the movement of the freshwater-saltwater mixing zone forcing groundwater stored in the aquifer to move back and forth (Palacios et al., 2019). Fluxes associated with these process may be as important as those related with tidal pumping or wave set up (Michael et al., 2005). The movement of the interface could be induced by the ***seasonal fluctuations on the water table*** (B) due to variable recharge (Michael et al., 2005), but also by the episodic recharge due to extreme precipitation events (e.g., Adyasari et al., 2021; Palacios et al., 2019; Yu et al., 2017).

4. **Shoreface circulation of seawater:** flow of recirculated seawater at the beach faces, mangroves or salt marshes driven by ***tidal pumping or wave set up*** (C). The process consist on the infiltration of seawater, filling and subsequently draining the nearshore aquifer (Anschutz et al., 2009; Robinson et al., 2018), generating a seawater recirculation cell (i.e., upper saline plume; Robinson et al., 2006) at the upper part of coastal aquifers. The upper saline plume limits in its lower boundary with the freshwater discharge tube, which is also constrained by the saline wedge (Robinson et al., 2007). The extent of the seawater recirculation is largely determined by the process driving the advective flow. Whilst wave set up is often restricted to flushing times on the orders of seconds to minutes and pathways lengths of centimeters, the tidal pumping flushes relatively larger depths (on the scale of meters) within hours or days (Santos et al., 2012).

5. **Porewater exchange:** centimeter-scale exchange of groundwater through the water-sediment interface. This process is governed by disparate driving forces of advective flow (Santos et al., 2012). These driving forces include (D) ***wave pumping*** driven by hydrostatic pressure oscillations, (E) ***flow- and topography- induced pressure gradients***, resulting from the interaction of bottom topography (e.g., ripples, benthic organisms, shells) with current- or wave-driven flows, (F) release of porewater induced by ***ripple migration*** or any resuspension/deposition dynamic, (G) ***shear***-induced groundwater flow formed by water column currents that extend into the bed, generating porewater flows parallel to the sediment surface (Brinkman layer), (H) ***convection*** driven by thermohaline gradients between the overlying water and porewater, (I) ***bioirrigation*** referring to the water flows associated with the flushing of underlying water or sediment reworking made by benthic organisms, (J) ***upwelling of gas bubbles*** generated in the sediment (e.g., $CO_2$, $CH_4$, $N_2$, $O_2$) by disparate biogeochemical processes that induce the creation of porewater recirculation cells in permeable sediments, and (K) ***compaction*** of sediment due to deposition of new sediment at the water-sediment interface inducing the release of stored porewater.

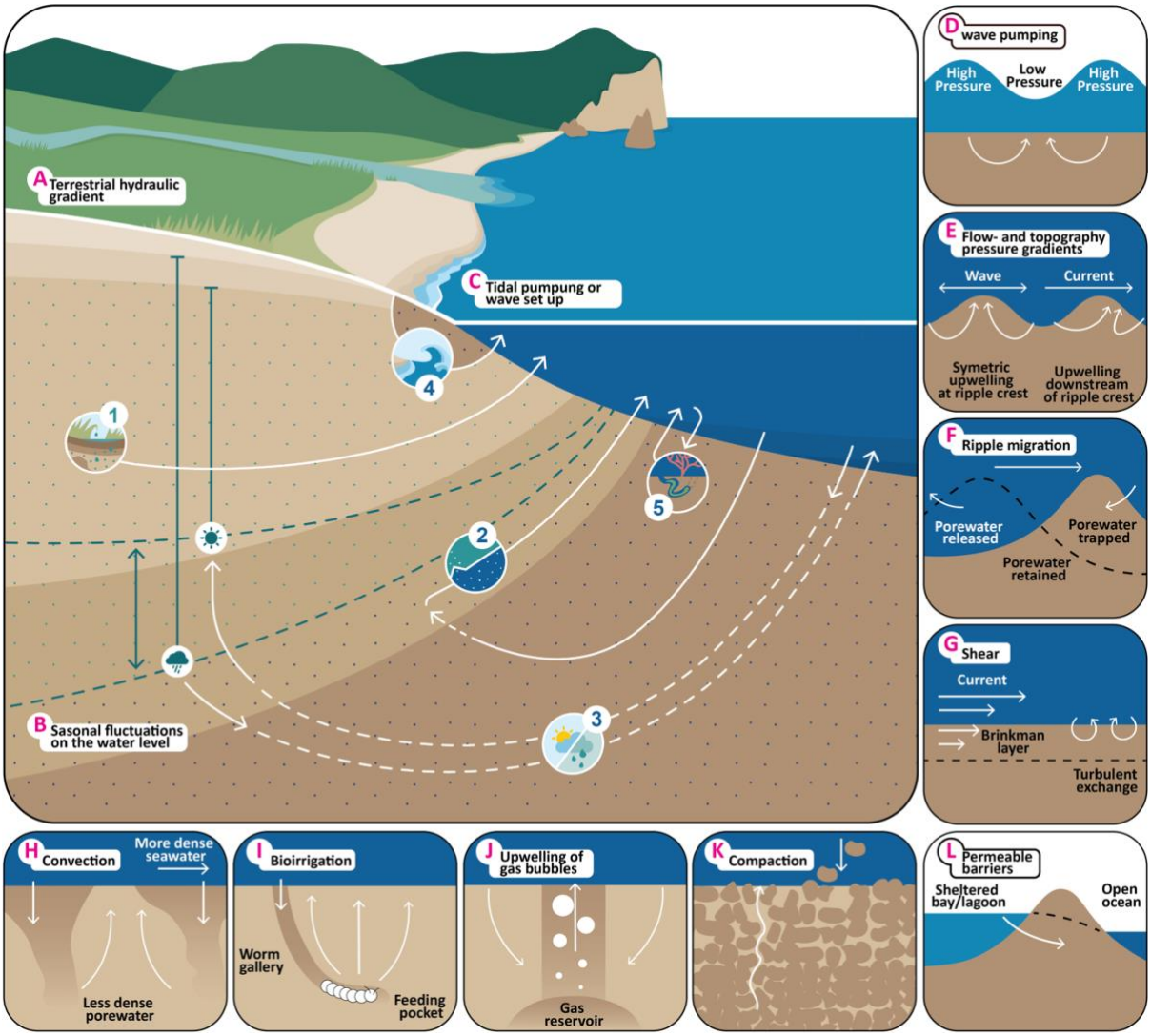


Figure 1.6. Pathways and driving forces of submarine groundwater discharge. Numbers from 1 to 5 refer to the SGD pathways: 1) terrestrial groundwater discharge, 2) density-driven seawater circulation, 3) seasonal exchange of seawater, 4) shoreface circulation of seawater, and 5) porewater exchange (Garcia-Orellana et al., 2021). Capital letters A-L refer to the forces driving advective groundwater flow following Santos et al. (2012). Based on Garcia-Orellana et al. (2021).

Notice that although the above-mentioned pathways may be explanatory of the main groundwater discharge processes occurring in coastal settings, there might be other discharge mechanisms that cannot be included within the definition of the five pathways. This is the case of the advective flow induced by (L) ***water level differences in permeable sand barriers*** which may be an important contributor to the overall water inflows and outflows in coastal lagoons (Tamborski et al., 2019). Also notice that in some cases, water actually discharging into the coastal ocean may be a mixture of groundwater driven by different forces and pathways (e.g.,

terrestrial groundwater often mixes with shoreface or density-driven seawater prior to its discharge). Some of the driving forces described here have been categorized as porewater exchange even though their spatiotemporal scales may be greater than those associate to this process (e.g., convection, upswelling of gas bubbles; Santos et al., 2012).

### 1.2.3. Quantification techniques

The disparate mechanisms driving the discharge of groundwater, as well as the different temporal (seconds to years) and spatial (millimeters to kilometers) scale of the underlying processes makes specially challenging the quantification of SGD. Most of the techniques tend to quantify overlapping processes, which prevents the isolation of specific pathways or driving forces (Taniguchi et al., 2019). Moreover, the applicability of these techniques is often limited to certain spatiotemporal scales, targeting only certain SGD pathways. This hinders the intercomparison of water flows reported by different SGD studies that used different techniques for their calculations. Withal, owing the complexities inherent to the quantification of SGD by using single techniques, the number of studies using multiple approaches have grown in the last years (e.g., Mulligan and Charette, 2006; Rodellas et al., 2021; Sadat-Noori et al., 2017; Taniguchi and Iwakawa, 2004). At the present day, the techniques for quantifying SGD can be grouped into the following categories: direct measurements, hydrological methods, geophysical methods, and geochemical tracing methods (Figure **1**.**7**).

#### *1.2.3.1. Direct measurements*

Direct measurement of SGD involves the use of instruments that enable the collection and quantitative assessment of the water effectively discharging through a certain bed area. Seepage meters is probably the most used tool for this purpose, especially due to low costs and easy fabrication process (Murdoch and Kelly, 2003). This device consists of an inverted bucket (also named benthic chamber) with an outflow port which is connected to a thin plastic bag. The benthic chamber is partially buried in the sediment for a certain time. Then, the flow of water into the chamber can be directly calculated by the change in volume of the plastic bag (Lee, 1977). This technique has been improved over the last decades, first by assessing the error associated with the measurement (e.g., Belanger and Montgomery, 1992), and secondly by installing

automized devices such as continuous head flowmeters (Taniguchi et al., 2003) or water quality sensors (Krupa et al., 1998). Although seepage meters provide a direct measurement of the inflowing groundwater at a specific site, extrapolating to a wider area requires the deployment of many seepage meters to account for the natural variability of heterogeneous systems (Rosenberry et al., 2020). Moreover, this technique may not capture some advective flow processes since the installation of the bucket can hamper small-scale porewater exchange processes.

#### *1.2.3.2. Hydrological methods*

The main techniques regarding hydrological methods for quantifying SGD are water balance approaches, Darcy's law estimates, and hydrological models.

- **Water balances:** the approach consists of constraining all water inputs (e.g., precipitation, injection of water in aquifers) and outputs (e.g., evaporation, surface runoff, pumping of water from aquifers, and groundwater discharge) of water into a specific system (Knee and Paytan, 2011). Since groundwater discharge is usually unknown, it can be determined by means of the difference between all water inputs and outputs (Gwak et al., 2014; Hajati et al., 2019; Taniguchi et al., 2003). The reliability of the method relies on appropriately constraining all terms, and therefore requires an extensive knowledge of the studied system. Some of the limitations related with this method are: (1) it only allows the quantification of fresh groundwater discharge (i.e., terrestrial groundwater discharge), (2) estimates of groundwater discharge may be inaccurate in systems where the magnitude of this process is equivalent to the uncertainties of the other water inputs/outputs (e.g., precipitation, river discharge), and (3) the method is often only applicable to basin- or large-scale areas (Knee and Paytan, 2011).

- **Darcy's law estimates:** groundwater discharge can be addressed by using Darcy's flow estimates. The basis of this method is that the flow is proportional to the cross-sectional area, the hydraulic gradient, and the hydraulic conductivity of the media (Prakash et al., 2018). It furthers assumes that water migrating through a coastal aquifer eventually discharges to the ocean. The method requires firstly the acquisition of data relative to

aquifer water table and sea level to further compute the hydraulic gradient and secondly, obtain a representative value for the hydraulic conductivity. Notice that the method only captures the groundwater of terrestrial groundwater and its main limitations are: (1) it considers that water flows through an homogeneous and isotropic aquifer, and (2) hydraulic conductivity may vary orders of magnitude within an aquifer and vary also with the direction of the flow (Freeze and Cherry, 1979; Knee and Paytan, 2011; Shackelford, 2013).

- **Hydrological models:** analytical and numerical models have been instrumental in the last years to characterize disparate processes affecting the discharge of groundwater to the sea. The models have been used for investigating SGD associated with rainfall events (Guo et al., 2012; Yu et al., 2017), SGD discharging through multi-layered aquifers (Guo and Li, 2015), SGD driven by tidal pumping (Li et al., 2016; Robinson et al., 2007) or wave set up (Anwar et al., 2014), SGD driven by changes in water depths of receiving water bodies (Rodellas et al., 2020), among other processes. Global models have also been used to determine the fresh groundwater discharge (Luijendijk et al., 2020).

#### *1.2.3.3. Geophysical methods*

Geophysical methods often rely on spatial or temporal variations on salinity or temperature. Although some of these methods do not provide a quantification of SGD or associated nutrients, may be instrumental in bridging the gap between basin- or large-scale methods (predominantly based on hydrological methods) and small- or local-scale (direct measurements or geochemical approaches) studies (Taniguchi et al., 2019).

- **Thermal infrared sensing:** anomalies of the sea surface temperature in coastal areas are (in some cases) indicative of groundwater discharge locations. This is based on the seasonal contrast between groundwater and seawater temperature; fresh SGD (and therefore mor buoyant) rise through the denser seawater and can be detected via thermal infrared (TIR) sensing based on the different temperature relative to the surrounding seawater (Garcia-Solsona et al., 2010; Mejias et al., 2008; Tamborski et al., 2015). The data acquisitions is often made by installing a TIR camera on light aircrafts

(e.g., Bejannin et al., 2017; Duarte et al., 2006; Lee et al., 2016a) or on an unmanned vehicles (Lee et al., 2016b; Young and Pradhanang, 2021). Handheld cameras and satellite TIR images can be used to identify small-scale and large-scale temperature variations, respectively (Jou-Claus et al., 2021; Röper et al., 2013; Tamborski et al., 2017c).

- **Geoelectrical methods:** the assessment of the electrical properties of the subsurface is instrumental for understanding the distribution of groundwater salinities in coastal aquifers, which allows the visualization of the freshwater-saltwater interface or the identification of preferential groundwater discharge areas (e.g., Costall et al., 2018; Stieglitz et al., 2007; Zarroca et al., 2014). These methods consist of an array of electrodes that inject current into the earth, which is then measured by other electrodes (Costall et al., 2018). The resistivity (inverse of conductivity) of the current depends on several factors inherent to the aquifer solids (e.g., porosity, clay content) and groundwater composition (e.g., salinity, temperature) (Palacios et al., 2019). In coastal aquifers, where freshwater mixes with seawater, the spatial variations on resistivity can be mostly associated with variations in groundwater salinity (Taniguchi et al., 2019). The electrodes can be deployed in different arrangements: on the ground surface (e.g., Breier et al., 2005; Swarzenski et al., 2006; Zarroca et al., 2014), directly into the ground (e.g., in piezometers wells; Palacios et al., 2019), on the land-sea interphase (electrodes array partially on the ground and on the sea surface), or towed by a boat (e.g., Manheim et al., 2004; Su et al., 2014).

- **Bathymetry and seismic profiling:** the investigation of the seafloor and sub-bottom sediments can be instrumental to identify origins and pathways of groundwater discharge (e.g., George et al., 2020; Goff, 2019; Virtasalo et al., 2019). The basis of these methods consists of the identification of geological features commonly associated with preferential pathways of groundwater flow (e.g., fractures, paleochannels, pockmarks) by mapping the surface and subsurface of the seabed using tools such as multibeam bathymetry or seismic profiling.

- **Eddy correlation:** the technique consists on estimating groundwater discharge based on the continuous measurement of the vertical velocity, temperature and/or salinity at the bottom of the water column (5 – 15 from the seabed) (Crusius et al., 2008). The method assumes that turbulent mixing is the dominant vertical transport in the water column near the water-sediment interface. Head or salinity steady-state mass balances can be used to determine heat or salinity eddy flux, which can be subsequentially transformed to a groundwater flux if there is enough temperature and salinity contrast between groundwater and the surrounding water (Crusius et al., 2008; Ganju, 2011; Hu and Hemond, 2020).

#### *1.2.3.4. Geochemical methods*

Geochemical methods involving the use of tracers have been by far the most employed techniques for quantifying SGD and derived fluxes of dissolved compounds to the coastal ocean (Figure **1.7**). Tracers commonly used to estimate groundwater flows are often naturally present in groundwater (and in higher amounts than in seawater) and present a conservative behavior (or easy to model) in seawater.

Although it only captures the discharge of fresh groundwater, perhaps the most obvious tracer of SGD is ***salinity***. Variations in salinity of coastal waters can be often attributed to the discharge of groundwater if no other sources of freshwater exist in the study site. Several studies have used salinity balances, sometimes combined with other tracers, to estimate SGD (e.g., Charette, 2007; Crotwell and Moore, 2003; Crusius et al., 2005). The main limitations of salinity as SGD tracer are that it does not capture the recirculated fraction of SGD, and it has interferences with other sources of freshwater (e.g., surface runoff).

Among all different SGD tracers, the ***radioactive isotopes*** of Ra isotopes and Rn are undoubtedly the most common (Garcia-Orellana et al., 2021). Actually, these radionuclides were used in 40% of the total SGD studies published between 2015 and 2019 (Taniguchi et al., 2019). These tracers are valuable tracers of SGD because (1) groundwater is enriched in Ra isotopes and Rn, since they are produced by their direct parents from rocks or sediments in the aquifers; (2)

they are useful for distinguishing origins and pathways of groundwater, since they belong to different decay chains (U and Th), (3) their different half-lives enable the assessment of processes occurring at different temporal scales; (4) they behave conservative in the coastal ocean; and (5) the coastal ocean integrates the signal of Ra isotopes and Rn entering through disparate groundwater pathways, allowing smoothing spatiotemporal variations inherent to SGD (Burnett et al., 2001).

Other U- and Th-series radionuclides have been employed to assess SGD. For instance, Charette et al. (2008) introduced new potential applications of uranium, since its depletion in coastal waters relative to offshore waters may be mediated by the continuous removal of this element due the recirculation of groundwater through coastal sediments. Thus, uranium is likely to be a good proxy for evaluating the recirculated fraction of SGD (Moore and Shaw, 2008). The daughter of $^{224}$Ra, thoron ($^{220}$Rn; $T_{1/2}$ = 56 s) has also been employed to identify preferential paths for groundwater discharge since one must be very close to the groundwater source to detect the short-lived radionuclide (Chanyotha et al., 2018, 2014; Swarzenski et al., 2017). The pair of isotopes $^{224}$Ra:$^{228}$Th has been also used for determining fluxes of porewater exchange (Cai et al., 2015, 2014; Hong et al., 2018). The method is based on the disequilibrium between the exchangeable activities of $^{224}$Ra (which is highly mobile) and $^{228}$Th (mainly adsorbed onto sediment surfaces) in shallow sediments (Cai et al., 2012).

***Other tracers*** of groundwater discharge include stable isotopes ($\delta^{18}$O and $\delta^{2}$H; Godoy et al., 2013; Rocha et al., 2016), silica (Oehler et al., 2019), methane (Cable et al., 1996a; Dulaiova et al., 2010; Kim and Hwang, 2002), and dissolved organic matter (DOM) through humification index (Nelson et al., 2015).

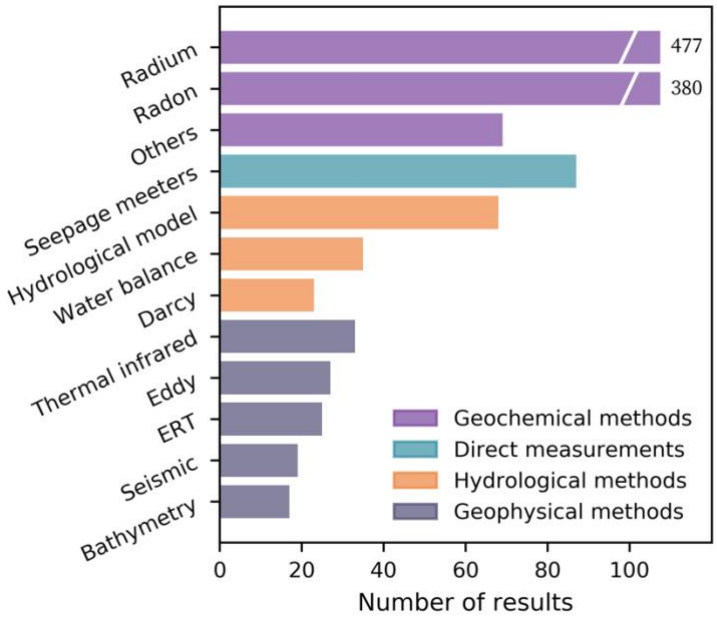


Figure 1.7. Systematic review of articles published containing the keywords 'submarine groundwater discharge' or 'submarine springs' and where methods to assess SGD (y-axis) are described. Notice that for some methods several keywords have been used (e.g., Radium: 224Ra, Ra-224, Radiu-224, etc.). The method ascribed as 'Others' refers to the use of tracers such as silica, $^{18}O$, and $^{2}H$. The research has been performed by using the research engine Web of Science on 28$^{th}$ of December, 2021.

### 1.2.4. Magnitude and implications

Most of the research related to SGD has been focused on the evaluation of water fluxes and those chemicals transported by this process. Unsurprisingly, the journals in which most of the SGD research is published belong to the subjects of oceanography; marine sciences, hydrology, and geosciences; and environmental sciences (Ma and Zhang, 2020). Besides its implication on global geochemical budgets, SGD has important implications in other areas of knowledge that have received lesser attention. The implications for marine biota (Lecher and Mackey, 2018), the role of microorganisms (Ruiz-González et al., 2021), or the social dimension (Alorda-Kleinglass et al., 2021; Erostate et al., 2020; Moosdorf and Oehler, 2017; Taniguchi et al., 2019) have been often overlooked in SGD studies.

#### *1.2.4.1. Hydrological*

Estimating the global significance of SGD in the total flows of water from the continents to the ocean is challenging. Hydrologists have been trying to provide a value for fresh groundwater discharge since the early '70s by means of water balances (see Taniguchi et al.,

2002). Early estimates of fresh SGD varied in orders of magnitude representing from 0.01 to 10% of the total river discharge (Garrels and Mackenzie, 1971; Nace, 1970; Zektser and Loaiciga, 1993; Zektzer et al., 1973). The first global estimate of fresh SGD based on local SGD seepage meters observations was presented by Taniguchi et al. (2007), who reported water flows similar to those previously reported by using hydrological methods (~7% of the river discharge). Sawyer et al. (2016) reported similar water flows relative to surface runoff (~6%) for the United States based on water budged analysis and continental hydrography and climate data. However, recent estimates of fresh SGD based on water budgets (Zhou et al., 2019), and numerical modelling (Luijendijk et al., 2020) suggest lower contributions of fresh groundwater discharge relative to total water inputs (1.3% and 0.6%, respectively) (Figure **1.8**).

Total estimates of SGD including not only the fresh component but also all processes involving the recirculation of seawater have also been determined at different scales (e.g., Kwon et al., 2014; Moore et al., 2008). Although some studies have shown that fresh SGD may represent a significant fraction of total SGD (16%, Garrison et al., 2003; 40%, Knee et al., 2010; 29%, Taniguchi et al., 2005), this estimates may be biased due to the selection of sites where fresh SGD exists. Conversely, many studies have shown that fresh SGD may represent less than 10% of the total SGD (Burnett et al., 2003a; Li et al., 1999; Riedl et al., 1972; Shellenbarger et al., 2006; Taniguchi, 2006). In comparison with riverine inputs Riedl et al. (1972) suggested that fluxes associated with the exchange of seawater in permeable shelf sediments (subtidal pumping) may be up to 2.5 higher than surface runoff. Moore et al. (2008) concluded that total SGD (fresh and saline) into the Atlantic Ocean may represent from 0.8 to 1.6 of the total riverine inputs, Rodellas et al. (2015) found that total SGD to the Mediterranean Sea was equal or larger by a factor 16 than riverine inputs, and a recent near-global estimate based on $^{228}$Ra inventories presented higher relative SGD flows, representing 3 to 4 times the discharge from rivers (Kwon et al., 2014).

#### *1.2.4.2. Geochemical*

Submarine groundwater discharge has been recognized as an important process regulating the transfer of solutes from land to the ocean (Santos et al., 2021). However, the implications of fresh and marine SGD are different since they are differently enriched in dissolved

compounds. On its way to the ocean, fresh groundwater is enriched in nutrients, metals, carbon, pollutants, and dissolved compounds, which originate from natural (e.g., vegetation, soils, sediments, microorganisms) or anthropogenic (e.g., agriculture, mining, industry) sources. When it eventually discharges, fresh SGD represent a net input of water and nutrients (Slomp and Van Cappellen, 2004). Conversely, saline water recirculating through coastal aquifers is often enriched with recycled nutrients, which are product of several biogeochemical transformations such as organic matter degradation (Santos et al., 2009; Wilson, 2005). Nitrogen, phosphorus, and silica can be slowly released from coastal sediments to the coastal ocean by saline SGD, which may represent a major source of this nutrients in areas with absence of any other nutrient input (Beck et al., 2017; Charbonnier et al., 2013; Rodellas et al., 2020). At global scale, loads of dissolved inorganic nitrogen (DIN), dissolved silica (DSi), and dissolved inorganic phosphorus (DIP) derived from saline SGD are expected to be much higher than those derived from fresh SGD (Cho et al., 2018; George et al., 2020).

In the last decades, several studies have demonstrated the relative significance of nutrient fluxes driven by SGD relative to riverine discharge or atmospheric deposition at global-, basin-, or local-scale. Rodellas et al. (2015) estimated that SGD-driven inputs of DIN, DIP, and DSi to the Mediterranean Sea may equal or exceed those from riverine discharge and atmospheric deposition. Zhang et al. (2020) compiled and upscaled local SGD studies to the whole China coastline and concluded that nutrients driven by SGD may be higher than 50% of the total nutrient sources including rivers, atmospheric deposition, and diffusion from sediments. An extensive review on local-scale SGD studies concluded that in almost a half of the compiled studies, SGD-driven nutrients exceeded river fluxes (Figure 1.6; Santos et al., 2021). These results emphasize the global importance of SGD, not only because of its contribution to nutrient ocean budgets, but especially because the ubiquitous character of SGD (specially along muddy and permeable sediments shorelines) makes it a fundamental process in those areas with absence of any other nutrient input.

Trace metals can be also released to coastal seawater through submarine groundwater discharge (e.g., Qu et al., 2020; Rodellas et al., 2014; Trezzi et al., 2016). For instance, fluxes of Ag, Co, Ni, and Zn driven by SGD in Jamaica Bay (USA) were found to be comparable with those

discharging through wastewater (Beck et al., 2009). SGD-driven Fe and Mn fluxes into de Sepetiba Bay (Brasil) were comparatively higher than those driven by riverine discharge (Sanders et al., 2012). SGD has also been recognized as a major pathway of trace metals in the Hampyeong Bay (Korea) (Rahman et al., 2013), in Bohai and Jiaozhou Bay (China) (Qu et al., 2020; Wang et al., 2019), and in the western Mediterranean Sea (Trezzi et al., 2016).

Submarine groundwater discharge may also be an important source of other dissolved compounds such as carbon (e.g., Chen et al., 2018b; Correa et al., 2020; Liu et al., 2014), barium (Shaw et al., 1998), strontium (Trezzi et al., 2017), rare earth elements (Johannesson et al., 2011; Johannesson and Burdige, 2007; Kim and Kim, 2011), and contaminants (Amato et al., 2016; Sawyer et al., 2016; Zhang et al., 2020).

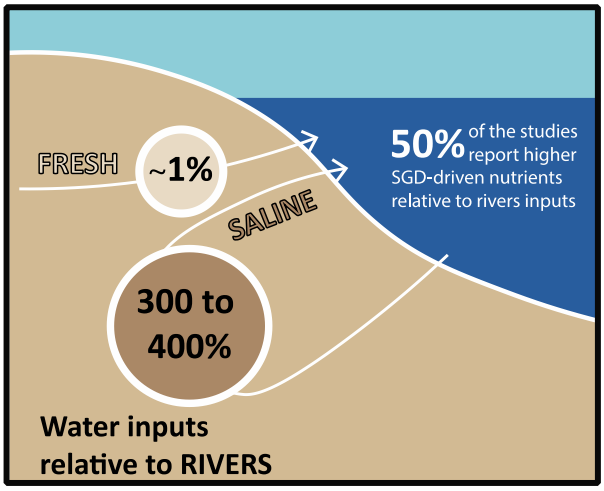


Figure 1.8. Global significance of SGD and SGD-derived nutrients to the coastal ocean. Percentages of SGD-water flows are expressed in relation to riverine inputs. Based on the estimations of Luijendijk et al. (2020) and Zhou et al. (2019) for freshwater inputs, Kwon et al. (2014) for saline water inputs, and Santos et al. (2021) for SGD-derived nutrient inputs.

#### *1.2.4.3. Biological*

Coastal environments are impacted by SGD which can modify temperature, salinity, and chemistry of the coastal waters. Environmental conditions generated by SGD can sustain or deteriorate entire ecosystems impacting in marine biota, from bacteria and phytoplankton to marine animals (Lecher and Mackey, 2018). Nutrients supplied by SGD, especially nitrogen and phosphorus, may relieve nutrient limitation conditions, enhancing the primary production of coastal zones (Andrisoa et al., 2019b; Garcés et al., 2011; Honda et al., 2018; Machado and

Imberger, 2014; Su et al., 2014). For instance, many studies documented diatom blooms induced by SGD (Lecher et al., 2016, 2015; Liefer et al., 2009) and its cascading effects. These effects include the nutrient transformation from inorganic to organic that can be subsequentially utilized by other genera (Gobler and Sañudo-Wilhelmy, 2001; Lee and Kim, 2007; Mackey et al., 2012). Groundwater salinity may also affecting the abundance and types of species in the area influenced by the discharge (Álvarez-Góngora and Herrera-Silveira, 2006; Lecher et al., 2017; Welti et al., 2015). Microorganisms, like viruses and bacteria, naturally present in groundwater or derived from anthropogenic sources (e.g., *Escherichia coli*; De Sieyes et al., 2008; Futch et al., 2010; Knee et al., 2008) can be also transported to the coastal ocean through SGD. Although the metabolic functions of these microorganisms are far from being understood, they may play a significant role in altering the composition of groundwater geochemical composition (Ruiz-González et al., 2021; Santoro et al., 2008; Seibert et al., 2020).

Loads of nutrients driven by SGD to the coastal ocean also affect macrophytes (microalgae and marine plants). These organisms uptake nutrients from the water column, through leaves and blades, or from porewater and sediments through their roots (Lecher and Mackey, 2018). Whilst some studies documented positive feedback between nutrient inputs and macroalgae blooms in areas where SGD is severely polluted with DIN (e.g., *Ulva spp*. ; Kwon et al., 2017; Takeuchi et al., 2017; Zhao et al., 2021), other have found negative responses to nutrient inputs by some benthic genera of macrophytes (e.g., *Zostera marina*; McClelland et al., 1997; Short and Burdick, 1996; Valiela et al., 1992).

The effect of SGD on marine animals has also been documented for corals, meiofauna, and benthic macrofauna, among others (e.g., Gagan et al., 2002; Ouisse et al., 2011). The low salinity, low pH, and excessive nutrient loading associated with SGD may have a negative influence on both the coverage and variety of coral species diversity (Amato et al., 2016; Crook et al., 2012; Lirman et al., 2003). Small animals (<500 µm in length) living in muddy and sandy sediments (meiofauna, e.g., warms, nematodes) may be positively or negatively affected in sites influences by groundwater discharge. Whilst some studies reported higher richness and diversity of these organisms in SGD-affected sites (Encarnação et al., 2013), others found the opposite pattern (Kotwicki et al., 2014; Migné et al., 2011). The stable environmental conditions and the

increased primary production in sites influenced by SGD promote the dominance of specific macrofauna species (e.g., marine worms, isopods, snails, crabs, oysters, mussels; Andrisoa et al., 2019a; Chen et al., 2018a; Encarnação et al., 2015; Miller and Ullman, 2004; Utsunomiya et al., 2017), including some fish species (e.g., *Lateobrax japonicas*, *Acanthopagrus schlegelii*, *Pseudopleuronectes yokohamae*; Hata et al., 2016; Utsunomiya et al., 2017).

#### *1.2.4.4. Social*

Submarine groundwater discharge has been studied fundamentally through the prism of natural sciences, with major efforts on understanding the process itself (e.g., driving forces, pathways) and its implications for the marine environment. On the contrary, the social dimension, including the economic, politic, and cultural implications of groundwater discharge has been barely studied. However, this trend is changing since the need for interdisciplinary research is becoming fundamental for understanding the interplay between society and environment. The publication of studies solely focusing on social aspects of SGD or literature reviews including sections regarding this topic evidences this shift (Alorda-Kleinglass et al., 2021; Erostate et al., 2020; Moosdorf and Oehler, 2017; Santos et al., 2021; Taniguchi et al., 2019).

There are many evidences that SGD played an important cultural role on the development of some ancient societies (Alorda-Kleinglass et al., 2021). Moosdorf and Oehler (2017), in their extensive review about societal uses of fresh SGD, describe, for instance, how some submarine springs were used as a freshwater resource since Mesopotamian times (~3000 BCE). Submarine springs are also present in many tales, legends and myths (Clendenon, 2009) and some places toponyms are given after the occurrence of SGD such as 'Olhos de água' ('eyes of water' in Portuguese; Carvalho et al., 2013) in Portugal, 'Punalu'u' ('driving spring' in Hawaiian; Moosdorf and Oehler, 2017) in Hawaii, and 'Sa font de sa cala' ('the spring of the cove' in Catalan; Alorda-Kleinglass et al., 2021) in Spain. At the present day, SGD continuous to be used for drinking, hygiene, agriculture, among other purposes (Moosdorf and Oehler, 2017).

Economic assessment of SGD is challenging since it requires the understanding of all different trade-off and synergies that the discharge of groundwater may generate (Alorda-Kleinglass et al., 2021). For instance, SGD can be understood as a freshwater resource, but it can

also be understood as the main nutrient supply for coastal fisheries. Both freshwater and fisheries can be exploited by coastal societies but knowing which use of these resources is more beneficial or economic for society requires profound investigation. Several authors attempted to estimate the economic costs of using SGD as a resource. For instance, Pongkijvorasin et al. (2010) examined the economic management of SGD in Kona (Hawaii) by using a model that linked groundwater and nearshore resources. Duarte et al. (2010) evaluated the trade-off between pumping groundwater and growth rate of the valuable marine algae. Burnett et al. (2018) developed a model to assess the interplay between groundwater pumping and the effects on nearshore fisheries. These assessments may be valuable for stakeholders and politicians for taking decisions and legislating on the use of ecosystem services provided by SGD (Alorda-Kleinglass et al., 2021; Erostate et al., 2020)

# Chapter 2: Objectives

Research on submarine groundwater discharge has been closely linked to the use of the radioactive tracers of Ra isotopes and Rn. At the present day, the tracers represent the most extensive and widespread tool for investigating the magnitude and implications of this process in a wide variety of environments, from small coves to the entire ocean. More than 30 years of research in this field have provided unvaluable knowledge, both about the process and about the tracers, and yet there are many questions that remain unsolved or need to be settled.

In this context, the Thesis presented here aims at improving the application of Ra isotopes and Rn as tracers of groundwater processes, from quantification techniques, the investigation of the physical and chemical processes affecting their distribution in groundwater, to their its application to hydrological and oceanographical processes, with especial emphasis on the study of submarine groundwater discharge.

Thus, the main goal of this thesis is addressed through three specific objectives linked to the research gaps described below:

**Objective 1:** The Radium Delayed Coincidence Counter (RaDeCC) is one of the most used equipment for quantifying Ra isotopes and related radionuclides. Despite the system has been in use since its development in 1996, no exhaustive evaluation has been made on assessing its quantification limits. The first specific objective of this Thesis is therefore to ***improve the Ra isotopes quantification techniques with the RaDeCC system*** by assessing its quantification thresholds to provide detailed quantification guidelines.

**Objective 2:** The use of Ra isotopes and Rn in hydrological studies is very limited, mainly because their behavior in groundwater is complex and the transport models used to describe this behavior are very simple. The second specific objective of this thesis is to ***provide a comprehensive analysis of the processes controlling the activities of Ra isotopes and Rn, and their activity ratios*** ($^{224}Ra/^{228}Ra$ and $^{222}Rn/^{226}Ra$) ***in groundwater***, by means of a new advective transport model. Furthermore, the model is used to present novel applications, which interrelate

the disciplines of hydrogeology (determination of groundwater transit times) and coastal oceanography (evaluating pathways and endmembers of submarine groundwater discharge).

**Objective 3:** The effect of extreme meteorological, hydrological, or oceanographical events on SGD and nutrient fluxes to the coastal ocean are barely described in the literature. This hinders the assessment of the role that these events may have for the coastal environment, or its implications for annual estimates. The third specific objective of this Thesis is to ***use the Ra isotopes for evaluating the significance of SGD and associated nutrient fluxes induced by extreme precipitation events*** in a Mediterranean coastal zone, the implications of neglecting these events on annual estimates, and its importance in the context of climate change.

# Chapter 3: Analytical methods

## 3.1. Ra isotopes, Rn, and nutrients in water

### 3.1.1. Preconcentration of Ra isotopes in Mn-fibers

The measurement of Ra isotopes in water generally requires collecting large water samples to obtain detectable sample activities. The typical sample volumes range from 50 to 200 L for coastal seawater, >200 L for open ocean water, and between 5 to hundreds of liters for groundwater (e.g., Le Roy et al., 2019; Molina-Porras et al., 2017a; Rodellas et al., 2017). After collection, the water samples are filtered through $MnO_2$-impregnated acrylic fibers (hereinafter Mn-fibers) that quantitatively extract Ra isotopes from solution (Figure **3.1**). The extraction method, pioneered by Moore and Reid (1973), enables the relatively fast preconcentration of Ra (filtration rate should be <1 L $min^{-1}$) onto 20 to 25 g of fiber that can be directly measured with minor preprocessing techniques (see Section 3.1.2).

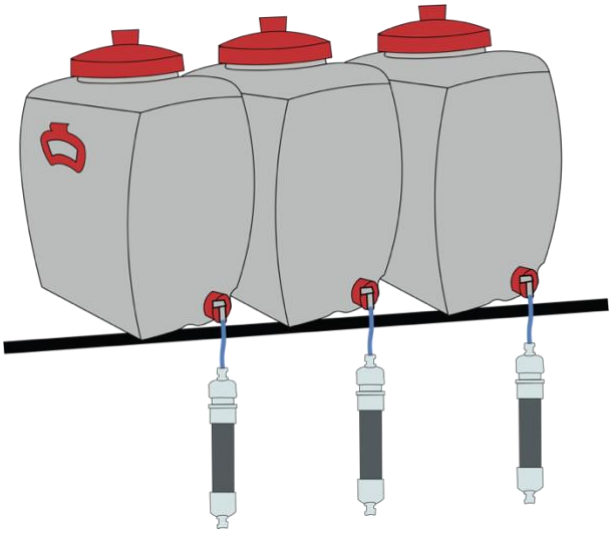

Figure 3.1. Schematic diagram of the gravity filtration of water samples through cartridges filled with Mn-fibers.

### 3.1.2. Ra isotopes through Radium Delayed Coincidence Counter (RaDeCC)

The Radium Delayed Coincidence Counter (RaDeCC) has become the most extensively used equipment to measure and quantify $^{223}Ra$ and $^{224}Ra$ isotopes in water samples (Figure **3.2**). The simplicity and sensitivity of the detection technique, the relatively low operational cost, and

its portability are some of its most valuable features that contributed to its worldwide expansion (the RaDeCC system is present in 68 universities and research centers from 26 different countries; Scientific Computer Instruments, 2021). More recently, the system has also been adapted for quantifying the activities of the long-lived Ra isotopes ($^{228}$Ra and $^{226}$Ra) (Geibert et al., 2013; Moore, 2008; Waska et al., 2008).

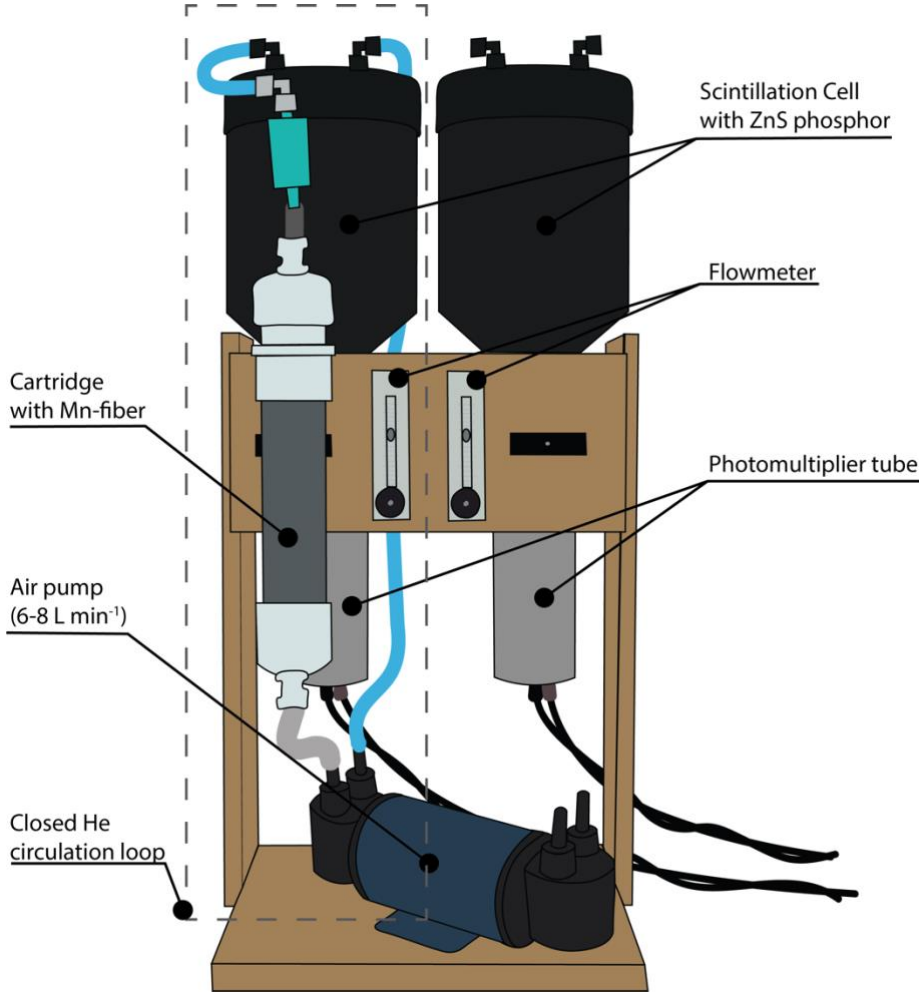


Figure 3.2. Schematic diagram of the Radium Delayed Coincidence Counter (RaDeCC).

#### *3.1.2.1. Description of the detection method*

Before measurement with the RaDeCC system, the Mn-fibers are rinsed with Ra-free deionized water to wash out any particles and sea salt and partially-dried to a water-fiber ratio of 1:1 (Sun and Torgersen, 1998; Moore, 2008). The samples are then placed in a sample chamber

connected to a closed He-circulation loop (Figure **3**.**2**). The He gas carries the decay products of adsorbed $^{223}$Ra and $^{224}$Ra ($^{219}$Rn and $^{220}$Rn, respectively) from the sample chamber to a 1.1 L ZnS phosphor scintillation cell (Lucas cell). When an alpha particle resulting from the decay of Rn (or its daughters) strikes the ZnS, light is emitted. Then, a photomultiplier tube (PMT) connected to the cell converts the light into an electronic pulse, which is amplified and directed to a delayed coincidence circuit (DCC). The DCC, originally pioneered by Giffin et al. (1963) for the assay of $^{219}$Rn and $^{220}$Rn from a 5 mL acid solution containing their parents ($^{231}$Pa and $^{232}$Th, respectively), was later adapted for short-lived Ra isotopes measurements (after pre-concentration onto Mn-fibers) by Moore and Arnold (1996). The DCC discriminates between $^{223}$Ra and $^{224}$Ra, based on the half-lives of the $^{219}$Rn and $^{220}$Rn daughter isotopes ($^{215}$Po and $^{216}$Po, respectively) (Figure **3**.**3**).

After any alpha decay is detected in the scintillation cell, three electronic circuits are triggered: the 219, the 220 and the Total circuit (Figure **3**.**3**). The electronics of the 219 and 220 circuit are designed to record a count only if it occurs within a specific time interval. After a delay of 0.01 ms ($t_{D\text{-}219}$) from the triggering event (to allow the elimination of the triggering pulse; Giffin et al., 1963), the 219 circuit is opened for 5.6 ms ($_{tG\text{-}219}$) (~3·$T_{1/2}$ of $^{215}$Po) registering any subsequent event in the so-called 219 channel. Simultaneously, the 220 circuit is opened for 600 ms ($t_{G\text{-}220}$) (~4·$T_{1/2}$ of $^{216}$Po) with a previous delay of 5.61 ms ($t_{D\text{-}220}$) to reduce the probability of a $^{215}$Po produced from $^{219}$Rn decaying in this time interval. Any decay event occurring within this time interval is recorded in the 220 channel. The Total channel records every decay event during the measurement period. Apart from the Rn-Po pairs, any other alpha decay products of $^{223}$Ra, $^{224}$Ra and $^{226}$Ra (e.g., $^{222}$Rn, $^{218}$Po, $^{214}$Po, $^{212}$Bi, $^{211}$Bi) can also trigger or be counted in the three-circuit system.

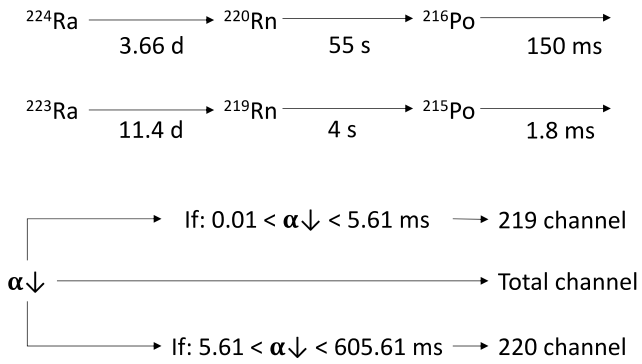


Figure 3.3. Decay systematics of $^{224}$Ra and $^{223}$Ra and schematic diagram of the delayed coincidence circuit (DCC). The symbol $\boldsymbol{\alpha}\downarrow$ represents an $\boldsymbol{\alpha}$-decay. Based on Moore and Arnold (1996).

Giffin et al. (1963) developed the chance coincidence equation to determine the number of random events occurring within the opening time of each gate ($Y\ CC$). To do so, the number of triggering events (i.e., events that initiate the opening of the circuits) and the opening time of the gate ($t_G$) should be known. Whilst the opening time of the gate can be configured from the RaDeCC set up, the number of triggering events is calculated after performing a measurement by subtracting the coincident events (219 and 220 channel) from the total number of events (Total channel) (Equation 3.1).

$$\boldsymbol{Y\ CC} = \frac{(\boldsymbol{cpmTot - cpm219 - cpm220})^2 \boldsymbol{t_G}}{\boldsymbol{1 - (cpmTot - cpm219 - cpm220) t_G}} \qquad \text{Equation 3.1}$$

#### *3.1.2.2. Short-lived Ra isotopes*

The activities of $^{223}$Ra and $^{224}$Ra in the Mn-fibers or Mn-cartridges can be directly determined by using the count rate of the 219 and 220 channel. To do so, Moore and Arnold (1996) developed a detailed quantification protocol not only to correct the count rate recorded in each channel for chance coincidence but also for 219-220 cross-talk interferences i.e., the number of counts relative to Rn-Po events that are registered in the non-respective channel. For high activity measurements (>10 cpm in the Total channel), Moore and Arnold (1996) recommended the use of the count rate in the Total channel corrected for background in order

to determine the $^{224}$Ra activities. The associated uncertainties derived from the counting were developed in Garcia-Solsona et al. (2008).

The common procedure to quantify both $^{223}$Ra and $^{224}$Ra activities from water samples using the RaDeCC system usually involves multiple measurements (Moore, 2008). The first run is conducted shortly after sample collection (1 - 5 days) to determine $^{223}$Ra and $^{224}$Ra activities. In case of high activities of $^{224}$Ra (>7 cpm in the 220 channel; Scholten et al., 2010), a second measurement is performed a week later to quantify $^{223}$Ra, when the $^{224}$Ra has decreased by ~75%, thereby reducing the $^{220}$Rn-$^{216}$Po chance coincidence events in the 219 channel. To determine the excess activities of $^{223}$Ra and $^{224}$Ra (i.e., activity not supported by the parent; $^{223}Ra_{ex}$ and $^{224}Ra_{ex}$) an additional measurement is performed 21 and/or 3 months after sample collection for quantifying the activities of the parent radionuclides $^{228}$Th and $^{227}$Ac, respectively.

#### *3.1.2.3. Long-lived Ra isotopes*

The activities of $^{228}$Ra can be determined with the RaDeCC system by evaluating the ingrowth rate of $^{228}$Th produced by the decay of $^{228}$Ra within the months following the sample collection. The method, developed by Moore (2008), consists on comparing the initial activity of $^{228}$Th adsorbed onto the fiber with that produced by the decay of $^{228}$Ra, after a certain elapsed time necessary to produce distinguishable amounts of $^{228}$Th associated with the decay of $^{228}$Ra. At least two measurements are necessary for applying this method, the first one conducted ~21 days after sample collection (to ensure the decay of $^{224}$Ra) for quantifying the initial $^{228}$Th in the sample, and the second measurement generally conducted 6 month after sample collection allowing significant ingrowth of $^{228}$Th. The activities of $^{228}$Th in both the first ($^{228}Th_1$) and second ($^{228}Th_2$) measurement are used for the quantification of $^{228}$Ra following the Bateman equations:

$$^{228}Ra = \frac{\lambda_{Th228}-\lambda_{Ra228}}{\lambda_{Th228}} \cdot \frac{^{228}Th_2 - {}^{228}Th_1 e^{-\lambda_{Th-228}t}}{e^{-\lambda_{Ra228}t} - e^{-\lambda_{Th228}t}} \qquad \text{Equation 3.2}$$

where $\lambda_{Th-228}$ and $\lambda_{Ra-228}$ are the decay constants of $^{228}$Th and $^{228}$Ra, respectively, and $t$ is the time elapsed from sample collection to the second measurement.

The activities of $^{226}$Ra can be quantified with the RaDeCC system by using the ingrowth rate of $^{222}$Rn (Geibert et al., 2013). Since $^{222}$Rn is continuously produced by the $^{226}$Ra adsorbed onto the fiber, significant amounts of $^{222}$Rn are produced if the measurement is long enough (>600 min). The count rate in the Total channel can be used to track the ingrowth rate of $^{222}$Rn and hence quantifying the $^{226}$Ra activities (Geibert et al., 2013). Alternatively, $^{226}$Ra can be also determined following the method described by Waska et al. (2008) which consists of hermetically sealing the Mn-fibers in a column for a few days and subsequently measuring the ingrown of $^{222}$Rn with the RaDeCC system.

#### *3.1.2.4. Efficiency of the RaDeCC system*

The efficiency of the RaDeCC counter for $^{223}$Ra and $^{224}$Ra measurements is usually calculated using single-tracer standards with known activities of $^{227}$Ac (in radioactive equilibrium with $^{223}$Ra) and $^{232}$Th (in radioactive equilibrium with $^{228}$Th and $^{224}$Ra) to calibrate the 219 channel (for $^{223}$Ra) and 220 channel (for $^{224}$Ra), respectively (Moore and Cai, 2013; Scholten et al., 2010). The total efficiency for determining $^{223}$Ra and $^{224}$Ra activities is a function of: (1) the fraction of the total decay events occurring within the scintillation cell (apparent system efficiency, $f_S$); (2) the fraction of alpha particles generated in the scintillation cell producing pulses that can be recorded by the photomultiplier tube (apparent cell efficiency, $f_C$); (3) the fraction of Rn that emanates from the sample (Mn-fiber, cartridge or sediment) (emanation efficiency, $f_E$) and (4) the fraction of Po events decaying between $t_D$ and $t_D$ + $t_G$, where $t_D$ is the delay time and $t_G$ is the opening time of the electronic circuits (gate efficiency, $f_{G-219}$ and $f_{G-220}$ for 219 and 220 circuits, respectively).

The Total efficiency of the 219 and 220 circuits (E 219 and E 220, respectively) can be theoretically calculated using Equations 3.3 and 3.4, respectively (Giffin et al., 1963).

$$\boldsymbol{E_{219} = f_{S-219} f_C^{\,2} f_E f_{G-219}} \qquad \text{Equation 3.3}$$

$$E_{220} = f_{S-220} f_C^{\,2} f_E f_{G-220} \qquad \text{Equation 3.4}$$

Notice that for a Rn-Po coincident event the detector should record two alpha decays and therefore, the cell efficiency is squared. Approximate values for these efficiencies are shown in Table 3.1 based on Giffin et al. (1963), Moore and Arnold (1996) and Moore and Cai (2013).

Table 3.1. Terms, definitions, and approximate values for RaDeCC counter efficiencies based on Giffin et al. (1963), Moore and Arnold (1996) and Moore and Cai (2013).

| Term | Definition | Values |
|---|---|---|
| *E 219 channel* | Total efficiency of the 219 channel | 0.49 |
| *E 220 channel* | Total efficiency of the 220 channel | 0.54 |
| $E_{Ra\text{-}226}$ | Total efficiency for $^{226}$Ra determination | 0.51 |
| $f_{S\text{-}219}$ | Apparent system efficiency of the 219 channel | 0.80 |
| $f_{S\text{-}220}$ | Apparent system efficiency of the 220 channel | 0.85 |
| $f_C$ | Apparent cell efficiency | 0.86 |
| $f_E$ | Emanation efficiency | 0.95 |
| $f_{G\text{-}219}$ | Gate efficiency of the 219 channel | 0.88 |
| $f_{G\text{-}220}$ | Gate efficiency of the 220 channel | 0.91 |

### 3.1.3. Long-lived Ra isotopes through gamma spectrometry

One of the most common techniques to quantify the activities of long-lived Ra isotopes ($^{226}$Ra and $^{228}$Ra) in water is the use of gamma spectrometers. This technique presents several advantages relative to the measurement with the RaDeCC system: (1) it requires a single measurement to concurrently determine $^{226}$Ra and $^{228}$Ra; (2) it does not require long waiting times (~6 months) for the measurement of $^{228}$Ra since it does not rely on $^{228}$Th ingrowth; and (3) the relative uncertainties are typically much lower than those derived from the RaDeCC system (5-10%) (Geibert et al., 2013; Moore, 2008; Waska et al., 2008). The quantification is based on the quantitative evaluation of the energy spectrum associated with the detection of photon emissions from a sample matrix. In this work, after the quantification of short-lived Ra isotopes with the RaDeCC system, the Mn-fibers were incinerated, to reduce the volume, and packed into 5.6 cm$^3$ counting vials (Charette et al., 2001). The process consists of placing each sample into

250 mL porcelain crucible, incinerating in an oven (Hobersal HD Series) at 820 ºC for 16 hours, grounding and homogenizing the ashes in laboratory mortars, transferring the ashes into sealed counting vials (to avoid Rn emanation from the vial), and aging the samples for a minimum of three weeks to ensure the radioactive equilibrium of $^{226}$Ra with its daughters. The samples were counted for 1 to 4 days, depending on the sample activity, in a well-type (14.5 mm diameter, 40 mm length), high-purity germanium counter (HPGe; Camberra). The detection system is composed of a high-purity germanium crystal provided with a well-type sample holder cooled by a liquid nitrogen Deware (-196 ºC) and placed in a shielding made of iron, copper and lead to maintain low counting background (Figure **3**.**4**). The activities of $^{228}$Ra and $^{226}$Ra were calculated through the $^{228}$Ac ($T_{1/2}$ = 6.1 h; quantum yield ($q_\gamma$) = 27.7%) and $^{214}$Pb ($T_{1/2}$ = 1.64·10$^{-4}$ s; $q_\gamma$ = 37.2 %) photopeaks at 911 and 352 keV, respectively. The choice of the $^{214}$Pb photopeak for the quantification of $^{226}$Ra activities instead of the direct photopeak of $^{226}$Ra (186 keV; $q_\gamma$ = 3.6%) or other $^{226}$Ra-daughters such as $^{214}$Bi (609 keV; $q_\gamma$ = 46.1%) is sustained because it presents higher overall efficiencies considering the relative low background, low auto-absorption, and higher quantum yields (Dulaiova and Burnett, 2004; Scholten et al., 2013). A gamma spectrometry software (Genie 2000; Canberra) was used to locate the peaks, compute the peak area, and correct the peak area by background (background was periodically monitored) and efficiency.

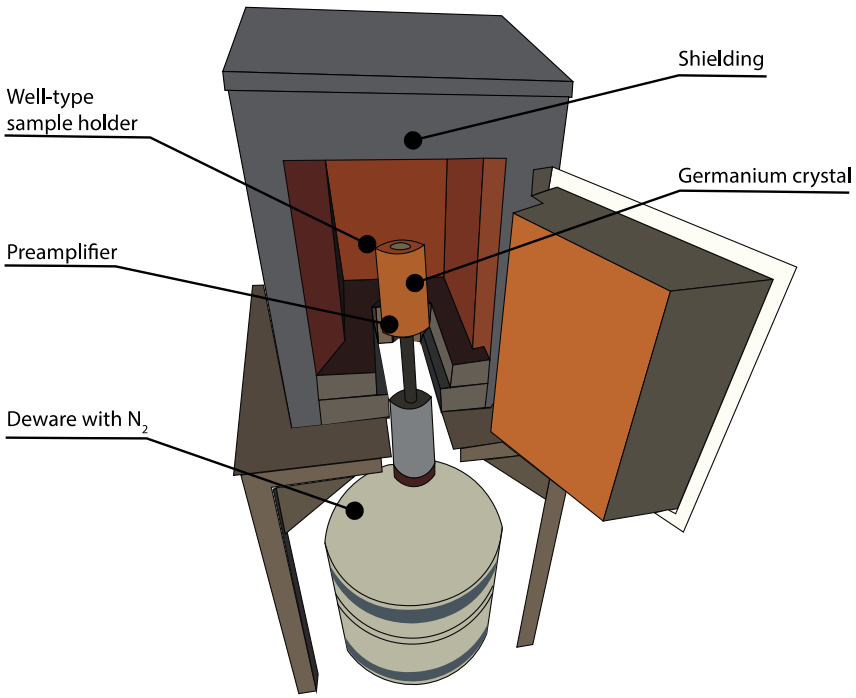


Figure 3.4. Detection system for the quantification of long-lived Ra isotopes ($^{226}$Ra and $^{228}$Ra). Well-type, high purity germanium detector and its components.

### 3.1.4. Radon through alpha spectrometry: RAD7

The activities of $^{222}$Rn in this work are quantified by using the RAD7 (Durridge Inc.), a radon-in-air detector adapted for measuring water activities with the RAD-$H_2O$ system (Durridge Inc.). Measuring the actual activity of $^{222}$Rn in water requires avoiding the sample to be in contact with air after its collection, to prevent radon losses due to emanation. The samples are therefore collected by placing a submersible pump into piezometric wells (or the first meter of the water column in case of seawater samples) and pumping the water into 250 mL glass vials or 2.5 L soda bottles (depending on sample activity). A tube connected to the submersible pump is used to fill the vials or bottles by placing the open end of the tube at the bottom of the containers. This procedure allows the water to overflow, keeping the vial full and continuously flushed with 'new' water, avoiding the contact with air. After a certain flushing time (i.e., time needed for the water renewal to equal approximately three times the volume of the container), the vial or soda bottle is tightly closed, making sure that no bubbles are in the vial. The $^{222}$Rn activity is measured by placing the sample in a close air loop which consist of an aerator cap with a glass frit, a drying

tube with desiccant, and a RAD7 counter (Figure **3.5**). During the measurement, the RAD7 internal pump introduces air through the glass frit into the sample allowing the $^{222}Rn$ to emanate and be routed from the sample container to the detector. There, high electronic fields are applied to attract the positively charged daughters of $^{222}Rn$, the $^{218}Po^{+}$ and $^{214}Po^{+}$, to a silicon semiconductor detector (Burnett and Kim, 2001). Other alpha-emitting polonium isotopes, such as $^{210}Po$ and $^{216}Po$ are also counted by the RAD7. However, the system has different energy windows enabling the discrimination of different polonium based on their decay energy, resulting therefore in relatively low backgrounds for each energy window (Burnett and Kim, 2001).

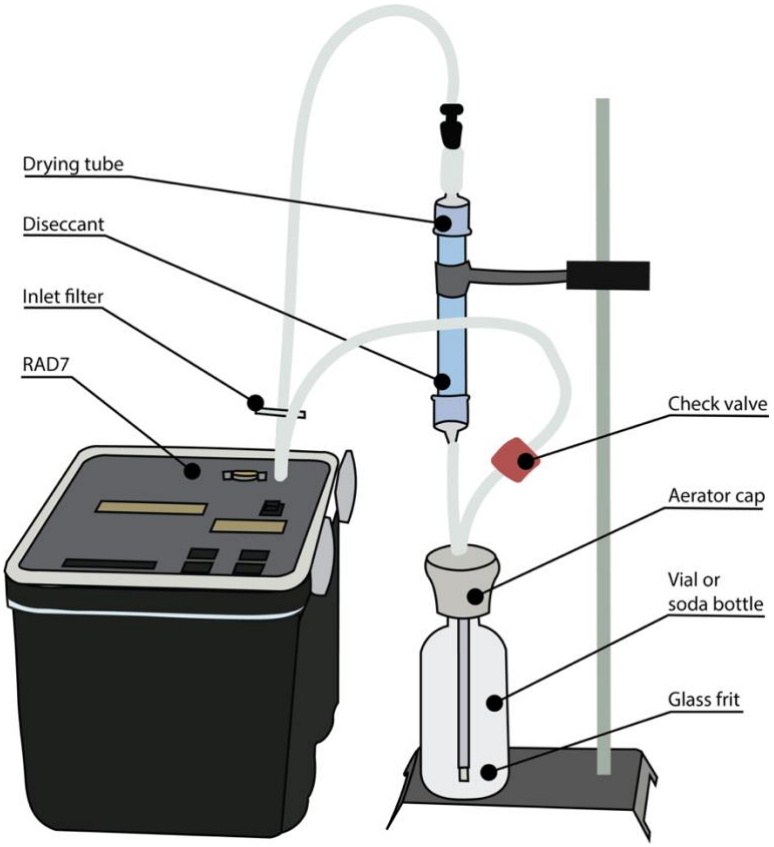


Figure 3.5. Schematic diagram of the RAD-$H_2O$ system for the measurement of $^{222}Rn$ activities in water samples.

### 3.1.5. Nutrients in water samples

The quantification of inorganic nutrients (nitrate, $NO_3^-$, nitrite, $NO_2^-$; ammonia, $NH_4^+$; phosphate, $PO_4^{3-}$; and silicate, $SiO_4^{2-}$) from water samples has been conducted by using a colorimetric method with an Autoanalyzer AA3 HR (Seal Analytica) at the *Institut de Ciències del Mar* (CSIC) in Barcelona. The samples were collected into 10 mL polyethylene vials after filtration

through nylon syringe filters (pore size: 0.45 µm). The vials were immediately stored in a portable fridge and subsequently frozen at the laboratory until analysis. Dissolved silicate was analyzed by a procedure which consists of the reduction of silico-molybdate complex to molybdenum blue by ascorbic acid. The molybdenum blue is then determined by colorimetry at 820 nm. The determination of dissolved phosphate is based on the colorimetric quantification of blue phosphor-molybdenum complex at 880 nm which is formed by the reaction of phosphate, molybdate ion, and antimony and the subsequent reduction with ascorbic acid. The measurement of nitrate and nitrite has been conducted by a procedure whereby nitrate is reduced to nitrite. The nitrite reduced from nitrate reacts with sulphanilamide to form a red complex which is proportional to the total amount of nitrite. The amount of this complex is then determined by a colorimetric method at 550 nm and the nitrate concentrations is determined by subtracting the total nitrite (reduced nitrate + nitrite) and the nitrite concentration. Dissolved ammonia has been quantified by a fluorometric method consisting of the formation of fluorescent chemical species that are excited at 370 nm to subsequently register their emission at 460 nm (Grasshoff et al., 1983). The detection limits of the method were 0.006, 0.003, 0.003, 0.020 and 0.016 µM for $NO_3^-$, $NO_2^-$, $NH_4^+$, $PO_4^{3-}$, and $SiO_4^{2-}$, respectively.

## 3.2. Ra isotopes in sediments

### 3.2.1. Bulk activity

The bulk activities of long-lived Ra isotopes ($^{226}$Ra and $^{228}$Ra) were determined by gamma spectrometry. The sediment samples were collected, dried in a stove for 24 to 48 h, homogenized, and placed in 100 cm$^3$ plastic vials. Then, the vials were hermetically sealed to avoid $^{222}$Rn emanation and to ensure the radioactive equilibrium of $^{226}$Ra and its daughters. After radioactive equilibration, activities of $^{228}$Ra and $^{226}$Ra were determined by using a coaxial high-purity germanium (HPGe) detector as explained above (section 0).

### 3.2.2. Radium distribution coefficient and retardation factor

The determination of the distribution coefficient of Ra ($K_D$ [m$^3$ kg$^{-1}$]) requires the measurement of surface-bound ($Ra_S$ [Bq kg$^{-1}$]) and dissolved ($Ra_W$ [Bq m$^{-3}$]) Ra activities. The sediment samples previously collected in the field were dried in the stove (<40 ◦C) and sieved

through a 2 mm sieve to remove gravels. After drying and sieving, the sediment samples were stored in hermetic plastic bags for at least 20 days to ensure the equilibrium between $^{224}$Ra and its parent $^{228}$Th. Adapting the method described by Cai et al. (2012) to determine the disequilibrium between $^{224}$Ra and $^{228}$Th in coastal sediment, weighted sediment subsamples were mixed with synthetic water to form a slurry. The salinity of the synthetic water was adjusted to the groundwater salinities measured at the site where the samples were. Since the processes of adsorption and desorption for Ra are relatively fast (e.g., Beneš et al., 1985; Gonneea et al., 2008; Nathwani and Phillips, 1979), the contact time between sediment and water was adjusted to two hours. After two hours, the slurry was filtered using a filtration system that enables the separation of solid and solute phases. The filtration system consists of a filtration chamber, a Büchner flask, and a vacuum pump. The slurry was spilled into the filtration chamber which contained a pre-weighted 142-mm GFF filter with 0.7 µm of nominal pore size. In the filtration process, the sediment is retained in the filter and the solution is conducted to a Büchner flask. The filtration terminates after adjusting the ratio water/(sediment + filter) of the sediment sample to 0.4 to 0.5 (Cai et al., 2012). The recovered water in the Büchner flask was filtered through Mn-fibers at a controlled flow rate (<1 L min−1) (Moore and Reid, 1973; Scholten et al., 2010). Both the activities of dissolved ($^{224}Ra_W$) and surface-bound ($^{224}Ra_S$) Ra were measured with the RaDeCC system from the Mn-fiber and the sediment samples, respectively. The determination of the distribution coefficient of Ra ($K_D$) was then calculated as follows (Equation 3.5).

$$K_D = \frac{^{224}Ra_S}{^{224}Ra_W} \qquad \text{Equation 3.5}$$

Assuming a dry bulk density of the soil ($\rho_b$) of 2.6 kg L$^{-1}$ and a porosity (φ) of 0.3, the retardation factor of Ra ($R_{Ra}$ [-]) was derived from Equation 3.6 according to Michael et al. (2011),

$$R_{Ra} = 1 + K_D \frac{\rho_b}{\phi}. \qquad \text{Equation 3.6}$$

# Chapter 4: Guidelines and limits for the quantification of U/Th series radionuclides with the Radium Delayed Coincidence Counter (RaDeCC)

## 4.1. Introduction

The Radium Delayed Coincidence Counter (RaDeCC) has become the most extensively used equipment to measure short-lived Ra isotopes due to the simplicity and sensitivity of the detection technique, the relatively low operational cost, and its portability. The counter is used to measure water samples from different settings such as seawater, pore-water, groundwater, rivers or water from brines (e.g. Moise et al., 2000; Moore et al., 2011; Moore and Krest, 2004). Although the system was originally designed to measure low activity $^{223}$Ra and $^{224}$Ra samples (Giffin et al., 1963; Moore and Arnold, 1996), samples commonly measured with the RaDeCC system span a wide range of $^{223}$Ra and $^{224}$Ra concentrations. Ra activities may be specially high in porewater and coastal aquifer samples given the influence of several parameters on Ra activities such as salinity, geological context or water-sediment ratio (Cerdà-Domènech et al., 2017; Gonneea et al., 2013a). However, the influence of different initial $^{223}$Ra, $^{224}$Ra, and $^{226}$Ra activities (and their activity ratios) in the quantification systematics of the RaDeCC system have never been studied in detail.

In this work, we examine the behavior of the counting system under different activities and activity ratios of $^{223}$Ra, $^{224}$Ra, and $^{226}$Ra through a set of simulations that reproduce the RaDeCC counting mechanism. The input data of the simulations is based on the statistical analysis of data registered by different laboratories worldwide using the RaDeCC system. Simulation results were used to define the maximum quantification limits of the RaDeCC system, which were validated against real measurements. According to the results, we provide new guidelines in the determination of the activities of $^{227}$Ac, $^{228}$Th and Ra isotopes with the RaDeCC system.

## 4.2. Methods

### 4.2.1. Analysis of registered data

RaDeCC measurements conducted in 8 different laboratories worldwide (Table **4.1**) from 2004 to 2018 have been gathered together (~17,000 measurements) to obtain statistical information on the count rates and counting times commonly measured with the RaDeCC system. The RaDeCC output files (RaDeCC.SUM) were parsed using *Python programming language* and filtered in order to remove unreliable measurements (i.e., measurements with spurious counts induced by electrical surges, Moore, 2008) and background measurements.

Table 4.1. Number of RaDeCC measurements performed by different laboratories used for the statistical analysis.

| Lab Name | Country | Number of Measurements | Relative abundance % |
|---|---|---|---|
| [1]CEREGE | France | 574 | 3 |
| [2]IAEA-EL | Monaco | 725 | 4 |
| [3]ICBM | Germany | 1,479 | 9 |
| [4]UK | Germany | 2,967 | 18 |
| [5]LEGOS | France | 714 | 4 |
| [6]SUNY | US | 2,050 | 12 |
| [7]UAB | Spain | 8,096 | 48 |
| [8]WHOI | US | 301 | 2 |
| **Total** | | 16,906 | |

1: European Centre for Research and Teaching in Environmental Geosciences, Aix-Marseille University; 2: International Atomic Energy Agency - Environmental Laboratories of Monaco; 3: Grup of Microbiogeochemistry, School of Mathematics and Science, Institute for Chemistry and Biology of the Marine Environment; 4: Department of Sedimentology, Coastal and Shelf Research, Institute of Geosciences, University of Kiel; 5: Observatoire Midi Pyrénées, Laboratoire d'Études en Géophysique et Océanographie Spatiales; 6: School of Marine and Atmospheric Sciences, Stony Brook University; 7: Grup de Recerca en Radioactivitat Ambiental de Barcelona, Universitat Autònoma de Barcelona; 8: Department of Marine Chemistry and Geochemistry, Woods Hole Oceanographic Institution

The applied data filters thus include only those measurements between counting times of 30 and 4,000 min and with activities higher than 0.01 and 0.1 cpm for the 219 and 220

channels, respectively and lower than 100 cpm in the Total channel. The filtered data includes measurements performed with the RaDeCC systems from different kind of samples (Mn-cartridges, Mn-fibers, sediments), including measurements of single- or mixed-tracer standards, and collected in different environments (e.g. open ocean, coastal waters and groundwaters). Notice that the applied data filters (*CT*<30 min) exclude, not only most of the background measurements but also some potentially high $^{224}$Ra activities measurements. The results from this analysis are used as reference values for the simulations presented in the following section (Section 0).

### 4.2.2. Ra isotopes RaDeCC simulations

A set of simulations have been developed using *Python programming language* to reproduce the RaDeCC counting systematics in order to evaluate the effect of different 219, 220 and Total channel count rates in the quantification of $^{223}$Ra, $^{224}$Ra, $^{226}$Ra, $^{228}$Ra, $^{228}$Th, and $^{227}$Ac activities using the RaDeCC system. The simulations consist of two stages, which are detailed below: (1) the generation of a dataset with the decay events that are registered by the RaDeCC depending on different initial activities of $^{223}$Ra, $^{224}$Ra, and $^{226}$Ra and (2) the evaluation of the delayed coincidence system response to these activities. The definition of the terms and values used in the simulations is shown in Table **4**.**2** and all the simulation codes are available in Diego-Feliu, (2020).

(1) A dataset consisting of a temporal vector with the decay events that occur during a single RaDeCC measurement is generated. This vector is used as an input file for the following simulation. From an initial arbitrary count rate of $^{223}$Ra, $^{224}$Ra, and $^{226}$Ra (see Table **4**.**3**), the subsequent decay products of each decay chain (e.g. Rn, Po, Pb, Bi) are randomly generated, following an exponential distribution according to their half-lives, and stored in individual lists. A specific vector is generated for each isotope and each selected initial count rate (based on the range of count rates obtained from the measurements described in Section 4.2.1). The resulting lists are temporal single isotope vectors with a length equal to a certain counting time (also arbitrary; see Table **4**.**3**) in which each decay event is located at a certain position within the vector. An additional list with background counts is created following a uniform distribution based on the average background measurements (and associated standard deviation) performed

with the RaDeCC systems at the Universitat Autònoma de Barcelona (UAB) (Table **4.2**). All the individual lists are added together into a final list, which contains the temporal position (within a certain counting time) of each alpha decay event produced in the simulated system.

Table 4.2. Definition of the terms and values used in the simulations. The model constants are based on Moore and Arnold (1996) and the background data is based on the registered data analyses from Section 4.2.1.

| Term | Definition | Values | Units |
|---|---|---|---|
| | **Model constants** | | |
| $t_{D-219}$ | *Delay time of 219 channel* | 0.01 | ms |
| $t_{D-220}$ | *Delay time of 220 channel* | 5.61 | ms |
| $t_{G-219}$ | *Gate time of 219 channel* | 5.60 | ms |
| $t_{G-220}$ | *Gate time of 220 channel* | 600 | ms |
| $BKG_{average}$ | *Average background of the Total channel* | 2.24 | cpm |
| $BKG_{STD}$ | *Standard deviation background of the Total channel* | 1.38 | cpm |
| | **Simulation inputs** | | |
| *Initial $^{223}Ra$* | Simulated initial $^{223}$Ra | | cpm |
| *Initial $^{224}Ra$* | Simulated initial $^{224}$Ra | | cpm |
| *Initial $^{226}Ra$* | Simulated initial $^{226}$Ra | | cpm |
| *CT* | Counting time | | min |
| | **Simulation outputs** | | |
| *219 channel* | Count rate of the 219 channel | | cpm |
| *220 channel* | Count rate of the 220 channel | | cpm |
| *Total channel* | Count rate of the Total channel | | cpm |
| *Final219* | Corrected 219 channel according Moore and Arnold (1996) | | cpm |
| *Final220* | Corrected 220 channel according Moore and Arnold (1996) | | cpm |
| | **Channel ratios** | | |
| $CR_{220/219}$ | *Ratio between the channels 220 and 219* | | |
| $CR_{TOT/220}^{*}$ | *Ratio between the Total channel and the first cycles of the 220 channel* | | |
| $CR_{(219+220)/TOT}$ | *Ratio ( 219 channel + 220 channel) / Total channel* | | |

(2) The delayed coincidence system is simulated to reproduce the count rates that would be produced within each channel of the RaDeCC system when specific initial count rates of $^{223}$Ra, $^{224}$Ra, and $^{226}$Ra are used as input data (input file obtained from the dataset described above). These simulations reproduce the counting mechanisms of the delayed coincidence system of the RaDeCC system, as presented by Moore and Arnold (1996). Analogous to the real RaDeCC system

(Section 3.1.2), after an initial simulated decay event at $t_0$ the subsequent events occurring between $[t_0 + t_D]$ and $[t_0 + t_D + t_G]$ are counted in the respective circuits (219 or 220), as shown in Figure **3.3**, where $t_0$ is the triggering event time, $t_D$ is the delay time and $t_G$ is the gate time (Table **4.2**). The outputs of these simulations include the count rates in the 219, 220 and Total channel (analogous to outputs from the RaDeCC system).

Table 4.3. Simulations inputs for Sections 4.3.3, 4.3.4, 4.3.5, and 4.3.7.

| **Section** | **Simulations** | ***CT*** | ***Initial $^{223}$Ra*** | ***Initial $^{224}$Ra*** | ***Initial $^{226}$Ra*** | ***$CR_{220/219}$*** |
|---|---|---|---|---|---|---|
| | **#** | **min** | **cpm** | **cpm** | **cpm** | |
| 4.3.3. Effect of high activity measurements ($^{223}$Ra) | 1,000 | 100 | 1 - 100 | 0 - 200 | 0 - 25 | 0 - 2 |
| 4.3.3. Effect of high activity measurements ($^{224}$Ra) | 1,400 | 100 | 0 - 10 | 0 - 100 | 0 - 25 | 10 - 20 |
| 4.3.4. Effect of 219-220 cross-talk | 18,250 | 400 | 0 - 5 | 0 - 25 | 0 - 25 | 0 - 250 |
| 4.3.5. Effect of $^{222}$Rn buildup ($^{223}$Ra) | 2,600 | 200 - 1,000 | 0.1 - 1.0 | 0.1 - 2.0 | 0 - 50 | 0 - 4 |
| 4.3.5. Effect of $^{222}$Rn buildup ($^{224}$Ra) | 1,400 | 200 - 1,000 | 0.1 - 1.0 | 0.1 - 2.0 | 0 - 50 | 10 - 20 |
| 4.3.7. Quantification of $^{226}$Ra via $^{222}$Rn buildup ($^{224}$Ra) | 360 | 10 - 1,400 | 0.1 | 0 - 8 | 0 - 470 | 8 |

### 4.2.3. Radium sampling and laboratory experiments

A set of measurements have been performed with the RaDeCC system to validate the detection limits derived from simulations. The samples used for this purpose were collected from an experimental site constructed in the lowest part of an alluvial aquifer at the Argentona ephemeral stream (NE of Barcelona, Spain) (Cerdà-Domènech et al., 2017) and in the Peníscola marshland (Castelló, Spain) (Rodellas et al., 2012). The collected water samples were processes according to the procedures detailed in Chapter 2. Two experiments were performed: the first experiment consisted of the reiterative measurement of a high activity $^{223}$Ra and $^{224}$Ra sample (~20 and 1,600 dpm $100L^{-1}$, respectively) over 39 days for the evaluation of the DCC under different count rates (due to the radioactive decay of $^{223}$Ra and $^{224}$Ra). Then, the excess activities of $^{223}$Ra ($^{223}Ra_{ex}$) and $^{224}$Ra ($^{224}Ra_{ex}$) were quantified from each measurement; the second experiment consisted of the measurement of 4 high activity $^{226}$Ra samples to evaluate the effect of $^{222}$Rn buildup on the quantification of $^{224}$Ra activities. For each measurement, the count rate registered in the 220 channel after each cycle (2 min) was corrected following Moore and Arnold (1996).

## 4.3. Results and discussion

### 4.3.1. Analyses of registered data

A statistical analysis of ~17,000 measurements performed with different RaDeCC systems is represented in Figure **4.1**. The distributions of the count rates registered in the 219 and 220 channels are shown in Figure **4.1**a and Figure **4.1**b, respectively. Both distributions exhibit a maximum in the lowest range of count rates, between 0.0 and 0.2 cpm for the 219 channel and between 0 and 2 cpm for the 220 channel. The median values for the 219, 220 and Total channels are 0.2, 1.9 and 7.2 cpm, respectively (Table **4.4**).

Table 4.4. Median values of the 219, 220, Total channel, and $CR_{220/219}$ for the characteristic counting times of the histogram from Figure 4.1c.

| Counting time | *219 channel* | *220 channel* | *Total channel* | $CR_{220/219}$ |
|---|---|---|---|---|
| min | cpm | cpm | cpm | |
| 30 - 300 | 0.4 | 4.3 | 12.0 | 12.7 |
| 300 - 700 | 0.2 | 1.1 | 4.7 | 8.9 |
| 700 - 1,200 | 0.1 | 0.8 | 4.1 | 13.0 |
| 30 - 4,000 | 0.2 | 1.9 | 7.2 | 11.5 |

The distribution of the counting times (Figure **4.1**c) is characterized by three peaks that are consistent with the standard measurement procedure of the RaDeCC system described by Moore (2008). According to this procedure, to determine $^{223}$Ra and $^{224}$Ra activities, a first run is conducted shortly after sample collection (1 - 5 days). These measurements frequently present higher $^{223}$Ra and $^{224}$Ra activities and lower counting times relative to the measurements commonly used to determine $^{227}$Ac, $^{228}$Th or $^{226}$Ra. The first peak (between 30 to 300 min) is consistent with these initial measurements presenting the highest median count rates in all the channels (0.4, 4.3 and 12.0 cpm for 219, 220 and Total channels, respectively). The second peak, between 300 and 700 min, presents lower count rates in the 219, 220 and Total channels (0.2, 1.1 and, 4.7 cpm, respectively) and a lower median value of the ratio between channels 220 and 219 ($CR_{220/219}$) relative to the first peak as shown in Figure **4.1**d. This could be attributed to those measurements performed in order to determine $^{223}$Ra activities when first runs presented high count rates in the 220 channel. In such cases, samples are measured again to allow $^{224}$Ra to

partially decay thereby reducing the channel ratio $CR_{220/219}$. Finally, due to the combination of high counting times (between 700 to 1200) and low count rates (0.1, 0.8, and, 4.1cpm for 219, 220 and Total channels, respectively), the third peak is associated with measurements of samples with low activities of $^{223}$Ra and $^{224}$Ra, generally used to determine $^{227}$Ac, $^{228}$Th or $^{226}$Ra (Table **4.4**). According to the data registered in the 8 laboratories, the range of initial $^{223}$Ra and $^{224}$Ra count rates used for the simulations in Section 4.3.4 and 4.3.5 is 0 - 5 and 0 - 25 cpm for $^{223}$Ra and $^{224}$Ra, respectively, which covers approximately 95% of the RaDeCC measurements.

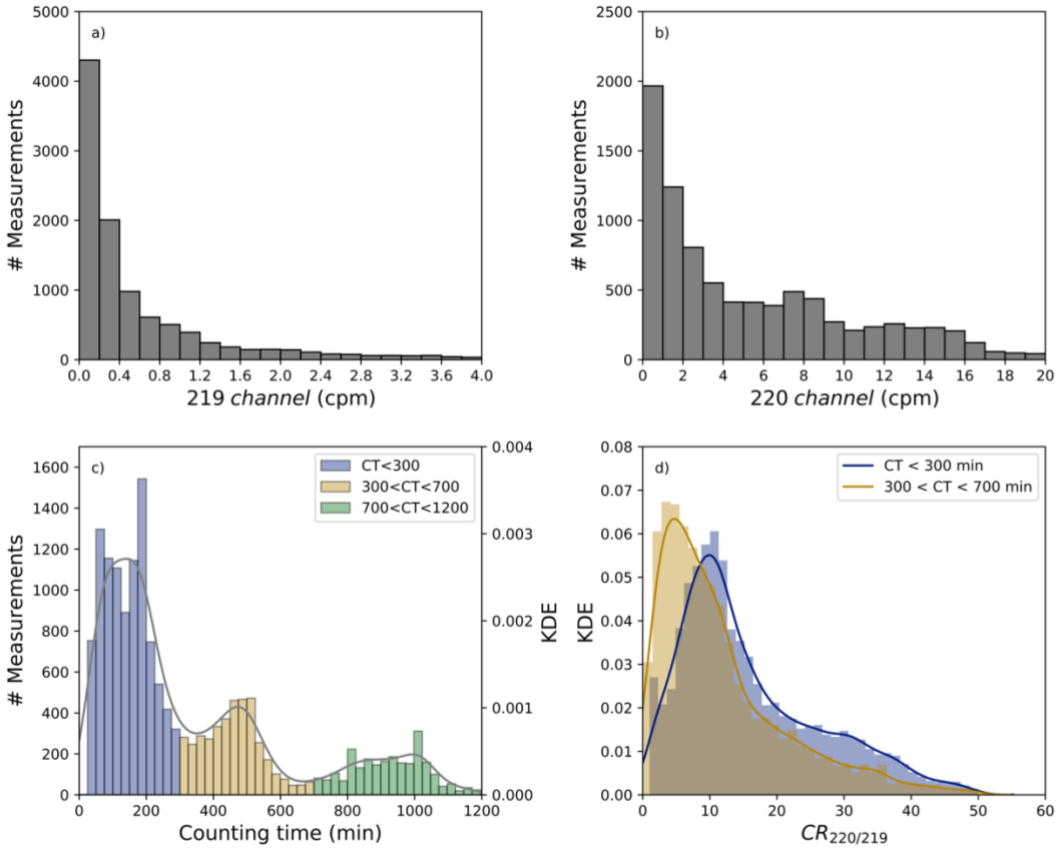


Figure 4.1. Histogram (a, b, and c) and Kernel Density Estimate (KDE) (c and d) of 16,906 measurements performed by 8 different laboratories between 2004 and 2018. a) count rate in the 219 channel (30<CT<800 min). b) count rate in the 220 channel (30<CT<300 min and $CR_{220/219}$ > 1). c) counting times. d) $CR_{220/219}$. Blue, yellow, and green colors indicate counting times of CT<300, 300<CT<700 and 700<CT<1200 min, respectively.

### 4.3.2. Systematics of the Delayed Coincidence Circuit

The delayed coincidence circuit (DCC) of the RaDeCC system is designed to differentiate between the decay products of $^{223}$Ra and $^{224}$Ra. As explained in Section 3.1.2, when a first signal is registered, the 219 and 220 gates are opened after a certain delay time. Any event occurring within the opening time of both gates will be recorded in the corresponding channel according to the time elapsed between the triggering and subsequent events (Figure **3.3**).

The functioning of the DCC can be explored using the ratio between the sum of the 219 and 220 channels and the Total channel ($CR_{(219+220)/TOT}$). In the optimal case, an initial decay of Rn triggers the circuit and is registered in the Total channel, the second decay (Po) is registered in the 219 or 220 channels, as well as in the Total channel, producing a ratio $CR_{(219+220)/TOT}$ = 0.5. Figure **4.2** shows the behavior of this ratio for real data (Figure **4.2**a and Figure **4.2**c) and simulations (Figure **4.2**b and Figure **4.2**d). Both real and simulated data likely present the same behavior, showing an increase of the ratio $CR_{(219+220)/TOT}$ as the Total channel count rate increases, which is linked to an increase of short-lived Ra isotopes activities. Higher activities of $^{223}$Ra and $^{224}$Ra cause the 219 and 220 circuits to be triggered more frequently, thereby increasing the fraction of 'on' time (i.e., the fraction of time in which the gates are open). This increase of Ra activities produces $CR_{(219+220)/TOT}$ higher than 0.5 as a consequence of (1) channel multi-registration and/or (2) concurrent registration of a single event in both channels. The channel multi-registration occurs when, after a triggering event, two (or more) subsequent events take place within the opening time of a specific circuit. Multi-registration will allow the channel ratio $CR_{(219+220)/TOT}$ to increase asymptotically to the value of 1. For high counting rates in the Total channel (>1,000 cpm), ratios above 1 are produced due to the effect of concurrent registration (Figure **4.2**c and Figure **4.2**d). The concurrent registration is the result of the independent behavior of the circuits from the DCC (Moore and Arnold, 1996). Both circuits can be triggered by different events and therefore, they can be open at the same time. Hence, if a decay event is produced when both circuits are open, the same event is registered in the Total channel and in both the 219 and 220 channels concurrently. In contrast with the multi-registration effect, which can be corrected by using the equations developed by Giffin et al. (1963), there is no protocol to correct the effect of the concurrent registration. Therefore, $^{223}$Ra and $^{224}$Ra activities cannot be

appropriately quantified using the RaDeCC system when the influence of concurrent registration may significantly affect the results (i.e., in high activity samples). In Section 4.3.3, we explore the limits of the applicability of the RaDeCC system and the appropriateness of the equations used to quantify $^{223}$Ra and $^{224}$Ra activities for high activity samples.

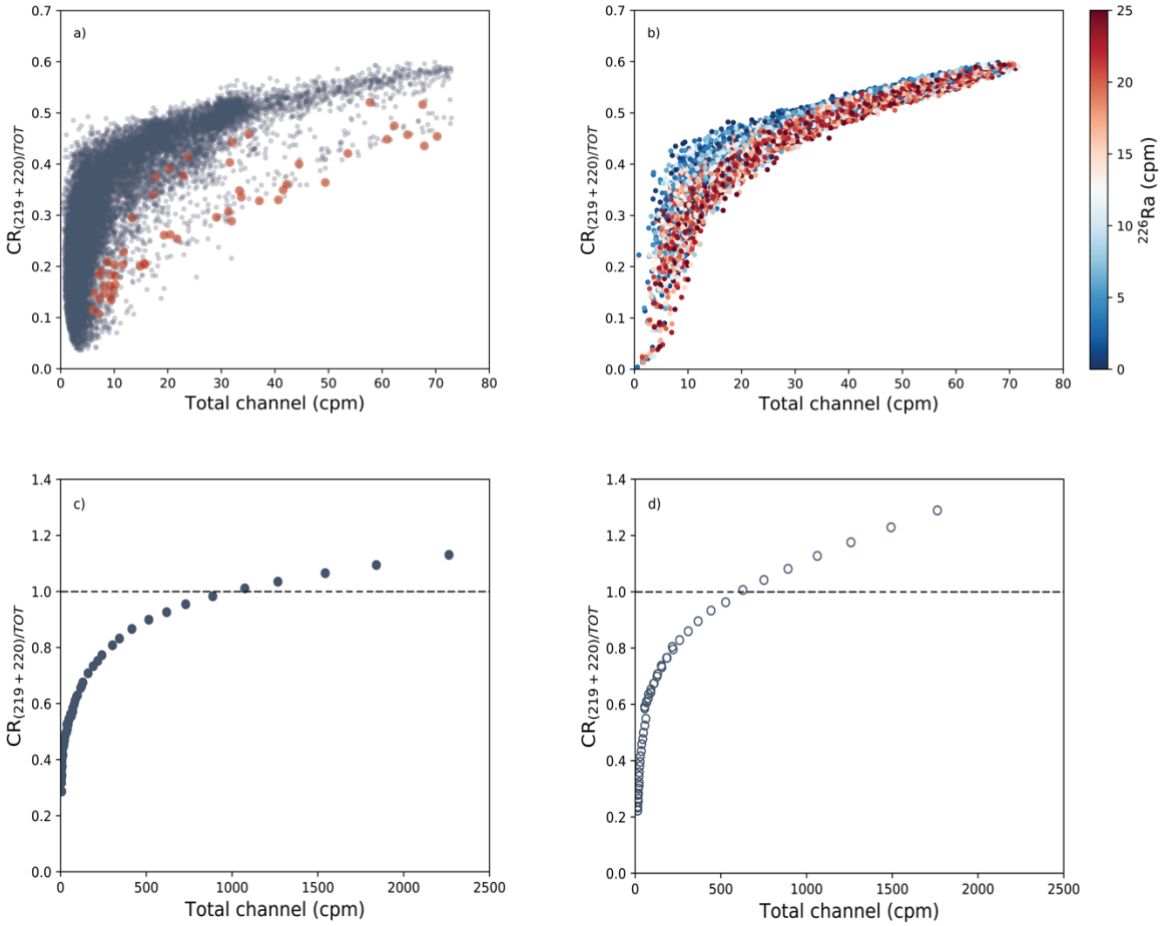


Figure 4.2. Relationship between the ratio $CR_{220/219}$ and the count rate in the Total channel. a) Data from 16,906 measurements performed by 8 different laboratories between 2004 and 2018. Red dots represent a set of high activity $^{226}$Ra measurements (Rodellas et al., 2012). b) Simulations (n=18,250) with initial $^{223}$Ra, $^{224}$Ra and $^{226}$Ra count rates ranging 0-5, 0-25 and 0-25 cpm, respectively. The color scale represents the simulated initial $^{226}$Ra count rate. c) Data from the reiterative measurement of a high $^{223}$Ra and $^{224}$Ra sample (20 and 1,600 dpm 100L$^{-1}$, respectively). d) Simulations (n=51) with initial $^{223}$Ra, $^{224}$Ra and $^{226}$Ra count rates ranging 0-250, 0-1,500 and 200 cpm, respectively.

High activities of $^{226}$Ra can also significantly influence the channel ratio $CR_{(219+220)/TOT}$ (Figure **4.2**b) due to the ingrowth of $^{222}$Rn (daughter of $^{226}$Ra) during the counting time. When a decay event of $^{222}$Rn occurs, the delayed coincidence circuit will be triggered, but its daughter ($^{218}$Po) will probably not decay within the opening times of the 219 and 220 gates due to its

'longer' half-life (3.04 min). It will decay instead most likely after the gates are closed and therefore trigger the circuit again. Thus, $CR_{(219+220)/TOT}$ decreases as the $^{224}Ra/^{226}Ra$ activity ratio decreases (Figure **4.2**b). An example of this process is shown in Figure **4.2**a where a set of samples collected in Peníscola marshland (Castelló, Spain) (Rodellas et al., 2012) characterized by extremely low $^{224}Ra/^{226}Ra$ activity ratios (< 0.1) are highlighted in red.

### 4.3.3. Effect of high activity measurements

In this section, we evaluate the reliability of using the count rate of the 219 and 220 channels and the correction equations proposed by Moore and Arnold (1996) to quantify the activities of $^{223}Ra$ and $^{224}Ra$ when measuring high activity samples with the RaDeCC system. To do so, a set of simulations was performed to assess the $^{223}Ra$ and $^{224}Ra$ quantification limits. For both $^{223}Ra$ and $^{224}Ra$, the ratio between $Initial^{223}Ra/Initial^{224}Ra$ was adjusted to avoid possible 219-220 cross-talk following the limits provided in Section 4.3.4 (Table **4.3**).

In order to evaluate the quantification systematics, the ratio between the corrected channel count rate (*Final219* or *Final220*) and the initial simulated count rate ($Initial^{223}Ra$ or $Initial^{224}Ra$, respectively) is a useful tool. Since the system ($f_S$), cell ($f_C$), and emanation efficiencies ($f_E$) are not influencing the simulations, this ratio should equal the gate efficiency of the specific channel (0.88 for $f_{G\text{-}219}$ and 0.91 for $f_{G\text{-}220}$). Deviations of the simulated ratio ($Final219/Initial^{223}Ra$ or $Final220/Initial^{224}Ra$) from the expected gate efficiency are thus indicative of the appropriateness of the quantification systematics and the corrections applied to account for chance coincidence and interferences between channels. Simulated ratios ($Final219/Initial^{223}Ra$ or $Final220/Initial^{224}Ra$) that deviate > 5% from the gate efficiency are indicative of erroneous quantification of Ra isotopes. We used 5% as a limit because this value corresponds to the minimum relative uncertainties that can be obtained for $^{223}Ra$ and $^{224}Ra$ measurements with the RaDeCC system (Garcia-Solsona et al., 2008).

The results of the simulations indicate that significant deviations (>5%) of the ratios $Final219/Initial^{223}Ra$ and $Final220/Initial^{224}Ra$ relative to the gate efficiency ($f_{G\text{-}219}$ = 0.88 and $f_{G\text{-}220}$ = 0.91, respectively) may occur for measurements with count rates in the Total channel above 200 cpm for $^{223}Ra$ and 100 cpm for $^{224}Ra$ (Figure **4.3**). Above these count rates, the determination

of triggering events (cpmTot – (cpm219 + cpm220)), which is necessary to apply the chance coincidence equations (see Section 3.1.2) is underestimated due to the concurrent registration effect. This effect occurs when a single decay event is registered in both the 219 and 220 channel concurrently, as explained in Section 4.3.2. Thus, the maximum quantification limits for $^{223}$Ra and $^{224}$Ra are 200 and 100 cpm in the Total channel, respectively. Above these conservative limits, the equations proposed by Moore and Arnold (1996) to correct the chance coincidence events and the interactions between channels might produce erroneous quantifications of the $^{223}$Ra (i.e., *Final219*) and $^{224}$Ra (i.e., *Final220*) activities. Notice that the limit for the quantification of $^{223}$Ra activities is higher than the limit for $^{224}$Ra quantification. This is due to the lower relative importance of the chance coincidence on the count rate correction for the 219 channel relative to the 220 channel, since the opening time of the 219 circuit is two orders of magnitude lower relative to the 220 circuit (5.6 and 600 ms, respectively). The median count rates in the Total channel for the data registered in different labs (7.2 cpm) is 2 orders of magnitude lower than the calculated limits. Nevertheless, the maximum detection limits of the RaDeCC system must be taken into account, especially when measuring samples highly enriched in $^{223}$Ra and $^{224}$Ra (e.g. groundwater, porewaters, water from brines). If the quantification limits are overpassed, an additional measurement should be performed after a certain time allowing the short-lived Ra isotopes to decrease in their activities.

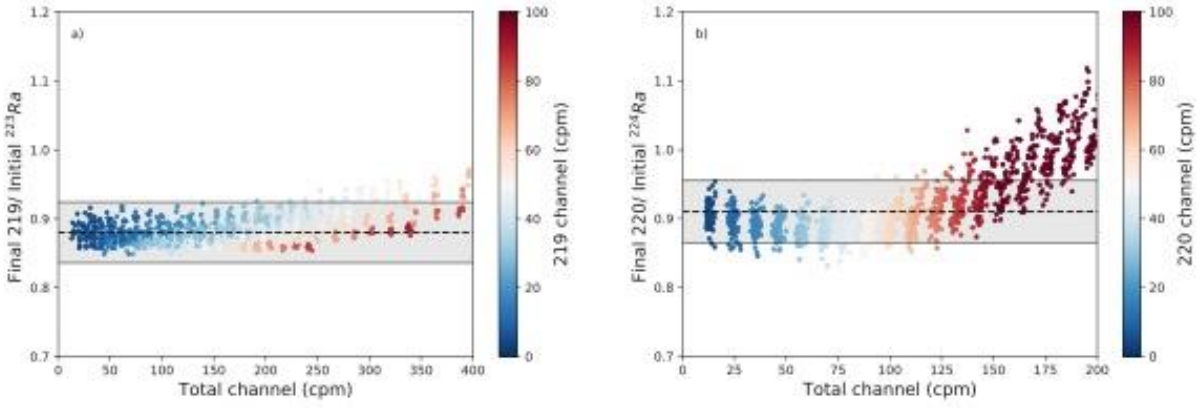


Figure 4.3. Results from simulations (n=2,290) with initial $^{223}$Ra, $^{224}$Ra and $^{226}$Ra count rates ranging 0-100, 0-100 and 0-25 cpm, respectively. (a) Ratio between corrected 219 channel and initial $^{223}$Ra simulated count rates (*Final219/Initial$^{223}$Ra*) against Total channel count rate. b) Ratio *Final220/Initial$^{224}$Ra* against Total channel count rate. The dashed line represents the gate efficiency ($f_G$) and the grey band an uncertainty of 5%. The color scale represents the count rate in the Total channel.

### 4.3.4. Effect of 219-220 cross-talk

In this section, we evaluate the influence of different activities of Ra isotopes on the quantification of $^{223}$Ra and $^{224}$Ra and the accuracy of the corrections proposed by Moore and Arnold (1996) to correct 219-220 cross-talk interferences. In order to perform this analysis, a set of simulations was conducted with initial $^{223}$Ra, $^{224}$Ra and $^{226}$Ra count rates of 0 - 5, 0 - 25 and 0 - 25 cpm, respectively, reproducing count rates from samples commonly measured with the RaDeCC system (see Section 4.3.1).

Simulation results for the 219 channel (Figure **4.4**a) show deviations of the ratio *Final219/Initial$^{223}$Ra* from the gate efficiency ($f_{G\text{-}219}$ = 0.88) that are mainly attributed to the influence of $^{224}$Ra on the 219 channel (i.e., channel cross-talk). The effect of $^{224}$Ra in the 219 channel is more evident in the lower range of *Initial$^{223}$Ra* count rates (0 - 0.5 cpm). Nevertheless, these deviations in relation to the 219 gate efficiency ($f_{G\text{-}219}$) result from the combination of low *Initial$^{223}$Ra* and high *Initial$^{224}$Ra* (>20 cpm) which would exhibit extremely high ratios between 220 and 219 channels ($CR_{220/219}$ > 40). It should be noted that these high $CR_{220/219}$ are not commonly measured in water samples (only 2.4% of registered data have $CR_{220/219}$ > 40; Section 4.3.1) and most of them are associated with single-tracer standard (e.g., $^{232}$Th) measurements for the determination of the efficiency of 220 channel (Section 4.3.1). For $CR_{220/219}$ < 40, the deviations range from -6 to 38%, which could represent up to 8 times the minimum relative uncertainty of 5% (Garcia-Solsona et al., 2008). As shown in Figure **4.4**b, high values of $CR_{220/219}$ correspond to a larger deviation between the ratio *Final219/Initial$^{223}$Ra* and the gate efficiency (i.e., $f_{G\text{-}219}$), thus leading to a higher potential error on the quantification of $^{223}$Ra. Therefore, the results from this study suggest that the $^{223}$Ra quantification might not be accurate (deviations larger than 5%) when (1) $CR_{220/219}$ > 10 or (2) $CR_{220/219}$ > 4 and *220 channel* > 5 cpm. These results agree with the study of Scholten et al. (2010), where single- and mixed-tracer ($^{227}$Ac and $^{228}$Th) Mn-fiber standards were prepared to calibrate the efficiencies of the RaDeCC system for $^{223}$Ra and $^{224}$Ra. Scholten et al. (2010) suggested that samples with relatively high $^{224}$Ra count rates (>7 cpm) may prevent a precise $^{223}$Ra determination. Thus, samples with these characteristics should not be quantified to avoid an overestimation of the $^{223}$Ra activities. Almost two thirds (65%) of the registered measurements from different labs examined in Section 4.3.1 present these

conditions, which would lead to an inappropriate quantification of $^{223}$Ra. However, it should be noted that most of these measurements were likely conducted shortly after the collection of the sample (when $^{224}$Ra activities are usually high compared with $^{223}$Ra), and thus they were most likely not used to quantify $^{223}$Ra activities.

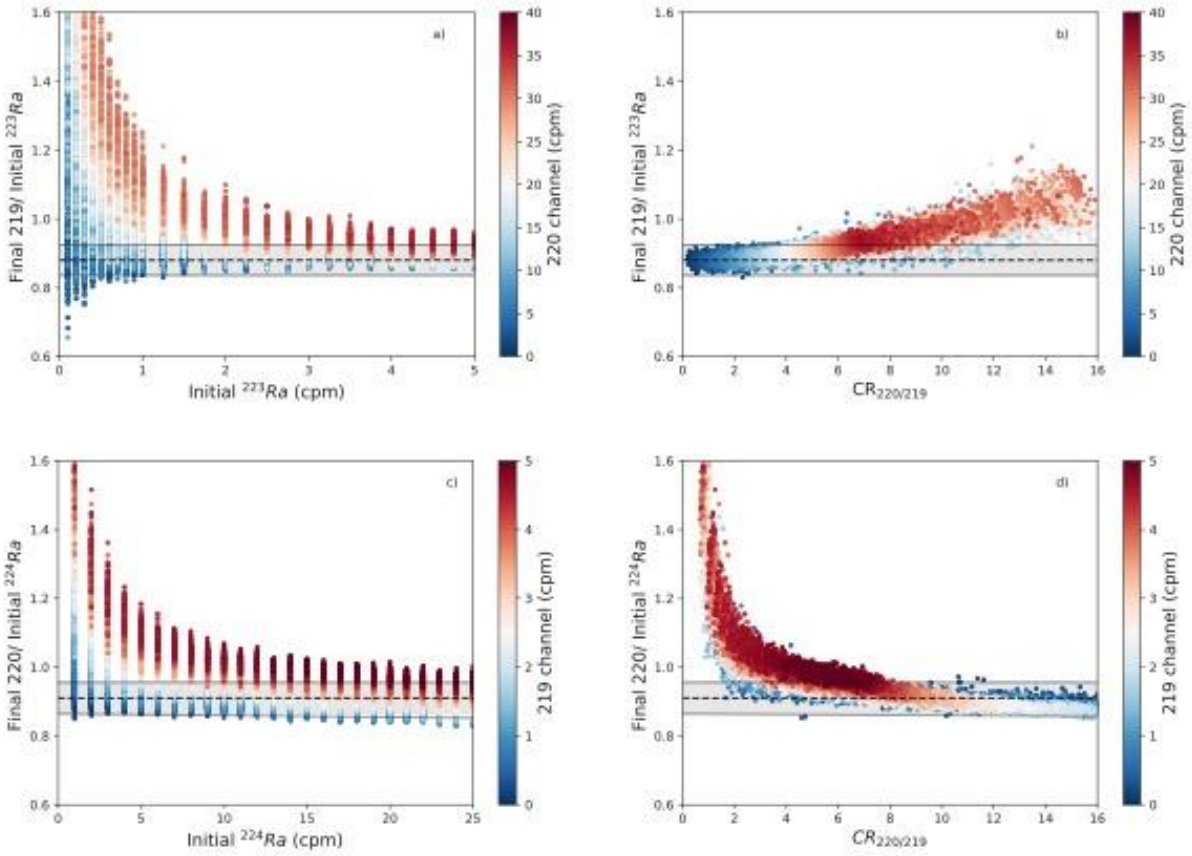


Figure 4.4. Results from simulations (n=18,250) with initial $^{223}$Ra, $^{224}$Ra and $^{226}$Ra count rates ranging 0-5, 0-25 and 0-25 cpm, respectively. The ratio between corrected 219 channel and initial $^{223}$Ra simulated count rates (*Final219/Initial$^{223}$Ra)* against (a) *Initial$^{223}$Ra* and (b) CR$_{220/219}$. The ratio *Final220/Initial$^{224}$Ra* against (c) *Initial$^{224}$Ra* and (d) CR$_{220/219}$. Colors represent the 219 (a and b) and 220 (c and d) channels count rate. The dashed line represents the gate efficiency ($f_G$) and the grey band an uncertainty of 5%. Solid lines indicate the CR$_{220/219}$ limits for quantification.

The influence of high $^{223}$Ra activities also produces relevant deviations of the ratio *Final220/Initial$^{224}$Ra* (Figure **4.4**c) from the gate efficiency ($f_{G\text{-}220}$ = 0.91). Measurements with $CR_{220/219}$ < 1 present the highest deviations, but they are not frequent in natural environments (only 3.6% of registered data have $CR_{220/219}$ < 1) and most of them are associated with single-tracer standard measurements for 219 channel efficiency determination (e.g. $^{227}$Ac). For $CR_{220/219}$

> 1, the deviations in relation to the theoretical value (i.e., $f_{G\text{-}220}$) range from -8 to 30% and tend to increase when $CR_{220/219}$ decreases. These deviations exceed 5% when: (1) $CR_{220/219}$ < 8 and *219 channel* > 1 cpm or (2) $CR_{220/219}$ < 2 (Figure **4**.**4**d). These two scenarios represent together 11% of the registered data from Section 4.3.1. If one of these cases is met, the $^{224}$Ra quantification should not be performed in order to avoid an overestimation of the $^{224}$Ra activities.

The above recommendations, which are summarized in Section 4.4, are also valid for the determination of $^{227}$Ac and $^{228}$Th activities with the RaDeCC system by measuring their daughters in radioactive equilibrium ($^{223}$Ra and $^{224}$Ra, respectively). However, in this latter case, due to their low activities in water samples, proper statistical quantification of these isotopes requires long counting times (800 - 1,200 min; Section 4.3.1) that can be highly influenced by the $^{222}$Rn buildup from the decay of $^{226}$Ra present in the fiber (Moore, 2008) (see Section 4.3.5). Similarly, these recommendations apply to the determination of surface exchangeable $^{224}$Ra and $^{228}$Th from sediments.

### 4.3.5. Effect of $^{222}$Rn buildup

The buildup of $^{222}$Rn from the decay of $^{226}$Ra produces a continuous increase of the count rate in the Total channel (see Section 4.3.2) that could lead to an erroneous correction of the 219 and 220 channel count rates (Moore, 2008). This effect would especially influence those measurements with low $^{223}$Ra and $^{224}$Ra activities (<2 cpm), commonly used to determine the activities of $^{227}$Ac and $^{228}$Th, mainly because they require long counting times (> 200 minutes) to obtain 400 counts in the respective channel (5% relative uncertainty). In this section, we evaluate the effect of $^{222}$Rn buildup through a set of simulations that reproduces characteristic measurements to determine $^{227}$Ac and $^{228}$Th activities (low activities and long counting times; Section 4.2.1). The simulated initial $^{223}$Ra, $^{224}$Ra, and $^{226}$Ra count rates ranged between 0 - 1, 0 - 2, and 0 - 50 cpm, respectively (Table **4**.**3**). The counting time was set to 1,000 min for initial count rates below 0.4 cpm. For higher count rates, the counting time was adjusted to achieve 400 counts in the respective channel (5% relative uncertainty).

The variation of the ratio $Final219/Initial^{223}Ra$ for different $Initial^{223}Ra$ and count rates in the Total channel is shown in Figure **4**.**5**a and Figure **4**.**5**b, respectively. There are no significant

deviations of this ratio relative to the gate efficiency ($f_{G\text{-}219}$ = 0.88) for the simulated count rates (*Initial*$^{226}$*Ra* up to 50 cpm), suggesting that due to the short opening time of the 219 circuit (5.6 ms), the influence of $^{222}$Rn buildup in the 219 channel is almost negligible. Conversely, the influence of $^{222}$Rn buildup in the 220 channel is significant due to its longer gate opening time (600 ms), producing significant increases of the ratio *Final220*/*Initial*$^{224}$*Ra* with the increase of $^{226}$Ra activities (Figure **4.5**c).

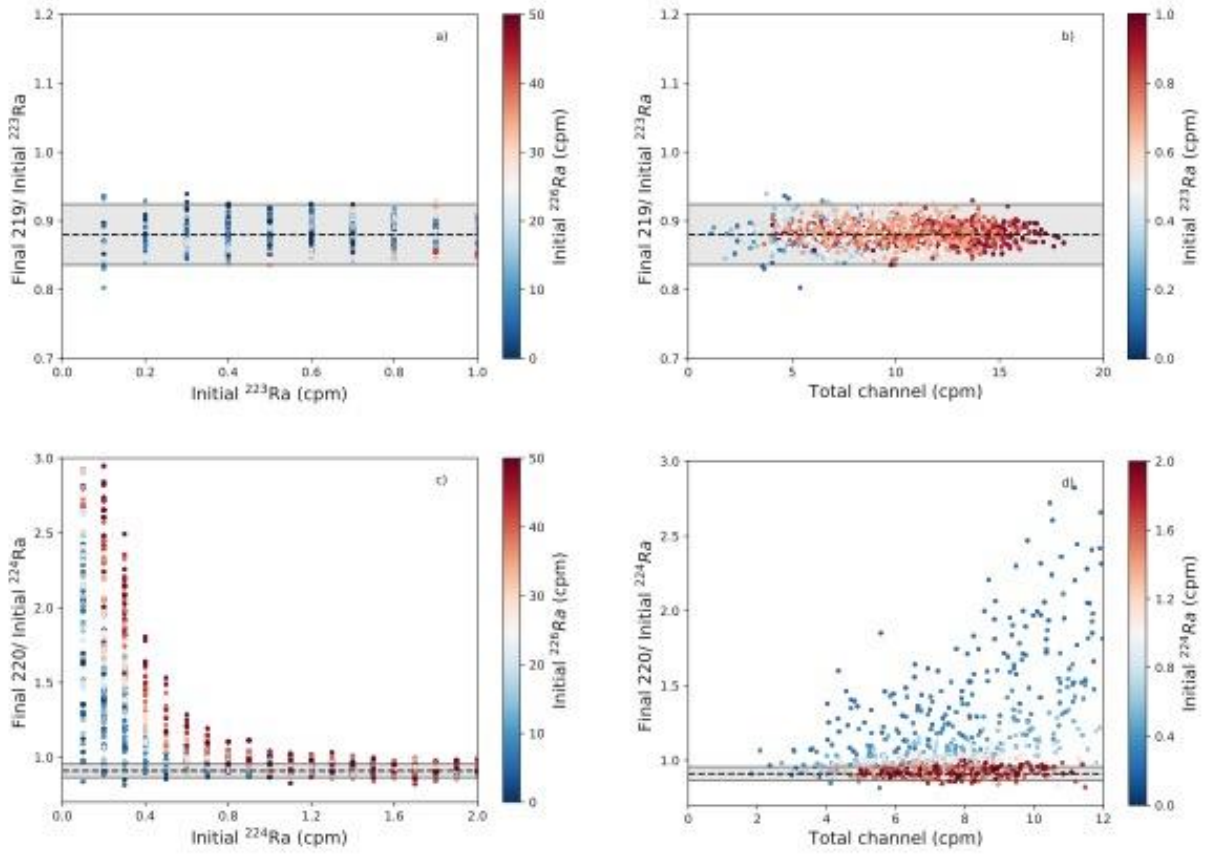


Figure 4.5. Results from simulations (n=4,000) with initial $^{223}$Ra, $^{224}$Ra and $^{226}$Ra count rates ranging 0.1-1.0, 0.1-2.0 and 0-50 cpm, respectively. The ratio between corrected 219 channel and initial $^{223}$Ra simulated count rates (*Final219/Initial*$^{223}$*Ra)* against (a) *Initial*$^{223}$*Ra* and (b) count rate in the Total channel. The ratio *Final220/Initial*$^{224}$*Ra* against (c) *Initial*$^{224}$*Ra* and (d) count rate in the Total channel. Colors represent the *Initial*$^{226}$*Ra* count rates in (a) and (c), *Initial*$^{223}$*Ra* in (b), and *Initial*$^{224}$*Ra* in (d). The dashed line represents the gate efficiency ($f_G$) and the grey band an uncertainty of 5%.

Regardless of the influence of the counting time (i.e., time for $^{222}$Rn ingrowth), which was adjusted for this simulation to obtain an uncertainty of 5% in the $^{224}$Ra quantification, the main factors that determine the deviation of the ratio *Final220*/*Initial*$^{224}$*Ra* are the activities of $^{224}$Ra

and $^{226}$Ra. For *Initial$^{224}$Ra* count rates below 1 cpm, deviations of the ratio *Final220*/*Initial$^{224}$Ra* from the gate efficiency ($f_{G\text{-}220}$ = 0.91) increase significantly as the Total channel count rate increases (Figure **4.5**d). A useful ratio for evaluating the possible overestimation due to $^{222}$Rn buildup is the ratio between the count rate in the Total channel and the count rate in the 220 channel from the first cycles of the measurement (<30 min; low influence of $^{222}$Rn buildup), defined here as $CR_{TOT/220}^{*}$. The results from these simulations suggest that ratios $CR_{TOT/220}^{*}$ above 12 may overestimate the $^{224}$Ra activities. We thus propose that when a conservative threshold of $CR_{TOT/220}^{*}$= 12 is overpassed, the counting should be stopped, and the sample purged before initializing again the measurement as recommended by (Moore, 2008).

### 4.3.6. On the use of the Total channel to quantify $^{224}$Ra activities

The activities of $^{224}$Ra are usually quantified with the equations proposed by Moore and Arnold (1996). These equations were designed to correct the count rate in each channel by the chance coincident events and possible interferences between 219 and 220 circuits (i.e., cross-talk). However, for high activity samples (>10 cpm in the Total channel), due to the relatively high effect of chance coincidence events (>0.9 cpm in the 220 channel), Moore (2008) suggested the use of the count rate in the Total channel to calculate $^{224}$Ra activities. To do so, the count rate in the Total channel (corrected by subtracting the background) is divided by the apparent total system efficiency ($E_{Tot}$), defined as the probability of recording a count following the decay of $^{224}$Ra in the fiber (Moore, 2008). Finally, the simultaneously quantified $^{223}$Ra activity is subtracted to compute the activity of $^{224}$Ra (Equation 4.1) as follows:

$$^{224}Ra(dpm) = \frac{Total\ channel\ (cpm) - background\ (cpm)}{E\ Tot} - {}^{223}Ra(dpm) \qquad \text{Equation 4.1}$$

Nevertheless, using the Total channel to quantify $^{224}$Ra implicitly assumes that all the counts are linked to Rn-Po decay events from $^{224}$Ra, with the only exception of the events related to background and $^{223}$Ra. However, as seen in Sections 4.3.2 and 4.3.5, counts registered in the Total channel will be highly influenced by the alpha decays related to $^{226}$Ra (e.g. $^{222}$Rn, $^{218}$Po,

$^{214}$Po), and thus they cannot be corrected to quantify $^{224}$Ra by simply subtracting the background and the $^{223}$Ra activity. In addition, this method strongly depends on the quantification of the activity of $^{223}$Ra. As shown in Section 4.3.4, the quantification of $^{223}$Ra activities might be highly sensitive to the recorded $^{224}$Ra activities and $^{224}$Ra/$^{223}$Ra activity ratios. Inappropriate quantifications of $^{223}$Ra activities will thus induce errors on the quantification of $^{224}$Ra from the Total channel. Considering these two factors (influence of $^{226}$Ra activities and potential inappropriate quantification of $^{223}$Ra activity), we suggest avoiding the use of the Total channel count rate to quantify $^{224}$Ra activities.

### 4.3.7. Quantification of $^{226}$Ra via $^{222}$Rn buildup

The buildup rate of $^{222}$Rn from $^{226}$Ra during a RaDeCC measurement can be used to determine $^{226}$Ra activities. Geibert et al. (2013) used the chance coincidence equations proposed by Moore and Arnold (1996) to correct the count rate in the Total channel in order to reduce the effect of $^{223}$Ra and $^{224}$Ra in the determination of $^{226}$Ra. Nevertheless, as explained in the previous section (Section 4.3.5) and as already mentioned by Moore (2008), the chance coincidence corrections would not properly correct the 219 and 220 channels under significant activities of $^{226}$Ra (>10 cpm). Here, we propose an optimized method based on the original idea of Geibert et al. (2013) which enables the quantification of $^{226}$Ra activities avoiding the use of the chance coincidence equations. The applicability of this method requires (1) long counting times (>600 min) to register a significant ingrowth of $^{222}$Rn and (2) radioactive equilibrium of $^{223}$Ra and $^{224}$Ra with their direct parents ($^{227}$Ac and $^{228}$Th, respectively) to avoid the decay of these isotopes during the measurement. Therefore, measurements for $^{226}$Ra determination should be performed 3 month after sample collection.

To evaluate the relation between the $Initial^{226}Ra$ and the resulting Total channel count rate over time, a set of simulations was performed (values for the simulations are presented in Table **4.3**). Figure **4.6**a shows the results of these simulations representing the characteristic slope of the Total channel count rate over time for different $Initial^{226}Ra$ count rates. This slope increases linearly with the increase of the $Initial^{226}Ra$ count rate (Figure **4.6**b) with a slope/$Initial^{226}Ra$ conversion factor ($m$) of $1.80 \pm 0.07 \cdot 10^{-4}$ min$^{-1}$. Notice that the method does not

require the equilibrium between $^{222}$Rn, $^{218}$Po, and $^{214}$Pb since the conversion factor is calculated from the exponential ingrowth of $^{222}$Rn (and its daughters) which is nearly linear for these relatively short (in comparison to $^{222}$Rn half-life). Hence, we propose the following equations to quantify $^{226}$Ra activities based on this conversion factor (*m*):

$$Initial^{226}Ra(cpm) = \frac{slope\ (cpm \cdot min^{-1})}{m\ (min^{-1})} \qquad \text{Equation 4.2}$$

$$^{226}Ra(dpm\ L^{-1}) = \frac{Final^{226}Ra(cpm)}{E_{Ra-226}\ (cpm\ dpm^{-1})\ V(L)} \qquad \text{Equation 4.3}$$

where $Initial^{226}Ra$ is the count rate of $^{226}$Ra derived from the slope observed in the accumulative count rate of the Total channel (*slope*) during the measurement (RaDeCC file output: *CPMTot*) due to $^{222}$Rn ingrowth and the conversion factor ($m$ =1.80±0.07·10$^{-4}$ min$^{-1}$). $^{226}Ra$ and $E_{Ra\text{-}226}$ represent the activity of $^{226}$Ra and the efficiency of the system for $^{226}$Ra determination (described below), respectively. Notice that under low activities of $^{226}$Ra, the $^{222}$Rn buildup may hardly develop and/or be associated with high uncertainties (Geibert et al., 2013). Therefore, we recommend the use of this method only for $^{226}$Ra activities higher than 10 dpm, as initially suggested by Geibert et al. (2013). Another consideration must be taken into account before applying this method: during long measurements, besides the buildup of $^{222}$Rn from $^{226}$Ra, significant amounts of $^{212}$Bi and $^{212}$Po due to ingrowth of $^{212}$Pb (from $^{224}$Ra) might be produced. Thus, the count rate in the total channel will be influenced by both, the ingrowth of $^{222}$Rn (and daughters) and the ingrowth of $^{212}$Pb (and daughters) leading to wrong quantifications of $^{226}$Ra activities. To minimize the effect of $^{212}$Pb ingrowth in the quantification, we recommend the use of this method when activities of $^{224}$Ra ($^{228}$Th) are below 1 cpm.

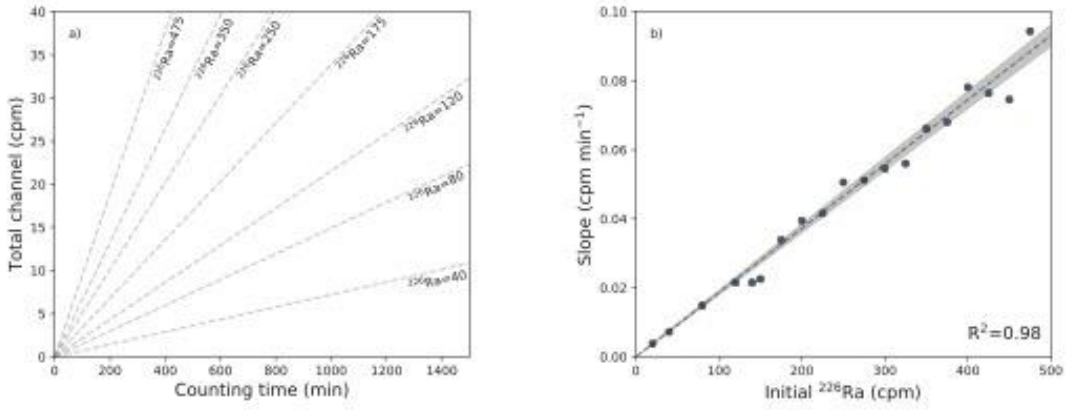


Figure 4.6. Results from simulations (n=360) with initial $^{223}$Ra, $^{224}$Ra and $^{226}$Ra count rates ranging 0.1, 0.8 and 40-475 cpm, respectively. a) Characteristic $^{222}$Rn buildup rate in the Total channel with counting time for different *Initial*$^{226}$*Ra* count rates. b) Slopes of the characteristic $^{222}$Rn buildup rate in the Total channel with counting time against *Initial*$^{226}$*Ra*. The dashed line represents the linear regression between slopes and *Initial*$^{226}$*Ra*.

The reliability of this method was tested and compared with the method presented by Geibert et al. (2013) by using a set of $^{226}$Ra samples collected in Península marshland (Spain) (Rodellas et al., 2012) and analyzed via γ-spectrometry and RaDeCC (Figure **4.7**). Whilst both methods present a good correlation with the measurements performed via γ-spectrometry for $^{226}$Ra activities ranging from 0 to 1000 dpm, the method presented by Geibert et al. (2013) exhibit higher deviations than the one presented in this work for activities higher than 1000 dpm due to the erroneous corrections applied to the count rate in the Total channel.

The presented method has several advantages in relation to the previous one presented by Geibert et al. (2013): (1) the count rate in the Total channel is not corrected by chance coincidence in order to avoid erroneous quantifications for high $^{226}$Ra activities (>1000 dpm); (2) the relative uncertainties are slightly lower (~8% and 10%, for this study and Geibert et al. (2013), respectively) because the mean error of the linear regression for the accumulative Total channel count rate over time is usually lower than the one for the corrected Total channel count rate used by Geibert et al. (2013), and (3) unlike the method proposed by Geibert et al. (2013), where several $^{226}$Ra standards are needed to calculate the system efficiency, this method only requires the use of a single $^{226}$Ra standard as described below.

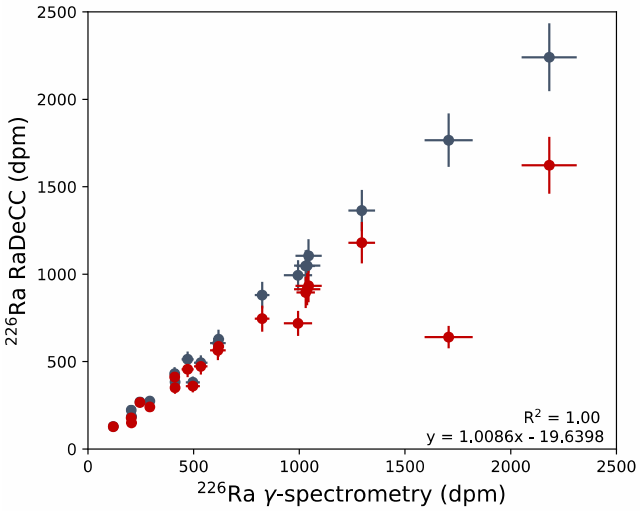


Figure 4.7. Intercomparison between the $^{226}$Ra activities quantified via $^{222}$Rn buildup with the RaDeCC system (blue dots, this study; red dots, Geibert et al. (2013)) and via γ-spectrometry from a set of samples collected in Peníscola marshland (Spain) (Rodellas et al., 2012). The dashed line represents the linear regression between $^{226}$Ra activities quantified with the method presented in this paper and the activities quantified via γ-spectrometry.

#### *4.3.7.1. Calibration of the RaDeCC system for $^{226}$Ra quantification*

In contrast with the efficiencies of the 219 and 220 channels, the efficiency to determine $^{226}$Ra activities ($E_{Ra\text{-}226}$) only depend on the apparent system efficiency ($f_S$) and the apparent cell efficiency ($f_C$), because the Total channel is registering all the decay events (i.e., gate efficiency ($f_G$) = 1) and the approach is based on the rate of ingrowth in the Total channel count rate (if the emanation efficiency ($f_E$) is assumed to be constant for the measurement, i.e. it will not affect the slope). The efficiency of the RaDeCC system to determine $^{226}$Ra can thus be expressed as:

$$E_{Ra-226} = f_S {f_C}^3 \qquad \text{Equation 4.4}$$

Notice that the apparent cell efficiency ($f_C$) is raised to the power 3 to account for the three alpha decays ($^{222}$Rn - $^{218}$Po - $^{214}$Po) that subsequentially occur after an initial $^{226}$Ra decay. The theoretical efficiency is 0.51 considering the values for $f_C$ and $f_S$ from Table 3.1. However, the

individual efficiencies for each RaDeCC system should be calculated by repeated measurements of standards with known activities of $^{226}$Ra.

### 4.3.8. Testing the quantification limits with laboratory measurements

In Sections 4.3.3, 4.3.4 and 4.3.5 we presented the limits for the quantification of $^{223}$Ra and $^{224}$Ra activities in case of high activity measurements, 219-220 cross-talk, and $^{222}$Rn buildup effect, respectively. Here, some of these limits are tested with measurements performed in the RaDeCC system of the UAB laboratory. In Section 4.3.3, we showed that the limit for the quantification of $^{224}$Ra is 100 cpm in the Total channel. Above this value, the quantification may overestimate the activities due to inappropriate correction of the count rate in the 220 channel. Considering that the limit provided in Section 4.3.3 is conservative and may depend on different circumstances (e.g. counting time, activity ratios), the results from the reiterative measurements of a high activity sample are in good agreement with these limits. The quantification of $^{224}$Ra activities remains constant (~1,600 dpm 100L$^{-1}$) when the measurements perform count rates in the Total channel below ~250 cpm. For measurements above 250 cpm in the Total channel, the quantified activities increase up to ~2,800 dpm 100L$^{-1}$ (Figure **4.8**a). Similarly, the different $^{223}$Ra quantifications of the same sample is also plotted against the ratio between 220 and 219 channel ($CR_{220/219}$) at the time of measurement (Figure **4.8**b). Above the ratio $CR_{220/219}$ > 10, the quantified activities of $^{223}$Ra increase from ~20 to 35 dpm 100L$^{-1}$ as the $CR_{220/219}$ increases, in strong agreement with the limits presented in Section 4.3.4. Finally, the limits presented in Section 4.3.5 on the influence of $^{222}$Rn buildup are investigated with 4 measurements of high activity $^{226}$Ra samples (Figure **4.8**c - Figure **4.8**f). The effect of $^{222}$Rn buildup in the $^{224}$Ra quantification is significant when the ratio between Total channel count rate and the count rate of the 220 channel from the first cycles is higher than $CR_{TOT/220}^{*}$ > 12. The grey band in Figure **4.8**c to Figure **4.8**f indicates the count rate in the Total channel which overpasses this limit.

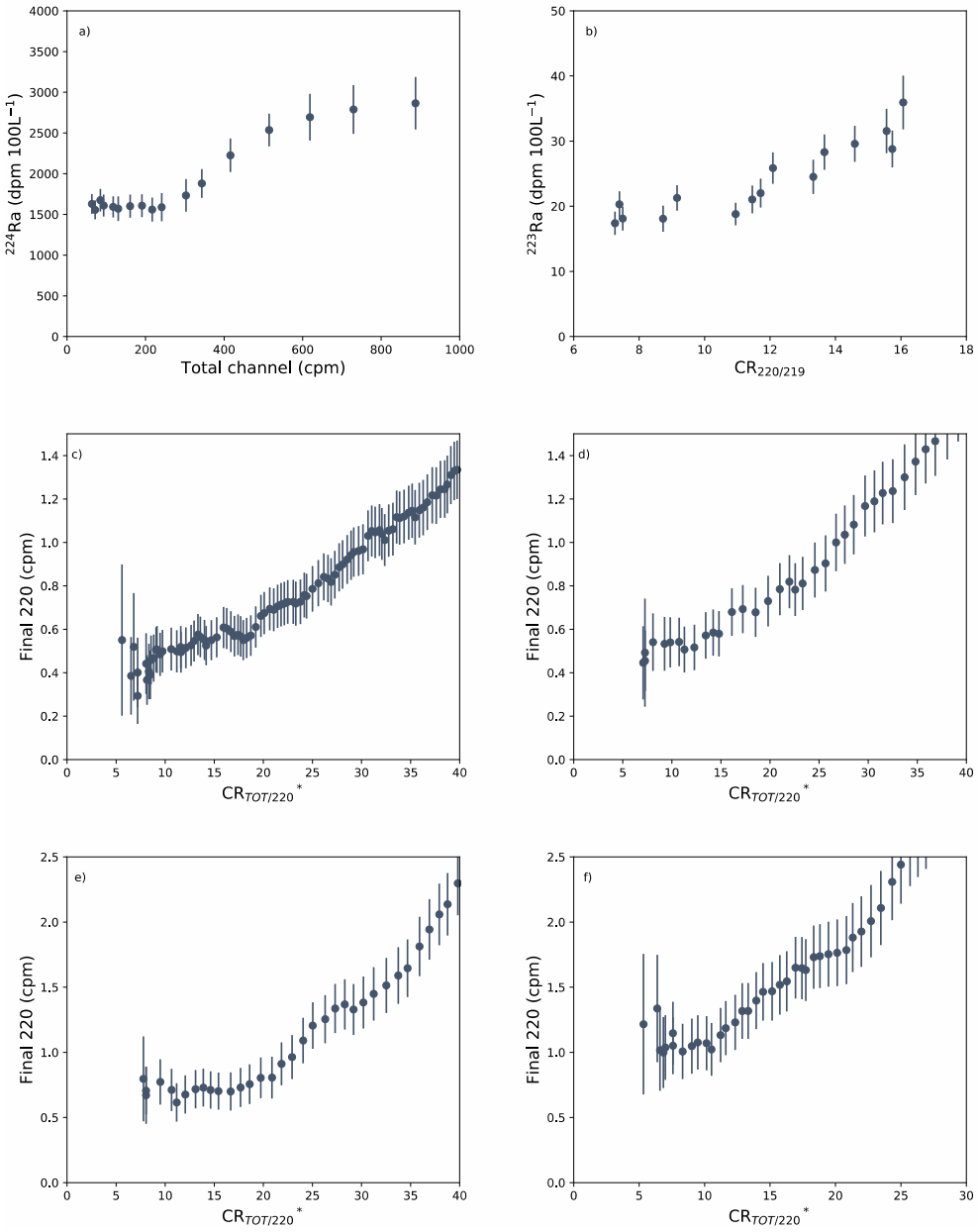


Figure 4.8. Compilation of measurements performed in the UAB laboratory. a) Quantification of $^{223}$Ra (b) and $^{224}$Ra (a) against Total channel count rate and $CR_{220/219}$, respectively, from the repeated measurement of a high activity $^{223}$Ra and $^{224}$Ra sample (20 and 1,600 dpm 100L$^{-1}$, respectively). The *Final220* count rate is evaluated in function of the Total channel count rate for four different measurements (c) - (f). The dashed lines indicate the quantification limits in cases of (a) high activity measurements, (b) 219-220 cross-talk effect, and (c to f) $^{222}$Rn buildup effect.

## 4.4. Guidelines

### 4.4.1. Measurement and quantification of $^{223}$Ra and $^{224}$Ra activities

The proper quantification of $^{223}$Ra and $^{224}$Ra activities using the RaDeCC system is highly dependent on (1) the count rate registered in the Total channel (Section 4.3.3), (2) its channel

ratio (*220 channel/219 channel; $CR_{220/219}$*) (Section 4.3.4), and (3) the $^{222}$Rn buildup (Section 4.3.5). The $^{222}$Rn buildup effect is treated in the following subsection since it is more significant for measurements that require long counting times (800 - 1,200 min) due to the low activities of the samples (e.g. measurements for $^{228}$Th, $^{228}$Ra or $^{227}$Ac determination).

The quantification of $^{223}$Ra activities should not be performed when the count rate in the Total channel overpass 200 cpm (Section 4.3.3). For lower count rates, the quantification should be prevented to avoid 219-220 cross-talk interferences due to the influence of $^{224}$Ra in the 219 channel when $CR_{220/219} > 10$ or when $CR_{220/219} > 4$ and *220 channel* > 5 cpm (see Section 4.3.4). The quantification of $^{223}$Ra under these conditions could produce an overestimation of the $^{223}$Ra activities up to ~40%. When these conditions are met and the quantification is not recommended, a further measurement can be performed after a certain time to allow the $CR_{220/219}$ and the count rate in the 220 channel to decrease, as already recommended by Moore (2008).

The quantification of $^{224}$Ra activities should never be derived from the Total channel count rate, as this channel is highly influenced by the activities of $^{223}$Ra and $^{226}$Ra (Section 4.3.6), contrary to previous recommendation for high activity samples (Moore, 2008). Therefore, independent of the sample activity, the quantification of the $^{224}$Ra activity should be based on the counting in the 220 channel and quantified using the equations proposed by Moore and Arnold (1996). To avoid inappropriate estimations of $^{224}$Ra activities, the quantification of $^{224}$Ra activities with the RaDeCC system should be performed under both of the following conditions: (1) the count rate in the Total channel should be lower than the maximum quantification limit of 100 cpm (Section 4.3.3) and (2) the $CR_{220/219}$ should be higher than 8, or higher than 2, when the 219 channel count rate does not exceed 1 cpm (Section 4.3.4). If the first condition is not met, further measurements can be performed to allow the activity of $^{224}$Ra to decrease. Contrarily, if the second condition is not met, no extra measurements can be performed to increase $CR_{220/219}$ and the potential overestimation of the quantified $^{224}$Ra activity (up to 30%) should be acknowledged.

The thresholds and guidelines for an appropriate quantification of $^{223}$Ra and $^{224}$Ra activities using the RaDeCC system based on the results of this study are summarized in Figure **4.9**.

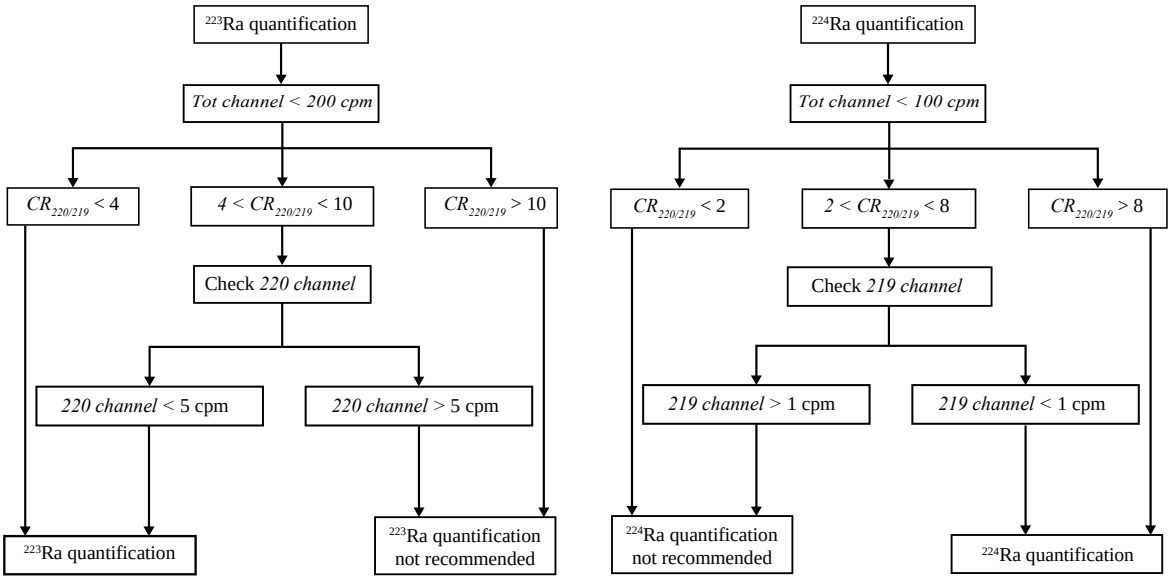


Figure 4.9. Schematic diagram of the guidelines to measure and quantify $^{223}$Ra and $^{224}$Ra samples with the RaDeCC system

### 4.4.2. Measurement and quantification of $^{227}$Ac and $^{228}$Th activities

The activities of $^{227}$Ac and $^{228}$Th are quantified with the RaDeCC system when their daughters ($^{223}$Ra and $^{224}$Ra, respectively) are in radioactive equilibrium (i.e., after 1 - 3 months after sample collection), usually conducting long measurements to reduce the analytical uncertainty. In addition to the above-mentioned recommendations for $^{223}$Ra and $^{224}$Ra, the quantification of $^{227}$Ac and $^{228}$Th activities will strongly depend on the buildup of $^{222}$Rn from $^{226}$Ra (Section 4.3.5). In the case of $^{227}$Ac ($^{223}$Ra) quantification, this effect is negligible due to the short opening time of the 219 channel ($t_{G\text{-}219}$ = 5.6 ms). Conversely, the $^{222}$Rn buildup will significantly affect the $^{228}$Th ($^{224}$Ra) quantification (Figure **4.5**b), especially for measurements with low counting rates in the 220 channel (< 1 cpm). In such cases, significant overestimations produced by $^{222}$Rn buildup may occur when the ratio between the count rates in the Total channel in the 220 channel from the first cycles ($CR_{TOT/220}^{*}$) exceed 12 (Section 4.3.5). In order to properly

quantify $^{224}$Ra or $^{228}$Th activities under these specific conditions, the counting should be stopped when the threshold of $CR_{TOT/220}^{*}$ = 12 is overpassed (or only the first cycles of the measurement be used), and the sample should be properly purged before conducting a new measurement of the same sample (Moore, 2008).

### 4.4.3. Measurement and quantification of $^{226}$Ra activities via $^{222}$Rn buildup

The activities of $^{226}$Ra can be determined by using the ingrowth rate of $^{222}$Rn in the Total channel using the RaDeCC system. In this work, we propose an improved simple method to quantify $^{226}$Ra activities based on this process and the approach described by Geibert et al. (2013). In contrast to the approach of Geibert et al. (2013), the method described in this study avoids correcting the count rate in the Total channel using the chance coincidence equations, since this correction may be inappropriate for high Ra activities (Section 4.3.2 and 4.3.7). The applicability of the method requires (1) long counting times (>600 min) to register a significant ingrowth of $^{222}$Rn; (2) radioactive equilibrium between $^{223}$Ra-$^{227}$Ac and $^{224}$Ra-$^{228}$Th and (3) the calibration of the RaDeCC system with the use of a single $^{226}$Ra standard. The activities of $^{226}$Ra can be easily calculated by dividing the slope of the count rate in the Total channel over time by the conversion factor ($1.80 \pm 0.07 \cdot 10^{-4}$ $min^{-1}$; Figure **4.6**b) and the efficiency of the counter for $^{226}$Ra

# Chapter 5: New perspectives on the use of $^{224}Ra/^{228}Ra$ and $^{222}Rn/^{226}Ra$ activity ratios in groundwater studies

## 5.1. Introduction

Ra isotopes and Rn are widely applied by marine scientific communities interested in quantifying SGD-derived inputs of solutes to the coastal ocean (e.g., Moore, 2006; Taniguchi et al., 2019). However, their use is still limited in coastal and inland hydrogeological studies and only a few applications have been carried out to evaluate velocities of groundwater and groundwater/seawater residence times in coastal aquifers. Most of these studies have used single radionuclides or the activity ratios of radionuclides from different decay chains (e.g., Duque et al., 2019; Kiro et al., 2013, 2014, 2015; Luo and Jiao, 2019; Michael et al., 2011; Tamborski et al., 2017). In contrast, the application of the activity ratios (ARs) of radionuclides from the same decay chain, which only requires the evaluation of the parent-daughter relationship, has been underexploited in hydrogeology. This is mainly because the classical analysis of Ra isotopes and Rn in groundwater is commonly performed by using advective transport models that deal separately with each radionuclide (e.g., Krest and Harvey, 2003; Michael et al., 2011; Tamborski et al., 2019). Consequently, these models do not account for the dependency of the production rates on the temporal distribution of parent radionuclide activities. The development of transport models that include not only the target radionuclide, but also the direct parent in the formulation is thus fundamental for the application of these radionuclides and their activity ratios in groundwater studies.

In this study, we propose the use of the ARs of $^{224}Ra/^{228}Ra$ and $^{222}Rn/^{226}Ra$, which are pairs of radionuclides belonging to the same decay chain, as proxies of hydrogeological processes. The aim of this study is thus to provide a comprehensive analysis of the processes that exert a control on the ARs of $^{224}Ra/^{228}Ra$ and $^{222}Rn/^{226}Ra$ in groundwater (e.g., production rates, retardation, and transit times), and to present novel applications, which interrelate the disciplines of hydrogeology (determination of groundwater transit times) and coastal oceanography (evaluating pathways and end-members of SGD). To this aim, an improved advective transport

model that integrates all radionuclides from the same decay chain into a single formulation was developed. The advective transport model and the applications of the ARs were tested at the experimental site of Argentona, a Mediterranean coastal aquifer.

## 5.2. Advective transport model of radionuclides

In order to evaluate all the possible sources and sinks of radionuclides in groundwater, we formulate two types of mass balances for all radionuclides in a decay chain, one for the radionuclides contained in the sediment grains of the aquifer, which we refer to as the solid part, and another one for the radionuclides dissolved in groundwater and adsorbed onto solid surfaces, which we refer to as the exchangeable part.

**Solid part:** For the mass balance in the solid part, we assume that (1) it is not affected by the processes occurring at the surface-groundwater interface (i.e., exchangeable part) such as ionic exchange or weathering and (2) it is in steady-state conditions, that is, the activities do not change with time. The model considers the radioactive decay and production of the target radionuclide including the process of $\alpha$-recoil. The $\alpha$-recoil process is included by a parameter ($\alpha$-recoil factor, $\mu$ [-]) that represents the fraction of $\alpha$-decays occurring in the solid part that are transferred to the exchangeable part ($0 \leq \mu \leq 1$). The activities in the solid part can be formulated as:

$$\begin{cases} s_i = constant & i = 1 \\ s_i = (1 - \mu_{i-1}) s_{i-1} & i = 2, \dots, n \end{cases} \quad \text{Equation 5.1}$$

where $i$ is the radionuclide number in the decay chain (e.g., $i = 1$ for $^{232}$Th and $i$ = 2 for $^{228}$Ra) and $s$ [Bq m$^{-3}$ of aquifer] is the sediment or solid activity. The activity produced by the mobilization from the solid mineral lattice of the sediment grains to the exchangeable part via $\alpha$-recoil ($f$ [Bq m$^{-3}$ of water]) can be expressed as follows:

$$\begin{aligned} f_i &= 0 && i = 1 \\ f_i &= \mu_{i-1} s_{i-1} \phi^{-1} && i = 2, \dots, n' \end{aligned} \qquad \text{Equation 5.2}$$

where $\phi$ [-] is the aquifer porosity. Notice, that by substituting Equation 5.1 into 5.2, we can express the $\alpha$-recoil ($f$) without the $\alpha$-recoil factor ($\mu$):

$$\begin{aligned} f_i &= 0 && i = 1 \\ f_i &= (s_{i-1} - s_i) \phi^{-1} && i = 2, \dots, n \end{aligned} \qquad \text{Equation 5.3}$$

Moreover, the sum of the $\alpha$-recoil of all radionuclides in a decay chain must equal the sediment activity of the first isotope ($s_1$) minus that of the last isotope ($s_n$) (Equation 5.4), provided that the sediment activity of an isotope is always lower than that of its parent ($s_i \leq s_{i-1}$; Equation 5.1), and that $\alpha$-recoil is the only process that produces this disequilibrium within sediment grains:

$$\sum_{i=2}^{n} f_i = (s_1 - s_2 + s_2 - s_3 + s_3 \dots - s_n)\phi^{-1} = (s_1 - s_n)\phi^{-1}. \qquad \text{Equation 5.4}$$

Equations 5.2 and 5.3 may be used to establish the $\alpha$-recoil of the various radionuclides.

**Exchangeable part:** The mass balance of the exchangeable part considers (1) the transport of radionuclides in groundwater, (2) the decay of the dissolved and adsorbed target radionuclide, and (3) the production from the parent radionuclide content in groundwater, on the solid surfaces, and in the alpha recoil zone. The model assumes that the dissolved and adsorbed radionuclides are in chemical equilibrium, and can be expressed as follows:

$$\begin{aligned} \phi \frac{\partial b_i}{\partial t} &= L(a_i) - \phi \lambda_i b_i && i = 1 \\ \phi \frac{\partial b_i}{\partial t} &= L(a_i) - \phi \lambda_i b_i + \phi \lambda_i b_{i-1} + \phi \lambda_i f_i && i = 2, \dots, n \end{aligned}, \qquad \text{Equation 5.5}$$

where $a$ [Bq m$^{-3}$ of water] is the activity in the water (hereinafter, dissolved activities), $b$ [Bq m$^{-3}$ of water] is the activity in the exchangeable part (dissolved and adsorbed), $t$ [s] is time, $\lambda$ [s$^{-1}$] is the decay constant, and $L(a)$ [Bq m$^{-3}$ s$^{-1}$] is a linear operator for transport, which may include terms for advection, diffusion, and dispersion (Bear, 1972):

$$L(a) = -\mathbf{q} \cdot \nabla a + \nabla \cdot (\phi \mathbf{D} \nabla a), \qquad \text{Equation 5.6}$$

where $\mathbf{q}$ [m s$^{-1}$] is the Darcy flux vector and $\mathbf{D}$ is a tensor for diffusion-dispersion coefficients.

The transport equation (Equation 5.5) is a general equation that can be simplified by assuming steady-state conditions ($\partial b/\partial t = 0$), neglecting the effect of dispersive and diffusive transport relative to advective one ($L(a) = -\mathbf{q} \cdot \nabla a$), and defining a travel time (hereinafter, transit time) $\tau$ [s] along a flow path ($\mathbf{x}$ [m]), such that:

$$\mathbf{x} = \int_{t=0}^{t=\tau} \mathbf{v} dt \Rightarrow \frac{da}{d\tau} = \mathbf{v} \cdot \nabla a, \qquad \text{Equation 5.7}$$

where $\mathbf{v}$ [m s$^{-1}$] is the groundwater velocity vector ($\mathbf{v} = \phi^{-1}\mathbf{q}$). Subsequently, the transport equation (Equation 5.5) becomes:

$$\begin{aligned} \frac{\partial a_i}{\partial \tau} &= -\lambda_i R_i a_i && i = 1 \\ \frac{\partial a_i}{\partial \tau} &= -\lambda_i R_i a_i + \lambda_i R_{i-1} a_{i-1} + \lambda_i f_i && i = 2, \dots, n \end{aligned}, \qquad \text{Equation 5.8}$$

or

$$\begin{aligned} \frac{\partial b_i}{\partial \tau} &= -\lambda_i R_i b_i && i = 1 \\ \frac{\partial b_i}{\partial \tau} &= -\lambda_i R_i b_i + \lambda_i R_i b_{i-1} + \lambda_i R_i f_i && i = 2, \dots, n \end{aligned} \quad , \qquad \text{Equation 5.9}$$

for dissolved (Equation 5.8) and exchangeable (Equation 5.9) activities, where $R$ [-] is a linear retardation factor ($R$ [-]; $b_i = R_i a_i$). Retardation is considered to be the reduction of the average velocity of a solute relative to the groundwater velocity (McKinley and Russell Alexander, 1993) due to the different solid-solution interaction processes (e.g., precipitation, dissolution, ionic exchange). Indeed, the retardation factor depends on the groundwater composition (e.g., salinity, pH), the characteristics of the geological matrix (e.g., cationic exchange capacity, grain size), and the geochemistry and half-life of each radionuclide. Thus, in a homogeneous system (i.e., no changes in geology or groundwater composition), the retardation factor is unique for each isotope in the decay chain, and can take values from 1 (for unreactive elements such as Rn) to infinite (Krishnaswami et al., 1982). When the main process of exchange between solid and solution is ionic exchange, the retardation factor can be directly related to the distribution coefficient (Michael et al., 2011):

$$R = 1 + K_D \frac{\rho_b}{\phi}, \qquad \text{Equation 5.10}$$

where $K_D$[m$^3$ kg$^{-1}$] is the distribution coefficient (the ratio of solid phase to solute concentrations of radionuclide) and $\rho_b$ [kg m$^{-3}$] is the sediment dry bulk mass density (Michael et al., 2011). Under this assumption, all isotopes from a certain element have the same retardation factor, provided that the adsorption-desorption processes are faster than the decay rates of the considered isotopes (Krishnaswami et al., 1982).

A particular case of the transport equation (Equation 5.9) would be when the exchangeable and dissolved activities do not change with groundwater transit times ($R_i\, \partial a_i/\partial \tau = \partial b_i/\partial \tau =$

0). We refer to this case as bulk radioactive equilibrium, which considers the production and decay of a radionuclide in its dissolved and adsorbed form plus the $\alpha$-recoil supply from the solid. In this case, Equation 5.9 becomes:

$$\begin{aligned} b_i &= 0 && i = 1 \\ b_i &= b_{i-1} + f_i && i = 2, \dots, n \end{aligned} \quad . \qquad \text{Equation 5.11}$$

The use of the transport model presented here has some limitations and considerations that should be taken into account before its application. The model neglects two processes that might influence the activities of radionuclides in groundwater: weathering and chemical precipitation. Whilst these processes might be relevant in specific areas (e.g., co-precipitation of Ra under high concentrations of barite or carbonates or in the presence of Fe and Mn (hydro)oxides; Beneš et al., 1984; Gonneea et al., 2013), they are often assumed to play a minor role in the distribution of Ra isotopes in groundwaters, in comparison to the production/decay and adsorption/desorption terms (Porcelli, 2008). The model also neglects potential Rn losses to the atmosphere, which are expected to be negligible in aquifers. However, if weathering, precipitation and/or evasion rates are hypothesized as relevant in the studied system, a source/sink term can be factored into the model's formulation (i.e., Equation 5.5) to account for these processes.

The assumption of steady-state conditions (i.e., activities not varying with time, $\partial b/\partial t = 0$), which is a common assumption for most of the advective transport models (e.g., Krest and Harvey, 2003; Michael et al., 2011; Tamborski et al., 2019, 2017a), may not be valid for systems subjected to non-periodical forcing such as waves, strong precipitation events (i.e., variable recharge), sea-level variability, or sea-level rise (Robinson et al., 2018). Therefore, a proper characterization of the processes affecting the study site and the activities of radionuclides is needed to apply the model presented in this study. It should be noted however that the average time that the radium isotopes reside in the system ($\partial a/\partial t = 0$) depends on both the decay

constant and the retardation factor of each radionuclide (i.e., $1/\lambda R$). The assumption of steady-state should thus be validated on this temporal scale (Rodellas et al., 2021). For instance, the dissolved activities of $^{226}Ra$ may reach steady-state in ~8 days and ~23 years for fresh ($R_{Ra} \approx 10^5$) and saline ($R_{Ra} \approx 10^2$) groundwater, respectively.

The model also considers that groundwater is flowing through a homogeneous aquifer (i.e., constant $R$ and $b/f$) and thus neglects potential heterogeneities of the aquifer matrix that can influence the parameters of the model. Finally, the model neglects dispersion and other mixing processes. This is particularly relevant for the saltwater-freshwater interphase in coastal aquifers, where the different end-members mix. Therefore, the model may only be applicable to either the fresh or the saline part of an aquifer, provided that groundwater is sufficiently enriched in Ra and Rn isotopes.

In the appendices (Appendix B), a simple analytical solution for Equation 5.9 was deduced by using vector-matrix notation. The analytical solution is used in the following sections to assess the behavior of Th, Ra, and Rn in groundwater (Section 5.3.1), and to evaluate the role of $\alpha$-recoil and retardation of Ra in the distribution of ARs of $^{224}Ra/^{228}Ra$ and $^{222}Rn/^{226}Ra$ in groundwater (Section 5.3.2 and 5.3.3, respectively). It should be noted that the analysis of the model parameters assumes that the activities of the inflowing water into the aquifer are negligible compared to those in groundwater. This assumption may be valid for most of the groundwater systems since the activities of surficial waters are commonly of orders of magnitude lower than those in groundwater (Cerdà-Domènech et al., 2017). However, this assumption may not be valid in sites where inflowing water is highly enriched in long-lived radionuclides (e.g., mining waters; Dias da Cunha et al., 2014). The input parameters used for the model in each section are shown in Table **5.1**.

## 5.3. Results and discussion

### 5.3.1. Thorium, radium, and radon enrichment in groundwater

In this section, we use the advective transport model (see Appendix B) to evaluate the different enrichment rates of Th, Ra, and Rn in groundwater flowing through an aquifer. For this purpose, a particular case is considered, in which the groundwater flowing through the aquifer is

saline and the production rate only depends on the exchangeable activity of the parent radionuclide ($b_{i-1}$) (i.e., there is no $\alpha$-recoil, $f = 0$). Therefore, typical retardation factors for Th and Ra in saline groundwater were used ($10^{10}$ and $10^{3}$, respectively; Kumar et al., 2020; Michael et al., 2011), and an arbitrary exchangeable activity for the parent radionuclides ($^{232}$Th and $^{230}$Th) of $10^{4}$ Bq m$^{-3}$ was imposed as exchangeable activity at the inflow boundary of the flow path ($b_0$) (see Table **5**.**1**). Notice that the selected $b_0$ has no influence on the different radionuclide enrichment rates.

Table 5.1. Values used for the model parameters in each section. The parameters $\boldsymbol{R}$, $\boldsymbol{f}$, and $\boldsymbol{b_0}$ refer to the retardation factor, the **α**-recoil activity, and the exchangeable activity at the inflow boundary of the flow path, respectively.

| | | ***5.3.1. Th, Ra and Rn enrichment in groundwater*** | | | ***5.3.2. Effect of alpha recoil supply*** | | | ***5.3.3. Effect of retardation factor of Ra*** | | |
|---|---|---|---|---|---|---|---|---|---|---|
| **Radionuclide** | $T_{1/2}$ | $R$ | $f$ | $b_0$ | $R$ | $f$ | $b_0$ | $R$ | $f$ | $b_0$ |
| | | - | Bq m$^{-3}$ | Bq m$^{-3}$ | - | Bq m$^{-3}$ | Bq m$^{-3}$ | - | Bq m$^{-3}$ | Bq m$^{-3}$ |
| ***$^{232}$Th decay chain*** | | | | | | | | | | |
| $^{232}$Th | 14.1 (Gy) | $10^{10}$ | 0 | $10^{4}$ | $10^{10}$ | 0 | 0 - $10^{9}$ | $10^{10}$ | 0 | 0 |
| $^{228}$Ra | 5.7 (y) | $10^{3}$ | 0 | 0 | $10^{3}$ | $10^{4}$ | 0 | 1 - $10^{8}$ | $10^{4}$ | 0 |
| $^{228}$Th | 1.9 (y) | $10^{10}$ | 0 | 0 | $10^{10}$ | 0 | 0 | $10^{10}$ | 0 | 0 |
| $^{224}$Ra | 3.6 (d) | $10^{3}$ | 0 | 0 | $10^{3}$ | $1.2 \cdot 10^{4}$ | 0 | 1 - $10^{8}$ | $1.2 \cdot 10^{4}$ | 0 |
| $^{220}$Rn | 55 (s) | 1 | 0 | 0 | - | - | - | - | - | - |
| ***$^{238}$U decay chain*** | | | | | | | | | | |
| $^{230}$Th | 75.4 (ky) | $10^{10}$ | 0 | $10^{4}$ | $10^{10}$ | 0 | 0 - $10^{9}$ | $10^{10}$ | 0 | 0 |
| $^{226}$Ra | 1.6 (ky) | $10^{3}$ | 0 | 0 | $10^{3}$ | $10^{4}$ | 0 | 1 - $10^{8}$ | $10^{4}$ | 0 |
| $^{222}$Rn | 3.8 (d) | 1 | 0 | 0 | 1 | $10^{4}$ | 0 | 1 | $10^{4}$ | 0 |

The evolution of the activities for the different radionuclides, as a function of groundwater transit times, is shown in Figure **5**.**1**. The results indicate that the effect of groundwater transit times on the activities of $^{232}$Th and $^{230}$Th is negligible, due to its large

retardation factor (Figure **5**.**1**a and Figure **5**.**1**c). Nevertheless, the exchangeable activities for $^{228}Th$ may be lower than those of $^{232}Th$. This is because the production rate of $^{228}Th$ depends on the activities of $^{228}Ra$, which is partially dissolved in groundwater, and can be removed by advective flow (Figure **5**.**1**a). The activities of Rn isotopes in groundwater increase with transit time, reaching the equilibrium with the exchangeable activity of its parent (Ra) at a specific groundwater transit time (Figure **5**.**1**a and Figure **5**.**1**c). Since Rn is a noble gas (i.e., not affected by chemical reactions), the characteristic groundwater transit time for achieving the equilibrium with its parent, corresponds to the time to reach secular equilibrium with Ra ($7 \cdot T_{1/2}$; ~7 min and ~27 days for $^{220}Rn$ and $^{222}Rn$, respectively) because it only depends on the half-live of each isotope ($R_{Rn} = 1$). Similarly, the activities of Ra isotopes increase with groundwater transit times. In this case however, the rate of increase and the specific time at which Ra isotopes achieve equilibrium with the exchangeable activities of their parent Th, not only depend on their half-lives but also on the retardation factor of Ra. Consequently, Ra isotopes require shorter groundwater transit times for achieving their equilibrium activities (i.e., $\partial a/\partial \tau = 0$) in groundwater (minutes, hours, and months for $^{224}Ra$ with $^{228}Th$, $^{228}Ra$ with $^{232}Th$, and $^{226}Ra$ with $^{230}Th$, respectively) than those needed to achieve radioactive secular equilibrium with their parents (~25 days, ~40 years and ~10,000 years for $^{224}Ra$, $^{228}Ra$, and $^{226}Ra$, respectively).

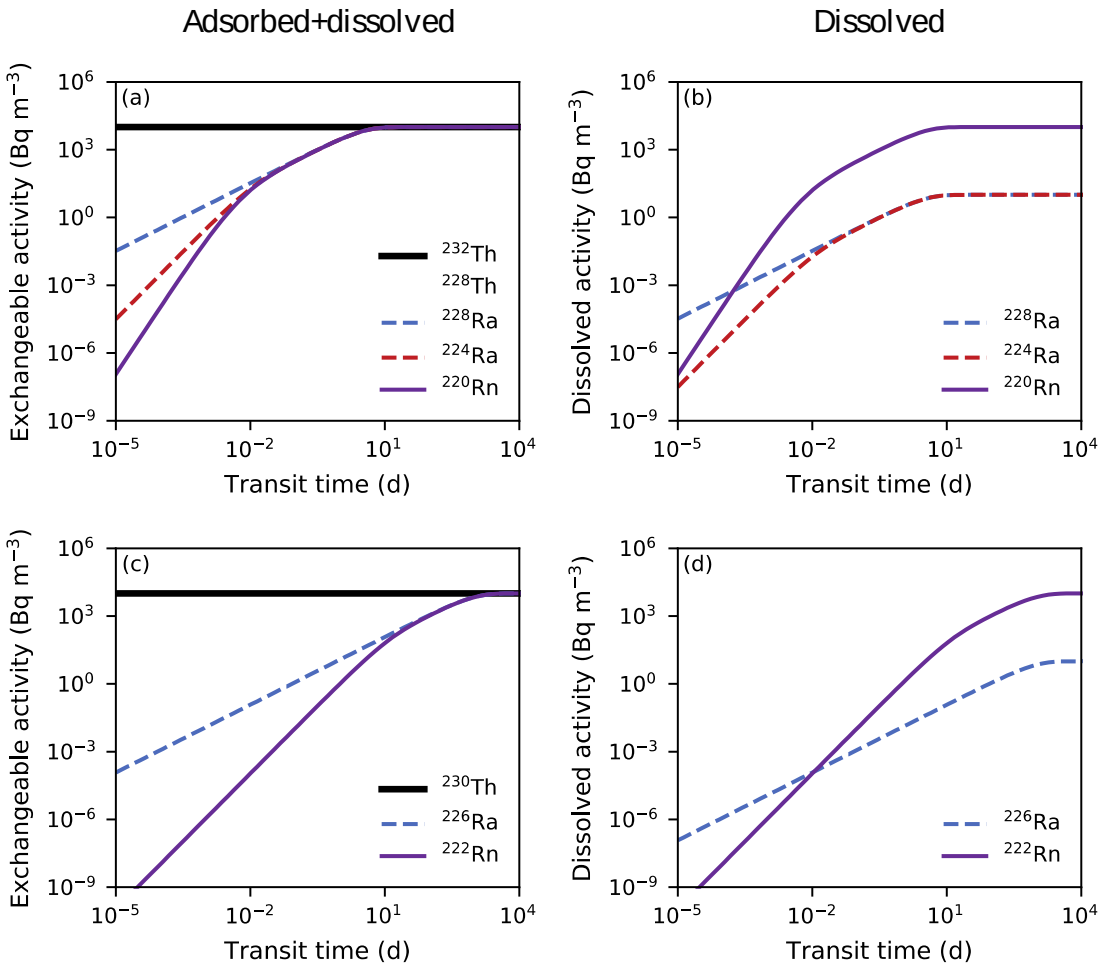


Figure 5.1. Exchangeable (adsorbed and dissolved) (a and c) and dissolved (b and d) activities of $^{232}$Th, $^{228}$Ra, $^{228}$Th, $^{224}$Ra, and $^{220}$Rn (a and b) and $^{230}$Th, $^{226}$Ra, and $^{222}$Rn (c and d) as a function of groundwater transit times under the conditions specified in Table 5.1.

Notice that the exchangeable activities of the daughter radionuclides are always lower than the exchangeable activities of their direct parents, until they reach equilibrium ($b_i = b_{i-1}$) at a specific transit time (Figure **5.1**a and Figure **5.1**c). Once this equilibrium is reached, the dissolved ARs between daughter and parent radionuclides can be described by $a_i/a_{i-1} = R_{i-1}/R_i$ (since $b_i = a_i R_i$). Thus, the dissolved ARs of $^{224}$Ra/$^{228}$Ra and $^{222}$Rn/$^{226}$Ra under these conditions are 1 and $R_{Ra}$, respectively, as shown in Figure **5.2**. Notably, these ARs for $^{224}$Ra/$^{228}$Ra and $^{222}$Rn/$^{226}$Ra are sometimes lower than those found in natural groundwaters (e.g., Copenhaver et al., 1993, 1992; Krishnaswami et al., 1991; Moise et al., 2000; Vinson et al., 2013, 2009). This is because, in this analysis, the production rate is assumed to depend solely on the

exchangeable activity ($b_{i-1}$) of the parent radionuclide, implicitly neglecting the role of the supply from the effective $\alpha$-recoil zone. Therefore, ARs found in natural groundwater samples cannot be explained without explicit consideration of the $\alpha$-recoil supply.

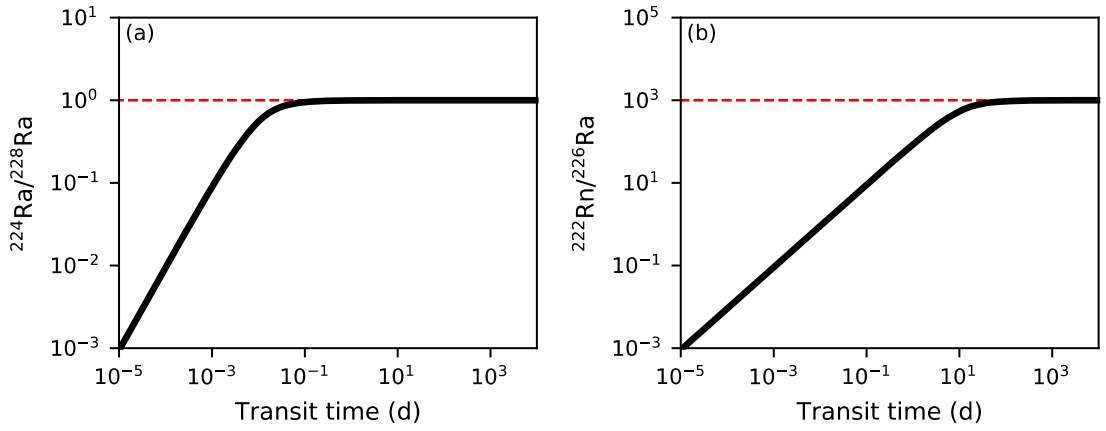


Figure 5.2. Dissolved activity ratios of $^{224}Ra/^{228}Ra$ (a) and $^{222}Rn/^{226}Ra$ (b) against groundwater transit times. Red dashed line indicates the ARs when the daughter radionuclides achieve the equilibrium with its parents (1 and $\boldsymbol{R_{Ra}}$ for $^{224}Ra/^{228}Ra$ and $^{222}Rn/^{226}Ra$, respectively).

### 5.3.2. The effect of alpha recoil supply on $^{224}Ra/^{228}Ra$ and $^{222}Rn/^{226}Ra$ activity ratios

The mobilization of radionuclides from the solid to groundwater due to the energy of an $\alpha$-decay, commonly known as $\alpha$-recoil, may be an important source of Rn and Ra isotopes to groundwater (e.g., Kigoshi, 1971; Sun and Semkow, 1998; Swarzenski, 2007). In this section, the models of the solid part and exchangeable part (see Section 5.2) are used to evaluate (1) the role of the grain size in the $\alpha$-recoil, (2) the bulk radioactive equilibrium of the $^{224}Ra/^{228}Ra$ and $^{222}Rn/^{226}Ra$ ARs, and (3) the importance of the $\alpha$-recoil supply relative to the source from the exchangeable activities of the parent radionuclide.

#### *5.3.2.1. The role of grain size in the supply from alpha recoil*

The supply from $\alpha$-recoil to groundwater depends on the activity of the parent radionuclide in the sediment grains or solids ($s$) as well as on the fraction of $\alpha$-decays occurring in the sediment grains that recoil into groundwater (i.e., $\alpha$-recoil factor, $\mu$). To evaluate the $\alpha$-recoil factor, a similar analysis to the one presented by Porcelli (2008) is proposed. This analysis is based on the determination of the fraction of $\alpha$-derived nuclides recoiling into groundwater, from the volume

ratio of the effective $\alpha$-recoil zone to the total sediment grain. For this approach it is assumed that (1) the sediment grains are spherical, (2) the volume of the effective $\alpha$-recoil zone depends on the characteristic travel distance of the generated $\alpha$-decay daughter radionuclide, $d_\alpha$ [µm], (3) the parent radionuclide is uniformly distributed in the sediment grain, (4) only half of the $\alpha$-decays occurring in the $\alpha$-recoil zone effectively recoil in groundwater, and (5) only $\alpha$-emitters produce the mobilization of the daughter radionuclide. This gives the following relation between the $\alpha$-recoil factor ($\mu$) and grain diameter ($d$ [µm]):

$$\mu = \frac{1}{2}\left(1 - \frac{\left(\frac{d}{2} - d_\alpha\right)^3}{\left(\frac{d}{2}\right)^3}\right) = 3\frac{d_\alpha}{d} - 6\frac{d_\alpha^2}{d^2} + 4\frac{d_\alpha^3}{d^3}. \qquad \text{Equation 5.12}$$

Notice that, if the grain diameter is much higher than the $\alpha$-recoil travel distance ($d >> d_\alpha$), Equation 5.12 can be simplified to $\mu \approx 3\frac{d_\alpha}{d}$. In Figure **5**.**3**a, the $\alpha$-recoil factor ($\mu$) is evaluated for different grain diameters. As expected, the $\alpha$-recoil factor decreases as the diameter of the sediment grain increases (e.g., the $\alpha$-recoil supply from sandy sediments is thus expected to be lower relative to muddy sediments). The ratio between the $\alpha$-recoil supply of daughter and parent radionuclides for $^{224}$Ra-$^{228}$Ra and $^{222}$Rn-$^{226}$Ra pairs can be derived from Equation 5.1 and 5.2 as follows:

$$\frac{f_{Ra-224}}{f_{Ra-228}} = \frac{\mu_{Th-228}}{\mu_{Th-232}}(1 - \mu_{Th-232}), \qquad \text{Equation 5.13}$$

$$\frac{f_{Rn-222}}{f_{Ra-226}} = \frac{\mu_{Ra-226}}{\mu_{Th-230}}(1 - \mu_{Th-230}). \qquad \text{Equation 5.14}$$

Considering the average $\alpha$-recoil distances reported by Sun and Semkow (1998) (407, 381, 370 and 331 Å for $^{224}$Ra, $^{222}$Rn, $^{226}$Ra, and $^{228}$Ra, respectively) and the derived $\alpha$-recoil vs grain diameter relationship (Figure **5**.**3**a), the $\alpha$-recoil pair ratios increase with grain diameter towards

the values ~1.2 and ~1.0 for $^{224}Ra$-$^{228}Ra$ and $^{222}Rn$-$^{226}Ra$ pairs, respectively. These values result from the ratio between average $\alpha$-recoil distances for daughter radionuclides relative to the parent radionuclides.

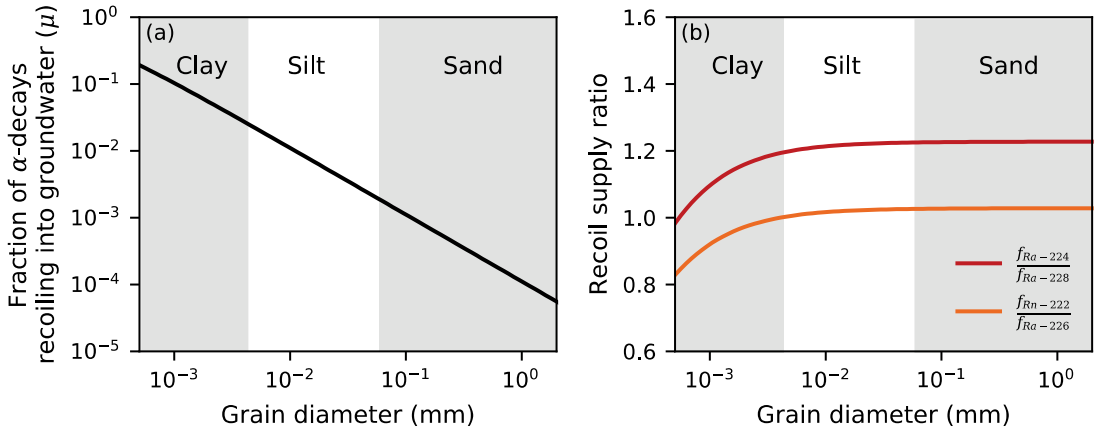


Figure 5.3. The fraction of $\boldsymbol{\alpha}$-decays recoiling into groundwater based on Porcelli (2008) (a) and recoil supply ratios for $^{224}Ra$-$^{228}Ra$ (red) and $^{222}Rn$-$^{226}Ra$ (orange) against the grain diameter.

### *5.3.2.2. The bulk radioactive equilibrium of $^{224}Ra/^{228}Ra$ and $^{222}Rn/^{226}Ra$ activity ratios*

The bulk radioactive equilibrium is a particular situation in which the activity of a radionuclide does not change with groundwater transit time ($R_i\,\partial a_i/\partial\tau = \partial b_i/\partial\tau = 0$) since its production rate, both from exchangeable and $\alpha$-recoil sources equals its decay rate. The radioactive equilibrium of dissolved ARs of $^{224}Ra/^{228}Ra$ and $^{222}Rn/^{226}Ra$ including the supply by $\alpha$-recoil can be derived from Equation 5.11 ($\partial a/\partial\tau = 0$), taking into consideration that the exchangeable activities of $^{228}Th$ are in equilibrium with its parent ($b_{Th\text{-}228} = b_{Ra\text{-}228}$; see Figure **5.1**):

$$\frac{a_{Ra-224}}{a_{Ra-228}} = 1 + \frac{f_{Ra-224}}{b_{Th-232}+f_{Ra-228}}, \qquad \text{Equation 5.15}$$

$$\frac{a_{Rn-222}}{a_{Ra-226}} = R_{Ra}\left(1 + \frac{f_{Rn-222}}{b_{Th-230}+f_{Ra-226}}\right). \qquad \text{Equation 5.16}$$

These equilibriums depend on (1) the exchangeable activity of the parent radionuclide ($b_{Th-232}$ for $^{224}$Ra/$^{228}$Ra and $b_{Th-230}$ for $^{222}$Rn/$^{226}$Ra), (2) the retardation factor of Ra, in the case of the $^{222}$Rn/$^{226}$Ra AR, and (3) the successive $\alpha$-recoil inputs (Equations 5.1 - 5.3). The $\alpha$-recoil supply strongly influences the bulk radioactive equilibrium of the ARs. The equilibrium of the dissolved ARs of $^{224}$Ra/$^{228}$Ra and $^{222}$Rn/$^{226}$Ra derived from Equation 5.15 and 5.16 range from 1.0 and $R_{Ra}$ when $\alpha$-recoil is negligible ($b >> f$) to 2.2 and $2 \cdot R_{Ra}$ when $\alpha$-recoil is the dominant source term ($f >> b$), respectively. Notice that the maximum equilibrium for dissolved ARs is obtained when using the maximum recoil supply ratios of ~1.2 and ~1.0 for $^{224}$Ra-$^{228}$Ra and $^{222}$Rn-$^{226}$Ra pairs, respectively. The estimated ranges of ARs are similar to those already suggested by Porcelli (2008). Therefore, groundwaters presenting ARs outside of these ranges are indicative of transit times shorter than those needed to achieve the bulk radioactive equilibrium (hereinafter, characteristic equilibrium transit times).

#### *5.3.2.3. Alpha recoil vs exchangeable activity of the parent radionuclide*

The relative importance of the exchangeable activities of the parent radionuclide ($b$) and $\alpha$-recoil ($f$) sources, not only influences the equilibrium ARs (when $\partial a/\partial \tau = 0$), but also their concentration in groundwater. It should be noted however, that this relative importance ($b/f$) has no influence on the characteristic equilibrium transit times. The advective transport model is used in this section to evaluate the dissolved ARs of $^{224}$Ra/$^{228}$Ra and $^{222}$Rn/$^{226}$Ra, depending on groundwater transit times for different ratios between exchangeable activity and $\alpha$-recoil (see Table **5.1**). The results displayed in Figure **5.4** show that higher $\alpha$-recoil supply values, in comparison to the exchangeable source ($b/f < 10^2$), produce ARs above the equilibrium ARs (Equation 5.15 and 5.16) for transit times lower than the characteristic equilibrium transit time. These ARs decrease towards the equilibrium values as groundwater transit time increases (Figure **5.4**). Maximum ARs are indeed observed when the exchangeable activities are negligible ($b = 0$) and transit times are short. As already noticed by Krishnaswami et al. (1982), these maximum values equal the ratio between the decay constants of the daughter and parent radionuclide for each AR ($\lambda_{Ra-224}/\lambda_{Ra-228} \sim 580$ for $^{224}$Ra/$^{228}$Ra and $\lambda_{Rn-222}/\lambda_{Ra-226} \sim 1.5 \cdot 10^5$ for $^{222}$Rn/$^{226}$Ra). These high ARs result from the faster regeneration of the short-lived relative to long-lived radionuclides (Gleeson et al., 2013; Rodellas et al., 2017; Tamborski et al., 2018) and are in

agreement with the high ARs found in areas exposed to short-scale processes such as porewater exchange or beach-face recirculation (Charette et al., 2003; Moore et al., 2011). Conversely, the ARs fall below the equilibrium values when the exchangeable activity of the parent radionuclide is considerably higher than the $\alpha$-recoil ($b/f > 10^3$), as already noticed in the previous section (i.e., neglecting the role of the $\alpha$-recoil supply; Figure **5.3**). It is also worth noting that the relevance of the exchangeable activities of the parent radionuclide relative to $\alpha$-recoil ($b/f$) may be lower for $^{224}$Ra/$^{228}$Ra than for $^{222}$Rn/$^{226}$Ra. This is because $^{232}$Th is the first radionuclide of the decay chain and thus its mobilization from mineral lattice to exchangeable fraction (adsorbed and dissolved) is not affected by $\alpha$-recoil, and may only depend on weathering processes (e.g., dissolution, breakdown of rocks or minerals; Porcelli, 2008). Conversely, $^{230}$Th is the fifth radionuclide of the $^{238}$U decay chain and its exchangeable activities are derived from the exchangeable content of its parent radionuclide ($^{234}$U) plus an additional recoil source ($f_{U-234}$).

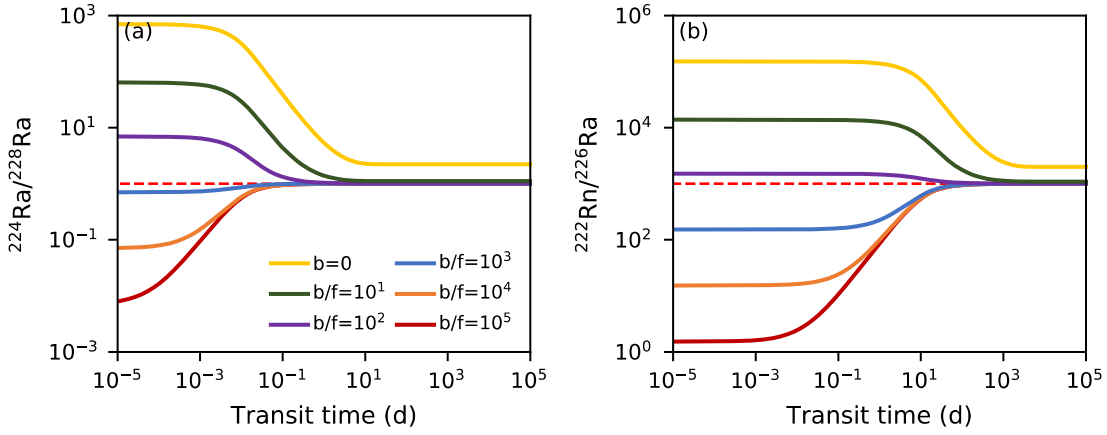


Figure 5.4. Activity ratios of $^{224}$Ra/$^{228}$Ra (a) and $^{222}$Rn/$^{226}$Ra (b) against groundwater transit times for different ratios of exchangeable activity and $\boldsymbol{\alpha}$-recoil sources ($\boldsymbol{b/f}$) represented by solid color lines. Red dash-lines in (a) and (b) represent AR $^{224}$Ra/$^{228}$Ra = 1 and AR $^{222}$Rn/$^{226}$Ra = $\boldsymbol{R_{Ra}}$, respectively.

### 5.3.3. The effect of Ra retardation factor on $^{224}$Ra/$^{228}$Ra and $^{222}$Rn/$^{226}$Ra activity ratios

The distribution of radionuclides in groundwater is strongly affected by their retardation factors (McKinley and Russell Alexander, 1993). To model the distribution of a certain radionuclide by using the advective transport model proposed in this study (Appendix B), the retardation factors from the target and parent radionuclides should be known ($R_U$, $R_{Th}$, $R_{Ra}$, and $R_{Rn}$). Evaluating AR distribution is simpler since only the retardation factors of the involved

radionuclides are required. In the case of the $^{222}$Rn/$^{226}$Ra AR, as Rn is the direct daughter of $^{226}$Ra and is a noble gas ($R_{Rn} = 1$), only the retardation factor of Ra is needed. For the AR of $^{224}$Ra/$^{228}$Ra, the retardation factors of Th and Ra are required, because $^{224}$Ra is produced from $^{228}$Th. Nevertheless, since the retardation factor of Th is commonly of orders of magnitude higher than that of Ra ($10^8$ to $10^{10}$ for Th and 10 to $10^6$ for Ra; Kumar et al., 2019; Thibault et al., 1990) it has a negligible effect on the AR of $^{224}$Ra/$^{228}$Ra. A fixed $R_{Th}$ of $10^{10}$ is used in this study, but identical results would have been obtained using a $R_{Th}$ of $10^8$. In this section, the ARs of $^{224}$Ra/$^{228}$Ra and $^{222}$Rn/$^{226}$Ra are evaluated against transit times for different Ra retardation factors (Figure **5.5**a and Figure **5.5**b). To do so, an arbitrary ratio between exchangeable activity and $\alpha$-recoil sources ($b/f$) of 10 is set and we consider ionic exchange as the principal mechanism of exchangeable-dissolved transfer of radionuclides (Table **5.1**).

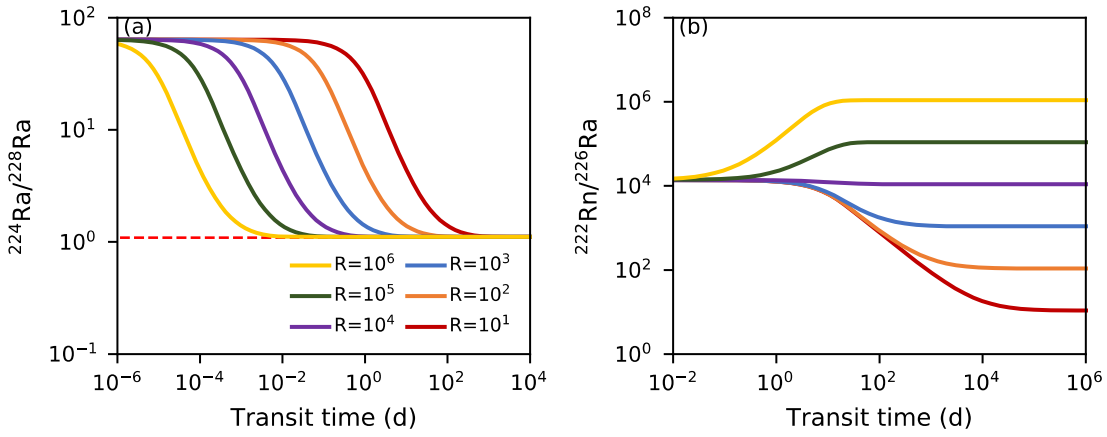


Figure 5.5. Activity ratios of $^{224}$Ra/$^{228}$Ra (a) and $^{222}$Rn/$^{226}$Ra (b) against transit times for different retardation factors represented by solid color lines. The red dashed line in (a) represents the equilibrium AR of $^{224}$Ra/$^{228}$Ra. The ratio between exchangeable activity and $\boldsymbol{\alpha}$-recoil sources ($\boldsymbol{b/f}$) is set to 10.

As already shown in previous sections, both ARs achieve bulk radioactive equilibrium (Equation 5.15 and 5.16) after a characteristic transit time. This characteristic transit time for reaching equilibrium strongly depends on the retardation factor of Ra and on the decay constants of each pair of radionuclides ($\lambda_{Ra-224}$ and $\lambda_{Ra-228}$ for $^{224}$Ra/$^{228}$Ra and $\lambda_{Rn-222}$ and $\lambda_{Ra-226}$ for $^{222}$Rn/$^{226}$Ra). The characteristic transit time decreases as the retardation factor increases. In other words, the Ra losses due to advective transport (i.e., $da/d\tau = \boldsymbol{v} \cdot \nabla a$; Equation 5.7) are higher when Ra is predominantly desorbed (i.e., low retardation factors; ~100) than when Ra is mostly

associated with solid surfaces (i.e., high retardation factors; ~$10^6$). However, it should be noted that while the Ra retardation factor does not influence the equilibrium of the $^{224}Ra/^{228}Ra$ AR (Equation 5.15), it does strongly influence the $^{222}Rn/^{226}Ra$ AR in equilibrium (Equation 5.16) as shown in Figure **5**.**5**a and Figure **5**.**5**b.

### 5.3.4. Characteristic equilibrium groundwater transit time

The characteristic equilibrium transit time for the $^{224}Ra/^{228}Ra$ and $^{222}Rn/^{226}Ra$ ARs to reach bulk radioactive equilibrium provides key information on the determination of groundwater transit times. As shown in previous sections, characteristic equilibrium transit times are highly dependent on the retardation factor of Ra ($R_{Ra}$), but they are independent of the relative importance of the exchangeable activities of the parent radionuclide and $\alpha$-recoil sources ($b/f$). Here the characteristic equilibrium transit times for the ARs of both $^{224}Ra/^{228}Ra$ and $^{222}Rn/^{226}Ra$ as a function of the Ra retardation factor are estimated (Figure **5**.**6**). Higher retardation factors, characteristic of freshwater environments ($10^6$), result in shorter times for equilibrium (~0.1 days for $^{224}Ra/^{228}Ra$ and 100 days for $^{222}Rn/^{226}Ra$) due to the minor effect of advection losses. Conversely, lower retardation factors, characteristic of saline environments, require longer equilibrium transit times (~3 years and 3,000 years for $^{224}Ra/^{228}Ra$ and $^{222}Ra/^{226}Ra$, respectively). Notice that the equilibrium transit times are approximately 3 orders of magnitude higher for $^{222}Rn/^{226}Ra$ than for $^{224}Ra/^{228}Ra$, mainly because of the different decay constants of $^{226}Ra$ and $^{228}Ra$ ($\lambda_{Ra-228} >> \lambda_{Ra-226}$, see Table **5**.**1**). Thus, from Figure **5**.**6**, three main areas can be identified depending on whether the ARs of $^{224}Ra/^{228}Ra$ and $^{222}Ra/^{226}Ra$ are in equilibrium or not. A first evaluation of groundwater transit times can thus be easily obtained from this simple analysis, when the ARs are measured in groundwater samples and the retardation factor of Ra is constrained.

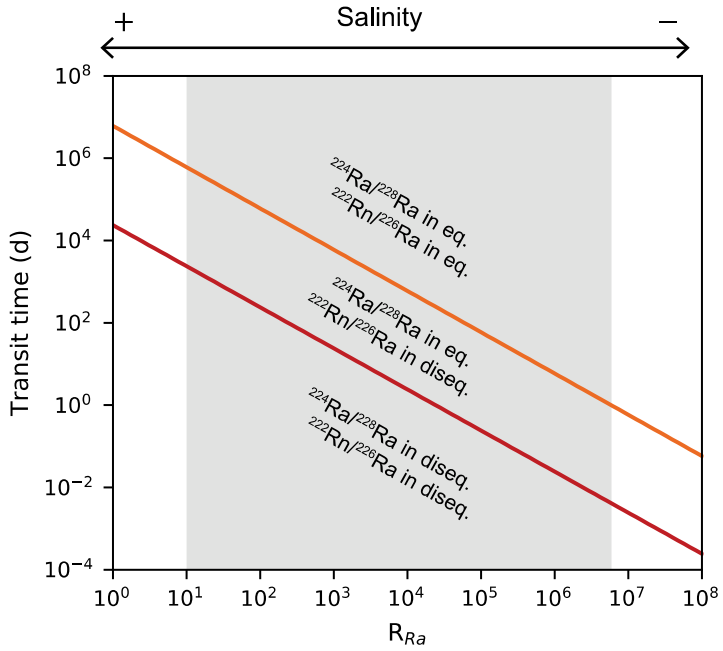


Figure 5.6. Characteristic groundwater transit time for the AR $^{224}Ra/^{228}Ra$ (red line) and $^{222}Rn/^{226}Ra$ (orange line) to achieve their equilibrium value (Equation 5.15 and 5.16, respectively), as a function of the retardation factor of Ra. The grey band indicates the common retardation factors of Ra based on Kumar et al. (2019).

### 5.3.5. Applications of $^{224}Ra/^{228}Ra$ and $^{222}Rn/^{226}Ra$ activity ratios

#### *5.3.5.1. Groundwater transit times determination*

In this section, the potential applications of the $^{224}Ra/^{228}Ra$ and $^{222}Rn/^{226}Ra$ ARs for determining transit times of groundwater flowing through an aquifer are tested. The advective transport model presented in this study (Appendix B) can be used to determine groundwater transit times in different hydrological environments, including inland and coastal aquifers, and for different groundwater compositions (fresh, brackish, and saline groundwater). Notice that the application of these ARs for determining groundwater transit times in freshwater systems is more complex, since the solubility of Ra isotopes in pristine groundwater is usually low. However, in recent years there have been many advances in the quantification of low concentrations of Ra isotopes (Molina-Porras et al., 2017a), as well as in their application to freshwater environments (Molina-Porras et al., 2020, 2017b). The two main applications of the model are (1) the determination of groundwater transit times between two sampling points located in the same flow path, where the groundwater Ra and Rn activities of each sample are used to set the initial

inflow ($a_0$), and the final outflow ($a$) boundary activities of Ra isotopes and Rn; and (2) the estimation of transit times from a recharge point (i.e., infiltration of water through the aquifer or seawater intrusion) to a sampling point (also known as groundwater age), where the activities of the inflowing water are used to set the initial inflow activities ($a_0$) and the sampling point is used to set the outflow boundary activities ($a$). Moreover, groundwater velocities can be derived from transit times if the flow path length from recharge, or between the two sampling points, is known (Equation 5.7).

The implementation of this method requires not only the quantification of $^{224}Ra/^{228}Ra$ and $^{222}Ra/^{226}Ra$ ARs, but also requires constraining the retardation factor of Ra ($R_{Ra}$) and the relation between production rates derived from the exchangeable activities of the parent radionuclide and $\alpha$-recoil ($b/f$) (see Section 5.3.2 and 5.3.3). The methods for determining production rates and retardation factor are summarized in Chapter 1.1.4.1) and a compilation of distribution coefficients of Ra is presented in appendix A.

Once these parameters ($^{224}Ra/^{228}Ra$ and $^{222}Ra/^{226}Ra$ ARs, $R_{Ra}$, and $b/f$ ratio) are constrained, groundwater transit times can be determined using two different approaches. The first approach consists of comparing the measured ARs with the bulk radioactive equilibrium ARs (Equation 5.15 and 5.16) to determine the ranges of groundwater transit times. Whilst this approach only enables the estimation of wide ranges of groundwater transit times, it can be applied without characterizing the ratio $b/f$ , which is often the most challenging parameter to determine. Given a specific Ra retardation factor, the characteristic equilibrium groundwater transit times for both ARs (the transit time required for the ARs to achieve the bulk radioactive equilibrium) can be derived directly from Figure **5.6**. If the measured groundwater samples present ARs out of equilibrium ranges (from 1.0 to 2.2 and $R_{Ra}$ to $2{\cdot}R_{Ra}$ for $^{224}Ra/^{228}Ra$ and $^{222}Rn/^{226}Ra$, respectively), they are indicative of groundwater transit times shorter than the characteristic equilibrium groundwater transit times. Conversely, ARs within the characteristic bulk radioactive equilibrium ranges may be indicative of longer groundwater transit times relative to the characteristic equilibrium transit times (Figure **5.6**). However, notice that ARs within these ranges may not have reached equilibrium under some ratios for exchangeable and $\alpha$-recoil sources (e.g., $b/f$ ranging from $10^2$ to $10^3$, see Figure **5.4**). To ensure that the ARs have reached equilibrium,

evaluating the variation of the ARs on different sampling points along the studied flow path is recommended. Moreover, this approach can only be used for determining groundwater ages, since the analysis performed to derive Figure **5.6** considers that the inflowing water has negligible initial activities of Rn and Ra ($a_0 = 0$).

The second approach is based on adjusting numerically the model presented in the appendix (Appendix B) to the measured ARs. Based on the input parameters of the model which comprise the retardation factor of Ra, the activities of the target radionuclides at the inflow boundary ($a_0$), and the relation between the production rate derived from the exchangeable activity of the parent radionuclide and the production from $\alpha$-recoil ($b/f$), the model can be used to determine the modeled ARs of $^{224}Ra/^{228}Ra$ and $^{222}Rn/^{226}Ra$ for a set of groundwater transit times (e.g., $10^{-5}$ to $10^{5}$ days as shown in Figure **5.5**). Subsequently, the results of the modeled ARs are compared with the measured ARs at the outflow boundary to evaluate a specific groundwater transit time. The uncertainties associated with the transit time determination can be assessed through a Monte Carlo analysis where the errors associated with each of the model's variables are considered. Within the Monte Carlo analysis (1) model variables (e.g., $R_{Ra}$ and $b/f$) are generated via normally distributed random values based on the mean and standard deviation of each parameter and (2) a set of stochastic simulations are performed to determine the groundwater transit time resulting from the combination of all input parameters. The distribution of groundwater transit times obtained from the Monte Carlo analysis can be adjusted (e.g., least-square fitting) to a probability density function (e.g., Normal, Poisson, Binomial, Beta) to obtain the statistics for empirical distribution (e.g., mean, median, standard deviation). In the following section (Section 5.3.6), the advective transport model is used to evaluate groundwater transit times for fresh groundwater from recharge and recirculated seawater in a coastal Mediterranean aquifer.

#### *5.3.5.2. Constraining pathways and end-members of SGD*

The advective transport model presented in this study can be applied in SGD studies to evaluate both the predominant pathways of groundwater discharge (e.g., porewater exchange, intertidal seawater recirculation, terrestrial groundwater discharge) (Michael et al., 2011; Taniguchi et al., 2019) and the SGD end-member.

**a) Evaluation of predominant SGD pathways:** SGD can be separated into 5 main pathways according to the groundwater origin, the physical forces driving the fluxes, and the spatiotemporal scale of each process: terrestrial groundwater discharge; density-driven seawater circulation; seasonal exchange of seawater; intertidal circulation of seawater; and porewater exchange (Michael et al., 2011; Robinson et al., 2018; Taniguchi et al., 2019). Considering the different spatiotemporal scales of each SGD pathway and their characteristic salinities (and therefore their characteristic Ra retardation factor), different SGD pathways are likely to present characteristic ARs (Figure **5.7**). As shown in Figure **5.7**, whereas short-scale processes characteristics of saline environments (low retardation factors) such as porewater exchange or intertidal seawater recirculation will likely present ARs in disequilibrium (Equation 5.15 and 5.16), long-scale processes involving freshwater (high retardation factors) such as terrestrial groundwater discharge are expected to present ARs close to the bulk radioactive equilibrium (Equation 5.15 and 5.16).

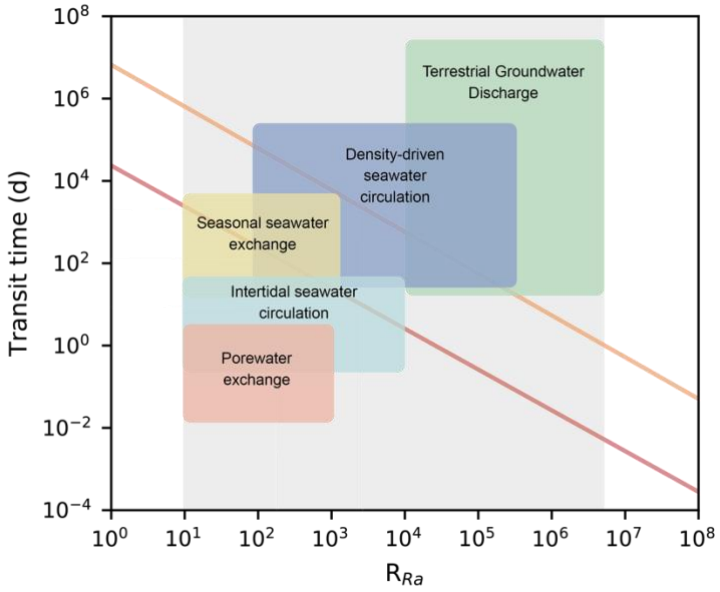


Figure 5.7. Characteristic groundwater transit time for the AR of $^{224}Ra/^{228}Ra$ (red line) and $^{222}Rn/^{226}Ra$ (orange line) to achieve their equilibrium value (Equation 5.15 and 5.16, respectively), as a function of the retardation factor of Ra and the temporal scales of different SGD pathways. The grey band indicates the common retardation factors of Ra based on Kumar et al. (2019).

**b) Selection of the SGD end-member:** Once released into coastal water by SGD, the activities of the short-lived isotopes ($^{224}$Ra and $^{222}$Rn) are expected to decrease at a faster rate than their parent isotopes ($^{228}$Ra and $^{226}$Ra, respectively) because: (1) the decay rates of $^{224}$Ra and $^{222}$Rn are higher relative to their parents ($^{228}$Ra and $^{226}$Ra, respectively); (2) $^{222}$Rn exhales to the atmosphere, and; (3) coastal waters are mixed with offshore waters, which are commonly depleted in short-lived ($^{224}$Ra and $^{222}$Rn) relative to long-lived ($^{228}$Ra and $^{226}$Ra) isotopes. Thus, one possible method to evaluate the SGD end-member consists of comparing the measured ARs of $^{224}$Ra/$^{228}$Ra and $^{222}$Rn/$^{226}$Ra in the coastal ocean ($AR_{SW}$) with those of groundwater samples ($AR_{GW}$) (Boehm et al., 2006; Moore et al., 2006; Rodellas et al., 2014) at a specific site. When SGD is the predominant source of Ra isotopes and Rn to the coastal ocean (i.e., absence of any significant source such as diffusion from sediments or rivers), the ARs in the coastal ocean are expected to be comparable or lower relative to those of the discharging groundwater ($AR_{SW} \leq AR_{GW}$). Any groundwater sample exhibiting lower ARs than those measured in the coastal waters may not be representative of the dominant SGD inflowing to the study site, and thus can be discarded as a relevant SGD end-member.

### 5.3.6. Applications of $^{224}$Ra/$^{228}$Ra and $^{222}$Rn/$^{226}$Ra activity ratios at the Argentona experimental site (western Mediterranean Sea)

The applications of the $^{224}$Ra/$^{228}$Ra and $^{222}$Rn/$^{226}$Ra ARs for determining groundwater transit times and evaluating the end-member and pathways of SGD, were tested at an experimental site located in the coastal alluvial aquifer of the Argentona ephemeral stream (40 km NE of the city of Barcelona, western Mediterranean Sea). The Argentona experimental site is described in detail in appendices (Appendix C). The physicochemical parameters and the Ra isotopes activities ($^{224}$Ra, $^{228}$Ra, and $^{226}$Ra), together with $^{222}$Rn, were monitored over two years (2015 and 2016) at the experimental site. Additionally, the retardation factor of Ra was determined via adsorption-desorption experiments (Table C.1) on sediment samples collected from two selected piezometers (N1-20 and N2-15). Detailed information on the sampling, analytical techniques, and the monitoring of Ra isotopes and Rn in the Argentona experimental site, are provided in Chapter 2 and appendix C.

#### *5.3.6.1. Groundwater transit times*

The hydrogeological patterns in the Argentona experimental site provide a good opportunity to use the ARs of $^{224}Ra/^{228}Ra$ and $^{222}Rn/^{226}Ra$ for the evaluation of two different processes. While in the shallower part of the aquifer the proposed method is tested to estimate the groundwater transit times of fresh groundwater from recharge, in the deeper part the groundwater transit times of recirculated seawater are estimated. The groundwater samples collected from the piezometer at 15 m depth in nest N2, were chosen as the referential samples to evaluate transit times from upstream recharge (hereinafter fresh-outflow), because it is the farthest piezometer from the sea (~100 m) and presented the lowest average salinity (0.5), indicating a negligible mixing with intruded seawater. Conversely, groundwater samples from nest N1 at depth 20 m that exhibiting the highest average salinity (32.4) were chosen to evaluate transit times for seawater recirculation (saline-outflow). In both cases, the groundwater transit time is determined from a recharge point to an outflow boundary, taking into consideration that the initial activities of Ra isotopes and Rn in the inflowing water are negligible ($a_0 = 0$) (i.e., the determined groundwater transit time corresponds to the groundwater age). This assumption is supported in this case because the activities of $^{224}Ra$, $^{226}Ra$, $^{228}Ra$ and $^{222}Rn$ in coastal waters are significantly lower (> 2-3 orders of magnitude) than those in groundwater (Figure C.2).

Indicative ranges of groundwater transit times can easily be estimated solely from the measured ARs and the retardation factor of Ra, without any extra analysis (Figure **5.8**). Since both the $^{224}Ra/^{228}Ra$ and $^{222}Rn/^{226}Ra$ ARs from the saline-outflow are in disequilibrium ($5 > 2.2$ and $4{,}500 > 2R_{Ra}$, respectively), and the experimentally determined $R_{Ra}$ is 170 (Table C.1), the derived groundwater transit times should be shorter than the characteristic equilibrium transit time for the ratio $^{224}Ra/^{228}Ra$ (~110 days; Figure **5.8**). In the case of the fresh-outflow, the $^{224}Ra/^{228}Ra$ AR is in equilibrium ($1.1$) but the AR of $^{222}Rn/^{226}Ra$ is in disequilibrium (5,900) and the retardation factor of Ra is 2,500 (Table C.1). Thus, groundwater transit times should range from the characteristic equilibrium transit time for $^{224}Ra/^{228}Ra$ and that for $^{222}Rn/^{226}Ra$ (from ~10 days to 5.5 years; Figure **5.8**). To constrain these ranges, the transit times can be more accurately determined by numerical adjustment to the model presented in the appendix (Appendix B), which can be coupled to a Monte Carlo analysis using 50,000 stochastic simulations to account

for the uncertainties associated with this approach. The mean and the standard deviation of each model input (i.e., $^{224}Ra/^{228}Ra$, $^{222}Rn/^{226}Ra$, and $R_{Ra}$) was used to generate normally distributed random values. In the case of the retardation factor of Ra, rather than using the analytical relative uncertainty (~10%), a higher error (25%) was assumed to account for the potential variability of this parameter due to heterogeneities of the geological matrix and the composition of groundwater as well as its dependency on other processes such as dissolution and precipitation. Since the ratio between exchangeable and $\alpha$-recoil sources ($b/f$) is unknown in the Argentona experimental site, the Monte Carlo simulations were performed for different $b/f$ ratios ranging from 0 to 50. The resulting distributions of groundwater transit times for upstream recharge and seawater recirculation were adjusted to different probability density functions (PDF) by using least-squares fitting (SciPy library for the Python programming language). The tested PDFs included Beta, Binomial, $\chi^2$, Noncentral $\chi^2$, *F*, Noncentral *F*, Gamma, Negative Binomial, Normal, Poisson, Student's *t* and Noncentral *t*. The PDFs which best fitted the Monte Carlo results were Noncentral *t and F* for the $^{224}Ra/^{228}Ra$ and $^{222}Rn/^{226}Ra$ AR-derived estimates, respectively. The PDF-statistics derived from the best fit to the data were used to derive the expected (mean, standard deviation, median, and 1$^{st}$ and 3$^{rd}$ quartile) groundwater transit times. The mean and standard deviation groundwater transit times for seawater recirculation were 7 ± 3 to 54 ± 19 days (by using $^{224}Ra/^{228}Ra$ and $^{222}Rn/^{226}Ra$, respectively) and 330 ± 300 days for the upstream recharge (only the AR $^{222}Rn/^{226}Ra$ can be used since $^{224}Ra/^{228}Ra$ is in equilibrium). Notice that the relative standard deviation of the upstream recharge estimate (~100%) may result from (1) the high relative standard deviation of $^{222}Rn/^{226}Ra$ in the fresh-outflow (40%), and (2) the closeness of the $^{222}Rn/^{226}Ra$ AR to the retardation factor of Ra (5,900 ± 2300 and 2,500 ± 200, respectively). However, 50% of the generated data via Monte Carlo simulations for upstream recharge fluctuate from 180 to 390 days (1$^{st}$ and 3$^{rd}$ quartile, respectively).

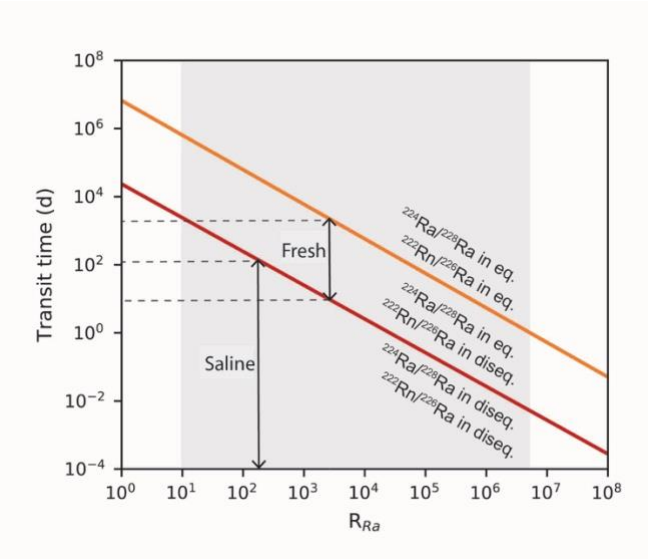


Figure 5.8. Determination of groundwater transit times for the fresh- and saline-outflow at the Argentona experimental site based on the equilibrium or disequilibrium of the $^{224}Ra/^{228}Ra$ and $^{222}Rn/^{226}Ra$ ARs

The discrepancy between the groundwater transit times derived from the $^{224}Ra/^{228}Ra$ (7 days) and $^{222}Rn/^{226}Ra$ (54 days) ARs in the saline-outflow can be induced by many factors. First, the experimental retardation factor of Ra used for the calculations was derived from adsorption-desorption experiments, which only consider ionic exchange. Thus, this approach neglects the role of other processes involved in the solid-solution distribution of Ra isotopes such as dissolution or precipitation. Secondly, whilst the assumption of steady-state ($\partial a/\partial t = 0$) may be a good approximation for shorter-lived Ra isotopes ($^{224}Ra$ and $^{228}Ra$), the activities of $^{226}Ra$ may be more influenced by non-periodical forcing such as waves, strong precipitation events, and sea-level variability, due to its longer half-life, (Robinson et al., 2018). Thirdly, the saline-outflow contains ~15% of meteoric groundwater (salinity of 32.4) with a different signal of radionuclides that can interfere with final estimates. Despite the above-mentioned assumptions, this assessment enables easy constraint of the temporal scales of fresh groundwater advection and seawater intrusion, thereby providing thus key information for understanding the hydrological functioning of the coastal aquifer.

In addition to transit times, in the Argentona experimental site, conservative groundwater velocities for the groundwater recharge and seawater recirculation, can be calculated by considering that the recharge point of the ephemeral stream occurs at the midpoint between its

source and the sampling piezometer (N2-15) (~3 km inland), and that the recirculation of seawater occurs at the shoreline (60 m). The linear velocities estimated for the shallow fresh groundwater part (~9 m $d^{-1}$), are one order of magnitude higher than the ones derived from a numerical model implemented at the alluvial aquifer of the Argentona ephemeral stream in 2009 (0.24 m $d^{-1}$; Catalan Water Agency, 2010). This discrepancy could be attributed to the assumption that the recharge point occurs at the midpoint of the aquifer since recharge in ephemeral streams commonly occurs after flood events that are more intense in the lower part of the aquifer. The groundwater velocities of the intruded seawater (~1 to 8 m $d^{-1}$) derived from the ARs agree with those determined by the tidal response method at the experimental site (from $10^{-2}$ to $10^{1}$ m $d^{-1}$; T. Goyetche, personal communication), reinforcing the validity of the developed approach.

#### *5.3.6.2. Pathways and endmembers of SGD*

In the Argentona experimental site, the 12 sampling locations across the perpendicular transect to the coastline provide an appropriate framework to investigate the pathways of SGD occurring at the site. Following the classification based on the temporal scale and the characteristic retardation factor of Ra for each pathway (Figure **5.7**), three main SGD pathways can be identified by using the distribution of salinity and ARs: (1) terrestrial groundwater discharge, derived from the lower salinities (0.5 - 1.7) and $^{224}Ra/^{228}Ra$ ARs close to the equilibrium in the upper part of the aquifer (N1-15, N2-15, and N3-15); (2) density-driven seawater circulation, occurring at the deeper part of the aquifer inferred by higher salinities (28.0 - 32.4) and $^{224}Ra/^{228}Ra$ and $^{222}Rn/^{226}Ra$ ARs in disequilibrium (N1-20, N2-25, and N3-25); and (3) intertidal seawater circulation, occurring at the nearshore piezometers (PP-20T and PP-15), which present intermediate salinities (1.6 - 9.1) and ARs (see Table C.1). The coastal seawater collected in front of the Argentona experimental site presented a $^{224}Ra/^{228}Ra$ AR value of 3.0 (Table C.1), which is above the bulk radioactive equilibrium of the $^{224}Ra/^{228}Ra$ AR (1.0 - 2.2; Equation 5.15 and 5.16). This indicates that the predominant SGD pathways may be density-driven seawater circulation and/or intertidal seawater circulation with a minor contribution from terrestrial groundwater discharge. These results are in agreement with those obtained through the application of cross-hole electrical resistivity tomography, which enabled the identification of two different mixing zones near the piezometer PP-20, that may be indicative of shallower

(wave/storm-induced) and deeper groundwater discharge areas (Palacios et al., 2019). The AR of $^{222}Rn/^{226}Ra$ is not used in this case due to the low activities of $^{226}Ra$ in the coastal waters (~12 ± 1 dpm·100L$^{-1}$) that indicate a lack of relevant SGD-driven $^{226}Ra$ inputs.

In order to evaluate the appropriate SGD endmember in the Argentona experimental site, the measured ARs of $^{224}Ra/^{228}Ra$ and $^{222}Rn/^{226}Ra$ in the coastal ocean ($AR_{SW}$) are compared with those from groundwater samples ($AR_{GW}$) (Figure **5.9**). The samples that were taken at the upper part of the aquifer presented lower $^{224}Ra/^{228}Ra$ ARs (1.1 - 2.5) relative to the coastal seawater sample ($AR_{SW} = 3.0$), indicating that they may not be representative endmembers of the dominant SGD inflowing to the study site. In contrast, the $^{224}Ra/^{228}Ra$ ARs of samples from the deeper part of the aquifer (> 15 m) were higher relative to the $AR_{SW}$ (Table C.1) and thus they could be representative samples for the SGD endmember. A common method of estimating the SGD end-member consists in averaging the tracer concentration from several groundwater samples collected at different locations (e.g., Beck et al., 2007; Rapaglia et al., 2010). Without any ancillary information, all the collected groundwater samples are usually incorporated into the average to determine the Ra or Rn activities of the SGD endmember. However, this averaged activity is usually skewed by the number of groundwater samples that are not representative of the dominant discharge process. Using only those groundwater samples presenting comparable or higher ARs relative to the coastal ocean sample ($AR_{SW} \leq AR_{GW}$), enables discarding the non-representative samples, and thus better constrain the SGD endmember. In the case of the Argentona experimental site, for instance, the average $^{224}Ra$ activity, considering all the samples collected is 210 Bq m$^{-3}$, whereas this average is 320 Bq m$^{-3}$ if only the representative groundwater samples are included in the average. This example illustrates that $^{224}Ra$-based SGD estimates may vary by a factor of 1.5 when the SGD endmember is not appropriately constrained. Using these ARs to better select the SGD endmember might thus decisively contribute to producing more accurate SGD estimates.

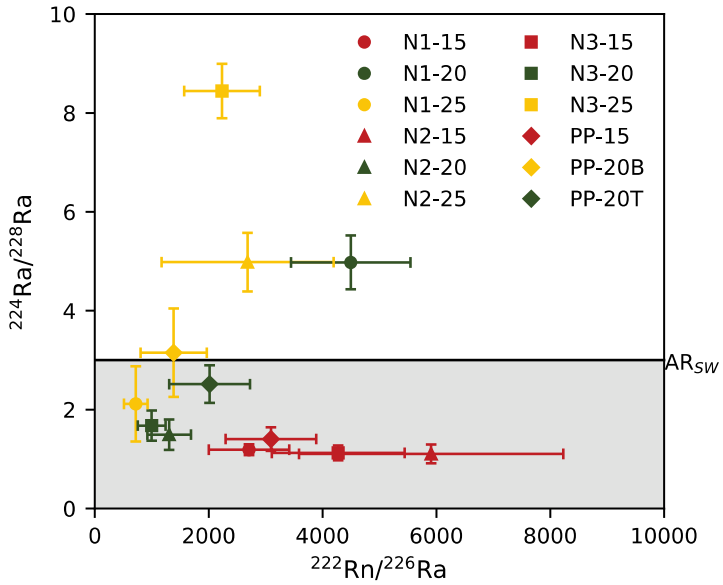


Figure 5.9. Average activity ratios of $^{224}$Ra/$^{228}$Ra and $^{222}$Rn/$^{226}$Ra and standard deviation (error bars) of the different campaigns for each piezometer. The gray band indicates the piezometers that exhibited lower $^{224}$Ra/$^{228}$Ra AR than that of seawater (black line).

# Chapter 6: Extreme precipitation events induce high fluxes of groundwater and associated nutrients to coastal ocean

## 6.1. Introduction

Fluxes of water and solutes supplied by SGD have been quantified at a variety of settings worldwide. However, most of the SGD investigations are conducted under baseflow conditions, that is, in the absence of any meteorological, hydrological, or oceanographical event (e.g., storms, monsoons, sea-level anomalies) which might significantly impact the magnitude of SGD. Only a few articles have focused on the evaluation of the temporal variations in SGD induced by episodic events (Adyasari et al., 2021; Gonneea et al., 2013b; Hu et al., 2006; Rodellas et al., 2020; Sugimoto et al., 2016). Extrapolating from SGD estimates derived under baseflow conditions to obtain annual fluxes neglects the role of such events, which may represent an important contributor to overall SGD fluxes.

Extreme precipitation events (EPE) represent one of the main natural hazards producing severe societal and economic costs in urban, agricultural, and mountainous areas (Booij, 2002; Camarasa-Belmonte and Soriano-García, 2012; Schumacher, 2017). The meteorological causes of these events include the formation of cyclones, fronts, monsoons, isolated thunderstorms, upslope flow precipitation, and others, and vary from region to region (Kunkel et al., 2012). The social and environmental consequences also vary geographically and depend on diverse aspects such as topography, soil characteristics, geological setting, land surface use and characteristics, and human-induced changes to the landscape and coastal areas (Schumacher, 2017). Due to the disparate causes and consequences associated with them, there are different ways for defining an 'extreme' precipitation event: some authors define such events as those exceeding an arbitrary threshold of 24h-accumulated rainfall (e.g., Lionello et al., 2006; Meenu et al., 2020); others use the $90^{th}$, $95^{th}$, or $99^{th}$ all-day or wet-day percentile (Pendergrass and Knutti, 2018). Whilst episodic increases in surface runoff linked to EPE are often well characterized (e.g., Camarasa-Belmonte and Tilford, 2002; Moore, 2007; Rajurkar et al., 2004), little is known about the influence of EPE on SGD-driven water flows and associated solute fluxes to the coastal ocean.

Extreme precipitation events may indeed promote aquifer recharge through the infiltration of rainwater (Ramos et al., 2020; Yu et al., 2017), although its effects on piezometric levels (quantitively and temporally) depend on several factors, such as soil composition, geological characteristics, the hydraulic parameters of the aquifer, and others. Infiltrated water displaces groundwater stored in the aquifer towards the sea, enhancing mixing processes in the coastal aquifer (Anwar et al., 2014; Palacios et al., 2019; Robinson et al., 2018). The significance of EPE on SGD may be exacerbated in areas subject to an arid or semi-arid climate, with scarce and unevenly distributed precipitation, and where extreme events may be the only form of recharge for the aquifer (Taylor et al., 2013). Understanding the role of EPE on SGD-driven water flows and associated solute fluxes is thus fundamental in order to (1) accurately constrain annual fluxes of any dissolved compound transported by SGD, (2) integrate episodic-induced SGD in global estimates, (3) evaluate the environmental impacts of these episodic events on coastal ecosystems and (4) foresee the role of SGD in the future climate change scenario.

This study evaluates the significance of SGD and the associated nutrient fluxes induced by EPE in a Mediterranean coastal zone, the implications of neglecting EPEs on annual estimates, and its importance in the context of climate change. The study was conducted at a typical Mediterranean ephemeral stream-dominated basin. These areas are characterised by rapid response to precipitation due to their geomorphological features (small catchment areas, sharp slopes, coastal alluvial aquifers, and sporadic surficial torrential courses; Camarasa-Belmonte and Segura Beltrán, 2001) and thus represent an ideal setting for gauging the influence of such events.

## 6.2. Field methods

Three samplings were conducted in the southern section of Maresme County during 2019 and 2020 (see Appendix C for details on the study site). The two first samplings (hereinafter P1 and P2, chronologically) were performed shortly after an EPE with an accumulated precipitation rate of ~90 mm in one day. The EPE took place on October 22$^{nd}$ 2019 and P1 and P2 were conducted on October 25$^{th}$ and 29$^{th}$, 2019 (~4 and 8 days after the rainfall event, respectively). The third sampling (named BF, after “baseflow”) was conducted on March 11$^{th}$ 2020, was not

affected by any rainfall event, and was therefore considered to have been conducted under baseflow conditions (accumulated rainfall of 18 mm in the prior 40 days). Seawater samples were collected at different stations from three perpendicular transects to the coastline corresponding to the ephemeral streams of Argentona, Cabrera de Mar, and Vilassar de Mar (Transects T1, T2, and T3, respectively; Figure C.1). Each transect consisted of 7 offshore stations distributed along the first 1000 m. The central transect (T2) had three additional stations at 1500, 2000, and 4000 m from the coastline. Coastal seawaters were collected directly from the shore by filling 25 L water containers. At each station, surface and deep (only selected stations) seawater samples were collected by placing a submersible pump at ~0.5 m depth and ~1 m above the seabed, respectively.

Samples were collected for Ra isotopes ($^{223}$Ra, $^{224}$Ra, $^{226}$Ra, and $^{228}$Ra; 25 – 120 L each sample), which are widely applied tracers of SGD and nutrient analysis. Depth profiles of salinity and temperature were performed at each station by using a YSI 600XL probe. Groundwater samples for Ra isotopes (10 – 25 L) and nutrients were collected periodically from 2015 to 2020 in several piezometers at the experimental site of the Medistraes project, located in the coastal alluvial aquifer of the Argentona ephemeral stream (corresponding to Transect 1). The experimental site consists of 16 piezometers located at 30 to 100 m from the coastline with screened depths of 15 to 25 m, with 2 m screened intervals for each (see Appendix C for more details about the experimental site; Figure C.1). Each piezometer was purged with a submersible pump to remove at least three times the volume of stagnant water before sampling. Continuous in-situ groundwater level, conductivity, and temperature time-series were monitored at a shallow piezometric well (N3-15; 15 m depth, 2 m screened interval, from 11 to 13 m, 80 m from the coastline) using a CTD diver. Salinity and groundwater temperature, as well as seawater samples, were measured in-situ with two handheld probes (HANNA HI98192 and WTW COND 330I). Rainfall data was obtained from a meteorological station from the Meteorological Catalan Service (Servei Meteorològic de Catalunya; SMC) at the municipality of Cabrils (see Figure C.1).

## 6.3. Results

### 6.3.1. Meteorological and hydrological context

The temporal evolution of groundwater level, conductivity, significant wave height, mean sea level (MSL), and accumulated precipitation from October 2019 to April 2020 are shown in Figure **6.1**. Three major precipitation events occurred in October 2019 (~90 mm), December 2019 (~100 mm), and January 2020 (~160 mm), which had a direct impact on groundwater level and conductivity. These events are considered extreme precipitation events following the threshold value derived from the 99$^{th}$ wet-day percentile (~75 mm). After each EPE, the groundwater table from the shallow piezometer (N3-15) rose between 60 and 130 cm, gradually recovering the previous values 7 to 10 days after the event. The magnitude in the increase of the groundwater level (60, 70, and 130 cm, respectively) correlated with the amount of accumulated rainfall corresponding to each EPE. Precipitation events were followed by a drastic reduction of groundwater conductivity at the shallow piezometer, reaching minimum values of ~1 mS cm$^{-1}$, and a subsequent gradual increase before the next precipitation event (Figure **6.1**). As inferred by electric resistivity tomography profiles shown in Palacios et al. (2019), conductivity variations in the piezometric wells of the study site were not derived from dilution with low-conductivity rainwater, but associated with the movement of the mixing zone due to EPE. Significant wave height fluctuations occurred, associated mainly with changes in wind and atmospheric pressure during the EPEs, increasing rapidly from 2 to 5 m above the baseline value of approximately 0.5 m. Similarly, the MSL presented oscillations linked to the EPE, which are usually associated with atmospheric fronts and strong winds, and also to seasonal meteorology, with higher MSL values from October to December than from January to April.

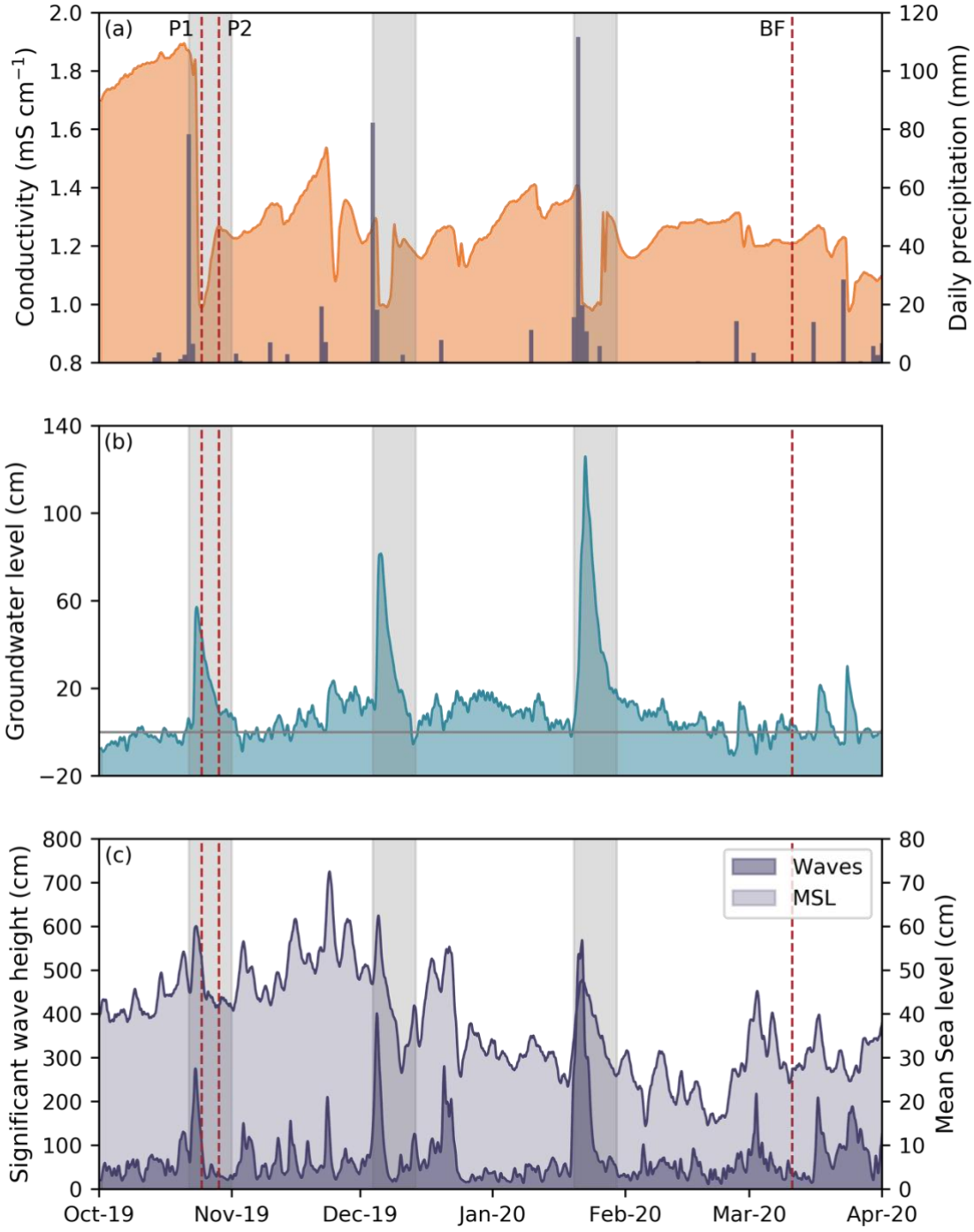


Figure 6.1. Temporal evolution of meteorological, oceanographical and hydrogeological data in Maresme County: (a) specific conductivity measured at the shallow piezometer N3-15 and accumulated precipitation (b) groundwater level, and (c) significant wave height and mean sea level. Groundwater level is displayed as the variation of groundwater level relative to the values of March 2020. The data from the buoy and CTD-diver was smoothed by using a low-pass filter (12 h averaged). Red lines indicate the groundwater and seawater samplings performed at the study site (P1, P2, and BF) and grey bands indicate the EPEs that occurred during the monitoring period (10 days after the event are included in the band).

### 6.3.2. Radium and nutrient concentrations

The activities of Ra isotopes in groundwater samples measured during the 2015-2020 period in the Medistraes site ranged from 10 to 940, 10 to 550, and 1 to 50 Bq $m^{-3}$ for $^{224}Ra$, $^{228}Ra$, and $^{226}Ra$, respectively (see Appendix C; Figure C.2). The activities of Ra increased with groundwater salinity, presenting some variations that are mostly associated with differences in the geological matrix (Beck and Cochran, 2013; Webster et al., 1995). The seawater activities of $^{224}Ra$ and $^{228}Ra$ isotopes generally decreased with increasing distance offshore for all transects and seawater samplings (Figure **6.2**). Maximum activities were found in the first sampling after the rainfall event (P1) for $^{224}Ra$ (median: 14.4 Bq $m^{-3}$, interquartile range (IQR): 11.7 – 19.9 Bq $m^{-3}$) and $^{228}Ra$ (5.8 Bq $m^{-3}$, IQR 4.9 – 7.1 Bq $m^{-3}$). The seawater activities of $^{224}Ra$ and $^{228}Ra$ in subsequent samplings (P2 and BF) were three to five times lower than those of the sampling after the rainfall event (4.0 Bq $m^{-3}$, IQR 2.4 – 10.2 Bq $m^{-3}$ for $^{224}Ra$; and 1.4 Bq $m^{-3}$, IQR 1.1 – 1.9 Bq $m^{-3}$ for $^{228}Ra$). Seawater activities of $^{226}Ra$ were low, and comparable to open seawater activities in all samplings (1.8 Bq $m^{-3}$, IQR 1.4 – 2.0 Bq $m^{-3}$), revealing the lack of major inputs for this Ra isotope.

Nutrient concentrations in groundwater from the experimental site of the Argentona ephemeral stream (2015-2020 period) ranged from 10 to 1070 µM for $NO_3^-$, 0.1 to 3.9 µM for $NO_2^-$, 0.3 to 40.1 µM for $NH_4^+$, 0.8 to 10.1 µM for $PO_4^{3-}$, and 50 to 230 µM for $SiO_4^{2-}$ (Figure C.3). Nitrate ($NO_3^-$) and silica ($SiO_4^{2-}$) presented a similar pattern, with maximum concentrations in low salinity samples (Sal < 10) and a downward trend with increasing groundwater salinity. Conversely, the concentrations of nitrite ($NO_2^-$), phosphate ($PO_4^{3-}$), and ammonia ($NH_4^+$) were relatively low for most of the groundwater samples, except for those collected at the shallow piezometers for nitrite, intermediate for phosphate, and deep for ammonia (see Appendix C; Figure C.3).

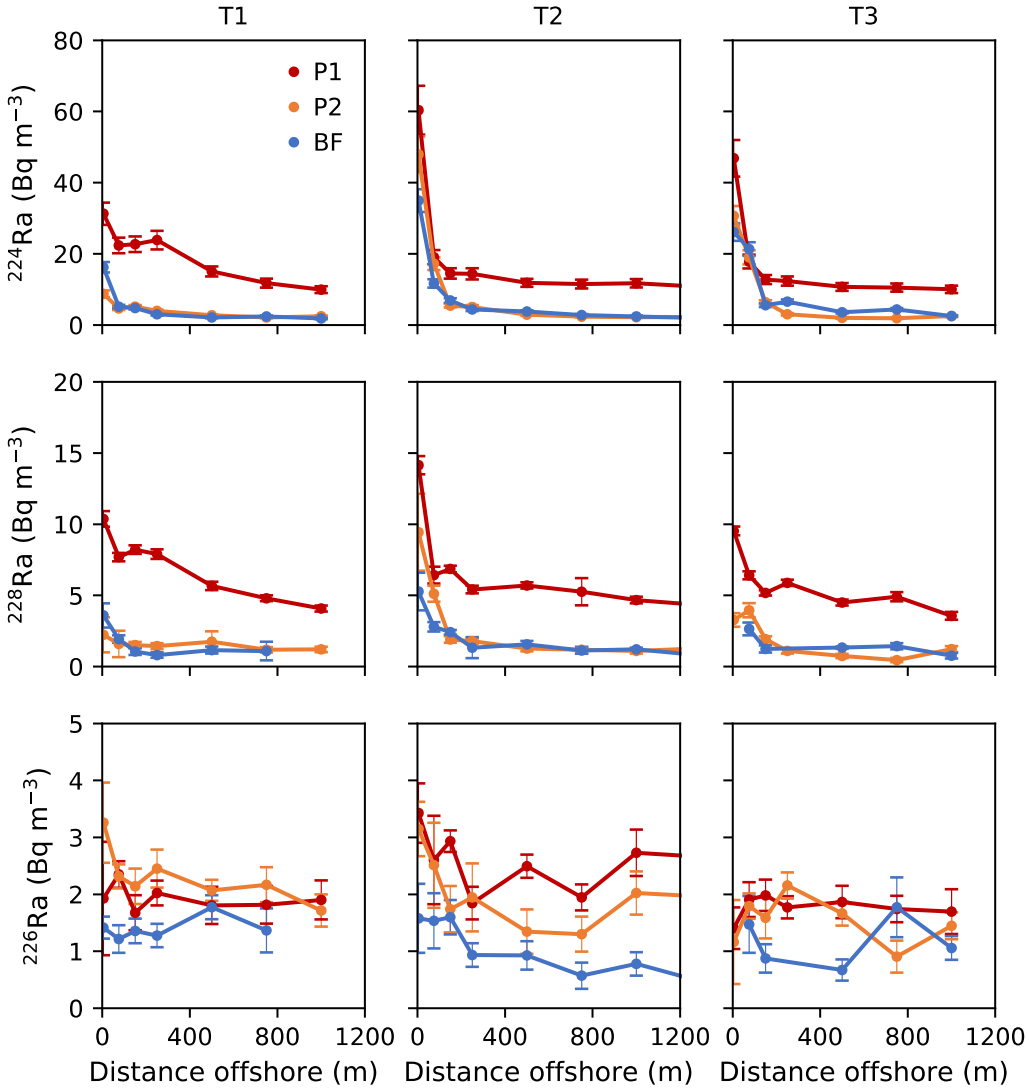


Figure 6.2. Radium isotopes activities ($^{224}$Ra, $^{228}$Ra, and $^{226}$Ra) in coastal seawater samples collected during the samplings performed in October 2019 (P1 and P2) and March 2020 (BF) for the three transects perpendicular to the coastline corresponding to the ephemeral streams of Argentona (T1), Cabrera de Mar (T2), and Vilassar de Mar (T3).

## 6.4. Discussion

### 6.4.1. Groundwater and nutrient fluxes calculation

#### *6.4.1.1. Pathways of submarine groundwater discharge*

In this study, we define terrestrial groundwater discharge as the combined discharge of meteoric groundwater and density-driven circulated seawater, and marine groundwater discharge as those processes solely involving the circulation of seawater through permeable sediments (i.e., beach-face circulation, porewater exchange).

Radium isotopes represent one of the most common techniques for quantifying the fluxes of groundwater and associated nutrients to the coastal ocean (Taniguchi et al., 2019). These isotopes can additionally be instrumental for differentiating SGD pathways, since their enrichment rates strongly depend on the transit time of groundwater through the coastal aquifer (Michael et al., 2011). Coastal seawater samples collected during the three samplings performed in Maresme County were enriched in both $^{224}$Ra and $^{228}$Ra relative to offshore waters (Figure **6.2**), suggesting the occurrence of a land-based Ra source. Whilst the enrichment in $^{224}$Ra may result from any groundwater discharge, regardless of spatiotemporal scale, due to its short half-life ($^{224}$Ra is enriched in all SGD pathways), coastal waters enriched in $^{228}$Ra may be indicative of long-scale SGD pathways (e.g., terrestrial groundwater discharge; Rodellas et al., 2017; Tamborski et al., 2017a).

The activity ratio (AR) of $^{224}$Ra/$^{228}$Ra can similarly be used to evaluate the temporal scale of SGD pathways (see Chapter 4). Thus, the $^{224}$Ra/$^{228}$Ra AR found in coastal seawater samples after the EPE from October 2019 decreased from a baseline value of 6 to approximately 4. This decrease is simultaneously followed by an increase in absolute $^{228}$Ra activities, which are two-times higher than those in baseflow conditions (Figure **6.2**). Both trends may indicate that the relative contribution of the terrestrial component of SGD, which is characterized by $^{224}$Ra/$^{228}$Ra ARs close to the equilibrium value (1.0 to 2.2; see Chapter 4), increased during the occurrence of the EPE. Thus, based on the application of Ra isotopes and the $^{224}$Ra/$^{228}$Ra activity ratio, the discharge of terrestrial and marine groundwater occurs concurrently at the study site.

#### *6.4.1.2. Submarine groundwater discharge*

Submarine groundwater discharge associated with terrestrial and marine water flows were determined by means of a steady-state mass balance of $^{224}Ra$ and $^{228}Ra$. The assumptions, considerations, and models used to estimate SGD are discussed in detail in appendix D. The sampling influenced by the EPE of October 2019 (P1) presented the highest total SGD (terrestrial and marine) (510 $\cdot 10^3$ $m^3$ $km^{-1}$ $d^{-1}$, IQR: 320 – 890 $\cdot 10^3$ $m^3$ $km^{-1}$ $d^{-1}$), one order of magnitude higher than those flows from subsequent samplings: 40 $\cdot 10^3$ $m^3$ $km^{-1}$ $d^{-1}$ (IQR: 30 – 90 $\cdot 10^3$ $m^3$ $km^{-1}$ $d^{-1}$) for P2 and 70 $\cdot 10^3$ $m^3$ $km^{-1}$ $d^{-1}$ (IQR: 40 – 110 $\cdot 10^3$ $m^3$ $km^{-1}$ $d^{-1}$) for BF (Figure **6**.**3**). Thus, the effect of this EPE on the discharge of groundwater lasts only for a few days, as the SGD estimates of the second sampling (P2; 8 days after the event) are comparable to those from baseflow conditions. Besides the similitudes in SGD estimates from these two samplings (P2 and BF), they also present similar groundwater levels, conductivities, and Darcy's flow estimates (Figure **6**.**1** and Figure D.1). Thus, the temporal extent of the EPE effects on SGD is consistent with the recovery of groundwater level, which commonly occurs from 7 to 10 days after the rainfall ceases (Figure **6**.**1**).

In baseflow conditions, the terrestrial component of SGD (including fresh and brackish density-driven discharge) represented 60% of the total SGD (Figure **6**.**3**). The relative contribution of this SGD component increased after the rainfall event of October 2019 to up to 75% of the total SGD. This is consistent with the variation on the $^{224}Ra/^{228}Ra$ AR in coastal seawater after the EPE (see Section 6.4.1.1) and coherent with Darcy's flow calculations (Appendix D). These estimates of the relative contribution of the terrestrial component are generally much larger than previous estimates for the Mediterranean Sea (1 - 25%, Rodellas et al., 2015), global estimates (10%, Kwon et al., 2014; 0.06%, Luijendijk et al., 2020), and local studies (5 - 55%; Beck et al., 2008; Kiro et al., 2014; Knee et al., 2016; Rodellas et al., 2017; Tamborski et al., 2017a). This difference most likely emphasizes the role of alluvial aquifers in ephemeral streams-dominated areas as a preferential pathway of terrestrial groundwater discharge (Jou-Claus et al., 2021). It should be noted however that any comparison between studies should be considered as semi-quantitative, firstly because the diverse geological settings where SGD studies are conducted result in diverse SGD pathways and implications, and secondly because different studies use

disparate methods that can capture different components of SGD depending on their spatial and temporal scales (Taniguchi et al., 2019).

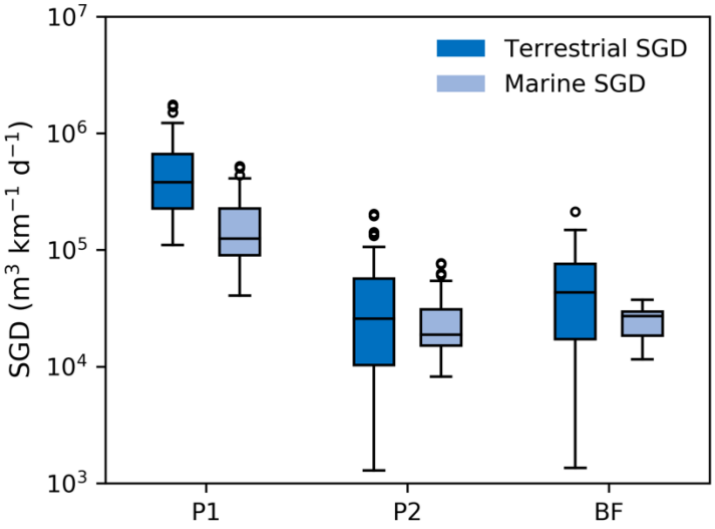


Figure 6.3. Coastal-normalized flow of terrestrial and marine submarine groundwater discharge (dark and light blue, respectively) for the three samplings at Maresme County.

#### *6.4.1.3. SGD-driven nutrient fluxes*

SGD-driven nutrient fluxes were estimated by considering the Ra-derived flows of terrestrial and marine SGD and the respective nutrient concentration in groundwater from both fractions (see Appendix D). Total SGD-driven fluxes in baseflow conditions for dissolved inorganic nitrogen (DIN), dissolved inorganic phosphorus (DIP), and dissolved silicate (DSi) derived from median SGD estimates in the study site were 16.2, 0.06, and 5.4 $\cdot 10^3$ mol $km^{-1}$ $d^{-1}$, respectively (Figure **6.4**). The median fluxes, normalized by the study site area, were lower compared with median SGD-derived nutrient fluxes estimated worldwide for DIP and DSi, but significantly higher for DIN (2.7 times higher; Santos et al., 2021). The DIN:DIP ratio was 390:1, much higher than the Redfield ratio of 16:1, but comparable with SGD-derived input in the Mediterranean Sea (80:1-430:1; Rodellas et al., 2015) and in studies worldwide (259±1090:1; Santos et al., 2021). The high loads of N and the disproportionate ratio DIN:DIP relative to the Readfield ratio in the study site may result from the lixiviation of nitrogen from agricultural activities (representing ~15% of the total land-use; Rufí-Salís et al., 2019), and the attenuation of P along groundwater flow paths due

to adsorption onto Mn/Fe oxides present in the coastal aquifer (Robinson et al., 2018; Spiteri et al., 2008b, 2007).

After an EPE, the supply of all nutrients increased due to the higher terrestrial and marine SGD associated with these episodes (Figure **6.4**). Fluxes after the EPE (P1) were 9 times higher for DIN and 7 times higher for DIP and DSi than those in baseflow conditions. The predominant pathway for DIN, DIP, and DSi discharge to the coastal ocean was the terrestrial component of SGD. This pathway represented ~60% of the total inputs of DIP and DSi in baseflow conditions and up to ~75% after an EPE (Figure **6.4**). Nitrogen inputs during EPE and in baseflow conditions were chiefly governed by the discharge of terrestrial SGD (~99% of the total DIN inputs; Figure **6.4**). The significant difference between the supply of nitrogen through terrestrial and marine SGD relies on the high concentrations of nitrate (~1,000 μM) in coastal aquifer freshwater (see appendix D; Figure D.1), which exceed the maximum groundwater concentration for drinking water set by the World Health Organization (WHO, 2011). Contrastingly, marine SGD is a relevant source of nitrite and ammonia, representing ~70% and ~40% of the total fluxes, respectively. It should be noticed that nutrient fluxes were estimated by multiplying the volumetric water flux of terrestrial and marine SGD by the minimum nutrient concentration from a set of onshore samples, selected following the criteria used for the Ra endmembers, as explained in the appendices (see appendix D). Since it was not possible to directly collect the discharging groundwater, by using onshore samples we are implicitly assuming that no nutrient transformation occurred between the sampling point and the discharge point, within the subterranean estuary (Cook et al., 2018b). It should also be noted that these SGD-derived nutrient estimates may be biased due to the groundwater endmember selection, since nutrient concentrations in discharging groundwaters may vary during EPE due to dilution, increasing lixiviation of fertilizers, or enhancement of biogeochemical reactions in the mixing zone of coastal aquifers (Spiteri et al., 2008a).

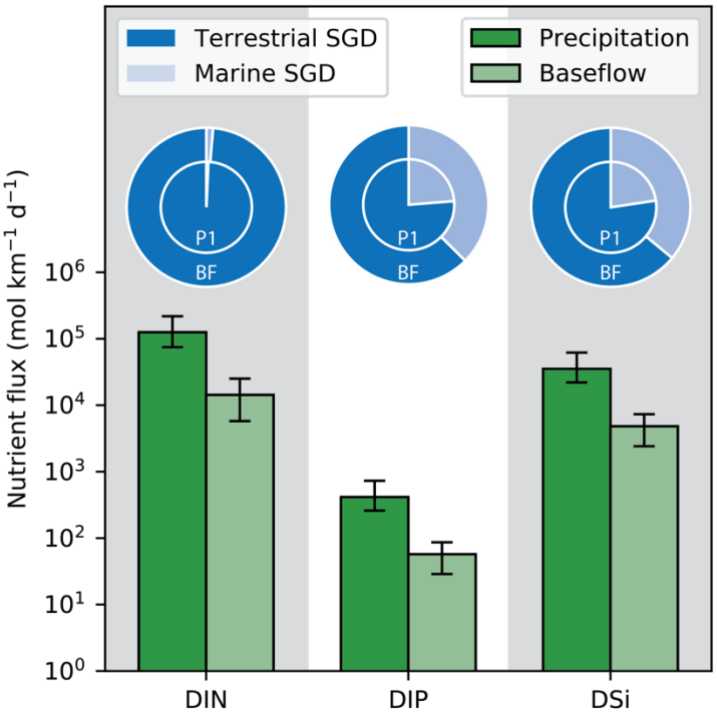


Figure 6.4. Median SGD-derived nutrient fluxes of dissolved inorganic nitrogen, dissolved inorganic phosphorus, and dissolved silicate at Maresme County during the EPE of October 2019 (P1) and in baseflow conditions (BF) (fluxes normalized by the coastline length). Error bars indicate the interquartile range (25% and 75% percentile). Inner and outer pie charts indicate the relative contribution of terrestrial (dark blue) and marine (light blue) SGD during EPE and in baseflow conditions, respectively.

### 6.4.2. Implications of EPE on SGD and associated nutrient fluxes

#### *6.4.2.1. Episodic events*

Although several studies have focused on understanding the seasonal dynamics of SGD (Charette, 2007; Gwak et al., 2014; Michael et al., 2005; Rodellas et al., 2017), limited research has been done on SGD driven by episodic events (Adyasari et al., 2021; Wilson et al., 2011). This is mainly because of the inherent difficulties related to monitoring and sampling during and after these extreme events. Some studies have already shown that SGD may vary in direct or delayed response to meteorological and oceanic episodic events such as sea-level anomalies (Gonneea et al., 2013b), waves (Bakhtyar et al., 2012; Rodellas et al., 2020; Sawyer et al., 2013), hurricanes (Hu et al., 2006), typhoons (Cho et al., 2021; Sugimoto et al., 2016), and temperature inversion (Moore and Wilson, 2005). Regarding SGD induced by precipitation events: Sugimoto et al. (2016) reported high values of SGD eleven days after a precipitation event in Obama Bay (Japan); Gwak

et al. (2014) suggested that SGD in the II-Gwang watershed (South Korea) was partially triggered by intensive precipitation events; and Uddameri et al. (2014) indicated that precipitation events associated with the Emili hurricane contributed to the SGD in Baffin Bay (USA). At our study site, the significant increase (1 order of magnitude; Figure **6.3**) in both the terrestrial and marine SGD after EPE, may be mediated by different processes: (1) increase of terrestrial groundwater discharge due to aquifer infiltration of rainfall, subsequent increase of hydraulic gradient, and displacement of stored water towards the sea (Anwar et al., 2014; Palacios et al., 2019; Santos et al., 2012; Yu et al., 2017), (2) increase in the exchange of seawater and density-driven discharge due to movements of the fresh-saltwater mixing zone, and (3) increase of shoreface circulation of seawater and porewater exchange due to the effect of sea level rise and waves associated with the EPE (Figure **6.1**).

The higher total SGD driven by EPE, especially the increase of terrestrial relative to marine SGD during these episodic events (Figure **6.3**), induces the transport of large amounts of nutrients from the freshwater fraction of coastal aquifers into the coastal ocean. These fluxes, which are substantially higher than those in baseflow conditions (Figure **6.4**), may represent a significant periodic and episode-related nutrient input of particular relevance in sites where surface water renewal is limited (e.g., coastal lagoons and/or semi-enclosed bays), EPE occurs frequently (e.g., Mediterranean region), and the response to EPE is fast due to the geological and geomorphological characteristics of the coastline (e.g., alluvial aquifers in ephemeral stream-dominated areas, such as Maresme County). However, in other areas the response to EPEs may be much slower. For instance; aquifers with a high thickness of vadose zones, confined aquifers with recharge areas far from the coastal zones, or systems with soils with water deficits (among other factors), may smooth or delay the effects of EPE. The biological and ecological implications of these events- which may include eutrophication, formation of red and green tides, and mass fish death (Hu et al., 2006; Lee et al., 2010; Montiel et al., 2019; Valiela et al., 1990; Zhao et al., 2021) are far from being understood, and require further attention.

#### *6.4.2.2. Annual SGD estimates*

A proper understanding of the temporal patterns of SGD in local to regional-scale studies is essential for deriving annual estimates for predicting reliable ocean budgets of nutrients and

other dissolved compounds (Luijendijk et al., 2020; Santos et al., 2021). However, most SGD studies are conducted in periods with stable meteorological conditions to evaluate baseflow SGD and associated nutrient, metal, or contaminant fluxes. Based on the results obtained from monitoring the EPE occurred at Maresme County in October 2019, the discharge of groundwater associated to this single event accounted for 13% (IQR: 5 – 40%) and 8% (IQR: 5 – 18%) of the annual terrestrial and marine fraction of SGD, respectively. Moreover, the nutrient inputs resulting from this event (lasting only 8 days; ~2% of the year) represented 13% (IQR: 5 – 40%) for DIN, and 11% (IQR: 5 – 30) for DIP and DSi, of the yearly supply of nutrients at the study site. The increase in SGD-driven nutrient fluxes during these events may be mediated, on the one hand by the total SGD increase, but also because this increase is more significant for terrestrial SGD, which presents higher concentrations of nutrients (see Appendix D; Figure D.1), relative to marine SGD. These results suggest that annual estimates based on samplings conducted in baseflow conditions may systematically underestimate SGD and associated nutrients, particularly at study sites affected by EPEs or other episodic events that can significantly impact SGD. Periodic and seasonal samplings may be taken as snapshots, and only representative of the time periods with similar environmental conditions. A better characterization of the hydrological and meteorological context is necessary in pursuit of more reliable annual estimates, which may include seasonal and episodic-related variations. In this scenario, alternative methods such as groundwater level monitoring, Darcy's law calculations, electric resistivity tomography characterization, among other methods, may be instrumental in the design of proper sampling strategies and to capture seasonal and episodic variations (e.g., Palacios et al., 2019).

#### *6.4.2.3. Climate change*

Climate change and its associated social and environmental impacts have become one of the most pressing scientific challenges for the 21$^{st}$ century. This requires the acquisition of a holistic and integrative knowledge of systems and processes for modelling and predicting future scenarios. Fundamental research relating environmental key variables (e.g., temperature, sea-level rise, precipitation) with social processes (e.g., land demand, coastal overpopulation, groundwater squeeze) becomes crucial to this aim. Research on SGD is no exception to this trend and, in recent decades, several studies have evaluated the key factors contributing to

groundwater flows discharging into the ocean. Some examples of SGD research linked to climate change include; understanding sea-level and/or tidal controls on SGD (Gonneea et al., 2013b; Wilson et al., 2015); the influence of land-use changes (Rufí-Salís et al., 2019); the relationship to increasing seawater intrusion (Werner et al., 2013); and the fate and evolution of nutrients in groundwater (Beusen et al., 2013; Tait et al., 2014; Van Meter et al., 2018).

The precipitation-recharge relationship is one of the key parameters influencing the discharge of groundwater. Indeed, the amount of precipitation and the frequency and/or distribution of rainfall events, together with the hydrogeological characteristics of the receiving aquifers, strongly affects both the quantity and chemical quality of terrestrial groundwater discharge to the ocean (Kundzewicz and Döll, 2009; Stigter et al., 2014). Climate models indicate substantial spatial variation in future changes to average precipitation. Whilst the increased specific humidity and transport of water vapor from tropic regions is likely to increase the amount of precipitation in high latitude land masses, precipitation in subtropical and semi-arid regions, like the Mediterranean Sea, is expected to decrease. Simultaneously, EPE in these regions are likely to increase in intensity and frequency (IPCC, 2021). Consequently, the yearly recharge of groundwater associated with precipitation in the Mediterranean region may diminish, also reducing the annual discharge of groundwater. In that scenario, EPEs may become a major driving force of SGD, having a dominant significance in the annual fluxes of solutes to the coastal ocean.

The potential relevance of EPEs on SGD in future conditions can be qualitatively evaluated for Maresme County by considering the period from October 2019 to April 2020, when 3 precipitation events of >75 mm occurred (Figure **6.1**). Since the historical recurrence of EPE in the area is around 13 months (based on the meteorological data from 2015 to 2020), this 7-month period can be considered as a future-like year with increased recurrence of EPE. Assuming that each one of the EPE produces an increase in SGD comparable to the event monitored in this study, the relative contribution of SGD during EPEs would represent 30% (IQR: 15 – 70%) and 22% (15 – 40%) of the annual SGD issued by the terrestrial and marine fraction, respectively. Similarly, nutrient fluxes associated with EPE for this period would represent 34% (IQR: 15 – 70%) for DIN and 30% (IQR: 15 – 60%) for DIP and DSi of the yearly nutrient inputs supplied by SGD. Notice that due to the assumptions made in the determination of groundwater and nutrient

fluxes (e.g., steady state, endmember selection; see appendix D), the estimates are seemingly conservative, especially considering that the monitored EPE is minor relative to other EPEs occurring in 2019 and 2020 (Figure **6**.**1**). These estimates emphasize the need for integrating episodic events, such as EPE, in future climate change scenarios, in order to properly constrain the fluxes of groundwater and solutes to the coastal ocean driven by SGD.

# Chapter 7: Conclusions and future perspectives

## 7.1. Conclusions

Radium isotopes and radon represent undoubtably one of the most valuable tools for assessing the significance of submarine groundwater discharge, yet reporting SGD estimates by means of these tracers is complex and requires profound knowledge regarding fundamental steps in the process of quantifying SGD using these radionuclides, from the tracer measurement techniques to the estimation of water and solute fluxes. This Thesis aimed at improving the use of Ra isotopes and Rn as SGD tracers by addressing a set of research gaps including (1) the analytical techniques for measuring and quantifying these radionuclides, (2) their geochemical behavior in groundwater systems, and (3) their applications as tracers of both groundwater systems and the coastal ocean.

Improving and revisiting analytical techniques is fundamental for any scientific discipline to advance in understanding processes and systems. This is especially significant when using tracer methods since the accuracy of the tracer-based estimates is closely linked to that of the analytical techniques. This Thesis included an assessment of the quantification systematics of the RaDeCC system, the most widely used counter for quantifying short-lived Ra isotopes, providing limits and guidelines to perform the quantification. Thus, this work represented a significant advance on pursue for better and more precise SGD estimates, as well as for any hydrological and oceanographic application of these tracers.

Understanding the behavior of Ra isotopes and Rn in groundwater is fundamental, as most of the SGD estimates rely on properly constraining the activities of these radionuclides in the discharging groundwater (endmember) which often represents a significant source of uncertainty in the overall quantification. Additionally, once the behavior of these radionuclides in known, new applications for tracing groundwater systems can be developed. In this Thesis, the behavior of Ra isotopes and Rn in groundwater was assessed using a novel transport model of radionuclides. This model represents an advance in assessing the distribution of these radionuclides, and their activity ratios in groundwater, allowing the use of these tracers for

evaluating Ra isotopes and Rn endmember, discriminating SGD pathways, and assessing the characteristics of the groundwater flow (i.e., velocity, transit times).

Estimates of SGD induced by extreme events such as heavy rainfall are very scarce in the literature because most of SGD studies are often conducted in baseflow conditions and also because sampling this kind of events is challenging due to the complicated meteorological or oceanographical conditions. In this Thesis, the effects of an extreme precipitation even on SGD estimates was evaluated by using Ra isotopes, thus representing one of the first works addressing the effect of these events on SGD and associated nutrient fluxes to the coastal ocean.

The above-mentioned research gaps have been addressed in three research articles presented in this Thesis as Chapter 4, 5, and 6. The detailed conclusions of this research articles are presented below:

### 7.1.1. Chapter 4. Guidelines for the quantification of Ra isotopes

*This work emphasizes the need for better praxis on the measurement and quantification of Ra isotopes with the RaDeCC system and proposes a set of quantification guidelines and limits based on empirical data and simulations.*

The aim of this study was to examine the behavior of the counting system of the RaDeCC system under different activities and activity ratios of $^{223}$Ra, $^{224}$Ra, and $^{226}$Ra through empirical data and a set of simulations that reproduce the RaDeCC counting mechanism. Results of the simulations showed that the proper quantification of $^{223}$Ra and $^{224}$Ra activities using the RaDeCC system is highly dependent on (1) the count rate registered in the Total channel, (2) its channel ratio (*220 channel/219 channel; $CR_{220/219}$*), and (3) the $^{222}$Rn buildup. High activity samples may produce the overestimation of $^{223}$Ra and $^{224}$Ra activities due to channel multiregistration (i.e., two or more events are registered during the opening time of a specific circuit) and/or concurrent registration (i.e., a single event is registered in both the 219 and 220 channel). The cross-talk effect (i.e., the counts relative to Rn-Po events that are registered in the non-respective channel) could produce an overestimation of the quantified $^{223}$Ra and $^{224}$Ra activities by up to ~40% and ~30%, respectively. Additionally, the quantification of $^{223}$Ra and $^{224}$Ra strongly depend on the

buildup of $^{222}$Rn from $^{226}$Ra during the measurement. Although this effect may not be relevant for short runs (counting times < 400 min), long measurements usually conducted for quantifying $^{227}$Ac and $^{228}$Th are likely to be significantly affected by these processes. In the case of $^{227}$Ac ($^{223}$Ra) quantification, due to the short opening time of the 219 channel ($t_{G\text{-}219}$ = 5.6 ms), this effect is negligible. In contrast, the $^{222}$Rn buildup significantly affect the $^{228}$Th ($^{224}$Ra) quantification, especially for measurements with low counting rates in the 220 channel (< 1 cpm).

This work also presents an improved simple method to quantify $^{226}$Ra activities based on the ingrowth rate of $^{222}$Rn in the Total channel using the RaDeCC system. The method described in this study, in contrast with previous methods (Geibert et al., 2013), avoids correcting the count rate in the Total channel using the chance coincidence equations, since this correction may be inappropriate for high Ra activities.

The thresholds for an appropriate quantification of $^{223}$Ra and $^{224}$Ra activities, and their parent radionuclides, $^{227}$Ac and $^{228}$Th activities using the RaDeCC system based on the results of this study are summarized and presented in the form of guidelines for easy and fast sample processing and quantification.

### 7.1.2. Chapter 5. Activity ratios of $^{224}$Ra/$^{228}$Ra and $^{222}$Rn/$^{226}$Ra

*This work aims on using the activity ratios of $^{224}$Ra/$^{228}$Ra and $^{222}$Rn/$^{226}$Ra as proxies of groundwater systems. The study describes the processes controlling the distribution of Ra isotopes and Rn, and their activity ratios in groundwater, and proposes novel applications such as the determination of groundwater transit times, and the assessment of pathways and endmembers of SGD.*

In this work, the processes affecting Ra isotopes and Rn, and their activity ratios, $^{224}$Ra/$^{228}$Ra and $^{222}$Rn/$^{226}$Ra in groundwater were assessed through a new advective transport model that integrates all radionuclides in a decay chain into one formulation. The analysis of the model's results indicates that the predominant parameters that affect the activity ratios of $^{224}$Ra/$^{228}$Ra and $^{222}$Rn/$^{226}$Ra in groundwater are groundwater transit times, α-recoil supply, and the retardation factor of Ra ($R_{Ra}$). The ARs evolve, depending on groundwater transit times,

towards the radioactive equilibrium between parent and daughter radionuclide. The α-recoil supply increases activity ratios to above the equilibrium activity ratios (1 and $R_{Ra}$ for $^{224}Ra/^{228}Ra$ and $^{222}Rn/^{226}Ra$, respectively), which cannot be explained solely by considering production rates derived from the exchangeable activity of the parent radionuclide. The retardation factor of Ra influences the characteristic groundwater transit times needed for achieving these equilibriums. Higher Ra retardation factors (characteristics of fresh groundwater; $10^6$) result in shorter transit times for equilibrium (~0.1 days for $^{224}Ra/^{228}Ra$ and 100 days for $^{222}Rn/^{226}Ra$) due to the minor effect of advection losses. Conversely, the ARs of $^{224}Ra/^{228}Ra$ and $^{222}Rn/^{226}Ra$ require longer transit times to reach equilibrium (~3 years and 3000 years for $^{224}Ra/^{228}Ra$ and $^{222}Rn/^{226}Ra$, respectively) when the retardation factors of Ra are low (characteristics of saline groundwater; $10^1$).

The ARs and the advective transport model have several applications in the fields of hydrogeology and coastal oceanography, and these were tested in a Mediterranean coastal aquifer. In hydrogeological studies, the model can be used to determine transit times (i.e., ages and velocities of groundwater), evaluate the connectivity between coastal aquifer and ocean, and distinguish the origins of groundwater. Whilst this study is focused on coastal systems, the application of this model can be extended to aquifers inland, provided that groundwater is sufficiently enriched in these pairs of radionuclides. The use of Ra isotopes and Rn thus provides relevant information on aquifer processes, which may be fundamental for the management of coastal groundwater resources. The combination of the groundwater-measured activity ratios of $^{224}Ra/^{228}Ra$ and $^{222}Rn/^{226}Ra$, and the advective transport model can also be applied to improve the estimation of SGD flows to the coastal ocean by constraining the predominant pathways of submarine groundwater discharge and the determination of the groundwater endmember, which is often one of the main sources of uncertainty in these types of study.

### 7.1.3. Chapter 6. SGD induced by extreme precipitation events

*This study highlights the role of extreme episodic events, such as heavy precipitation on the discharge of groundwater and associated nutrients to the Mediterranean Sea. The work represents one of the first attempts for monitoring fluxes of SGD driven by extreme precipitation*

*events and assess the implications of neglecting them on annual estimates, and their importance in the context of climate change implications for the annual discharge of groundwater.*

This work assessed the role of extreme precipitation events as potential drivers of SGD and SGD-driven nutrients to the coastal ocean. The lack of studies assessing the impact of these episodic events mask the implications that they may have for coastal geochemical cycles, coastal ecosystems, nutrient budgets, and hydrological cycle estimates. We have assessed the fluxes of SGD induced by an EPE in an ephemeral stream-dominated basin of the western Mediterranean Sea. SGD induced by the EPE increased by one order of magnitude and represented up to 13 and 8% of the total annual discharge of groundwater of terrestrial and marine SGD, respectively. Similarly, fluxes of nutrients driven by SGD during an EPE represented 11 - 13% of the annual total SGD, and up to ~30% during abnormally rainy seasons. This study highlights the relevance of these extreme events on the discharge of groundwater and solutes to the coastal ocean, noting their implications for annual SGD estimates and the possible consequences on coastal biogeochemistry cycles. The results of this study contribute to the understanding of the evolution of SGD with respect to future climate change scenarios, presenting an opportunity for streamlining future research in order to help managers and policy makers to better estimate SGD and its related consequences.

## 7.2. Future perspectives

In recent decades, many advances have been made in understanding the magnitude of submarine groundwater discharge at local-, basin-, and global-scale and its geochemical, biological, and social implications. Simultaneously, the use of Ra isotopes and Rn as tracers of SGD has been improved through the assessment of their geochemical behavior and the development of new approaches, models, and techniques that enabled their expansion as a reliable tool in hydrology and oceanography. Within this process of continuous improvement many questions have been resolved or addressed while many others have raised. Most of these questions or research gaps that should be addressed in the forthcoming years have been discussed previously in recent review articles (Garcia-Orellana et al., 2021; Santos et al., 2021;

Taniguchi et al., 2019). Here, I summarize the main research gaps related to both the use of Ra isotopes and Rn, and the assessment of SGD (Table 7.1).

Table 7.1. Summary of the research gaps, future work, and key references related to the use of Ra isotopes and Rn as tracers of SGD.

| Topic | Research gap | Future work | Key works |
|---|---|---|---|
| ***Ra isotopes and Rn*** | | | |
| **Analytical developments** | Some of the techniques used for measuring or quantifying Ra isotopes and Rn need to be revisited or improved to provide more reliable estimates, and/or increase the data resolution. | Reducing the water volume needed for determining Ra activities.<br>Testing the efficiency of Ra extraction using Mn-fibers under different groundwater composition (e.g., pH, $O_2$, ORP, presence of Fe or/and Mn).<br>Developing instruments allowing the continuous monitoring of Ra activities in water. | 1,2,3 |
| **Experimental developments** | There is no standard experimental procedure for determining some of the key parameters used to model the distribution of Ra isotopes and Rn in groundwater. | Developing standard techniques for assessing production rates, $\alpha$-recoil, distribution coefficients of Ra, retardation factors, and diffusion coefficients.<br>Developing experiments reproducing field conditions (e.g., column sediment experiments) | 4,5,6 |
| **Transport models of radionuclides** | Current transport models are based on assumptions (e.g., steady state, homogeneous composition of aquifer and groundwater) that make difficult their application to coastal aquifers. | Developing transport models that assess the complex reactions occurring in the subterranean estuary (transient, 2-dimensional, dispersive-advective) | 7,8,9 |
| **Spatial and temporal variability** | Better understanding of the spatiotemporal variation of Ra isotopes and Rn in coastal aquifers is needed to improve the use of these tracers for hydrological and oceanographical purposes. | Developing highly instrumented experimental sites for monitoring the activities of Ra isotopes and Rn in fresh, brackish, and saline groundwater or/and in multiple geological contexts.<br>Long- and short- term monitoring of Ra isotopes and Rn in groundwater. | 10,11,12 |
| **Temporal scales** | Ra isotopes and Rn are used in some cases indistinctively to assess processes with disparate spatiotemporal scales. | Delimiting which processes are subjected to be traced by each tracer depending on its rate of decay or/and production. | 9,13,14 |
| **Constraining sources and sinks** | The estimation of sources and sinks of Ra isotopes and Rn often represents the main uncertainty in tracer-derived estimates. | Improving the approaches for assessing processes such as diffusion from sediments, atmospheric evasion, and tracer residence time. | 15,16,17 |
| **Development of new applications** | The use of Ra isotopes and Rn for assessing the characteristics of groundwater flow in coastal or inland aquifers is limited. | Developing new applications of Ra isotopes and Rn in groundwater systems such as assessing age, velocity, origin, or/and transit time of groundwater for both freshwater and saline water environments. | 18,19,20 |
| ***Submarine groundwater discharge*** | | | |
| **Distinguishing SGD pathways** | Quantifying different SGD pathways (different spatiotemporal scales, salinity, and fluid composition) is needed to properly assess the magnitude and implications of SGD. | Assessing the driving forces of and spatiotemporal scales of SGD pathways<br>Using multiple approaches targeting specific components of SGD | 9,13,21 |

Table 7.1. Summary of the research gaps, future work, and key references related to the use of Ra isotopes and Rn as tracers of SGD.

| Topic | Research gap | Future work | Key works |
|---|---|---|---|
| **Spatial and temporal biases** | Most of SGD research is conducted in sites with expected groundwater flows and in baseflow conditions, preventing the temporal and spatial extrapolation of snap-shoot and local samplings. | Long- and short-term monitoring of SGD in sites with seasonal or/and episodic related variations.<br>Development of regional and global approaches to quantify SGD (e.g., hydrological models, remote sensing, continuous measurements) | 22,23,24 |
| **Climate change** | The effects that climate change has on the magnitude and composition of SGD are unknown. | Conducting studies attempting the evaluation of specific key factors affecting SGD (e.g., sea level anomalies, seawater intrusion, land-use changes).<br>Gathering all available information to perform predictions and future scenarios.<br>Generating global datasets of multiple parameters to allow the modelling and upscaling of local data. | 25.26.27 |
| **Uncertainties assessment** | Uncertainties associated to the calculation of SGD, whether from specific parameters (standard error of Ra isotopes and Rn quantification) or from model conceptualization (e.g., steady state, endmember selection), are often overlooked. | Proper SGD estimates should include assessment of uncertainty by means of error propagation (if possible), stochastic approaches (e.g., Monte Carlo), and/or sensitivity analysis to account for the variability of certain parameters. | 13,15,28 |
| **Terminology standardization** | Terms and definitions used in SGD research often represent a source of disagreement and may lead to wrong interpretations and misconceptions. | More efforts should be made to clarify the terms and definitions associated with SGD and to find agreements within the communities directly working with this process and external communities. | 14,29,30 |
| **Social dimension** | Most of the SGD research have been addressed through the prism of natural sciences, neglecting the social implications that SGD may have including politics, economics, ecosystem services, stakeholders' analysis, among others. | Assess the economic significance of SGD in multiple sites.<br>Evaluate the ecosystem services associated with SGD.<br>Evaluate trade-off of different SGD associated ecosystem services. | 31,32,33 |

1: Vieira et al. (2021); 2: Moore (2008); 3: Scholten et al. (2010); 4: Beck and Cochran (2013); 5: Tachi et al. (2001); 6: Webster et al. (1995); 7: Kiro et al. (2014); 8: Krest and Harvey (2003); 9: Michael et al. (2011); 10: Cho and Kim (2016); 11: Cerdà-Domènech et al. (2017); 12: Cook et al. (2018); 13: Garcia-Orellana et al. (2021); 14: Taniguchi et al. (2019); 15: Rodellas et al. (2021); 16: Beck et al. (2007); 17: Schubert et al. (2012); 18: Kiro et al. (2015); 19: Molina-Porras et al. (2020); 20: Moise et al. (2000); 21: Santos et al. (2012); 22: Adyasari et al. (2021); 23: Luijendijk et al. (2020); 24: Shalev et al. (2009); 25: Gonneea et al. (2013); 26: Rufí-Salís et al. (2019); 27: Werner et al. (2013); 28: Burnett et al. (2007); 29: Monsen et al. (2002); 30: Duque et al. (2020); 31: Alorda-Kleinglass et al. (2021); 32: Moosdorf and Oehler (2017); 33: Erostate et al. (2020).

# Appendices

## A) Appendix A. Ra distribution coefficient compilation

Table A.1. Compilation of Ra distribution coefficients ($K_D$) in fresh solution from literature. The data include the type of solution and sorbent materials, as well as the different variables analysed in the experimental settings (water:sorbent ratio, temperature, contact time, pH, salinity, cationic exchange capacity (CEC), and specific surface area).

| Solution | Sorbent material | Water:sorbent ratio (L kg$^{-1}$) | Temperature (ºC) | Contact time (h) | pH | Salinity | CEC (meq 100 g$^{-1}$) | Specific surface Area (m$^2$ g$^{-1}$) | $K_D$ (L kg$^{-1}$) | Reference |
|---|---|---|---|---|---|---|---|---|---|---|
| Synthetic water | Organic | | | | | | | | 2400 | Sheppard and Thibault (1990) |
| Synthetic water | | 10 | | | | | | | 150 | Beneš (1982) |
| Synthetic water | | 50 | | | | | | | 230 | |
| Synthetic water | | 500 | | | | | | | 370 | |
| Synthetic water | | 10 | | | | | | | 100 | |
| Synthetic water | | 50 | | | | | | | 120 | |
| Synthetic water | | 500 | | | | | | | 370 | |
| Synthetic water | | 10 | | | | | | | 40 | |
| Synthetic water | | 50 | | | | | | | 50 | |
| Synthetic water | | 500 | | | | | | | 70 | |
| Synthetic water | Kaolinite | 5000 | 25 | 17 | 7.6 | | 6.2 | 13 | 3210 | Beneš et al. (1985) |
| Synthetic water | Kaolinite | 2500 | 25 | 17 | 7.6 | | 6.2 | 13 | 2710 | |
| Synthetic water | Kaolinite | 500 | 25 | 17 | 7.6 | | 6.2 | 13 | 1900 | |
| Synthetic water | Kaolinite | 400 | 25 | 17 | 7.6 | | 6.2 | 13 | 1890 | |
| Synthetic water | Kaolinite | 200 | 25 | 17 | 7.6 | | 6.2 | 13 | 1710 | |
| Synthetic water | Kaolinite | 100 | 25 | 17 | 7.6 | | 6.2 | 13 | 1090 | |
| Synthetic water | Kaolinite | 50 | 25 | 17 | 7.6 | | 6.2 | 13 | 740 | |
| Synthetic water | Kaolinite | 40 | 25 | 17 | 7.6 | | 6.2 | 13 | 610 | |
| Synthetic water | Kaolinite | 25 | 25 | 17 | 7.6 | | 6.2 | 13 | 430 | |
| Synthetic water | Kaolinite | 20 | 25 | 17 | 7.6 | | 6.2 | 13 | 400 | |
| Synthetic water | Kaolinite | 10 | 25 | 17 | 7.6 | | 6.2 | 13 | 200 | |
| Synthetic water | Montmorillonite | 5000 | 25 | 17 | 7.5 | | 90.8 | 750 | 8120 | |
| Synthetic water | Montmorillonite | 3333 | 25 | 17 | 7.5 | | 90.8 | 750 | 7850 | |
| Synthetic water | Montmorillonite | 2000 | 25 | 17 | 7.5 | | 90.8 | 750 | 7760 | |
| Synthetic water | Montmorillonite | 1000 | 25 | 17 | 7.5 | | 90.8 | 750 | 8010 | |
| Synthetic water | Montmorillonite | 500 | 25 | 17 | 7.5 | | 90.8 | 750 | 6540 | |
| Synthetic water | Montmorillonite | 400 | 25 | 17 | 7.5 | | 90.8 | 750 | 6380 | |
| Synthetic water | Montmorillonite | 200 | 25 | 17 | 7.5 | | 90.8 | 750 | 4800 | |
| Synthetic water | Montmorillonite | 100 | 25 | 17 | 7.5 | | 90.8 | 750 | 3900 | |
| Synthetic water | Montmorillonite | 50 | 25 | 17 | 7.5 | | 90.8 | 750 | 2450 | |
| Synthetic water | Montmorillonite | 25 | 25 | 17 | 7.5 | | 90.8 | 750 | 1640 | |
| Synthetic water | Montmorillonite | 10 | 25 | 17 | 7.5 | | 90.8 | 750 | 660 | |
| Synthetic water | Quartz | 5000 | 25 | 17 | | | | | 1950 | Beneš et al. (1984) |

Table A.1. Compilation of Ra distribution coefficients ($K_D$) in fresh solution from literature. The data include the type of solution and sorbent materials, as well as the different variables analysed in the experimental settings (water:sorbent ratio, temperature, contact time, pH, salinity, cationic exchange capacity (CEC), and specific surface area).

| Solution | Sorbent material | Water:sorbent ratio | Temperature | Contact time | pH | Salinity | CEC | Specific surface Area | $K_D$ | Reference |
|---|---|---|---|---|---|---|---|---|---|---|
| | | (L $kg^{-1}$) | (ºC) | (h) | | | (meq 100 $g^{-1}$ ) | ($m^2$ $g^{-1}$) | (L $kg^{-1}$) | |
| Synthetic water | Quartz | 3333 | 25 | 17 | | | | | 1690 | |
| Synthetic water | Quartz | 500 | 25 | 17 | | | | | 1350 | |
| Synthetic water | Quartz | 200 | 25 | 17 | | | | | 990 | |
| Synthetic water | Quartz | 100 | 25 | 17 | | | | | 830 | |
| Synthetic water | Quartz | 50 | 25 | 17 | | | | | 550 | |
| Synthetic water | Quartz | 25 | 25 | 17 | | | | | 430 | |
| Synthetic water | Quartz | 10 | 25 | 17 | | | | | 170 | |
| Groundwater | | | | | 7.2 | 0.3 | | | 13000 | Copenhaver et al. (1992) |
| Synthetic water | Bedded Salt | | | | | | | | 1 | Serne and Relyea (1982) |
| Synthetic water | Dome Salt | | | | | | | | 10 | |
| Synthetic water | Basalt | | | | | | | | 50 | |
| Synthetic water | Tuff | | | | | | | | 200 | |
| Synthetic water | Granite | | | | | | | | 50 | |
| Synthetic water | Purified smectite | 500 | | 480 | 7.0 | | 110.2 | | 17000 | Tachi et al. (2001) |
| Synthetic water | Purified smectite | 500 | | 480 | 8.0 | | 110.2 | | 16000 | |
| Synthetic water | Purified smectite | 500 | | 480 | 7.0 | | 110.2 | | 660 | |
| Synthetic water | Purified smectite | 500 | | 480 | 8.0 | | 110.2 | | 600 | |
| Synthetic water | Purified smectite | 500 | | 480 | 9.0 | | 110.2 | | 790 | |
| Synthetic water | Purified smectite | 500 | | 480 | 10.0 | | 110.2 | | 1500 | |
| Synthetic water | Purified smectite | 500 | | 480 | 11.0 | | 110.2 | | 1900 | |
| Synthetic water | Purified smectite | 50 | | 480 | 7.0 | | 110.2 | | 410 | |
| Synthetic water | Purified smectite | 50 | | 480 | 8.0 | | 110.2 | | 400 | |
| Synthetic water | Purified smectite | 50 | | 480 | 9.0 | | 110.2 | | 740 | |
| Synthetic water | Purified smectite | 50 | | 480 | 10.0 | | 110.2 | | 640 | |
| Synthetic water | Bentonite | 500 | | 480 | 7.0 | | 60.1 | | 3300 | |
| Synthetic water | Bentonite | 500 | | 480 | 8.0 | | 60.1 | | 4100 | |
| Synthetic water | Bentonite | 500 | | 480 | 9.0 | | 60.1 | | 6200 | |
| Synthetic water | Bentonite | 500 | | 480 | 10.0 | | 60.1 | | 13000 | |
| Synthetic water | Bentonite | 500 | | 480 | 11.0 | | 60.1 | | 16000 | |
| Synthetic water | Bentonite | 500 | | 480 | 7.0 | | 60.1 | | 340 | |
| Synthetic water | Bentonite | 500 | | 480 | 8.0 | | 60.1 | | 750 | |
| Synthetic water | Bentonite | 500 | | 480 | 9.0 | | 60.1 | | 730 | |
| Synthetic water | Bentonite | 500 | | 480 | 10.0 | | 60.1 | | 1000 | |
| Synthetic water | Bentonite | 500 | | 480 | 11.0 | | 60.1 | | 950 | |
| Synthetic water | Bentonite | 50 | | 480 | 7.0 | | 60.1 | | 210 | |
| Synthetic water | Bentonite | 50 | | 480 | 8.0 | | 60.1 | | 320 | |
| Synthetic water | Bentonite | 50 | | 480 | 9.0 | | 60.1 | | 290 | |
| Synthetic water | Bentonite | 50 | | 480 | 10.0 | | 60.1 | | 290 | |
| Synthetic water | Bentonite | 50 | | 480 | 11.0 | | 60.1 | | 440 | |
| Synthetic water | Granite | | | | | | | | 1300 | Crawford et al. (2006) |
| Synthetic water | Sand | | | | | | | | 40 | Sheppard et al. (2006) |

Table A.1. Compilation of Ra distribution coefficients ($K_D$) in fresh solution from literature. The data include the type of solution and sorbent materials, as well as the different variables analysed in the experimental settings (water:sorbent ratio, temperature, contact time, pH, salinity, cationic exchange capacity (CEC), and specific surface area).

| Solution | Sorbent material | Water:sorbent ratio | Temperature | Contact time | pH | Salinity | CEC | Specific surface Area | $K_D$ | Reference |
|---|---|---|---|---|---|---|---|---|---|---|
| | | (L kg$^{-1}$) | (ºC) | (h) | | | (meq 100 g$^{-1}$ ) | (m$^2$ g$^{-1}$) | (L kg$^{-1}$) | |
| Synthetic water | Loam | | | | | | | | 30 | |
| Synthetic water | Clay | | | | | | | | 30 | |
| Synthetic water | Organic | | | | | | | | 200 | |
| Synthetic water | Pasture soils | 494 | | | 5,3 | | 8,7 | | 70 | Vandenhove and Van Hees (2007) |
| Synthetic water | Pasture soils | 546 | | | 5,9 | | 43,8 | | 300 | |
| Synthetic water | Pasture soils | 579 | | | 6,4 | | 51,7 | | 390 | |
| Synthetic water | Pasture soils | 526 | | | 4,6 | | 5,1 | | 40 | |
| Synthetic water | Pasture soils | 557 | | | 7,5 | | 24,0 | | 210 | |
| Synthetic water | Pasture soils | 431 | | | 5,5 | | 24,5 | | 90 | |
| Synthetic water | Pasture soils | 474 | | | 5,3 | | 8,5 | | 450 | |
| Synthetic water | Pasture soils | 528 | | | 5,7 | | 8,1 | | 90 | |
| Synthetic water | Pasture soils | 479 | | | 5,9 | | 10,0 | | 50 | |
| Synthetic water | Sand | | | | | | | | 3100 | Environmental Modelling for Radiation Safety (2008) |
| Synthetic water | Loam | | | | | | | | 1100 | |
| Synthetic water | Clay | | | | | | | | 3800 | |
| Synthetic water | Marine sediment | | | | | 5,0 | | | 270 | Eagle et al. (2008) |
| Synthetic water | Marine sediment | | | | | 5,0 | | | 480 | |
| Synthetic water | Marine sediment | | | | | 5,0 | | | 410 | |
| Synthetic water | Sandy loam | | | | | | | | 1900 | International Atomic Energy Agency (2010) |
| Synthetic water | Clay | | | | | | | | 38000 | |
| Synthetic water | Organic | | | | | | | | 1300 | |
| Synthetic water | Montmorillonite | 300 | 25 | 48 | 5,0 | 0,6 | 82,3 | | 9580 | Tamamura et al. (2014) |
| Synthetic water | Montmorillonite | 300 | 25 | 48 | 5,0 | 5,8 | 82,3 | | 170 | |
| Synthetic water | Montmorillonite | 30 | 25 | 48 | 5,0 | 5,8 | 82,3 | | 130 | |
| Synthetic water | Kaolinite | 300 | 25 | 48 | 5,0 | 0,6 | 3,1 | | 960 | |
| Synthetic water | Kaolinite | 300 | 25 | 48 | 5,0 | 5,8 | 3,1 | | 30 | |
| Synthetic water | Kaolinite | 30 | 25 | 48 | 5,0 | 0,6 | 3,1 | | 680 | |
| Synthetic water | Kaolinite | 30 | 25 | 48 | 5,0 | 5,8 | 3,1 | | 30 | |
| Groundwater | Sand | | | | 6,1 | 0,3 | | | 480 | Liu et al. (2019) |
| Groundwater | Sand | | | | 6,3 | 0,4 | | | 370 | |
| Groundwater | Sand | | | | 5,8 | 2,5 | | | 60 | |
| Groundwater | Sand | | | | 6,0 | 0,9 | | | 170 | |
| Groundwater | Sand | | | | 5,2 | 0,5 | | | 300 | |

Table A.2. Compilation of Ra distribution coefficients ($K_D$) in saline solution from literature. The data include the type of solution and sorbent materials, as well as the different variables analysed in the experimental settings (water:sorbent ratio, temperature, contact time, pH, salinity, cationic exchange capacity (CEC), and specific surface area).

| Solution | Sorbent material | Water:sorbent ratio | Temperature | Contact time | pH | Salinity | CEC | Specific surface Area | $K_D$ | Reference |
|---|---|---|---|---|---|---|---|---|---|---|
| | | (L $kg^{-1}$) | (ºC) | (h) | | | (meq 100 $g^{-1}$ ) | ($m^2$ $g^{-1}$) | (L $kg^{-1}$) | |
| Seawater | Marsh sediments | 33 | 2 | 8 | 7 | | | | 31.1 | Rama and Moore (1996) |
| Seawater | Marsh sediments | 33 | 25 | 8 | 7 | | | | 15.5 | |
| Seawater | Marsh sediments | 33 | 70 | 8 | 7 | | | | 1652.1 | |
| Seawater | Marsh sediments | | | | | | | | 13.6 | |
| Seawater | Mississippi shelf | 33 | 2 | 8 | 7 | | | | 145.8 | |
| Seawater | Mississippi shelf | 33 | 25 | 8 | 7 | | | | 76.8 | |
| Seawater | Mississippi shelf | 33 | 70 | 8 | 7 | | | | 46.6 | |
| Seawater | Amazon Shelf | 33 | 2 | 8 | 7 | | | | 102.0 | |
| Seawater | Amazon Shelf | 33 | 25 | 8 | 7 | | | | 45.7 | |
| Seawater | Amazon Shelf | 33 | 70 | 8 | 7 | | | | 27.2 | |
| Seawater | Kaolinite | 80 | | 20 | | | 27 | | 76.8 | Webster et al. (1995) |
| Seawater | Silty clay | 3659 | | 240 | | | | | 21000.0 | Li and Chan (1979) |
| Seawater | Silty clay | 3659 | | 240 | | | | | 228.4 | |
| Synthetic water | Sand | | | | | | | | 1.6 | Colbert and Hammond (2008) |
| Synthetic water | Clay | | | | | | | | 5.6 | |
| Synthetic water | Marine sediment | | | | | 15 | | | 210.0 | Gonneea et al. (2008) |
| Synthetic water | Marine sediment | | | | | 25 | | | 210.0 | |
| Synthetic water | Marine sediment | | | | | 15 | | | 445.0 | |
| Synthetic water | Marine sediment | | | | | 25 | | | 420.0 | |
| Synthetic water | Marine sediment | | | | | 15 | | | 330.0 | |
| Synthetic water | Marine sediment | | | | | 25 | | | 220.0 | |
| Synthetic water | Montmorillonite | 300 | 25 | 48 | 5 | 29.22 | 82.3 | | 35.9 | Tamamura et al. (2014) |
| Synthetic water | Montmorillonite | 300 | 25 | 48 | 5 | 58.44 | 82.3 | | 15.6 | |
| Synthetic water | Montmorillonite | 30 | 25 | 48 | 5 | 29.22 | 82.3 | | 22.2 | |
| Synthetic water | Montmorillonite | 30 | 25 | 48 | 5 | 58.44 | 82.3 | | 4.8 | |
| Synthetic water | Kaolinite | 300 | 25 | 48 | 5 | 29.22 | 3.1 | | 38.0 | |
| Synthetic water | Kaolinite | 300 | 25 | 48 | 5 | 58.44 | 3.1 | | 24.9 | |
| Synthetic water | Kaolinite | 30 | 25 | 48 | 5 | 29.22 | 3.1 | | 7.1 | |
| Synthetic water | Kaolinite | 30 | 25 | 48 | 5 | 58.44 | 3.1 | | 6.0 | |
| Seawater | Marine sediment | 20.9 | | 1 | | | | 0.16 | 6.9 | Beck and Cochran (2013) |
| Seawater | Marine sediment | 18.2 | | 1 | | | | 0.16 | 6.4 | |
| Seawater | Marine sediment | 9.3 | | 1 | | | | 0.16 | 2.7 | |
| Seawater | Marine sediment | 4.7 | | 1 | | | | 0.16 | 2.1 | |
| Seawater | Marine sediment | 4.6 | | 1 | | | | 0.16 | 2.0 | |
| Seawater | Marine sediment | 3.2 | | 1 | | | | 0.16 | 1.6 | |
| Seawater | Marine sediment | 3.5 | | 1 | | | | 0.16 | 1.5 | |
| Seawater | Marine sediment | 3.2 | | 1 | | | | 0.16 | 1.4 | |
| Seawater | Marine sediment | 2.2 | | 1 | | | | 0.16 | 1.2 | |
| Seawater | Marine sediment | 1.9 | | 1 | | | | 0.16 | 1.2 | |

Table A.2. Compilation of Ra distribution coefficients ($K_D$) in saline solution from literature. The data include the type of solution and sorbent materials, as well as the different variables analysed in the experimental settings (water:sorbent ratio, temperature, contact time, pH, salinity, cationic exchange capacity (CEC), and specific surface area).

| Solution | Sorbent material | Water:sorbent ratio | Temperature | Contact time | pH | Salinity | CEC | Specific surface Area | $K_D$ | Reference |
|---|---|---|---|---|---|---|---|---|---|---|
| | | (L kg$^{-1}$) | (ºC) | (h) | | | (meq 100 g$^{-1}$ ) | (m$^2$ g$^{-1}$) | (L kg$^{-1}$) | |
| Seawater | Marine sediment | 1.6 | | 1 | | | | 0.16 | 1.6 | |
| Seawater | Marine sediment | 1.2 | | 1 | | | | 0.16 | 1.7 | |
| Seawater | Marine sediment | 1.0 | | 1 | | | | 0.16 | 1.6 | |
| Seawater | Marine sediment | 0.9 | | 1 | | | | 0.16 | 1.2 | |
| Seawater | Marine sediment | 0.8 | | 1 | | | | 0.16 | 1.5 | |
| Seawater | Marine sediment | 0.7 | | 1 | | | | 0.16 | 1.3 | |
| Seawater | Marine sediment | 0.6 | | 1 | | | | 0.16 | 1.1 | |
| Seawater | Marine sediment | 0.6 | | 1 | | | | 0.16 | 1.3 | |
| Seawater | Marine sediment | 0.5 | | 1 | | | | 0.16 | 1.2 | |
| Seawater | Marine sediment | 0.4 | | 1 | | | | 0.16 | 1.0 | |
| Seawater | Marine sediment | 0.4 | | 1 | | | | 0.16 | 1.0 | |
| Seawater | Marine sediment | 0.4 | | 1 | | | | 0.16 | 0.9 | |
| Seawater | Marine sediment | 0.4 | | 1 | | | | 0.16 | 0.8 | |
| Seawater | Marine sediment | 0.4 | | 1 | | | | 0.16 | 0.9 | |
| Seawater | Marine sediment | | | 1 | | | | 0.04 | 1.8 | |
| Seawater | Marine sediment | | | 1 | | | | 0.10 | 1.5 | |
| Seawater | Marine sediment | | | 1 | | | | 0.09 | 1.0 | |
| Seawater | Marine sediment | | | 1 | | | | 0.10 | 0.9 | |
| Seawater | Marine sediment | | | 1 | | | | 0.22 | 2.2 | |
| Seawater | Marine sediment | | | 1 | | | | 0.26 | 3.0 | |
| Seawater | Marine sediment | | | 1 | | | | 0.39 | 3.5 | |
| Seawater | Marine sediment | | | 1 | | | | 0.73 | 3.2 | |
| Seawater | Marine sediment | | | 1 | | | | 0.75 | 2.9 | |
| Seawater | Marine sediment | | | 1 | | | | 0.95 | 3.9 | |
| Seawater | Marine sediment | | | 1 | | | | 2.24 | 6.5 | |
| Seawater | Marine sediment | | | 1 | | | | 5.18 | 15.6 | |
| Seawater | Marine sediment | | | 1 | | | | 10.31 | 19.5 | |
| Seawater | Ferrihydrite | | | 1 | | | | | 1560.9 | |
| Seawater | Lepidocrocite | | | 1 | | | | | 175.0 | |
| Seawater | Geothite | | | 1 | | | | | 19.6 | |
| Seawater | Hematite | | | 1 | | | | | 75.6 | |
| Seawater | Mn Fiber | | | 1 | 1.6 | | | | 70.5 | |
| Seawater | Mn Fiber | | | 1 | 5.0 | | | | 340.3 | |
| Seawater | Mn Fiber | | | 1 | 6.3 | | | | 857.0 | |
| Seawater | Mn Fiber | | | 1 | 6.3 | | | | 621.4 | |
| Seawater | Mn Fiber | | | 1 | 6.5 | | | | 411.8 | |
| Seawater | Mn Fiber | | | 1 | 6.9 | | | | 518.8 | |
| Seawater | Mn Fiber | | | 1 | 7.3 | | | | 394.7 | |
| Seawater | Mn Fiber | | | 1 | 7.3 | | | | 519.8 | |
| Seawater | Mn Fiber | | | 1 | 7.4 | | | | 716.7 | |
| Seawater | Mn Fiber | | | 1 | 7.9 | | | | 361.0 | |

Table A.2. Compilation of Ra distribution coefficients ($K_D$) in saline solution from literature. The data include the type of solution and sorbent materials, as well as the different variables analysed in the experimental settings (water:sorbent ratio, temperature, contact time, pH, salinity, cationic exchange capacity (CEC), and specific surface area).

| Solution | Sorbent material | Water:sorbent ratio (L kg$^{-1}$) | Temperature (ºC) | Contact time (h) | pH | Salinity | CEC (meq 100 g$^{-1}$ ) | Specific surface Area (m$^2$ g$^{-1}$) | $K_D$ (L kg$^{-1}$) | Reference |
|---|---|---|---|---|---|---|---|---|---|---|
| Seawater | Sand | | | 1 | 1.4 | | | 0.15 | 0.2 | |
| Seawater | Sand | | | 1 | 2.1 | | | 0.15 | 0.2 | |
| Seawater | Sand | | | 1 | 2.8 | | | 0.15 | 0.2 | |
| Seawater | Sand | | | 1 | 3.1 | | | 0.15 | 0.1 | |
| Seawater | Sand | | | 1 | 5.2 | | | 0.15 | 0.3 | |
| Seawater | Sand | | | 1 | 5.6 | | | 0.15 | 0.2 | |
| Seawater | Sand | | | 1 | 6.2 | | | 0.15 | 0.5 | |
| Seawater | Sand | | | 1 | 6.6 | | | 0.15 | 0.7 | |
| Seawater | Sand | | | 1 | 7.1 | | | 0.15 | 0.8 | |
| Seawater | Sand | | | 1 | 7.3 | | | 0.15 | 0.9 | |
| Seawater | Sand | | | 1 | 7.5 | | | 0.15 | 1.4 | |
| Seawater | Sand | | | 1 | 8.1 | | | 0.15 | 1.5 | |
| Seawater | Sand | | | 1 | 9.7 | | | 0.15 | 2.0 | |
| Seawater | Sand | | | 1 | 1.6 | | | 0.3 | 0.0 | |
| Seawater | Sand | | | 1 | 3.4 | | | 0.3 | 0.0 | |
| Seawater | Sand | | | 1 | 5.3 | | | 0.3 | 0.1 | |
| Seawater | Sand | | | 1 | 7.1 | | | 0.3 | 0.1 | |
| Seawater | Sand | | | 1 | 7.2 | | | 0.3 | 0.2 | |
| Seawater | Sand | | | 1 | 8.1 | | | 0.3 | 0.3 | |
| Seawater | Sand | | | 1 | 8.7 | | | 0.3 | 0.3 | |
| Seawater | Sand | | | 1 | 9.1 | | | 0.3 | 0.4 | |
| Seawater | Sand | | | 1 | 9.8 | | | 0.3 | 0.4 | |
| Seawater | Sand | | | 1 | 10.4 | | | 0.3 | 1.4 | |
| Seawater | Sand | | | 1 | 2.6 | | | 0.73 | 0.2 | |
| Seawater | Sand | | | 1 | 3.8 | | | 0.73 | 0.3 | |
| Seawater | Sand | | | 1 | 3.8 | | | 0.73 | 0.8 | |
| Seawater | Sand | | | 1 | 5.3 | | | 0.73 | 0.9 | |
| Seawater | Sand | | | 1 | 5.4 | | | 0.73 | 1.0 | |
| Seawater | Sand | | | 1 | 6.1 | | | 0.73 | 1.7 | |
| Seawater | Sand | | | 1 | 6.7 | | | 0.73 | 2.9 | |
| Seawater | Sand | | | 1 | 7.2 | | | 0.73 | 3.7 | |
| Seawater | Sand | | | 1 | 8.2 | | | 0.73 | 8.4 | |
| Seawater | Sand | | | 1 | 9.0 | | | 0.73 | 9.7 | |
| Groundwater | Sand | | | | 6.4 | 10.98 | | | 14.0 | Liu et al. (2019) |
| Groundwater | Sand | | | | 6.21 | 22.13 | | | 6.9 | |
| Groundwater | Sand | | | | 6.4 | 20.02 | | | 7.7 | |
| Groundwater | Sand | | | | 6.23 | 7.34 | | | 21.0 | |
| Groundwater | Sand | | | | 6.22 | 8.12 | | | 18.9 | |
| Groundwater | Sand | | | | 6.31 | 10.55 | | | 14.6 | |
| Groundwater | Sand | | | | N/A | N/A | | | 0.0 | |
| Groundwater | Sand | | | | 7.33 | 28.28 | | | 5.5 | |

Table A.2. Compilation of Ra distribution coefficients ($K_D$) in saline solution from literature. The data include the type of solution and sorbent materials, as well as the different variables analysed in the experimental settings (water:sorbent ratio, temperature, contact time, pH, salinity, cationic exchange capacity (CEC), and specific surface area).

| Solution | Sorbent material | Water:sorbent ratio (L kg$^{-1}$) | Temperature (ºC) | Contact time (h) | pH | Salinity | CEC (meq 100 g$^{-1}$ ) | Specific surface Area (m$^2$ g$^{-1}$) | $K_D$ (L kg$^{-1}$) | Reference |
|---|---|---|---|---|---|---|---|---|---|---|
| Groundwater | Sand | | | | 7.37 | 28.73 | | | 5.4 | |
| Groundwater | Sand | | | | 7.25 | 30.75 | | | 5.0 | |
| Groundwater | Sand | | | | 7.48 | 29.68 | | | 5.2 | |
| Groundwater | Sand | | | | 7.48 | 29.83 | | | 5.2 | |
| Groundwater | Sand | | | | 7.36 | 30.05 | | | 5.1 | |
| Groundwater | Sand | | | | 7.39 | 31.18 | | | 4.9 | |
| Groundwater | Sand | | | | 7.75 | 29.35 | | | 5.3 | |
| Groundwater | Sand | | | | 7.57 | 27.72 | | | 5.6 | |
| Groundwater | Sand | | | | 7.42 | 30.47 | | | 5.1 | |
| Groundwater | Sand | | | | 7.38 | 30.89 | | | 5.0 | |
| Groundwater | Sand | | | | 7.79 | 29.25 | | | 5.3 | |
| Groundwater | Sand | | | | 7.57 | 30.02 | | | 5.1 | |
| Groundwater | Sand | | | | 7.43 | 30.34 | | | 5.1 | |
| Groundwater | Sand | | | | 7.46 | 30.47 | | | 5.1 | |
| Groundwater | Sand | | | | 7.63 | 31.06 | | | 5.0 | |
| Groundwater | Sand | | | | 7.52 | 31.43 | | | 4.9 | |
| Groundwater | Sand | | | | 7.52 | 30.59 | | | 5.0 | |
| Groundwater | Sand | | | | 7.48 | 31.16 | | | 4.9 | |
| Groundwater | Sand | | | | 7.75 | 30.5 | | | 5.0 | |
| Groundwater | Sand | | | | 7.61 | 30.92 | | | 5.0 | |
| Groundwater | Sand | | | | 7.55 | 31.06 | | | 5.0 | |
| Groundwater | Sand | | | | 7.55 | 31.2 | | | 4.9 | |
| Groundwater | Sand | | | | 7.81 | 30.93 | | | 5.0 | |
| Groundwater | Sand | | | | 7.64 | 31.29 | | | 4.9 | |
| Groundwater | Sand | | | | 7.58 | 31.34 | | | 4.9 | |
| Groundwater | Sand | | | | 7.42 | 30.81 | | | 5.0 | |
| Groundwater | Sand | | | | 7.86 | 31.62 | | | 4.9 | |
| Groundwater | Sand | | | | 7.74 | 31.63 | | | 4.9 | |
| Groundwater | Sand | | | | 7.67 | 31.79 | | | 4.8 | |
| Groundwater | Sand | | | | 7.6 | 31.13 | | | 4.9 | |

## B) Appendix B. Simple solution for the advective transport model

Equation 5.9 can be rewritten in vector-matrix notation as:

$$\frac{\partial \boldsymbol{b}}{\partial \tau} = \boldsymbol{R\Lambda_1 b} + \boldsymbol{R\Lambda_2 f} \qquad \text{Equation B.1}$$

with

$$\boldsymbol{R} = \begin{pmatrix} R_1 & 0 & 0 & \cdots \\ 0 & R_2 & 0 & \cdots \\ 0 & 0 & R_3 & \cdots \\ \vdots & \vdots & \vdots & \ddots \end{pmatrix};\ \boldsymbol{\Lambda_1} = \begin{pmatrix} -\lambda_1 & 0 & 0 & \cdots \\ \lambda_2 & -\lambda_2 & 0 & \cdots \\ 0 & \lambda_3 & -\lambda_3 & \cdots \\ \vdots & \vdots & \vdots & \ddots \end{pmatrix};$$

Equation B.2

$$\boldsymbol{\Lambda_2} = \begin{pmatrix} \lambda_1 & 0 & 0 & \cdots \\ 0 & \lambda_2 & 0 & \cdots \\ 0 & 0 & \lambda_3 & \cdots \\ \vdots & \vdots & \vdots & \ddots \end{pmatrix};\ \boldsymbol{b} = \begin{pmatrix} b_1 \\ b_2 \\ b_3 \\ \vdots \end{pmatrix};\boldsymbol{f} = \begin{pmatrix} 0 \\ \mu_1 s_1 \\ \mu_2 s_2 \\ \vdots \end{pmatrix}$$

So,

$$\mathbf{R\Lambda_1} = \begin{pmatrix} -\lambda_1 \mathrm{R}_1 & 0 & 0 & \cdots \\ \lambda_2 \mathrm{R}_2 & -\lambda_2 \mathrm{R}_2 & 0 & \cdots \\ 0 & \lambda_2 \mathrm{R}_3 & -\lambda_2 \mathrm{R}_3 & \cdots \\ \vdots & \vdots & \vdots & \ddots \end{pmatrix};$$

Equation B.3

$$\mathbf{R\Lambda_2} = \begin{pmatrix} \lambda_1 \mathrm{R}_1 & 0 & 0 & \cdots \\ 0 & \lambda_2 \mathrm{R}_2 & 0 & \cdots \\ 0 & 0 & \lambda_2 \mathrm{R}_3 & \cdots \\ \vdots & \vdots & \vdots & \ddots \end{pmatrix}$$

The solution of Equation B.1 is:

$$\mathbf{b} = \exp(\tau \mathbf{R\Lambda_1})(\mathbf{b_0} - \mathbf{b}_\infty) + \mathbf{b}_\infty \qquad \text{Equation B.4}$$

$$\mathbf{b}_\infty = -\mathbf{\Lambda_1^{-1}\Lambda_2 f} \qquad \text{Equation B.5}$$

$$\exp(-\tau \mathbf{R\Lambda_1}) = \mathbf{P exp}(\tau \mathbf{P_D})\mathbf{P^{-1}} \qquad \text{Equation B.6}$$

where $\mathbf{b}_0$ and $\mathbf{b}_\infty$ contain the bulk activities at the inflow boundary and at bulk radioactive equilibrium, respectively; $\mathbf{P}$ is a matrix, whose columns are the eigenvectors of $\mathbf{R\Lambda_1}$. $\mathbf{P_D}$ is a diagonal matrix containing the eigenvalues of $\mathbf{R\Lambda_1}$. The following relation exists between these matrices (Meyer, 2000, chapter 7.2):

$$\mathbf{P^{-1}R\Lambda_1 P} = \mathbf{P_D} \qquad \text{Equation B.7}$$

As $\mathbf{R\Lambda_1}$is triangular (see Equation B.3), the eigenvalues are simply the diagonal values of $\mathbf{R\Lambda_1}$**.** That is,

$$\mathbf{exp}(\tau\mathbf{P_D}) = \begin{pmatrix} \mathbf{exp}(\tau\mathbf{P_{D,1}}) & 0 & 0 & \cdots \\ 0 & \mathbf{exp}(\tau\mathbf{P_{D,2}}) & 0 & \cdots \\ 0 & 0 & \mathbf{exp}(\tau\mathbf{P_{D,3}}) & \cdots \\ \vdots & \vdots & \vdots & \ddots \end{pmatrix} = \begin{pmatrix} \exp(-\tau\mathbf{R_1}\lambda_1) & 0 & 0 & \cdots \\ 0 & \exp(-\tau\mathbf{R_2}\lambda_2) & 0 & \cdots \\ 0 & 0 & \exp(-\tau\mathbf{R_3}\lambda_3) & \cdots \\ \vdots & \vdots & \vdots & \ddots \end{pmatrix} \quad \text{Equation B.8}$$

Given the triangular structure of matrix $\mathbf{R\Lambda_1}$(Equation B.3), matrix $\mathbf{P}$ becomes:

$$P = \begin{pmatrix} 1 & 0 & 0 & \cdots \\ \frac{\lambda_2 R_2}{(\lambda_2 R_2 - \lambda_1 R_1)} & 1 & 0 & \cdots \\ \frac{\lambda_2 R_2 \lambda_3 R_3}{(\lambda_2 R_2 - \lambda_1 R_1)(\lambda_3 R_3 - \lambda_1 R_1)} & \frac{\lambda_3 R_3}{(\lambda_3 R_3 - \lambda_2 R_2)} & 1 & \cdots \\ \frac{\lambda_2 R_2 \lambda_3 R_3 \lambda_4 R_4}{(\lambda_2 R_2 - \lambda_1 R_1)(\lambda_3 R_3 - \lambda_1 R_1)(\lambda_4 R_4 - \lambda_1 R_1)} & \frac{\lambda_3 R_3 \lambda_4 R_4}{(\lambda_3 R_3 - \lambda_2 R_2)(\lambda_4 R_4 - \lambda_2 R_2)} & \frac{\lambda_4 R_4}{(\lambda_4 R_4 - \lambda_3 R_3)} & \cdots \\ \vdots & \vdots & \vdots & \ddots \end{pmatrix} \quad \text{Equation B.9}$$

The solution is very similar to that of Bateman (1910), but including the retardation factor. Here matrix-vector notation is used, for reasons of mathematical elegance.

# C) Appendix C. Maresme County and experimental site of Argentona

## C1) Study site

Maresme County is a coastal region located to the NE of the city of Barcelona (Spain, western Mediterranean Sea) that extends from the Catalan Littoral Mountain Range to the Mediterranean Sea (Figure C.1). The county has a population density of ca. 1100 hab·km$^{-2}$, and is highly anthropized, with 15% agricultural and 30% urban land use (Rufí-Salís et al., 2019). The geomorphology of the area is structurally associated with the fracturing and sinking of blocks (NW-SE direction), which developed in a set of stream valleys (Catalan Water Agency, 2010). The geology of these valleys is dominated by Quaternary detrital sediments that constitute layers of gravels, sands, and clays, which result from chemical weathering and the dragging of granite materials through torrential courses. These Quaternary deposits constitute different aquifers corresponding with each stream valley (Figure C.1). Simultaneously, each stream valley forms an ephemeral stream. In Maresme County there are around 40 ephemeral streams, which represents a density of 1 ephemeral stream per kilometer of coastline. Annual precipitation in the area ranges from 350 to 930 mm y$^{-1}$ (2015 to 2020) and is mainly governed by EPE occurring in the autumn and spring seasons. Precipitation events with >75 mm d$^{-1}$ (corresponding to the 99$^{th}$ wet-day percentile) are here considered as extreme precipitation events (EPE) (Pendergrass and Knutti, 2018) and have a recurrence of ca. 13 months. In this area most of these streams are hydraulically disconnected from their alluvial aquifers and, therefore, surface runoff takes place only after the most significant rain events, with floods occurring in a period of hours after the EPE. The nature of tides in the Maresme region is semidiurnal, with an amplitude in the order of a few centimeters (~20 – 40 cm). The bathymetry of the Barcelona - Maresme continental shelf is dominated by steps and ridges, with moderate slopes (1.1°), and an average shelf width of 13 km (Durán et al., 2014).

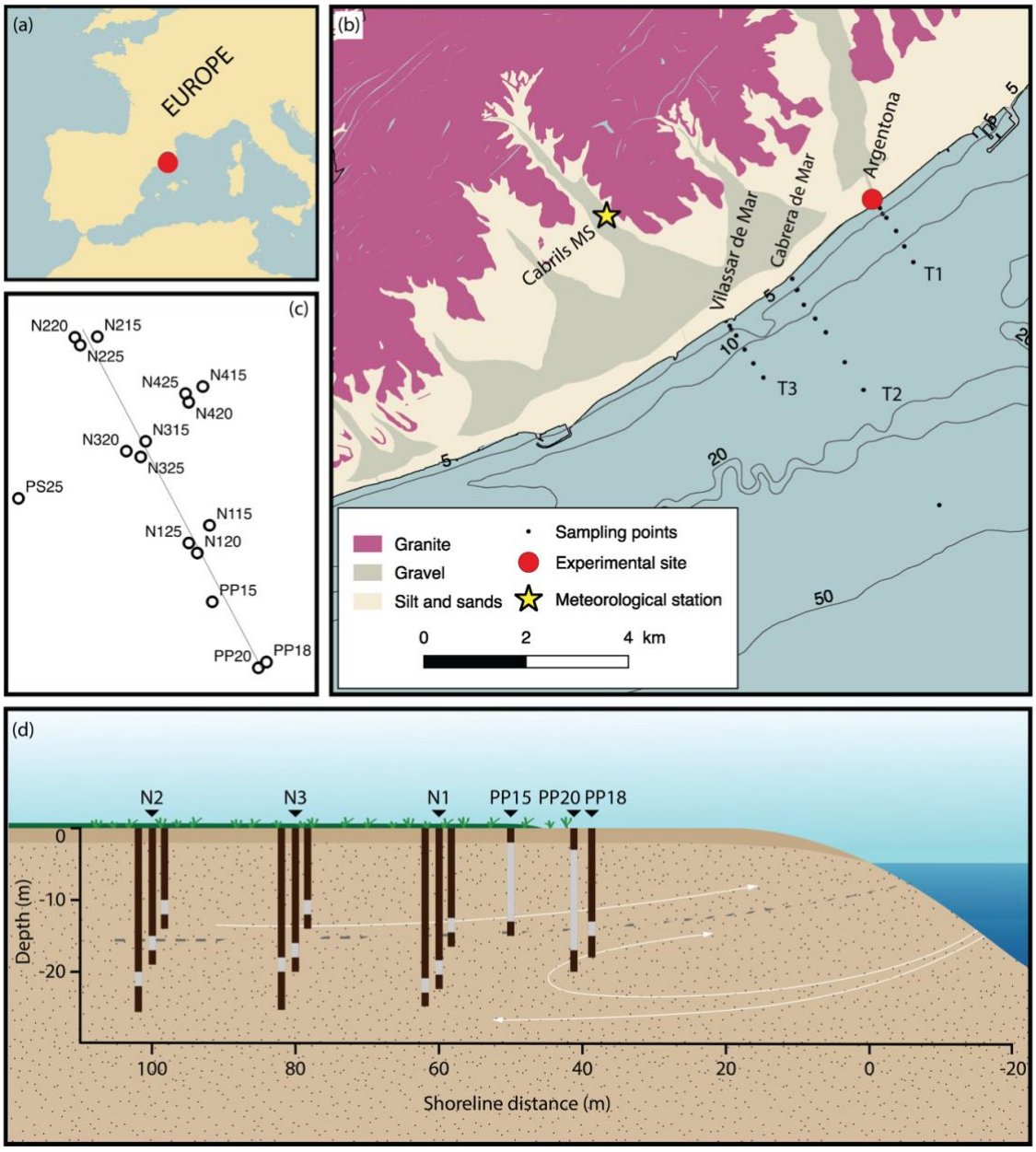


Figure C.1. Study site map. (a) Location map of Maresme County, (b) geological description, bathymetry, and sampling stations, (c) location map of the Medistraes site piezometers, and (d) schematic diagram of the piezometers and their screening sections within the perpendicular transect of the experimental site of Medistraes. T1, T2, and T3 are the offshore transects associated with the ephemeral streams of Argentona, Cabrera de Mar, and Vilassar de Mar, respectively.

The Argentona experimental site, located in the coastal alluvial aquifer of the Argentona ephemeral stream, consists of 16 piezometers distributed along a perpendicular and a parallel transect to the coastline, with groundwater sampling depths ranging from 15 to 25 m (see Palacios et al., 2019 for more details about the experimental site). The geology of the aquifer is

dominated by detrital quaternary sediments that constitute layers of gravels, sands, and clays which are the product of chemical weathering and rock fracture of the granitic. Fresh groundwater flows towards the sea in the shallow part of the aquifer (the upper ~15 m), whereas the deep aquifer area (deeper than 20 m) is influenced by seawater intrusion, as inferred from the application of direct measurement at the piezometers and electrical resistivity tomography (Palacios et al., 2019). Most of the piezometers are gathered in nests (N1, N3, N2) of three piezometers with screening intervals of 2-m, located at different depths (15, 20, and 25 m, approximately) (Figure C.1). The three remaining piezometers (PP-15, PP-20, and PP-18) are the closest to the sea, with sampling depths of 15, 20, and 18 m, respectively.

### C2) Radium and radon isotopes in the Argentona experimental site

The results of $^{222}$Rn and Ra isotopes activities against the salinity of each piezometer for different samplings in the Argentona experimental site are shown in Figure C.2. Radium activities spanned a wide range from 10 to 940, 10 to 550, and 1 to 50 Bq m$^{-3}$ for $^{224}$Ra, $^{228}$Ra, and $^{226}$Ra, respectively. These variations in Ra concentrations are mainly associated with differences in the geological context and in the groundwater salinity of each piezometer (Figure C.2). The shallow aquifer <15 m presents the lowest Ra concentrations (e.g., 10 to 50 Bq m$^{-3}$ of $^{224}$Ra) in agreement with the lowest salinity (0.5 to 2.2). In contrast, the intermediate and deep piezometers presented higher activities (e.g., 60 to 940 Bq m$^{-3}$ of $^{224}$Ra) correlating with the higher salinities (4.4 to 33.9) of the bottom aquifer. Radon activities were 1 to 3 orders of magnitude larger than Ra activities ranging from $5{\cdot}10^3$ to $45{\cdot}10^3$ Bq m$^{-3}$. Nevertheless, aside from the groundwater samples collected from deeper piezometers (≥ 20 m) that presented higher Rn concentrations ($20{\cdot}10^3$ to $45{\cdot}10^3$ Bq m$^{-3}$), most of the groundwater samples presented relatively constant $^{222}$Rn concentrations ($5{\cdot}10^3$ - $20{\cdot}10^3$ Bq m$^{-3}$; Figure C.2). The ARs of $^{224}$Ra/$^{228}$Ra ranged from 1.1 to 1.4 for the shallow piezometers and from 1.5 to 8.4 for the deeper piezometers (> 15 m depth). The ARs of $^{222}$Rn/$^{226}$Ra ranged from 2,700 to 5,900 for shallow piezometers and 700 to 4,500 for deeper piezometers (Table C.1). The retardation factor of Ra for the two selected piezometers (N1-20 and N2-15) (Table C.1), which were determined by reproducing the groundwater salinities measured at the site, are 170, for the sample collected at depth 20 in the nest N1 (piezometer N1-20), which is influenced by saline groundwater, and 2,500 for the sediment sample collected

at the freshwater zone at nest N2 (<15 m). These results are in concordance with the typical retardation factors of Ra for saline and fresh groundwater, respectively (Beck and Cochran, 2013; Michael et al., 2011) and within the ranges reported in the extensive review of Appendix A (1 - $10^5$).

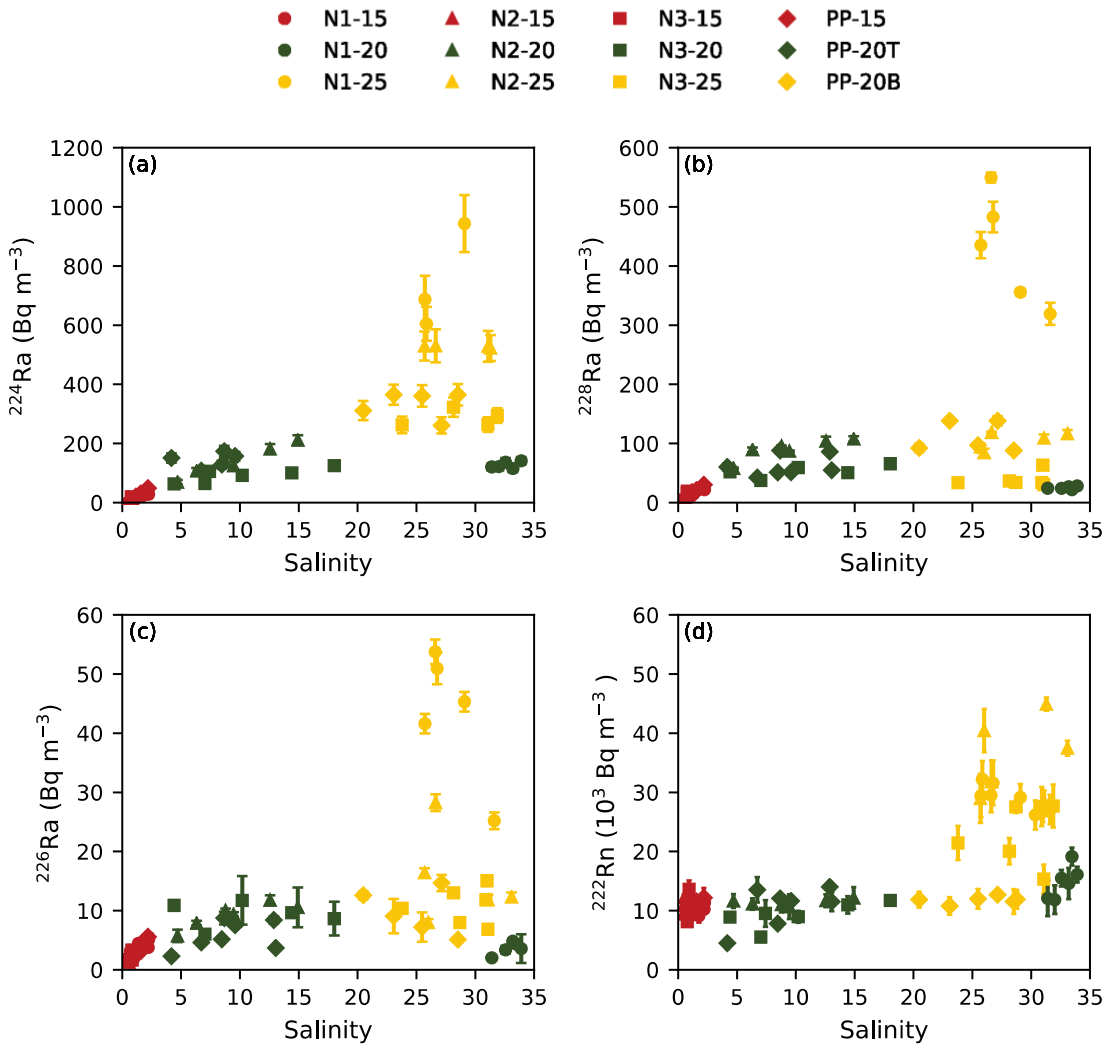


Figure C.2. Activities of (a) $^{224}$Ra, (b) $^{228}$Ra, (c) $^{226}$Ra, and (d) $^{222}$Rn against salinity for groundwater samples collected from the different piezometers and sampling campaigns. Red, green and blue colors indicate shallow (<15 m), intermediate, and deep (>20 m) piezometers, respectively.

Table C.1. Distance from the shoreline, depth, screened interval, salinity, ARs of $^{224}Ra/^{228}Ra$ and $^{222}Rn/^{226}Ra$, and retardation factor of Ra from the piezometers located in the perpendicular transect to the shoreline of the Argentona ephemeral stream experimental site.

| Piezometer name | Nest | Shoreline distance | Screened interval | Salinity | $^{224}Ra/^{228}Ra$ | $^{222}Rn/^{226}Ra$ | $R_{Ra}$ |
|---|---|---|---|---|---|---|---|
| | | m | m | | | $10^3$ | |
| N1-15 | N1 | 62.9 | 12.5-14.5 | 1.7 ± 0.4 | 1.2 ± 0.1 | 2.7 ± 0.7 | n.a |
| N1-20* | N1 | 60.2 | 18.4-20.4 | 32.4 ± 1.3 | 5.0 ± 0.5 | 4.5 ± 1.0 | 170 ± 30 |
| N1-25 | N1 | 62.3 | 20.9-22.8 | 28.0 ± 2.3 | 2.1 ± 0.8 | 0.7 ± 0.2 | n.a |
| N3-15 | N3 | 80.1 | 10.0-12.0 | 0.8 ± 0.1 | 1.1 ± 0.2 | 4.3 ± 1.2 | n.a |
| N3-20 | N3 | 79.7 | 16.0-18.0 | 9.7 ± 4.9 | 1.7 ± 0.3 | 1.0 ± 0.2 | n.a |
| N3-25 | N3 | 78.1 | 18.0-20.0 | 29.4 ± 2.8 | 8.4 ± 0.6 | 2.2 ± 0.7 | n.a |
| N2-15** | N2 | 97.9 | 10.0-12.0 | 0.5 ± 0.1 | 1.1 ± 0.2 | 5.9 ± 2.3 | 2,500 ± 200 |
| N2-20 | N2 | 99.8 | 15.0-17.0 | 9.5 ± 3.8 | 1.5 ± 0.3 | 1.3 ± 0.4 | n.a |
| N2-25 | N2 | 98.3 | 20.0-22.0 | 29.0 ± 3.2 | 5.0 ± 0.6 | 2.7 ± 1.5 | n.a |
| PP-15 | | 52.4 | 2.0-13.0 | 1.6 ± 0.5 | 1.4 ± 0.2 | 3.1 ± 0.8 | n.a |
| PP-20B | | 39.5 | 3.0-18.0 | 25.6 ± 3.3 | 3.1 ± 0.9 | 1.4 ± 0.6 | n.a |
| PP-20T | | 39.5 | 3.0-18.0 | 9.1 ±3.2 | 2.5 ± 0.4 | 2.0 ± 0.7 | n.a |
| Seawater | | -5 | - | 37.9 | 3.0 ± 0.3 | n.a. | |

n.a: Not analyzed. *Saline-outflow. **Fresh-outflow.

### C3) Nutrients in the Argentona experimental site

The concentrations of nutrients in groundwaters from the experimental site of the Argentona ephemeral stream ranged from 10 to 1070 µM for $NO_3^-$, 0.1 to 3.9 for $NO_2^-$, 0.3 to 40.1 for $NH_4^+$, 0.8 to 10.1 for $PO_4^{3-}$, and 50 to 230 for $SiO_4^{2-}$ (Figure C.3). Nitrate ($NO_3^-$) and silica ($SiO_4^{2-}$) presented a similar pattern, with maximum concentrations in low salinity (Sal < 10) samples and a downward trend with increasing groundwater salinity. Conversely, the concentrations of nitrite ($NO_2^-$), phosphate ($PO_4^{3-}$), and ammonia ($NH_4^+$) were relatively low for most of the groundwater samples, except for those collected at the shallow piezometers for nitrite, intermediate for phosphate, and deep for ammonia (Figure C.3).

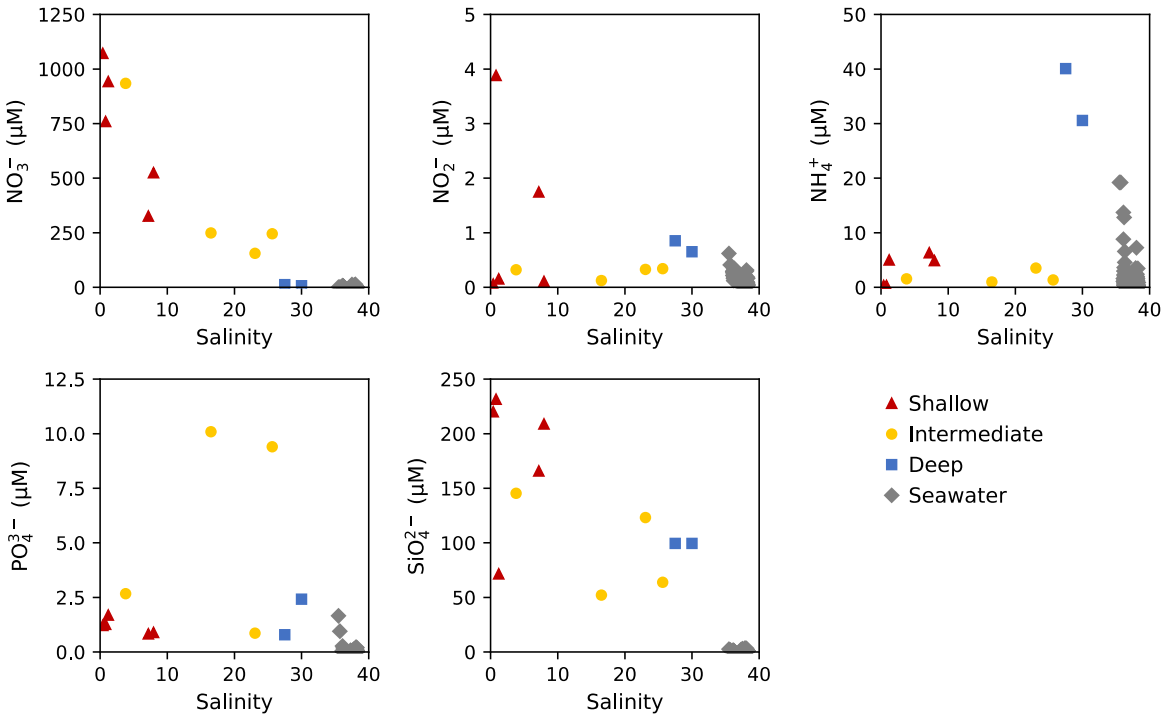


Figure C.3. Concentrations of nitrate ($\mathbf{NO_3^-}$), nitrite ($\mathbf{NO_2^-}$), ammonia ($\mathbf{NH_4^+}$), phosphate ($\mathbf{PO_4^{3-}}$), and silica ($\mathbf{SiO_4^{2-}}$) in groundwater and seawater samples collected at the experimental site of the Argentona ephemeral stream and at the different coastal seawater stations during the samplings from October 2019 and March 2020. Red, yellow, and blue indicate the depth of the groundwater samples (shallow, <15 m; intermediate, from 15 to 20 m; and deep, >20 m, respectively) and gray color represent the seawater samples.

# D) Appendix D. Submarine groundwater discharge in the Maresme County

## D1) SGD and nutrient fluxes via Ra mass balance

In this appendix, we develop the methodology used for determining the SGD and associated nutrient fluxes to the coastal ocean. This includes the definition of the conceptual model and the discussion of the model assumptions used in the calculations.

### D1.1) Ra mass balance

The magnitude of SGD and its associated nutrient fluxes are quantified in this study by using Ra isotopes, which is one of the most commonly applied techniques (Taniguchi et al., 2019). Whilst single isotopes can be used for quantifying SGD driven by single pathways, the combination of different isotopes is instrumental in discriminating SGD in sites with multiple pathways (Charette, 2007; Rodellas et al., 2017; Tamborski et al., 2017b). In this study, Ra isotopes are used for discriminating and quantifying both the fluxes of terrestrial and marine SGD. Whilst terrestrial SGD represents a net input of water to the ocean, marine SGD comprises disparate discharge processes solely involving the circulation of seawater through permeable sediments or the coastal aquifer (i.e., porewater exchange, shoreface circulation of seawater, seasonal exchange of seawater; Michael et al., 2011). A steady-state mass balance of short-lived $^{224}$Ra ($T_{1/2}$ = 3.66 d) and long-lived $^{228}$Ra ($T_{1/2}$ = 5.75 y) isotopes was constructed as follows:

$$\begin{aligned} F_{TSGD} \cdot {}^{228}Ra_{TSGD} + F_{MSGD} \cdot {}^{228}Ra_{MSGD} &= \frac{I_{ex-Ra228}}{T_F} + I_{Ra228} \cdot \lambda_{Ra228} \\ F_{TSGD} \cdot {}^{224}Ra_{TSGD} + F_{MSGD} \cdot {}^{224}Ra_{MSGD} &= \frac{I_{ex-Ra224}}{T_F} + I_{Ra224} \cdot \lambda_{Ra224} \end{aligned} \quad \text{Equation D.1}$$

The two terms on the right-hand side of Equation D1 represent the Ra outputs and include the offshore exchange of Ra, due to the mixing between coastal and open ocean waters, and Ra decay. The terms $I$ and $I_{ex}$ refer to the mean inventories [Bq m$^{-1}$] of Ra and excess Ra (inventory of excess Ra concentrations in coastal waters relative to open ocean), respectively, $T_F$ is the Ra flushing time [d], and $\lambda$ is the Ra decay constant [d$^{-1}$]. The mean Ra inventories were determined by averaging the activity (or excess activity) [Bq m$^{-3}$] of Ra at each station normalized by depth and distance to the shore. The normalization was made by integrating the rectangular trapezoid area confined within the distance between two subsequent stations and their respective depth.

The two terms on the right-hand-side of Equation D1 account for Ra inputs to the study site, which are supplied via terrestrial (combined discharge of meteoric groundwater and density-driven circulated seawater) and marine (processes solely involving the circulation of seawater through permeable sediments; beach-face circulation, porewater exchange) SGD [$F_{Ra}$; Bq $m^{-1}$ $d^{-1}$]. The activities [Bq $m^{-3}$] of Ra in the discharging groundwater ($Ra_{TSGD}$ and $Ra_{MSGD}$; Ra endmember) were used to convert the Ra flux of both isotopes concurrently, to a coastline-normalized volumetric flow [$m^3$ $km^{-1}$ $d^{-1}$] for each of the SGD pathways (Terrestrial SGD, $F_{TSGD}$ and Marine SGD, $F_{MSGD}$). The terms and values used for the Ra mass balance for each sampling are shown in Table D1.

Table D.1. Definition of terms, values and units used for the Ra mass balance for each sampling (P1, P2 and BF). Data in brackets represent the interquartile range (1st and 3rd quartile).

| **Term** | **Definition** | **Values** | | | **Units** |
|---|---|---|---|---|---|
| | | **P1** | **P2** | **BF** | |
| $I_{Ra224}$ | $^{224}$Ra inventory | 113±15 | 26±2 | 31±9 | $\cdot 10^3$ Bq·$m^{-1}$ |
| $I_{ex-Ra224}$ | $^{224}$Ra excess inventory | 98±15 | 23±2 | 28±9 | $\cdot 10^3$ Bq·$m^{-1}$ |
| $I_{Ra228}$ | $^{228}$Ra inventory | 46±3 | 11±2 | 9±3 | $\cdot 10^3$ Bq·$m^{-1}$ |
| $I_{ex-Ra228}$ | $^{228}$Ra excess inventory | 41±3 | 10±2 | 8±3 | $\cdot 10^3$ Bq·$m^{-1}$ |
| $F_{Ra-224}$*[1] | $^{224}$Ra flux | 62±9 | 9±1 | 11±4 | $\cdot 10^3$ Bq·$m^{-1}$·$d^{-1}$ |
| $F_{Ra-228}$*[1] | $^{228}$Ra flux | 16.8±1.3 | 1.8±0.4 | 1.6±0.5 | $\cdot 10^3$ Bq·$m^{-1}$·$d^{-1}$ |
| $F_{Ra-224}/F_{Ra-228}$ | $^{224}$Ra/$^{228}$Ra flux ratio | 3.7±0.3 | 5.2±1.2 | 7.6±2.7 | - |
| $T_F$*[2] | Ra flushing time | 2.4±0.9 | 5.6±1.9 | 5.0±1.7 | d |
| ***Unknowns*** | | | | | |
| $F_{FSGD}$ | Fresh SGD flow | 380 (235 - 660) | 25 (10 - 55) | 45 (15 - 75) | $\cdot 10^3$ $m^3$·$km^{-1}$·$d^{-1}$ |
| $F_{RSGD}$ | Recirculated SGD flow | 125 (90 - 225) | 20 (15 - 30) | 25 (20 - 30) | $\cdot 10^3$ $m^3$·$km^{-1}$·$d^{-1}$ |

*[1] Flux of Ra supplied by terrestrial and marine SGD, left-hand side of Equation D1
*[2] Radium fluxing time determined as water apparent age following Moore (2000)

## D1.2) Model assumptions and considerations

### D1.2.1) Sources and sinks of Ra

The proposed model for quantifying the Ra flux to the sea assumes that terrestrial and marine groundwater discharge are the only sources of Ra at the study site (Equation D.1). Diffusive fluxes of Ra from sediments were considered negligible, due to the presence of coarse-grained sands with low specific surface area (Luek and Beck, 2014) and are assumed to represent low (10%) inputs compared to the total Ra inputs (Beck et al., 2007; Garcia-Orellana et al., 2014). Ra inputs from surface water were also discarded for the sampling conducted in March 2020 (BF) due to the total absence of runoff during the sampling period. In October 2019, 4 days before the first sampling conducted at the study site, runoff occurred in direct response to an EPE (~90 mm). However, considering the flushing time of Ra isotopes in the coastal system (see D.1.2.2), the Ra delivered by this punctual runoff may have decreased by >90% for the first sampling (P1) and by >99% for the second sampling (P2), due to decay and mixing with offshore waters. It is thus assumed that runoff for these samplings represents a minor source of Ra at the study site relative to that from SGD. Atmospheric deposition was discarded as a major source of Ra since its contribution in small-scale study sites is often <<1%. Production of Ra from dissolved Th was implicitly included by reporting the activities of Ra isotopes as 'excess' Ra activities (activities non-supported by their progenitors). The decay of Ra and the exchange with offshore waters were considered as the major sinks of Ra. The decay was assessed via the Ra inventories at in the study site and the offshore exchange, by evaluating the flushing time of Ra ($T_F$).

### D1.2.2) Radium flushing time

The flushing time of Ra ($T_F$) is a parameter that describes the transport of Ra in surface water bodies due to advection and dispersion processes (Monsen et al., 2002). In Ra mass balances, this parameter is fundamental for evaluating the exchange of Ra between coastal and offshore waters. In this work, rather than evaluating Ra flushing times, we used $^{224}Ra/^{228}Ra$ of coastal and offshore waters (1,000 m from coastline) to determine the water apparent age ($T_W$) (Moore, 2000). The water apparent age is a good proxy for temporal scales of advective and mixing processes occurring at the study site. Coastal waters in Maresme County presented

$^{224}Ra/^{228}Ra$ activity ratios ranging from 1.6 to 2.9 times higher than those of offshore waters, which led to seawater apparent ages of 2.4±0.9, 5.6±1.9, and 5.0±1.7 days for the first, second, and third sampling, respectively. The lower seawater residence time of the first sampling is coherent with the oceanographic conditions (e.g., higher winds, waves and currents that enhanced advection and exchange with offshore waters) linked to the extreme precipitation event occurring 4 days before (see Figure **6**.**1**).

### D1.2.3) Steady state conditions

Steady state conditions (i.e., tracer inventories do not vary with time; $da/(dt \cdot V) = 0$) are often assumed in Ra mass balances (e.g., Beck et al., 2008; Rodellas et al., 2017). This assumption implies that Ra inputs and outputs are balanced for a time period equivalent to the tracer residence time in the system (Rodellas et al., 2021). In Maresme County, the tracer residence time ranged from 1.6 to 2.6 days for $^{224}Ra$ and from 2.4 to 5.6 days for $^{228}Ra$. The tracer residence time can be estimated by dividing the radium inventory in surface waters by the sum of all losses (i.e., radioactive decay and exchange with offshore waters) (Rodellas et al., 2021). The assumption of steady state may therefore not be valid due to the significant difference between Ra activities from the first and second samplings (P1 and P2; Figure **6**.**2**), which were carried out only 4 days apart. However, assuming steady state conditions instead of a continuous decrease of activities in coastal waters ($-da/dt$) (the pattern that was observed in the EPE from 2019; Figure **6**.**2**), results in conservative estimates of SGD induced by EPE.

### D1.2.4) Endmember selection

Due to the large spatial variability of Ra isotopes in the groundwater activity at the experimental site of Argentona, constraining the Ra activity of the SGD endmember for both the terrestrial and marine components is particularly difficult. To overcome this limitation, we used the activity ratio of $^{224}Ra/^{228}Ra$ measured in the potential groundwater endmembers and the coastal ocean, which can help in identifying the most likely endmembers. Endmembers were selected according to the following conditions: (1) the selection of the terrestrial Ra endmembers ($Ra_{TSGD}$) was constrained to groundwater samples with low salinities (Sal < 5); and (2) the $^{224}Ra/^{228}Ra$ activity ratios of both endmembers must satisfy the following equation:

$$\frac{^{224}Ra_{TSGD}}{^{228}Ra_{TSGD}} < \frac{F_{Ra224}}{F_{Ra228}} < \frac{^{224}Ra_{MSGD}}{^{228}Ra_{MSGD}}, \quad \text{Equation D.2}$$

where $F_{Ra-224}/F_{Ra-228}$ is the ratio between the total fluxes of $^{224}$Ra and $^{228}$Ra to the coastal ocean for each of the three samplings. A terrestrial and marine SGD was determined for each of any possible combinations between terrestrial and marine Ra endmembers that satisfied the above-mentioned conditions, and we reported the final SGD fluxes as the median value and the interquartile range. Conservative fluxes of nutrients were computed by multiplying the minimum concentrations of nutrients within the terrestrial and marine endmembers (discriminated by conditions 1 and 2), and the median ($\pm$ interquartile range) of each SGD component (terrestrial and marine).

### D2) Darcy's law calculations

The relative significance of EPE in annual SGD estimates derived from the Ra mass balance was compared with Darcy flux estimates ($Q = -k_h \cdot i$). For these calculations, hydraulic conductivity ($k_h$ [m s$^{-1}$]) was assumed to be in the order of $10^{-3}$ m s$^{-1}$ (characteristic of clean sands) in the range of local studies (personal communication T. Goyetche and L. Del Val). The hydraulic gradient was determined as the difference between mean sea level (MSL) data and groundwater level data acquired from a CTD diver deployed in a piezometric well at the experimental site of the Argentona ephemeral stream (N3-15, 80 m from the shoreline). Absolute Darcy flux results (Figure D.1) should only be taken as indicative. In fact, the relative variation of Darcy flux during EPE can be used as a proxy for groundwater discharge. Results indicate that the EPE from October 2019, December 2019, and January 2020 represented 2, 4, and 6%, respectively, of the annual groundwater discharge. The relative significance of EPE derived from these calculations is slightly lower than those obtained from the Ra mass balance. This discrepancy can be associated with the different discharge processes that each method captures. Whilst Ra mass balance enables the quantification of processes with different spatiotemporal scales and different compositions of groundwater (e.g., terrestrial groundwater discharge, porewater exchange), Darcy's law only captures the discharge of meteoric or brackish groundwater due to the hydraulic gradient at the shallowest aquifer.

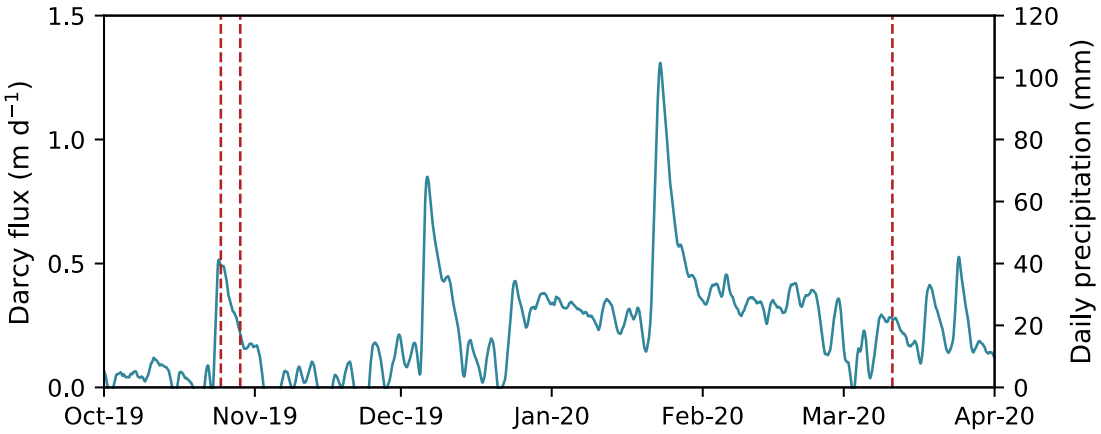


Figure D.1. Temporal evolution of Darcy flux from October 2019 to April 2020 at the experimental site of the Argentona ephemeral stream. Red lines indicate the groundwater and seawater samplings performed at the study site (P1, P2, and BF) and grey bands indicate the major precipitation events of October 2019, December 2019, and January 2020.

# References

Abarca, E., Prabhakar Clement, T., 2009. A novel approach for characterizing the mixing zone of a saltwater wedge. Geophys. Res. Lett. 36, 1–5. https://doi.org/10.1029/2008GL036995

Adyasari, D., Montiel, D., Mortazavi, B., Dimova, N., 2021. Storm-Driven Fresh Submarine Groundwater Discharge and Nutrient Fluxes From a Barrier Island. Front. Mar. Sci. 8, 1–17. https://doi.org/10.3389/fmars.2021.679010

Alorda-Kleinglass, A., Ruiz-Mallén, I., Diego-Feliu, M., Rodellas, V., Bruach-Menchén, J.M., Garcia-Orellana, J., 2021. The social implications of Submarine Groundwater Discharge from an Ecosystem Services perspective: A systematic review. Earth-Science Rev. 221, 103742. https://doi.org/10.1016/j.earscirev.2021.103742

Álvarez-Góngora, C., Herrera-Silveira, J.A., 2006. Variations of phytoplankton community structure related to water quality trends in a tropical karstic coastal zone. Mar. Pollut. Bull. 52, 48–60. https://doi.org/10.1016/j.marpolbul.2005.08.006

Amato, D.W., Bishop, J.M., Glenn, C.R., Dulai, H., Smith, C.M., 2016. Impact of submarine groundwater discharge on marine water quality and reef biota of Maui. PLoS One 11, 1–28. https://doi.org/10.1371/journal.pone.0165825

Andrisoa, A., Lartaud, F., Rodellas, V., Neveu, I., Stieglitz, T.C., 2019a. Enhanced Growth Rates of the Mediterranean Mussel in a Coastal Lagoon Driven by Groundwater Inflow. Front. Mar. Sci. 6, 1–14. https://doi.org/10.3389/fmars.2019.00753

Andrisoa, A., Stieglitz, T.C., Rodellas, V., Raimbault, P., 2019b. Primary production in coastal lagoons supported by groundwater discharge and porewater fluxes inferred from nitrogen and carbon isotope signatures. Mar. Chem. 210, 48–60. https://doi.org/10.1016/j.marchem.2019.03.003

Anschutz, P., Smith, T., Mouret, A., Deborde, J., Bujan, S., Poirier, D., Lecroart, P., 2009. Tidal sands as biogeochemical reactors. Estuar. Coast. Shelf Sci. 84, 84–90. https://doi.org/10.1016/j.ecss.2009.06.015

Anwar, N., Robinson, C.E., Barry, D.A., 2014. Influence of tides and waves on the fate of nutrients in a nearshore aquifer: Numerical simulations. Adv. Water Resour. 73, 203–213. https://doi.org/10.1016/j.advwatres.2014.08.015

Assumus, A., 1995. Early History of X Rays. Beam Line 10–24.

Aston, F.W., Baxter, G.P., Brauner, B., Debierne, A., Leduc, A., Richards, T.W., Soddy, F., Urbain, G., 1923. Report of the International Committee on Chemical Elements: 1923. J. Am. Chem. Soc. 45, 867–874. https://doi.org/10.1021/ja01657a001

Bakhtyar, R., Barry, D.A., Brovelli, A., 2012. Numerical experiments on interactions between wave motion and variable-density coastal aquifers. Coast. Eng. 60, 95–108. https://doi.org/10.1016/j.coastaleng.2011.09.001

Barberio, M.D., Gori, F., Barbieri, M., Billi, A., Devoti, R., Doglioni, C., Petitta, M., Riguzzi, F., Rusi, S., 2018. Diurnal and semidiurnal cyclicity of Radon (222Rn) in groundwater, Giardino Spring, Central Apennines, Italy. Water (Switzerland) 10, 1–11. https://doi.org/10.3390/w10091276

Bateman, H., 1910. Solution of a system of differential equations occurring in the theory of radioactive transformations. Math. Proc. Cambridge Philos. Soc. 423–427.

Bear, J., 1972. Dynamics of Fluids in Porous Media, Dynamics of Fluids in Porous Media. American Elsevier Publishing Company, New York.

Beck, A.J., Cochran, J.K., Sañudo-Wilhelmy, S.A., 2009. Temporal trends of dissolved trace metals in jamaica bay, ny: Importance of wastewater input and submarine groundwater discharge in an urban estuary. Estuaries and Coasts 32, 535–550. https://doi.org/10.1007/s12237-009-9140-5

Beck, A.J., Cochran, M.A., 2013. Controls on solid-solution partitioning of radium in saturated marine sands. Mar. Chem. 156, 38–48. https://doi.org/10.1016/j.marchem.2013.01.008

Beck, A.J., Rapaglia, J.P., Cochran, J.K., Bokuniewicz, H.J., 2007. Radium mass-balance in Jamaica Bay, NY: Evidence for a substantial flux of submarine groundwater. Mar. Chem. 106, 419–441. https://doi.org/10.1016/j.marchem.2007.03.008

Beck, A.J., Rapaglia, J.P., Cochran, J.K., Bokuniewicz, H.J., Yang, S., 2008. Submarine groundwater discharge to Great South Bay, NY, estimated using Ra isotopes. Mar. Chem. 109, 279–291. https://doi.org/10.1016/j.marchem.2007.07.011

Beck, M., Reckhardt, A., Amelsberg, J., Bartholomä, A., Brumsack, H.J., Cypionka, H., Dittmar, T., Engelen, B., Greskowiak, J., Hillebrand, H., Holtappels, M., Neuholz, R., Köster, J., Kuypers, M.M.M., Massmann, G., Meier, D., Niggemann, J., Paffrath, R., Pahnke, K., Rovo, S., Striebel, M., Vandieken, V., Wehrmann, A., Zielinski, O., 2017. The drivers of biogeochemistry in beach ecosystems: A cross-shore transect from the dunes to the low-water line. Mar. Chem. 190, 35–50. https://doi.org/10.1016/j.marchem.2017.01.001

Bejannin, S., van Beek, P., Stieglitz, T., Souhaut, M., Tamborski, J.J., 2017. Combining airborne thermal infrared images and radium isotopes to study submarine groundwater discharge along the French Mediterranean coastline. J. Hydrol. Reg. Stud. 13, 72–90. https://doi.org/10.1016/j.ejrh.2017.08.001

Belanger, T. V., Montgomery, M.T., 1992. Seepage meter errors. Limnol. Oceanogr. 37, 1787–1795. https://doi.org/10.4319/lo.1992.37.8.1787

Beneš, P., 1982. Physico-chemical forms and migration in continental waters of radium from uranium mining and milling. Environ. Migr. long-lived radionuclides. Proc. Symp. Knoxville, July 1981, (International At. Energy Agency, Vienna, STI/PUB/597) 3–23.

Beneš, P., Borovec, Z., Strejc, P., 1985. Interaction of radium with freshwater sediments and their mineral components - II. Kaolinite and montmorillonite. J. Radioanal. Nucl. Chem. Artic. 89, 339–351. https://doi.org/10.1007/BF02040598

Beneš, P., Strejc, P., Lukavec, Z., 1984. Interaction of radium with freshwater sediments and their mineral components. I. - Ferric hydroxide and quartz. J. Radioanal. Nucl. Chem. Artic. 82, 275–285. https://doi.org/10.1007/BF02037050

Beusen, A.H.W., Slomp, C.P., Bouwman, A.F., 2013. Global land-ocean linkage: Direct inputs of nitrogen to coastal waters via submarine groundwater discharge. Environ. Res. Lett. 8. https://doi.org/10.1088/1748-9326/8/3/034035

Blanchard, R.L., Oakes, D., 1965. Relationships between uranium and radium in coastal marine shells and their environment. J. Geophys. Res. 70, 2911–2921. https://doi.org/10.1029/JZ070i012p02911

Boehm, A.B., Paytan, A., Shellenbarger, G.G., Davis, K.A., 2006. Composition and flux of groundwater from a California beach aquifer: Implications for nutrient supply to the surf zone. Cont. Shelf Res. 26, 269–282.

https://doi.org/10.1016/j.csr.2005.11.008

Boehm, A.B., Shellenbarger, G.G., Paytan, A., 2004. Groundwater discharge: Potential association with fecal indicator bacteria in the surf zone. Environ. Sci. Technol. 38, 3558–3566. https://doi.org/10.1021/es035385a

Bokuniewicz, H., 1980. Groundwater seepage into Great South Bay, New York. Estuar. Coast. Mar. Sci. 10, 437–444. https://doi.org/10.1016/S0302-3524(80)80122-8

Bokuniewicz, H.J., 1992. Analytical Descriptions of Subaqueous Groundwater Seepage. Estuaries 15, 458. https://doi.org/10.2307/1352390

Bollinger, M.S., Moore, W.S., 1984. Radium fluxes from a salt marsh. Nature 309, 444–446.

Booij, M.J., 2002. Extreme daily precipitation in Western Europe with climate change at appropriate spatial scales. Int. J. Climatol. 22, 69–85. https://doi.org/10.1002/joc.715

Breier, J.A., Breier, C.F., Edmonds, H.N., 2005. Detecting submarine groundwater discharge with synoptic surveys of sediment resistivity, radium, and salinity. Geophys. Res. Lett. 32, 1–4. https://doi.org/10.1029/2005GL024639

Broecker, W.S., 1965. An application of natural radon to problems in ocean circulation, in: In Symposium on Diffusion in Ocean and Fresh Waters. pp. 116--145.

Broecker, W.S., Cromwell, J., Li, Y.H., 1968. Rates of vertical eddy diffusion near the ocean floor based on measurements of the distribution of excess 222Rn. Earth Planet. Sci. Lett. 5, 101–105. https://doi.org/10.1016/S0012-821X(68)80022-6

Broecker, W.S., Kaufman, A., 1970. Near-surface and near-bottom radon results for the 1969 North Pacific Geosecs Station. J. Geophys. Res. 75, 7679–7681. https://doi.org/10.1029/JC075i036p07679

Broecker, W.S., Li, Y.H., Cromwell, J., 1967. Radium-226 and radon-222: Concentration in Atlantic and Pacific Oceans. Science (80-. ). 158, 1307–1310. https://doi.org/10.1126/science.158.3806.1307

Brosnan, T., Becker, M.W., Lipo, C.P., 2019. Coastal groundwater discharge and the ancient inhabitants of Rapa Nui (Easter Island), Chile. Hydrogeol. J. 27, 519–534. https://doi.org/10.1007/s10040-018-1870-7

Burnett, K.M., Wada, C.A., Taniguchi, M., Sugimoto, R., Tahara, D., 2018. Evaluating the tradeoffs between groundwater pumping for snow-melting and nearshore fishery productivity in Obama City, Japan. Water (Switzerland) 10. https://doi.org/10.3390/w10111556

Burnett, W.C., Bokuniewicz, H.J., Huettel, M., Moore, W.S., Taniguchi, M., 2003a. Groundwater and pore water inpunts to the coastal zone. Biogeochemistry 66, 3–33. https://doi.org/10.1023/B:BIOG.0000006066.21240.53

Burnett, W.C., Cable, J.E., Corbett, D.R., 2003b. Radon Tracing of Submarine Groundwater Discharge in Coastal Environments, in: Land and Marine Hydrogeology. Elsevier, pp. 25–43. https://doi.org/10.1016/B978-044451479-0/50015-7

Burnett, W.C., Cowart, J.B., Deetae, S., 1990. Radium in the Suwannee River and estuary: Spring and river input to the Gulf of Mexico. Biogeochemistry 10, 237–255. https://doi.org/10.1007/BF00003146

Burnett, W.C., Dulaiova, H., 2003. Estimating the dynamics of groundwater input into the coastal zone via continuous radon-222 measurements. J. Environ. Radioact. 69, 21–35. https://doi.org/10.1016/S0265-931X(03)00084-5

Burnett, W.C., Kim, G., 2001. A continuous monitor for assessment of 222 Rn in the coastal ocean. J. Radioanal. Nucl. Chem. 249, 167–172. https://doi.org/https://doi.org/10.1023/A:1013217821419

Burnett, W.C., Santos, I.R., Weinstein, Y., Swarzenski, P.W., Herut, B., 2007. Remaining uncertainties in the use of Rn-222 as a quantitative tracer of submarine groundwater discharge. IAHS-AISH Publ. 312, 109–118. https://doi.org/10.17146/aij.2015.355

Burnett, W.C., Taniguchi, M., Oberdorfer, J.A., 2001. Measurement and significance of the direct discharge of groundwater into the coastal zone. J. Sea Res. 46, 109–116. https://doi.org/10.1016/S1385-1101(01)00075-2

Cable, J.E., Bugna, G.C., Burnett, W.C., Chanton, J.P., 1996a. Application of 222 Rn and CH 4 for assessment of groundwater discharge to the coastal ocean. Limnol. Oceanogr. 41, 1347–1353. https://doi.org/10.4319/lo.1996.41.6.1347

Cable, J.E., Burnett, W.C., Chanton, J.P., Weatherly, G.L., 1996b. Estimating groundwater discharge into the northeastern Gulf of Mexico using radon-222. Earth Planet. … 144, 591–604. https://doi.org/10.1016/S0012-821X(96)00173-2

Cable, J.E., Martin, J.B., 2008. In situ evaluation of nearshore marine and fresh pore water transport into Flamengo Bay, Brazil. Estuar. Coast. Shelf Sci. 76, 473–483. https://doi.org/10.1016/j.ecss.2007.07.045

Cai, P., Shi, X., Hong, Q., Li, Q., Liu, L., Guo, X., Dai, M., 2015. Using 224Ra/228Th disequilibrium to quantify benthic fluxes of dissolved inorganic carbon and nutrients into the Pearl River Estuary. Geochim. Cosmochim. Acta 170, 188–203. https://doi.org/10.1016/j.gca.2015.08.015

Cai, P., Shi, X., Moore, W.S., Dai, M., 2012. Measurement of 224Ra:228Th disequilibrium in coastal sediments using a delayed coincidence counter. Mar. Chem. 138–139, 1–6. https://doi.org/10.1016/j.marchem.2012.05.004

Cai, P., Shi, X., Moore, W.S., Peng, S., Wang, G., Dai, M., 2014. 224Ra:228Th disequilibrium in coastal sediments: Implications for solute transfer across the sediment-water interface. Geochim. Cosmochim. Acta 125, 68–84. https://doi.org/10.1016/j.gca.2013.09.029

Camarasa-Belmonte, A.M., Segura Beltrán, F., 2001. Flood events in Mediterranean ephemeral streams (ramblas) in Valencia region, Spain. Catena 45, 229–249. https://doi.org/10.1016/S0341-8162(01)00146-1

Camarasa-Belmonte, A.M., Soriano-García, J., 2012. Flood risk assessment and mapping in peri-urban Mediterranean environments using hydrogeomorphology. Application to ephemeral streams in the Valencia region (eastern Spain). Landsc. Urban Plan. 104, 189–200. https://doi.org/10.1016/j.landurbplan.2011.10.009

Camarasa-Belmonte, A.M., Tilford, K.A., 2002. Rainfall-runoff modelling of ephemeral streams in the Valencia region (eastern Spain). Hydrol. Process. 16, 3329–3344. https://doi.org/10.1002/hyp.1103

Carvalho, L.F., Rocha, C., Fleming, A., Veiga-Pires, C., Aníbal, J., 2013. Interception of nutrient rich submarine groundwater discharge seepage on European temperate beaches by the acoel flatworm, Symsagittifera roscoffensis. Mar. Pollut. Bull. 75, 150–156. https://doi.org/10.1016/j.marpolbul.2013.07.045

Catalan Water Agency, 2010. Model numèric de l'aqüífer al·luvial de la riera d'argentona.

Cerdà-Domènech, M., Rodellas, V., Folch, A., Garcia-orellana, J., 2017. Constraining the temporal variations of Ra isotopes and Rn in the groundwater end-member : Implications for derived SGD estimates. Sci. Total Environ. 595, 849–857.

https://doi.org/10.1016/j.scitotenv.2017.03.005

Chabaux, F., Bourdon, B., Riotte, J., 2008. Chapter 3 U-Series Geochemistry in Weathering Profiles, River Waters and Lakes. Radioact. Environ. 13, 49–104. https://doi.org/10.1016/S1569-4860(07)00003-4

Chabaux, F., Riotte, J., Dequincey, O., 2003. U-Th-Ra fractionation during weathering and river transport. Uranium-series Geochemistry 52, 533–576. https://doi.org/10.2113/0520533

Chanyotha, S., Kranrod, C., Burnett, W.C., Lane-Smith, D., Simko, J., 2014. Prospecting for groundwater discharge in the canals of Bangkok via natural radon and thoron. J. Hydrol. 519, 1485–1492. https://doi.org/10.1016/j.jhydrol.2014.09.014

Chanyotha, S., Sola, P., Kritsananuwat, R., Lane-Smith, D., Burnett, W.C., 2018. Improved measurements of thoron (220Rn) in natural waters. J. Radioanal. Nucl. Chem. 318, 777–784. https://doi.org/10.1007/s10967-018-6110-z

Charbonnier, C., Anschutz, P., Poirier, D., Bujan, S., Lecroart, P., 2013. Aerobic respiration in a high-energy sandy beach. Mar. Chem. 155, 10–21. https://doi.org/10.1016/j.marchem.2013.05.003

Charette, M. a., Splivallo, R., Herbold, C., Bollinger, M.S., Moore, W.S., 2003. Salt marsh submarine groundwater discharge as traced by radium isotopes. Mar. Chem. 84, 113–121. https://doi.org/10.1016/j.marchem.2003.07.001

Charette, M.A., 2007. Hydrologic forcing of submarine groundwater discharge: Insight from a seasonal study of radium isotopes in a groundwater-dominated salt marsh estuary. Limnol. Oceanogr. 52, 230–239. https://doi.org/10.4319/lo.2007.52.1.0230

Charette, M.A., Buesseler, K.O., Andrews, J.E., 2001. Utility of radium isotopes for evaluating the input and transport of groundwater-derived nitrogen to a Cape Cod estuary. Limnol. Oceanogr. 46, 465–470. https://doi.org/10.4319/lo.2001.46.2.0465

Charette, M.A., Moore, W.S., Burnett, W.C., 2008. Chapter 5 Uranium- and Thorium-Series Nuclides as Tracers of Submarine Groundwater Discharge. Radioact. Environ. 13, 155–191. https://doi.org/10.1016/S1569-4860(07)00005-8

Charette, M.A., Sholkovitz, E.R., 2002. Oxidative precipitation of groundwater-derived ferrous iron in the subterranean estuary of a coastal bay. Geophys. Res. Lett. 29, 85-1-85–4. https://doi.org/10.1029/2001GL014512

Chen, X., Cukrov, N.N., Santos, I.R., Rodellas, V., Cukrov, N.N., Du, J., 2020. Karstic submarine groundwater discharge into the Mediterranean: Radon-based nutrient fluxes in an anchialine cave and a basin-wide upscaling. Geochim. Cosmochim. Acta 268, 467–484. https://doi.org/10.1016/j.gca.2019.08.019

Chen, X., Lao, Y., Wang, J., Du, J., Liang, M., Yang, B., 2018a. Submarine Groundwater-Borne Nutrients in a Tropical Bay (Maowei Sea, China) and Their Impacts on the Oyster Aquaculture. Geochemistry, Geophys. Geosystems 19, 932–951. https://doi.org/10.1002/2017GC007330

Chen, X., Zhang, F., Lao, Y., Wang, X., Du, J., Santos, I.R., 2018b. Submarine Groundwater Discharge-Derived Carbon Fluxes in Mangroves: An Important Component of Blue Carbon Budgets? J. Geophys. Res. Ocean. 123, 6962–6979. https://doi.org/10.1029/2018JC014448

Cho, H., Kim, G., 2016. Determining groundwater Ra end-member values for the estimation of the magnitude of submarine groundwater discharge using Ra isotope tracers. Geophys. Res. Lett. 43, 3865–3871.

https://doi.org/10.1002/2016GL068805

Cho, H., Kim, T.-H., Moon, J.-H., Song, B.-C., Hwang, D.-W., Kim, T., Im, D.-H., 2021. Estimating submarine groundwater discharge in Jeju volcanic island (Korea) during a typhoon (Kong-rey) using humic-fluorescent dissolved organic matter-Si mass balance. Sci. Rep. 11, 941. https://doi.org/10.1038/s41598-020-79381-0

Cho, H.M., Kim, G., Kwon, E.Y., Moosdorf, N., Garcia-Orellana, J., Santos, I.R., 2018. Radium tracing nutrient inputs through submarine groundwater discharge in the global ocean. Sci. Rep. 8, 4–10. https://doi.org/10.1038/s41598-018-20806-2

Church, T.M., 1996. An underground route for the water cycle. Nature 380, 579–580. https://doi.org/10.1038/380579a0

Clendenon, C., 2009. Ancient Greek hydromyths about the submarine transport of terrestrial fresh water through seabeds offshore of Karstic regions. Acta Carsologica 38, 293–302. https://doi.org/10.3986/ac.v38i2-3.129

Colbert, S.L., Hammond, D.E., 2008. Shoreline and seafloor fluxes of water and short-lived Ra isotopes to surface water of San Pedro Bay, CA. Mar. Chem. 108, 1–17. https://doi.org/10.1016/j.marchem.2007.09.004

Condomines, M., Gourdin, E., Gataniou, D., Seidel, J.L., 2012. Geochemical behaviour of Radium isotopes and Radon in a coastal thermal system (Balaruc-les-Bains, South of France). Geochim. Cosmochim. Acta 98, 160–176. https://doi.org/10.1016/j.gca.2012.09.010

Cook, P.G., Rodellas, V., Andrisoa, A., Stieglitz, T.C., 2018a. Exchange across the sediment-water interface quantified from porewater radon profiles. J. Hydrol. 559, 873–883. https://doi.org/10.1016/j.jhydrol.2018.02.070

Cook, P.G., Rodellas, V., Stieglitz, T.C., 2018b. Quantifying Surface Water , Porewater , and Groundwater Interactions Using Tracers : Tracer Fluxes , Water Fluxes , and End-member Concentrations Water Resources Research. Water Resour. Res. 54, 2452–2465. https://doi.org/10.1002/2017WR021780

Copenhaver, S.A., Krishnaswami, S., Turekian, K.K., Epler, N., Cochran, J.K., 1993. Retardation of 238U and 232Th decay chain radionuclides in Long Island and Connecticut aquifers. Geochim. Cosmochim. Acta 57, 597–603. https://doi.org/10.1016/0016-7037(93)90370-C

Copenhaver, S.A., Krishnaswami, S., Turekian, K.K., Shaw, H., 1992. 238 U and 232 Th series nuclides in groundwater from the J-13 well at the Nevada Test Site: Implications for ion retardation. Geophys. Res. Lett. 19, 1383–1386. https://doi.org/10.1029/92GL01437

Correa, R.E., Tait, D.R., Sanders, C.J., Conrad, S.R., Harrison, D., Tucker, J.P., Reading, M.J., Santos, I.R., 2020. Submarine groundwater discharge and associated nutrient and carbon inputs into Sydney Harbour (Australia). J. Hydrol. 580, 124262. https://doi.org/10.1016/j.jhydrol.2019.124262

Costall, A., Harris, B., Pigois, J.P., 2018. Electrical Resistivity Imaging and the Saline Water Interface in High-Quality Coastal Aquifers. Surv. Geophys. 39, 753–816. https://doi.org/10.1007/s10712-018-9468-0

Crawford, J., Neretnieks, I., Malmström, M., 2006. Data and uncertainty assessment coefficients in granitic rock for use in SR-Can calculations, Skb.

Crook, E.D., Potts, D., Rebolledo-Vieyra, M., Hernandez, L., Paytan, A., 2012. Calcifying coral abundance near low-pH springs: Implications for future ocean acidification. Coral Reefs 31, 239–245. https://doi.org/10.1007/s00338-011-0839-y

Crotwell, A.M., Moore, W.S., 2003. Nutrient and Radium Fluxes from Submarine Groundwater Discharge to Port Royal Sound, South Carolina. Aquat. Geochemistry 9, 191–208. https://doi.org/10.1023/B:AQUA.0000022954.89019.c9

Crusius, J., Berg, P., Koopmans, D.J., Erban, L., 2008. Eddy correlation measurements of submarine groundwater discharge. Mar. Chem. 109, 77–85. https://doi.org/10.1016/j.marchem.2007.12.004

Crusius, J., Koopmans, D., Bratton, J.F., Charette, M.A., Kroeger, K., Henderson, P., Ryckman, L., Halloran, K., Colman, J.A., 2005. Submarine groundwater discharge to a small estuary estimated from radon and salinity measurements and a box model. Biogeosciences 2, 141–157. https://doi.org/10.5194/bg-2-141-2005

Davidson, M.R., Dickson, B.L., 1986. A Porous Flow Model for Steady State Transport of Radium in Groundwater. Water Resour. Res. 22, 34–44. https://doi.org/10.1029/WR022i001p00034

Davis, K.S., 1924. The History of Radium. Radiology 2, 334–342. https://doi.org/10.1148/2.5.334

De Sieyes, N.R., Yamahara, K.M., Layton, B.A., Joyce, E.H., Boehm, A.B., 2008. Submarine discharge of nutrient-enriched fresh groundwater at Stinson Beach, California is enhanced during neap tides. Limnol. Oceanogr. 53, 1434–1445. https://doi.org/10.4319/lo.2008.53.4.1434

Devaputra, D., Thompson, T.G., Utterback, C.L., 1932. The Radioactivity of Sea Water. ICES J. Mar. Sci. 7, 358–366. https://doi.org/10.1093/icesjms/7.3.358

Dias da Cunha, K.M., Henderson, H., Thomson, B.M., Hecht, A.A., 2014. Ground water contamination with 238U, 234U, 235U, 226Ra and 210Pb from past uranium mining: cove wash, Arizona. Environ. Geochem. Health 36, 477–487. https://doi.org/10.1007/s10653-013-9575-2

Diego-Feliu, M., 2020. Guidelines and limits for the quantification of U/Th series radionuclides with the Radium Delayed Coincidence Counter (RaDeCC) - Codes. https://doi.org/10.5281/ZENODO.3596482

Duarte, T.K. eo, Hemond, H.F., Frankel, D., Frankel, S., 2006. Assessment of submarine groundwater discharge by handheld aerial infrared imagery: Case study of Kaloko fishpond and bay, Hawai'i. Limnol. Oceanogr. Methods 4, 227–236. https://doi.org/10.4319/lom.2006.4.227

Duarte, T.K., Pongkijvorasin, S., Roumasset, J., Amato, D., Burnett, K., 2010. Optimal management of a Hawaiian coastal aquifer with nearshore marine ecological interactions. Water Resour. Res. 46, 1–12. https://doi.org/10.1029/2010WR009094

Dulaiova, H., Burnett, W.C., 2006. Radon loss across the water-air interface (Gulf of Thailand) estimated experimentally from 222Rn-224Ra. Geophys. Res. Lett. 33, 1–4. https://doi.org/10.1029/2005GL025023

Dulaiova, H., Burnett, W.C., 2004. An efficient method for γ-spectrometric determination of radium-226,228 via manganese fibers. Limnol. Oceanogr. Methods 2, 256–261. https://doi.org/10.4319/lom.2004.2.256

Dulaiova, H., Camilli, R., Henderson, P.B., Charette, M.A., 2010. Coupled radon, methane and nitrate sensors for large-scale assessment of groundwater discharge and non-point source pollution to coastal waters. J. Environ. Radioact. 101, 553–563. https://doi.org/10.1016/j.jenvrad.2009.12.004

Duque, C., Knee, K.L., Russoniello, C.J., Sherif, M., Abu Risha, U.A., Sturchio, N.C., Michael, H.A., 2019. Hydrogeological processes and near shore spatial variability of radium and radon isotopes for the characterization of submarine groundwater

discharge. J. Hydrol. 579, 124192. https://doi.org/https://doi.org/10.1016/j.jhydrol.2019.124192

Duque, C., Michael, H.A., Wilson, A.M., 2020. The Subterranean Estuary: Technical Term, Simple Analogy, or Source of Confusion? Water Resour. Res. 56, 1–7. https://doi.org/10.1029/2019WR026554

Durán, R., Canals, M., Sanz, J.L., Lastras, G., Amblas, D., Micallef, A., 2014. Morphology and sediment dynamics of the northern Catalan continental shelf, northwestern Mediterranean Sea. Geomorphology 204, 1–20. https://doi.org/10.1016/j.geomorph.2012.10.004

Ellins, K.K., Roman-Mas, A., Lee, R., 1990. Using 222Rn to examine groundwater/surface discharge interaction in the Rio Grande de Manati, Puerto Rico. J. Hydrol. 115, 319–341. https://doi.org/10.1016/0022-1694(90)90212-G

Elsinger, R.J., Moore, W.S., 1983. 224Ra, 228Ra, and 226Ra in Winyah Bay and Delaware Bay. Earth Planet. Sci. Lett. 64, 430–436. https://doi.org/10.1016/0012-821X(83)90103-6

Encarnação, J., Leitão, F., Range, P., Piló, D., Chícharo, M.A., Chícharo, L., 2015. Local and temporal variations in near-shore macrobenthic communities associated with submarine groundwater discharges. Mar. Ecol. 36, 926–941. https://doi.org/10.1111/maec.12186

Encarnação, J., Leitão, F., Range, P., Piló, D., Chícharo, M.A., Chícharo, L., 2013. The influence of submarine groundwater discharges on subtidal meiofauna assemblages in south Portugal (Algarve). Estuar. Coast. Shelf Sci. 130, 202–208. https://doi.org/10.1016/j.ecss.2013.04.013

Environmental Modelling for Radiation Safety, 2008. Quantification of radionuclide transfer in terrestrial and freshwater environments.

Erostate, M., Huneau, F., Garel, E., Ghiotti, S., Vystavna, Y., Garrido, M., Pasqualini, V., 2020. Groundwater dependent ecosystems in coastal Mediterranean regions: Characterization, challenges and management for their protection. Water Res. 172, 115461. https://doi.org/10.1016/j.watres.2019.115461

Evans, R.D., Kip, A.F., 1938. The radium content of marine sediments from the East Indies, the Philippines, and Japan, and of the Mesozoic fossil clays of the East Indies. Am. J. Sci. s5-36, 321–336. https://doi.org/10.2475/ajs.s5-36.215.321

Evans, R.D., Kip, A.F., Moberg, E.G., 1938. The radium and radon content of Pacific Ocean water, life, and sediments. Am. J. Sci. s5-36, 241–259. https://doi.org/10.2475/ajs.s5-36.214.241

Eve, A.S., 1909. X. On the amount of radium present in sea-water . London, Edinburgh, Dublin Philos. Mag. J. Sci. 18, 102–107. https://doi.org/10.1080/14786440708636675

Fleury, P., Bakalowicz, M., de Marsily, G., 2007. Submarine springs and coastal karst aquifers: A review. J. Hydrol. 339, 79–92. https://doi.org/10.1016/j.jhydrol.2007.03.009

Freeze, R.A., Cherry, J.A., 1979. Groundwater.

Futch, J.C., Griffin, D.W., Lipp, E.K., 2010. Human enteric viruses in groundwater indicate offshore transport of human sewage to coral reefs of the Upper Florida Keys. Environ. Microbiol. 12, 964–974. https://doi.org/10.1111/j.1462-2920.2010.02141.x

Gagan, M.K., Ayliffe, L.K., Opdyke, B.N., Hopley, D., Scott-Gagan, H., Cowley, J., 2002. Coral oxygen isotope evidence for recent groundwater fluxes to the Australian Great Barrier Reef. Geophys. Res. Lett. 29, 1–4.

https://doi.org/10.1029/2002GL015336

Ganju, N.K., 2011. A novel approach for direct estimation of fresh groundwater discharge to an estuary. Geophys. Res. Lett. 38, 1–6. https://doi.org/10.1029/2011GL047718

Garcés, E., Basterretxea, G., Tovar-Sánchez, A., 2011. Changes in microbial communities in response to submarine groundwater input. Mar. Ecol. Prog. Ser. 438, 47–58. https://doi.org/10.3354/meps09311

Garcia-Orellana, J., Cochran, J.K., Bokuniewicz, H.J., Daniel, J.W.R., Rodellas, V., Heilbrun, C., 2014. Evaluation of 224Ra as a tracer for submarine groundwater discharge in Long Island Sound (NY). Geochim. Cosmochim. Acta 141, 314–330. https://doi.org/10.1016/j.gca.2014.05.009

Garcia-Orellana, J., Rodellas, V., Tamborski, J.J., Diego-Feliu, M., van Beek, P., Weinstein, Y., Charette, M.A., Alorda-Kleinglass, A., Michael, H.A., Stieglitz, T., Scholten, J., 2021. Radium isotopes as submarine groundwater discharge (SGD) tracers: Review and recommendations. Earth-Science Rev. 103681. https://doi.org/10.1016/j.earscirev.2021.103681

Garcia-Solsona, E., Garcia-Orellana, J., Masqué, P., Dulaiova, H., 2008. Uncertainties associated with 223Ra and 224Ra measurements in water via a Delayed Coincidence Counter (RaDeCC). Mar. Chem. 109, 198–219. https://doi.org/10.1016/j.marchem.2007.11.006

Garcia-Solsona, E., Garcia-Orellana, J., Masqué, P., Garcés, E., Radakovitch, O., Mayer, A., Estradé, S., Basterretxea, G., 2010. An assessment of karstic submarine groundwater and associated nutrient discharge to a Mediterranean coastal area (Balearic Islands, Spain) using radium isotopes. Biogeochemistry 97, 211–229. https://doi.org/10.1007/s10533-009-9368-y

Garrels, R.M., Mackenzie, F.T., 1971. Evolution of sedimentary rocks. Norton.

Garrison, G.H., Glenn, C.R., McMurtry, G.M., 2003. Measurement of submarine groundwater discharge in Kahana Bay, O'ahu, Hawai'i. Limnol. Oceanogr. 48, 920–928. https://doi.org/10.4319/lo.2003.48.2.0920

Gasparini, P., 1984. History of radioactivity, in: Uranium Geochemistry, Mineralogy, Geology, Exploration and Resources. Springer Netherlands, Dordrecht, pp. 1–3. https://doi.org/10.1007/978-94-009-6060-2_1

Geibert, W., Annett, A.L., van Beek, P., Garcia-Orellana, J., Hsieh, Y., Masqué, P., 2013. 226 Ra determination via the rate of 222 Rn ingrowth with the Radium Delayed Coincidence Counter ( RaDeCC ). Limnol. Oceanogr. Methods 11, 594–603. https://doi.org/10.4319/lom.2013.11.594

George, C., Moore, W.S., White, S.M., Smoak, E., Joye, S.B., Leier, A., Wilson, A.M., 2020. A New Mechanism for Submarine Groundwater Discharge From Continental Shelves. Water Resour. Res. 56. https://doi.org/10.1029/2019WR026866

Giffin, C., Kaufman, A., Broecker, W., 1963. Delayed coincidence counter for the assay of actinon and thoron. J. Geophys. Res. 68, 1749–1757. https://doi.org/10.1029/JZ068i006p01749

Gleeson, J., Santos, I.R., Maher, D.T., Golsby-Smith, L., 2013. Groundwater-surface water exchange in a mangrove tidal creek: Evidence from natural geochemical tracers and implications for nutrient budgets. Mar. Chem. 156, 27–37. https://doi.org/10.1016/j.marchem.2013.02.001

Gobler, C.J., Sañudo-Wilhelmy, S.A., 2001. Temporal variability of groundwater seepage and brown tide blooms in a Long Island embayment. Mar. Ecol. Prog. Ser. 217, 299–309. https://doi.org/10.3354/meps217299

Godoy, J.M., Souza, T.A., Godoy, M.L.D.P., Moreira, I., Carvalho, Z.L., Lacerda, L.D., Fernandes, F.C., 2013. Groundwater and surface water quality in a coastal bay with negligible fresh groundwater discharge: Arraial do Cabo, Brazil. Mar. Chem. 156, 85–97. https://doi.org/10.1016/j.marchem.2013.05.004

Goff, J.A., 2019. Modern and Fossil Pockmarks in the New England Mud Patch: Implications for Submarine Groundwater Discharge on the Middle Shelf. Geophys. Res. Lett. 46, 12213–12220. https://doi.org/10.1029/2019GL084881

Gonneea, M.E., Morris, P.J., Dulaiova, H., Charette, M.A., Gonneea, M.E., Morris, P.J., Dulaiova, H., Charette, M.A., Eagle, M., Morris, P.J., Dulaiova, H., Charette, M.A., Gonneea, M.E., Morris, P.J., Dulaiova, H., Charette, M.A., 2008. New perspectives on radium behavior within a subterranean estuary. Mar. Chem. 109, 250–267. https://doi.org/10.1016/j.marchem.2007.12.002

Gonneea, M.E., Mulligan, A.E., Charette, M.A., 2013a. Seasonal cycles in radium and barium within a subterranean estuary: Implications for groundwater derived chemical fluxes to surface waters. Geochim. Cosmochim. Acta 119, 164–177. https://doi.org/10.1016/j.gca.2013.05.034

Gonneea, M.E., Mulligan, A.E., Charette, M.A., 2013b. Climate-driven sea level anomalies modulate coastal groundwater dynamics and discharge. Geophys. Res. Lett. 40, 2701–2706. https://doi.org/10.1002/grl.50192

Grasshoff, K., Kremling, K., Ehrhardt, M., 1983. Methods of seawater analysis.

Guo, Q., Li, H., 2015. Terrestrial-originated submarine groundwater discharge through deep multilayered aquifer systems beneath the seafloor. Hydrol. Process. 29, 295–309. https://doi.org/10.1002/hyp.10163

Guo, Q., Li, H., Zhou, Z., Huang, Y., 2012. Rainfall infiltration-derived submarine groundwater discharge from multi-layered aquifer system terminating at the coastline. Hydrol. Process. 26, 985–995. https://doi.org/10.1002/hyp.8188

Gwak, Y.-S., Kim, S.-H.S.-W., Lee, Y.-W., Khim, B.-K., Hamm, S.-Y., Kim, S.-H.S.-W., 2014. Estimation of submarine groundwater discharge in the Il-Gwang watershed using water budget analysis and 222 Rn mass balance. Hydrol. Process. 28, 3761–3775. https://doi.org/10.1002/hyp.9927

Hajati, M.C., Sutanudjaja, E., Moosdorf, N., 2019. Quantifying Regional Fresh Submarine Groundwater Discharge With the Lumped Modeling Approach CoCa-RFSGD. Water Resour. Res. 55, 5321–5341. https://doi.org/10.1029/2018WR024248

Hata, M., Sugimoto, R., Hori, M., Tomiyama, T., Shoji, J., 2016. Occurrence, distribution and prey items of juvenile marbled sole Pseudopleuronectes yokohamae around a submarine groundwater seepage on a tidal flat in southwestern Japan. J. Sea Res. 111, 47–53. https://doi.org/10.1016/j.seares.2016.01.009

Herran, N., Roqué, X., 2009. Tracers of modern technoscience. Dynamis 29, 123–130. https://doi.org/10.4321/S0211-95362009000100006

Hevesy, G. von, 1962. Adventures in radioisotope research. New York,Pergamon Press,.

Hevesy, G. von, 1915. Exchange of atoms between solid and liquid phases. Phys. Z 16, 52.

Hevesy, G. von, Rona, E., 1914. The velocity of dissolution of molecular layers. Z. phys. Chem 89, 294.

Honda, H., Sugimoto, R., Kobayashi, S., 2018. Submarine Groundwater Discharge and its Influence on Primary Production in Japanese Coasts: Case Study in Obama Bay. pp. 101–115. https://doi.org/10.1007/978-981-10-7383-0_8

Hong, Q., Cai, P., Geibert, W., Cao, Z., 2018. Benthic fluxes of metals into the Pearl River Estuary based on 224 Ra / 228 Th disequilibrium : From alkaline earth ( Ba ) to redox sensitive elements ( U , Mn , Fe ). Geochim. Cosmochim. Acta 237, 223–239. https://doi.org/10.1016/j.gca.2018.06.036

Hopke, P.K., 1989. Use of Electrostatic Collection of 218Po for Measuring Rn. Health Phys. 57, 39–42. https://doi.org/10.1097/00004032-198907000-00005

Horányi, G., 2004. Chapter 1 Historical background, in: Interface Science and Technology. Routledge, pp. 1–4. https://doi.org/https://doi.org/10.1016/S1573-4285(04)80055-3

Hu, C., Muller-Karger, F.E., Swarzenski, P.W., 2006. Hurricanes, submarine groundwater discharge, and Florida's red tides. Geophys. Res. Lett. 33, 2005GL025449. https://doi.org/10.1029/2005GL025449

Hu, I.H., Hemond, H.F., 2020. A Multi-Function Sensor for Eddy Correlation Measurements of Benthic Flux. IEEE Sens. J. 20, 1509–1526. https://doi.org/10.1109/JSEN.2019.2946968

Hussain, N., 1995. Supply rates of natural U-Th series radionuclides from aquifer solids into groundwater. Geophys. Res. Lett. 22, 1521–1524. https://doi.org/10.1029/95GL01006

Hwang, D.-W., Lee, Y.-W., Kim, G., 2005. Large submarine groundwater discharge and benthic eutrophication in Bangdu Bay on volcanic Jeju Island, Korea. Limnol. Oceanogr. 50, 1393–1403. https://doi.org/10.4319/lo.2005.50.5.1393

International Atomic Energy Agency, 2010. Handbook of Parameter Values for the Prediction of Radionuclide Transfer in Terrestrial and Freshwater Environments. Vienna.

International Atomic Energy Agency, 1984. The Behaviour of Radium in Waterways and Aquifers. Int. At. Energy Agency 87–168.

IPCC, 2021. Assessment Report 6 Climate Change 2021: The Physical Science Basis.

Ivanovich, M., Harmon, R.., 1992. Uranium-series Disequilibrium: Applications to Earth, Marine, and Environmental Sciences. Clarendon Press.

Jeong, J., Kim, G., Han, S., 2012. Influence of trace element fluxes from submarine groundwater discharge (SGD) on their inventories in coastal waters off volcanic island, Jeju, Korea. Appl. Geochemistry 27, 37–43. https://doi.org/10.1016/j.apgeochem.2011.08.014

Johannes, R., 1980. The Ecological Significance of the Submarine Discharge of Groundwater. Mar. Ecol. Prog. Ser. 3, 365–373. https://doi.org/10.3354/meps003365

Johannesson, K.H., Burdige, D.J., 2007. Balancing the global oceanic neodymium budget: Evaluating the role of groundwater. Earth Planet. Sci. Lett. 253, 129–142. https://doi.org/10.1016/j.epsl.2006.10.021

Johannesson, K.H., Chevis, D.A., Burdige, D.J., Cable, J.E., Martin, J.B., Roy, M., 2011. Submarine groundwater discharge is an important net source of light and middle REEs to coastal waters of the Indian River Lagoon, Florida, USA. Geochim. Cosmochim. Acta 75, 825–843. https://doi.org/10.1016/j.gca.2010.11.005

Joly, J., 1908. XXXVII. The radioactivity of sea-water . London, Edinburgh, Dublin Philos. Mag. J. Sci. 15, 385–393. https://doi.org/10.1080/14786440809463781

Jou-Claus, S., Folch, A., Garcia-Orellana, J., 2021. Applicability of Landsat 8 thermal infrared sensor for identifying submarine groundwater discharge springs in the Mediterranean Sea basin. Hydrol. Earth Syst. Sci. 25, 4789–4805. https://doi.org/10.5194/hess-25-4789-2021

Key, R.M., Guinasso, N.L., Schink, D.R., 1979. Emanation of radon-222 from marine sediments. Mar. Chem. 7, 221–250. https://doi.org/10.1016/0304-4203(79)90041-0

Kigoshi, K., 1971. Alpha-Recoil Thorium-234: Dissolution into Water and the Uranium-234/Uranium-238 Disequilibrium in Nature. Science (80-. ). 173, 47–48. https://doi.org/10.1126/science.173.3991.47

Kim, G., Hwang, D.W., 2002. Tidal pumping of groundwater into the coastal ocean revealed from submarine 222Rn and CH4 monitoring. Geophys. Res. Lett. 29, 21–24. https://doi.org/10.1029/2002gl015093

Kim, I., Kim, G., 2011. Large fluxes of rare earth elements through submarine groundwater discharge (SGD) from a volcanic island, Jeju, Korea. Mar. Chem. 127, 12–19. https://doi.org/10.1016/j.marchem.2011.07.006

Kim, J., Kim, G., 2017. Inputs of humic fluorescent dissolved organic matter via submarine groundwater discharge to coastal waters off a volcanic island (Jeju, Korea). Sci. Rep. 7, 1–9. https://doi.org/10.1038/s41598-017-08518-5

King, J.N., 2011. 9.16 - Analytical Characterization of Selective Benthic Flux Components in Estuarine and Coastal Waters*, in: Wolanski, E., McLusky, D. (Eds.), Treatise on Estuarine and Coastal Science. Academic Press, Waltham, pp. 397–423. https://doi.org/https://doi.org/10.1016/B978-0-12-374711-2.00917-7

Kiro, Y., Weinstein, Y., Starinsky, A., Yechieli, Y., 2015. Application of radon and radium isotopes to groundwater flow dynamics: An example from the Dead Sea. Chem. Geol. 411, 155–171. https://doi.org/10.1016/j.chemgeo.2015.06.014

Kiro, Y., Weinstein, Y., Starinsky, A., Yechieli, Y., 2014. The extent of seawater circulation in the aquifer and its role in elemental mass balances: A lesson from the Dead Sea. Earth Planet. Sci. Lett. 394, 146–158. https://doi.org/10.1016/j.epsl.2014.03.010

Kiro, Y., Weinstein, Y., Starinsky, A., Yechieli, Y., 2013. Groundwater ages and reaction rates during seawater circulation in the Dead Sea aquifer. Geochim. Cosmochim. Acta 122, 17–35. https://doi.org/10.1016/j.gca.2013.08.005

Kiro, Y., Yechieli, Y., Voss, C.I., Starinsky, A., Weinstein, Y., 2012. Modeling radium distribution in coastal aquifers during sea level changes: The Dead Sea case. Geochim. Cosmochim. Acta 88, 237–254. https://doi.org/10.1016/j.gca.2012.03.022

Knee, K.L., Crook, E.D., Hench, J.L., Leichter, J.J., Paytan, A., 2016. Assessment of Submarine Groundwater Discharge (SGD) as a Source of Dissolved Radium and Nutrients to Moorea (French Polynesia) Coastal Waters. Estuaries and Coasts 39, 1651–1668. https://doi.org/10.1007/s12237-016-0108-y

Knee, K.L., Garcia-Solsona, E., Garcia-Orellana, J., Boehm, A.B., Paytan, A., 2011. Using radium isotopes to characterize water ages and coastal mixing rates: A sensitivity analysis. Limnol. Oceanogr. Methods 9, 380–395. https://doi.org/10.4319/lom.2011.9.380

Knee, K.L., Layton, B.A., Street, J.H., Boehm, A.B., Paytan, A., 2008. Sources of nutrients and fecal indicator bacteria to nearshore waters on the north shore of Kaua'i (Hawai'i, USA). Estuaries and Coasts 31, 607–622. https://doi.org/10.1007/s12237-008-9055-6

Knee, K.L., Paytan, A., 2011. Submarine Groundwater Discharge: A Source of Nutrients, Metals, and Pollutants to the Coastal Ocean, in: Treatise on Estuarine and Coastal Science. Academic Press, pp. 125–162. https://doi.org/10.1016/B978-0-12-374711-2.00109-1

Knee, K.L., Street, J.H., Grossman, E.G., Paytan, A., 2010. Nutrient inputs to the coastal ocean from submarine groundwater discharge in a groundwater-dominated system: Relation to land use (Kona coast, Hawaii, U.S.A.). Limnol. Oceanogr. 55, 1105–1122. https://doi.org/10.4319/lo.2010.55.3.1105

Koczy, F.F., 1958. Natural radium as a tracer m the ocean. Proc. 2nd United Nations Int. Conf. Peac. Uses At. Energy, 18, 351--357.

Koczy, F.F., Rosholt, J.N., 1962. Radioactivity in Oceanography, in: Nuclear Radiation in Geophysics / Kernstrahlung in Der Geophysik. Springer Berlin Heidelberg, Berlin, Heidelberg, pp. 18–46. https://doi.org/10.1007/978-3-642-92837-6_2

Kohout, F.., 1966. Submarine springs: a neglected phenomenon of coastal hydrology. Hydrology 26, 391--413.

Kotwicki, L., Grzelak, K., Czub, M., Dellwig, O., Gentz, T., Szymczycha, B., Böttcher, M.E., 2014. Submarine groundwater discharge to the Baltic coastal zone: Impacts on the meiofaunal community. J. Mar. Syst. 129, 118–126. https://doi.org/10.1016/j.jmarsys.2013.06.009

Kovarik, A.F., 1931. The Age of the Earth-Radioactivity Methods of its Determination. Sci. Mon. 32, 309–318.

Krall, L., Auqué-Sanz, L., Garcia-Orellana, J., Trezzi, G., Tullborg, E.L., Suksi, J., Porcelli, D., Andersson, P., 2020. Radium isotopes to trace uranium redox anomalies in anoxic groundwater. Chem. Geol. 531, 119296. https://doi.org/10.1016/j.chemgeo.2019.119296

Krest, J.M., Harvey, J.W., 2003. Using natural distributions of short-lived radium isotopes to quantify groundwater discharge and recharge. Limnol. Oceanogr. 48, 290–298. https://doi.org/10.4319/lo.2003.48.1.0290

Krishnaswami, S., Bhushan, R., Baskaran, M., 1991. Radium isotopes and 222Rn in shallow brines, Kharaghoda (India). Chem. Geol. Isot. Geosci. Sect. 87, 125–136. https://doi.org/10.1016/0168-9622(91)90046-Y

Krishnaswami, S., Graustein, W.C., Turekian, K.K., Dowd, J.F., 1982. Radium, thorium and radioactive lead isotopes in groundwaters: Application to the in situ determination of adsorption-desorption rate constants and retardation factors. Water Resour. Res. 18, 1663–1675. https://doi.org/10.1029/WR018i006p01663

Krupa, S.L., Belanger, T. V, Heck, H.H., Brock, J.T., Jones, B.J., Krupa, S.L., Belanger, T. V, Heck, H.H., Brock, J.T., Jonesf, B.J., 1998. Krupaseep — The Next Generation Seepage Meter. J. Coast. Res. 1998, 210–213.

Kumar, A., Rout, S., Pulhani, V., Kumar, A.V., 2020. A review on distribution coefficient (Kd) of some selected radionuclides in soil/sediment over the last three decades. J. Radioanal. Nucl. Chem. 323, 13–26. https://doi.org/10.1007/s10967-019-06930-x

Kundzewicz, Z.W., Döll, P., 2009. Will groundwater ease freshwater stress under climate change? Hydrol. Sci. J. 54, 665–675. https://doi.org/10.1623/hysj.54.4.665

Kunkel, K.E., Easterling, D.R., Kristovich, D.A.R., Gleason, B., Stoecker, L., Smith, R., 2012. Meteorological Causes of the Secular Variations in Observed Extreme Precipitation Events for the Conterminous United States. J. Hydrometeorol. 13, 1131–1141. https://doi.org/10.1175/JHM-D-11-0108.1

Kwon, E.Y., Kim, G., Primeau, F., Moore, W.S., Cho, H., DeVries, T., Sarmiento, J.L., Charette, M.A., Cho, Y., 2014. Global estimate of submarine groundwater discharge based on an observationally constrained radium isotope model. Geophys. Res. Lett. 41, 8438–8444. https://doi.org/10.1002/2014GL061574

Kwon, H.K., Kang, H., Oh, Y.H., Park, S.R., Kim, G., 2017. Green tide development associated with submarine groundwater discharge in a coastal harbor, Jeju, Korea. Sci. Rep. 7, 1–9. https://doi.org/10.1038/s41598-017-06711-0

Le Roy, E., Sanial, V., Lacan, F., van Beek, P., Souhaut, M., Charette, M.A., Henderson, P.B., 2019. Insight into the measurement of dissolved 227Ac in seawater using radium delayed coincidence counter. Mar. Chem. 212, 64–73. https://doi.org/10.1016/j.marchem.2019.04.002

Lecher, A.L., Fisher, A.T., Paytan, A., 2016. Submarine groundwater discharge in Northern Monterey Bay, California: Evaluation by mixing and mass balance models. Mar. Chem. 179, 44–55. https://doi.org/10.1016/j.marchem.2016.01.001

Lecher, A.L., Mackey, K., 2018. Synthesizing the Effects of Submarine Groundwater Discharge on Marine Biota. Hydrology 5, 60. https://doi.org/10.3390/hydrology5040060

Lecher, A.L., Mackey, K., Kudela, R., Ryan, J., Fisher, A., Murray, J., Paytan, A., 2015. Nutrient loading through submarine groundwater discharge and phytoplankton growth in Monterey bay, CA. Environ. Sci. Technol. 49, 6665–6673. https://doi.org/10.1021/acs.est.5b00909

Lecher, A.L., Mackey, K.R.M., Paytan, A., 2017. River and Submarine Groundwater Discharge Effects on Diatom Phytoplankton Abundance in the Gulf of Alaska. Hydrology 4. https://doi.org/10.3390/hydrology4040061

Lee, D.R., 1977. A device for measuring seepage flux in lakes and estuaries1. Limnol. Oceanogr. 22, 140–147. https://doi.org/10.4319/lo.1977.22.1.0140

Lee, E., Kang, K.M., Hyun, S.P., Lee, K.Y., Yoon, H., Kim, S.H., Kim, Y., Xu, Z., Kim, D.J., Koh, D.C., Ha, K., 2016a. Submarine groundwater discharge revealed by aerial thermal infrared imagery: a case study on Jeju Island, Korea. Hydrol. Process. 30, 3494–3506. https://doi.org/10.1002/hyp.10868

Lee, E., Yoon, H., Hyun, S.P., Burnett, W.C., Koh, D.C., Ha, K., Kim, D.J., Kim, Y., Kang, K.M., 2016b. Unmanned aerial vehicles (UAVs)-based thermal infrared (TIR) mapping, a novel approach to assess groundwater discharge into the coastal zone. Limnol. Oceanogr. Methods 14, 725–735. https://doi.org/10.1002/lom3.10132

Lee, Y.-W., Kim, G., Lim, W.A., Hwang, D.W., 2010. A relationship between submarine groundwater-borne nutrients traced by Ra isotopes and the intensity of dinoflagellate red-tides occurring in the southern sea of Korea. Limnol. Oceanogr. 55, 1–10. https://doi.org/10.4319/lo.2010.55.1.0001

Lee, Y.W., Kim, G., 2007. Linking groundwater-borne nutrients and dinoflagellate red-tide outbreaks in the southern sea of Korea using a Ra tracer. Estuar. Coast. Shelf Sci. 71, 309–317. https://doi.org/10.1016/j.ecss.2006.08.004

Levy, D.M., Moore, W.S., 1985. 224Ra in continental shelf waters. Deep Sea Res. Part B. Oceanogr. Lit. Rev. 32, 1007. https://doi.org/10.1016/0198-0254(85)93730-6

Li, L., Barry, D.A., Stagnitti, F., Parlange, J.-Y., 1999. Submarine groundwater discharge and associated chemical input to a coastal sea. Water Resour. Res. 35, 3253–3259. https://doi.org/10.1029/1999WR900189

Li, X., Hu, B.X., Tong, J., 2016. Numerical study on tide-driven submarine groundwater discharge and seawater recirculation in heterogeneous aquifers. Stoch. Environ. Res. Risk Assess. 30, 1741–1755. https://doi.org/10.1007/s00477-015-1200-8

Li, X., Ke, T., Wang, Y., Zhou, T., Li, D., Tong, F., Wen, J., 2020. Hydraulic Conductivity Behaviors of Karst Aquifer With Conduit-Fissure Geomaterials. Front. Earth Sci. 8, 1–10. https://doi.org/10.3389/feart.2020.00030

Li, Y.-H., Mathieu, G., Biscaye, P., Simpson, H.J., 1977. The flux of 226Ra from estuarine and continental shelf sediments. Earth Planet. Sci. Lett. 37, 237–241. https://doi.org/10.1016/0012-821X(77)90168-6

Li, Y.H., Chan, L.H., 1979. Desorption of Ba and 226Ra from river-borne sediments in the Hudson estuary. Earth Planet. Sci. Lett. 43, 343–350. https://doi.org/10.1016/0012-821X(79)90089-X

Liefer, J.D., MacIntyre, H.L., Novoveská, L., Smith, W.L., Dorsey, C.P., 2009. Temporal and spatial variability in Pseudo-nitzschia spp. in Alabama coastal waters: A “hot spot” linked to submarine groundwater discharge? Harmful Algae 8, 706–714. https://doi.org/10.1016/j.hal.2009.02.003

Lionello, P., Bhend, J., Buzzi, A., Della-Marta, P.M., Krichak, S.O., Jansà, A., Maheras, P., Sanna, A., Trigo, I.F., Trigo, R., 2006. Chapter 6 Cyclones in the Mediterranean region: Climatology and effects on the environment, in: Developments in Earth and Environmental Sciences. pp. 325–372. https://doi.org/10.1016/S1571-9197(06)80009-1

Lirman, D., Orlando, B., Maciá, S., Manzello, D., Kaufman, L., Biber, P., Jones, T., 2003. Coral communities of Biscayne Bay, Florida and adjacent offshore areas: Diversity, abundance, distribution, and environmental correlates. Aquat. Conserv. Mar. Freshw. Ecosyst. 13, 121–135. https://doi.org/10.1002/aqc.552

Liu, Q., Charette, M.A., Henderson, P.B., McCorkle, D.C., Martin, W., Dai, M., 2014. Effect of submarine groundwater discharge on the coastal ocean inorganic carbon cycle. Limnol. Oceanogr. 59, 1529–1554. https://doi.org/10.4319/lo.2014.59.5.1529

Liu, Y., Jiao, J.J., Mao, R., Luo, X., Liang, W., Robinson, C.E., 2019. Spatial Characteristics Reveal the Reactive Transport of Radium Isotopes ( 224 Ra, 223 Ra, and 228 Ra) in an Intertidal Aquifer. Water Resour. Res. 55, 10282–10302. https://doi.org/10.1029/2019WR024849

Luek, J.L., Beck, A.J., 2014. Radium budget of the York River estuary (VA, USA) dominated by submarine groundwater discharge with a seasonally variable groundwater end-member. Mar. Chem. 165, 55–65. https://doi.org/10.1016/j.marchem.2014.08.001

Luijendijk, E., Gleeson, T., Moosdorf, N., 2020. Fresh groundwater discharge insignificant for the world’s oceans but important for coastal ecosystems. Nat. Commun. 11. https://doi.org/10.1038/s41467-020-15064-8

Luo, X., Jiao, J.J., 2019. Unraveling controlling factors of concentration discharge relationships in a fractured aquifer dominant spring-shed : Evidence from mean transit time and radium reactive transport model. J. Hydrol. 571, 528–544. https://doi.org/10.1016/j.jhydrol.2019.01.066

Ma, Q., Zhang, Y., 2020. Global research trends and hotspots on submarine groundwater discharge (SGD): A bibliometric analysis. Int. J. Environ. Res. Public Health 17. https://doi.org/10.3390/ijerph17030830

Machado, D.A., Imberger, J., 2014. Modeling the impact of natural and anthropogenic nutrient sources on phytoplankton dynamics in a shallow coastal domain, Western Australia. Environ. Fluid Mech. 14, 87–111.

https://doi.org/10.1007/s10652-013-9296-1

Mackey, K.R.M., Mioni, C.E., Ryan, J.P., Paytan, A., 2012. Phosphorus cycling in the red tide incubator region of Monterey Bay in response to upwelling. Front. Microbiol. 3, 1–14. https://doi.org/10.3389/fmicb.2012.00033

Manheim, F.T., 1967. Section of Geological sciences: Evidence for Submarine Discharge of water on the Atlantic continental slope of the southern United States, and suggestions for further search. Trans. N. Y. Acad. Sci. 29, 839–853. https://doi.org/10.1111/j.2164-0947.1967.tb02825.x

Manheim, F.T., Krantz, D.E., Bratton, J.F., 2004. Studying ground water under delmarva coastal bays using electrical resistivity. Ground Water 42, 1052–1068. https://doi.org/10.1111/j.1745-6584.2004.tb02643.x

Matson, G.C., Sanford, S., 1913. Geology and ground waters of Florida. US Government Printing Office.

McClelland, J.W., Valiela, I., Michener, R.H., 1997. Nitrogen-stable isotope signatures in estuarine food webs: A record of increasing urbanization in coastal watersheds. Limnol. Oceanogr. 42, 930–937. https://doi.org/10.4319/lo.1997.42.5.0930

McKinley, I.G., Russell Alexander, W., 1993. Assessment of radionuclide retardation: uses and abuses of natural analogue studies. J. Contam. Hydrol. 13, 249–259. https://doi.org/10.1016/0169-7722(93)90060-6

Meenu, S., Gayatri, K., Malap, N., Murugavel, P., Samanta, S., Prabha, T. V., 2020. The physics of extreme rainfall event: An investigation with multisatellite observations and numerical simulations. J. Atmos. Solar-Terrestrial Phys. 204, 105275. https://doi.org/10.1016/j.jastp.2020.105275

Mehta, N., Kocar, B., 2018. Deciphering and Predicting Microscale Controls on Radon Production in Soils, Sediments and Rock. Soil Syst. 2, 30. https://doi.org/10.3390/soilsystems2020030

Meier, H., Zimmerhackl, E., Zeitler, G., Menge, P., 2015. Parameter Studies of Radionuclide Sorption in Site-Specific Sediment/Groundwater Systems. Radiochim. Acta 66–67. https://doi.org/10.1524/ract.1994.6667.special-issue.277

Mejias, M., Garcia-Orellana, J., Plata, J.L., Marina, M., Garcia-Solsona, E., Ballesteros, B.J., Masqué, P., López, J., Fernández-Arrojo, C., 2008. Methodology of hydrogeological characterization of deep carbonate aquifers as potential reservoirs of groundwater. Case of study: The Jurassic aquifer of El Maestrazgo (Castell??n, Spain). Environ. Geol. 54, 521–536. https://doi.org/10.1007/s00254-007-0845-0

Meyer, C.D., 2000. Matrix Analysis and Applied Linear Algebra, Other Titles in Applied Mathematics. Society for Industrial and Applied Mathematics.

Mialock, U., 1915. Determinación del contenido radiactivo de las sales en las aguas del Atlántico y del Pacífico entre Montevideo y el Callao.

Michael, H.A., Charette, M.A., Harvey, C.F., 2011. Patterns and variability of groundwater flow and radium activity at the coast: A case study from Waquoit Bay, Massachusetts. Mar. Chem. 127, 100–114. https://doi.org/10.1016/j.marchem.2011.08.001

Michael, H.A., Mulligan, A.E., Harvey, C.F., 2005. Seasonal oscillations in water exchange between aquifers and the coastal ocean. Nature 436, 1145–1148. https://doi.org/10.1038/nature03935

Migné, A., Ouisse, V., Hubas, C., Davoult, D., 2011. Freshwater seepages and ephemeral macroalgae proliferation in an intertidal bay: II. Effect on benthic biomass and metabolism. Estuar. Coast. Shelf Sci. 92, 161–168.

https://doi.org/10.1016/j.ecss.2010.12.023

Miller, D.C., Ullman, W.J., 2004. Ecological Consequences of Ground Water Discharge to Delaware Bay, United States. Ground Water 42, 959–970. https://doi.org/DOI 10.1111/j.1745-6584.2004.tb02635.x

Moise, T., Starinsky, A., Katz, A., Kolodny, Y., 2000. Ra isotopes and Rn in brines and ground waters of the Jordan-Dead Sea Rift Valley: Enrichment, retardation, and mixing. Geochim. Cosmochim. Acta 64, 2371–2388. https://doi.org/10.1016/S0016-7037(00)00369-0

Molina-Porras, A., Condomines, M., Legeay, P.L., Bailly-Comte, V., Seidel, J.L., 2020. Radium Isotopes as a Tracer of Water Sources and Mixing in the Vidourle Stream (South of France). Aquat. Geochemistry 26, 119–136. https://doi.org/10.1007/s10498-020-09371-1

Molina-Porras, A., Condomines, M., Seidel, J.L., 2017a. Determination of low-level Radium isotope activities in fresh waters by gamma spectrometry. Appl. Radiat. Isot. 120, 119–125. https://doi.org/10.1016/j.apradiso.2016.12.010

Molina-Porras, A., Condomines, M., Seidel, J.L., 2017b. Radium isotopes, radon and 210Pb in karstic waters: Example of the Lez system (South of France). Chem. Geol. 466, 327–340. https://doi.org/10.1016/j.chemgeo.2017.06.022

Monsen, N.E., Cloern, J.E., Lucas, L. V., Monismith, S.G., 2002. A comment on the use of flushing time, residence time, and age as transport time scales. Limnol. Oceanogr. 47, 1545–1553. https://doi.org/10.4319/lo.2002.47.5.1545

Montiel, D., Lamore, A., Stewart, J., Dimova, N., 2019. Is Submarine Groundwater Discharge (SGD) Important for the Historical Fish Kills and Harmful Algal Bloom Events of Mobile Bay? Estuaries and Coasts 42, 470–493. https://doi.org/10.1007/s12237-018-0485-5

Moore, R.J., 2007. The PDM rainfall-runoff model. Hydrol. Earth Syst. Sci. 11, 483–499. https://doi.org/10.5194/hess-11-483-2007

Moore, W.S., 2010. The effect of submarine groundwater discharge on the ocean. Ann. Rev. Mar. Sci. 2, 59–88. https://doi.org/10.1146/annurev-marine-120308-081019

Moore, W.S., 2008. Fifteen years experience in measuring 224Ra and 223Ra by delayed-coincidence counting. Mar. Chem. 109, 188–197. https://doi.org/10.1016/j.marchem.2007.06.015

Moore, W.S., 2006. The role of submarine groundwater discharge in coastal biogeochemistry. J. Geochemical Explor. 88, 389–393. https://doi.org/10.1016/j.gexplo.2005.08.082

Moore, W.S., 2000. Ages of continental shelf waters determined from 223Ra and 224Ra. J. Geophys. Res. 105, 117–122. https://doi.org/10.1029/1999JC000289

Moore, W.S., 1999. The subterranean estuary: A reaction zone of ground water and sea water. Mar. Chem. 65, 111–125. https://doi.org/10.1016/S0304-4203(99)00014-6

Moore, W.S., 1996. Large groundwater inputs to coastal waters revealed by 226Ra enrichments. Nature 380, 612–614. https://doi.org/10.1038/380612a0

Moore, W.S., 1969. Measurement of Ra228 and Th228 in Sea Water. J. Geophys. Res. 74, 694–704. https://doi.org/10.1029/JB074i002p00694

Moore, W.S., 1967. Amazon and Mississippi river concentrations of uranium, thorium, and radium isotopes. Earth Planet. Sci. Lett. 2, 231–234. https://doi.org/https://doi.org/10.1016/0012-821X(67)90134-3

Moore, W.S., Arnold, R., 1996. Ra in coastal waters using a delayed coincidence counter. J. Geophys. Res. 101, 1321. https://doi.org/10.1029/95JC03139

Moore, W.S., Beck, M., Riedel, T., Rutgers van der Loeff, M., Dellwig, O., Shaw, T.J., Schnetger, B., Brumsack, H.J., 2011. Radium-based pore water fluxes of silica, alkalinity, manganese, DOC, and uranium: A decade of studies in the German Wadden Sea. Geochim. Cosmochim. Acta 75, 6535–6555. https://doi.org/10.1016/j.gca.2011.08.037

Moore, W.S., Blanton, J.O., Joye, S.B., 2006. Estimates of flushing times, submarine groundwater discharge, and nutrient fluxes to Okatee Estuary, South Carolina. J. Geophys. Res. Ocean. 111, 1–14. https://doi.org/10.1029/2005JC003041

Moore, W.S., Cai, P., 2013. Calibration of RaDeCC systems for 223Ra measurements. Mar. Chem. 156, 130–137. https://doi.org/10.1016/j.marchem.2013.03.002

Moore, W.S., Krest, J.M., 2004. Distribution of 223Ra and 224Ra in the plumes of the Mississippi and Atchafalaya Rivers and the Gulf of Mexico. Mar. Chem. 86, 105–119. https://doi.org/10.1016/j.marchem.2003.10.001

Moore, W.S., Oliveira, J., 2008. Determination of residence time and mixing processes of the Ubatuba, Brazil, inner shelf waters using natural Ra isotopes. Estuar. Coast. Shelf Sci. 76, 512–521. https://doi.org/10.1016/j.ecss.2007.07.042

Moore, W.S., Reid, D.F., 1973. Extraction of Radium from Natural Waters Using Manganese-Impregnated Acrylic Fibers. J. Geophys. Res. 78, 8880–8886. https://doi.org/10.1029/JC078i036p08880

Moore, W.S., Sarmiento, J.L., Key, R.M., 2008. Submarine groundwater discharge revealed by 228Ra distribution in the upper Atlantic Ocean. Nat. Geosci. 1, 309–311. https://doi.org/10.1038/ngeo183

Moore, W.S., Shaw, T.J., 2008. Fluxes and behavior of radium isotopes, barium, and uranium in seven Southeastern US rivers and estuaries. Mar. Chem. 108, 236–254. https://doi.org/10.1016/j.marchem.2007.03.004

Moore, W.S., Wilson, A.M., 2005. Advective flow through the upper continental shelf driven by storms, buoyancy, and submarine groundwater discharge. Earth Planet. Sci. Lett. 235, 564–576. https://doi.org/10.1016/j.epsl.2005.04.043

Moosdorf, N., Oehler, T., 2017. Societal use of fresh submarine groundwater discharge: An overlooked water resource. Earth-Science Rev. 171, 338–348. https://doi.org/10.1016/j.earscirev.2017.06.006

Moosdorf, N., Stieglitz, T., Waska, H., Dürr, H.H., Hartmann, J., 2015. Submarine groundwater discharge from tropical islands: a review. Grundwasser 20, 53–67. https://doi.org/10.1007/s00767-014-0275-3

Mulligan, A.E., Charette, M.A., 2006. Intercomparison of submarine groundwater discharge estimates from a sandy unconfined aquifer. J. Hydrol. 327, 411–425. https://doi.org/10.1016/j.jhydrol.2005.11.056

Murdoch, L.C., Kelly, S.E., 2003. Factors affecting the performance of conventional seepage meters. Water Resour. Res. 39. https://doi.org/10.1029/2002WR001347

Nace, R.L., 1970. World hydrology: status and prospects, in: Symposium on World Water Balance. pp. 1--10.

Nathwani, J.S., Phillips, C.R., 1979. Adsorption of 226Ra by soils (I). Chemosphere 8, 285–291. https://doi.org/10.1016/0045-

6535(79)90111-5

Nelson, C.E., Donahue, M.J., Dulaiova, H., Goldberg, S.J., La Valle, F.F., Lubarsky, K., Miyano, J., Richardson, C., Silbiger, N.J., Thomas, F.I.M., 2015. Fluorescent dissolved organic matter as a multivariate biogeochemical tracer of submarine groundwater discharge in coral reef ecosystems. Mar. Chem. 177, 232–243. https://doi.org/10.1016/j.marchem.2015.06.026

Oehler, T., Tamborski, J.J., Rahman, S., Moosdorf, N., Ahrens, J., Mori, C., Neuholz, R., Schnetger, B., Beck, M., 2019. DSi as a Tracer for Submarine Groundwater Discharge. Front. Mar. Sci. 6, 1–13. https://doi.org/10.3389/fmars.2019.00563

Orr, J.C., Guinasso, N.L., Schink, D.R., 1985. 222 Rn surpluses in warm-core rings. J. Geophys. Res. 90, 8903. https://doi.org/10.1029/JC090iC05p08903

Ouisse, V., Riera, P., Migné, A., Leroux, C., Davoult, D., 2011. Freshwater seepages and ephemeral macroalgae proliferation in an intertidal bay: I Effect on benthic community structure and food web. Estuar. Coast. Shelf Sci. 91, 272–281. https://doi.org/10.1016/j.ecss.2010.10.034

Palacios, A., Ledo, J.J., Linde, N., Luquot, L., Bellmunt, F., Folch, A., Marcuello, A., Queralt, P., Pezard, P.A., Martínez, L., Bosch, D., Carrera, J., 2019. Time-lapse cross-hole electrical resistivity tomography (CHERT) for monitoring seawater intrusion dynamics in a Mediterranean aquifer. Hydrol. Earth Syst. Sci. Discuss. 1–30. https://doi.org/10.5194/hess-2019-408

Pendergrass, A.G., Knutti, R., 2018. The Uneven Nature of Daily Precipitation and Its Change. Geophys. Res. Lett. 45, 11,980-11,988. https://doi.org/10.1029/2018GL080298

Peterson, R.N., Santos, I.R., Burnett, W.C., 2010. Evaluating groundwater discharge to tidal rivers based on a Rn-222 time-series approach. Estuar. Coast. Shelf Sci. 86, 165–178. https://doi.org/10.1016/j.ecss.2009.10.022

Pettersson, H., 1930. Teneur en radium des dépots de mer profonde" Princesse-Alice" et" Challenger".

Piggot, C.S., 1932. Radium-content of ocean-bottom sediments. Trans. Am. Geophys. Union 13, 233. https://doi.org/10.1029/TR013i001p00233

Piggot, C.S., Urry, W.D., 1942. Time relations in ocean sediments. Geol. Soc. Am. Bull. 53, 1187–1210. https://doi.org/10.1130/GSAB-53-1187

Pongkijvorasin, S., Roumasset, J., Duarte, T.K., Burnett, K., 2010. Renewable resource management with stock externalities: Coastal aquifers and submarine groundwater discharge. Resour. Energy Econ. 32, 277–291. https://doi.org/10.1016/j.reseneeco.2009.09.001

Porcelli, D., 2008. Chapter 4 Investigating Groundwater Processes Using U- and Th-Series Nuclides. Radioact. Environ. 13, 105–153. https://doi.org/10.1016/S1569-4860(07)00004-6

Porcelli, D., Swarzenski, P.W., 2003. The Behavior of U- and Th-series Nuclides in Groundwater. Rev. Mineral. Geochemistry 52, 317–361. https://doi.org/10.2113/0520317

Post, V.E.A., 2005. Fresh and saline groundwater interaction in coastal aquifers: Is our technology ready for the problems ahead? Hydrogeol. J. 13, 120–123. https://doi.org/10.1007/s10040-004-0417-2

Prakash, R., Srinivasamoorthy, K., Gopinath, S., Saravanan, K., 2018. Measurement of submarine groundwater discharge using

diverse methods in Coleroon Estuary, Tamil Nadu, India. Appl. Water Sci. 8, 1–11. https://doi.org/10.1007/s13201-018-0659-0

Puigdomenech, I., Bergstrom, U., 1995. Calculation of distribution coefficients for radionuclides in soils and sediments. Nucl. Saf. 36, 142–154.

Qu, W., Wang, C., Luo, M., Zheng, C., Li, H., 2020. Distributions, quality assessments and fluxes of heavy metals carried by submarine groundwater discharge in different types of wetlands in Jiaozhou Bay, China. Mar. Pollut. Bull. 157, 111310. https://doi.org/10.1016/j.marpolbul.2020.111310

Rahman, M.D.M., Lee, Y.G., Kim, G., Lee, K., Han, S., 2013. Significance of submarine groundwater discharge in the coastal fluxes of mercury in Hampyeong Bay, Yellow Sea. Chemosphere 91, 320–327. https://doi.org/10.1016/j.chemosphere.2012.11.052

Rajurkar, M.P., Kothyari, U.C., Chaube, U.C., 2004. Modeling of the daily rainfall-runoff relationship with artificial neural network. J. Hydrol. 285, 96–113. https://doi.org/10.1016/j.jhydrol.2003.08.011

Rama, Moore, W.S., 1996. Using the radium quartet for evaluating groundwater input and water exchange in salt marshes. Geochim. Cosmochim. Acta 60, 4645–4652. https://doi.org/10.1016/S0016-7037(96)00289-X

Rama, Moore, W.S., 1984. Mechanism of transport of U-Th series radioisotopes from solids into ground water. Geochim. Cosmochim. Acta 48, 395–399. https://doi.org/10.1016/0016-7037(84)90261-8

Ramos, N.F., Folch, A., Fernàndez-Garcia, D., Lane, M., Thomas, M., Gathenya, J.M., Wara, C., Thomson, P., Custodio, E., Hope, R., 2020. Evidence of groundwater vulnerability to climate variability and economic growth in coastal Kenya. J. Hydrol. 586, 124920. https://doi.org/10.1016/j.jhydrol.2020.124920

Rapaglia, J.P., Ferrarin, C., Zaggia, L., Moore, W.S., Umgiesser, G., Garcia-Solsona, E., Garcia-Orellana, J., Masqué, P., 2010. Investigation of residence time and groundwater flux in Venice Lagoon: Comparing radium isotope and hydrodynamical models. J. Environ. Radioact. 101, 571–581. https://doi.org/10.1016/j.jenvrad.2009.08.010

Relyea, J.F., 1982. Theoretical and experimental considerations for the use of the column method for determining retardation factors. Radioact Waste Manag. Nucl Fuel Cycle 3, 151–166.

Riedl, R.J., Huang, N., Machan, R., 1972. The subtidal pump: a mechanism of interstitial water exchange by wave action. Mar. Biol. 13, 210–221. https://doi.org/10.1007/BF00391379

Robinson, C.E., Gibbes, B., Li, L., 2006. Driving mechanisms for groundwater flow and salt transport in a subterranean estuary. Geophys. Res. Lett. 33, 3–6. https://doi.org/10.1029/2005GL025247

Robinson, C.E., Li, L., Barry, D.A., 2007. Effect of tidal forcing on a subterranean estuary. Adv. Water Resour. 30, 851–865. https://doi.org/10.1016/j.advwatres.2006.07.006

Robinson, C.E., Xin, P., Santos, I.R., Charette, M.A., Li, L., Barry, D.A., 2018. Groundwater dynamics in subterranean estuaries of coastal unconfined aquifers: Controls on submarine groundwater discharge and chemical inputs to the ocean. Adv. Water Resour. 115, 315–331. https://doi.org/10.1016/j.advwatres.2017.10.041

Rocha, C., Veiga-Pires, C., Scholten, J., Knoeller, K., Gröcke, D.R., Carvalho, L., Anibal, J., Wilson, J., 2016. Assessing land-ocean

connectivity via submarine groundwater discharge (SGD) in the Ria Formosa Lagoon (Portugal): Combining radon measurements and stable isotope hydrology. Hydrol. Earth Syst. Sci. 20, 3077–3098. https://doi.org/10.5194/hess-20-3077-2016

Rodellas, V., Cook, P.G., McCallum, J., Andrisoa, A., Meulé, S., Stieglitz, T.C., 2020. Temporal variations in porewater fluxes to a coastal lagoon driven by wind waves and changes in lagoon water depths. J. Hydrol. 581, 124363. https://doi.org/https://doi.org/10.1016/j.jhydrol.2019.124363

Rodellas, V., Garcia-Orellana, J., Garcia-Solsona, E., Masqué, P., Domínguez, J.A., Ballesteros, B.J., Mejías, M., Zarroca, M., 2012. Quantifying groundwater discharge from different sources into a Mediterranean wetland by using 222Rn and Ra isotopes. J. Hydrol. 466–467, 11–22. https://doi.org/10.1016/j.jhydrol.2012.07.005

Rodellas, V., Garcia-Orellana, J., Masqué, P., Feldman, M., Weinstein, Y., 2015. Submarine groundwater discharge as a major source of nutrients to the Mediterranean Sea. Proc. Natl. Acad. Sci. 112, 3926–3930. https://doi.org/10.1073/pnas.1419049112

Rodellas, V., Garcia-Orellana, J., Tovar-Sánchez, A., Basterretxea, G., López-Garcia, J.M., Sánchez-Quiles, D., Garcia-Solsona, E., Masqué, P., 2014. Submarine groundwater discharge as a source of nutrients and trace metals in a Mediterranean bay (Palma Beach, Balearic Islands). Mar. Chem. 160, 56–66. https://doi.org/10.1016/j.marchem.2014.01.007

Rodellas, V., Garcia-Orellana, J., Trezzi, G., Masqué, P., Stieglitz, T.C., Bokuniewicz, H.J., Cochran, J.K., Berdalet, E., 2017. Using the radium quartet to quantify submarine groundwater discharge and porewater exchange. Geochim. Cosmochim. Acta 196, 58–73. https://doi.org/10.1016/j.gca.2016.09.016

Rodellas, V., Stieglitz, T.C., Tamborski, J.J., Beek, P. Van, Andrisoa, A., Cook, P.G., 2021. Conceptual uncertainties in groundwater and porewater fl uxes estimated by radon and radium mass balances 1–19. https://doi.org/10.1002/lno.11678

Röper, T., Greskowiak, J., Massmann, G., 2013. Detecting Small Groundwater Discharge Springs Using Handheld Thermal Infrared Imagery. Groundwater 52, 936–942. https://doi.org/10.1111/gwat.12145

Rosenberg, N.D., Lupton, J.E., Kadko, D., Collier, R., Lilley, M.D., Pak, H., 1988. Estimation of heat and chemical fluxes from a seafloor hydrothermal vent field using radon measurements. Nature 334, 604–607. https://doi.org/10.1038/334604a0

Rosenberry, D.O., Duque, C., Lee, D.R., 2020. History and evolution of seepage meters for quantifying flow between groundwater and surface water: Part 1 – Freshwater settings. Earth-Science Rev. 204, 103167. https://doi.org/10.1016/j.earscirev.2020.103167

Rufí-Salís, M., Garcia-Orellana, J., Cantero, G., Castillo, J., Hierro, A., Rieradevall, J., Bach, J., 2019. Influence of land use changes on submarine groundwater discharge. Environ. Res. Commun. 1, 031005. https://doi.org/10.1088/2515-7620/ab1695

Ruiz-González, C., Rodellas, V., Garcia-Orellana, J., 2021. The microbial dimension of submarine groundwater discharge: current challenges and future directions. FEMS Microbiol. Rev. 45, 1–25. https://doi.org/10.1093/femsre/fuab010

Rutherford, E., 1900. I. A radio-active substance emitted from thorium compounds. London, Edinburgh, Dublin Philos. Mag. J. Sci. 49, 1–14. https://doi.org/10.1080/14786440009463821

Sadat-Noori, M., Santos, I.R., Tait, D.R., Reading, M.J., Sanders, C.J., 2017. High porewater exchange in a mangrove-dominated

estuary revealed from short-lived radium isotopes. J. Hydrol. 553, 188–198. https://doi.org/10.1016/j.jhydrol.2017.07.058

Sajih, M., Bryan, N.D., Livens, F.R., Vaughan, D.J., Descostes, M., Phrommavanh, V., Nos, J., Morris, K., 2014. Adsorption of radium and barium on goethite and ferrihydrite: A kinetic and surface complexation modelling study. Geochim. Cosmochim. Acta 146, 150–163. https://doi.org/10.1016/j.gca.2014.10.008

Sanders, C.J., Santos, I.R., Barcellos, R., Silva Filho, E. V., 2012. Elevated concentrations of dissolved Ba, Fe and Mn in a mangrove subterranean estuary: Consequence of sea level rise? Cont. Shelf Res. 43, 86–94. https://doi.org/10.1016/j.csr.2012.04.015

Santoro, A.E., Francis, C.A., De Sieyes, N.R., Boehm, A.B., 2008. Shifts in the relative abundance of ammonia-oxidizing bacteria and archaea across physicochemical gradients in a subterranean estuary. Environ. Microbiol. 10, 1068–1079. https://doi.org/10.1111/j.1462-2920.2007.01547.x

Santos, I.R., Burnett, W.C., Chanton, J., Dimova, N., Peterson, R.N., 2009. Land or ocean?: Assessing the driving forces of submarine groundwater discharge at a coastal site in the gulf of mexico. J. Geophys. Res. Ocean. 114, 1–11. https://doi.org/10.1029/2008JC005038

Santos, I.R., Chen, X., Lecher, A.L., Sawyer, A.H., Moosdorf, N., Rodellas, V., Tamborski, J.J., Cho, H., Dimova, N., Sugimoto, R., Bonaglia, S., Li, H., Hajati, M.-C., Li, L., 2021. Submarine groundwater discharge impacts on coastal nutrient biogeochemistry. Nat. Rev. Earth Environ. 108–119. https://doi.org/10.1038/s43017-021-00152-0

Santos, I.R., Eyre, B.D., Huettel, M., 2012. The driving forces of porewater and groundwater flow in permeable coastal sediments: A review. Estuar. Coast. Shelf Sci. 98, 1–15. https://doi.org/10.1016/j.ecss.2011.10.024

Satterly, J., 1911. On the radium content of various fresh and sea waters and some other substances. Proc. Camb. Phil. Soc 16, 360--364.

Sawyer, A.H., David, C.H., Famiglietti, J.S., 2016. Continental patterns of submarine groundwater discharge reveal coastal vulnerabilities. Science (80-. ). 353, 705–707. https://doi.org/10.1126/science.aag1058

Sawyer, A.H., Shi, F., Kirby, J.T., Michael, H.A., 2013. Dynamic response of surface water-groundwater exchange to currents, tides, and waves in a shallow estuary. J. Geophys. Res. Ocean. 118, 1749–1758. https://doi.org/10.1002/jgrc.20154

Schmidt, A., Santos, I.R., Burnett, W.C., Niencheski, F., Knöller, K., 2011. Groundwater sources in a permeable coastal barrier: Evidence from stable isotopes. J. Hydrol. 406, 66–72. https://doi.org/10.1016/j.jhydrol.2011.06.001

Scholten, J.C., Osvath, I., Pham, M.K., 2013. 226Ra measurements through gamma spectrometric counting of radon progenies: How significant is the loss of radon? Mar. Chem. 156, 146–152. https://doi.org/10.1016/j.marchem.2013.03.001

Scholten, J.C., Pham, M.K., Blinova, O., Charette, M.A., Dulaiova, H., Eriksson, M., 2010. Preparation of Mn-fiber standards for the efficiency calibration of the delayed coincidence counting system (RaDeCC). Mar. Chem. 121, 206–214. https://doi.org/10.1016/j.marchem.2010.04.009

Schubert, M., Paschke, A., Lieberman, E., Burnett, W.C., 2012. Air–Water Partitioning of 222 Rn and its Dependence on Water Temperature and Salinity. Environ. Sci. Technol. 46, 3905–3911. https://doi.org/10.1021/es204680n

Schumacher, R.S., 2017. Heavy Rainfall and Flash Flooding, in: Oxford Research Encyclopedia of Natural Hazard Science. Oxford University Press, pp. 1–40. https://doi.org/10.1093/acrefore/9780199389407.013.132

Scientific Computer Instruments, 2021. RaDeCC [WWW Document]. URL https://www.radecc.com/ (accessed 10.4.21).

Seibert, S.L., Degenhardt, J., Ahrens, J., Reckhardt, A., Schwalfenberg, K., Waska, H., 2020. Investigating the land-sea transition zone, in: YOUMARES 9 - The Oceans: Our Research, Our Future. Springer International Publishing, Cham, pp. 45–56. https://doi.org/10.1007/978-3-030-20389-4_3

Semkow, T.M., 1990. Recoil-emanation theory applied to radon release from mineral grains. Geochim. Cosmochim. Acta 54, 425–440. https://doi.org/10.1016/0016-7037(90)90331-E

Serne, R.J., Relyea, J.F., 1982. The Status of Radionuclide Sorption-Desorption Studies Performed by the WRIT Program, in: The Technology of High-Level Nuclear Waste Disposal.

Shackelford, C.D., 2013. Geoenvironmental Engineering, in: Reference Module in Earth Systems and Environmental Sciences. Elsevier, pp. 1–29. https://doi.org/10.1016/B978-0-12-409548-9.05424-5

Shaler, N.S., 1894. Evidences as to Change of Sealevel. Geol. Soc. Am. Bull. 6, 141–166. https://doi.org/10.1130/GSAB-6-141

Shalev, E., Lazar, A., Wollman, S., Kington, S., Yechieli, Y., Gvirtzman, H., 2009. Biased monitoring of fresh water-salt water mixing zone in coastal aquifers. Ground Water 47, 49–56. https://doi.org/10.1111/j.1745-6584.2008.00502.x

Shaw, T.J., Moore, W.S., Kloepfer, J., Sochaski, M.A., 1998. The flux of barium to the coastal waters of the southeastern USA: The importance of submarine groundwater discharge. Geochim. Cosmochim. Acta 62, 3047–3054. https://doi.org/10.1016/S0016-7037(98)00218-X

Shellenbarger, G.G., Monismith, S.G., Paytan, A., 2006. The importance of submarine groundwater discharge to the nearshore nutrient supply in the Gulf of Aqaba (Israel). Limnol. Oceanogr. 51, 1876–1886.

Sheppard, M.I., Thibault, D.H., 1990. Default soil solid/liquid partition coefficients, K(d)S, for four major soil types: A compendium. Health Phys. 59, 471–482.

Sheppard, S.C., Sheppard, M.I., Tait, J.C., Sanipelli, B.L., 2006. Revision and meta-analysis of selected biosphere parameter values for chlorine, iodine, neptunium, radium, radon and uranium. J. Environ. Radioact. 89, 115–137. https://doi.org/10.1016/j.jenvrad.2006.03.003

Short, F.T., Burdick, D.M., 1996. Quantifying eelgrass habitat loss in relation to housing development and nitrogen loading in Waquoit Bay, Massachusetts. Estuaries 19, 730–739. https://doi.org/10.2307/1352532

Slomp, C.P., Van Cappellen, P., 2004. Nutrient inputs to the coastal ocean through submarine groundwater discharge: Controls and potential impact. J. Hydrol. 295, 64–86. https://doi.org/10.1016/j.jhydrol.2004.02.018

Smith, A.J., 2004. Mixed convection and density-dependent seawater circulation in coastal aquifers. Water Resour. Res. 40, 1–16. https://doi.org/10.1029/2003WR002977

Soddy, F., 1923. The Origins of the Conception of Isotopes. Sci. Mon. 17, 305–317.

Soddy, F., 1909. The Interpretation of Radium and the Structure of the Atom. London.

Spiteri, C., Slomp, C.P., Charette, M.A., Tuncay, K., Meile, C., 2008a. Flow and nutrient dynamics in a subterranean estuary (Waquoit Bay, MA, USA): Field data and reactive transport modeling. Geochim. Cosmochim. Acta 72, 3398–3412.

https://doi.org/10.1016/j.gca.2008.04.027

Spiteri, C., Slomp, C.P., Regnier, P., Meile, C., Van Cappellen, P., 2007. Modelling the geochemical fate and transport of wastewater-derived phosphorus in contrasting groundwater systems. J. Contam. Hydrol. 92, 87–108. https://doi.org/10.1016/j.jconhyd.2007.01.002

Spiteri, C., Slomp, C.P., Tuncay, K., Meile, C., 2008b. Modeling biogeochemical processes in subterranean estuaries: Effect of flow dynamics and redox conditions on submarine groundwater discharge of nutrients. Water Resour. Res. 44, 1–18. https://doi.org/10.1029/2007WR006071

Stieglitz, T.C., Rapaglia, J., Krupa, S.C., 2007. An effect of pier pilings on nearshore submarine groundwater discharge from a (partially) confined aquifer. Estuaries and Coasts 30, 543–550. https://doi.org/10.1007/bf03036520

Stigter, T.Y., Nunes, J.P., Pisani, B., Fakir, Y., Hugman, R., Li, Y., Tomé, S., Ribeiro, L., Samper, J., Oliveira, R., Monteiro, J.P., Silva, A., Tavares, P.C.F., Shapouri, M., Cancela da Fonseca, L., El Himer, H., 2014. Comparative assessment of climate change and its impacts on three coastal aquifers in the Mediterranean. Reg. Environ. Chang. 14, 41–56. https://doi.org/10.1007/s10113-012-0377-3

Strutt, R.J., 1906. On the distribution of radium in the Earth's crust and on the Earth's internal heat. Proc. R. Soc. London. Ser. A, Contain. Pap. a Math. Phys. Character 77, 472–485. https://doi.org/10.1098/rspa.1906.0042

Su, N., Burnett, W.C., MacIntyre, H.L., Liefer, J.D., Peterson, R.N., Viso, R., 2014. Natural Radon and Radium Isotopes for Assessing Groundwater Discharge into Little Lagoon, AL: Implications for Harmful Algal Blooms. Estuaries and Coasts 37, 893–910. https://doi.org/10.1007/s12237-013-9734-9

Sugimoto, R., Honda, H., Kobayashi, S., Takao, Y., Tahara, D., Tominaga, O., Taniguchi, M., 2016. Seasonal Changes in Submarine Groundwater Discharge and Associated Nutrient Transport into a Tideless Semi-enclosed Embayment (Obama Bay, Japan). Estuaries and Coasts 39, 13–26. https://doi.org/10.1007/s12237-015-9986-7

Sun, H., Semkow, T.M., 1998. Mobilization of thorium, radium and radon radionuclides in ground water by successive alpha-recoils. J. Hydrol. 205, 126–136. https://doi.org/10.1016/S0022-1694(97)00154-6

Sun, Y., Torgersen, T., 1998. The effects of water content and Mn-fiber surface conditions on 224Ra measurement by 220Rn emanation. Mar. Chem. 62, 299–306. https://doi.org/10.1016/S0304-4203(98)00019-X

Swarzenski, P.W., 2007. U/Th Series Radionuclides as Coastal Groundwater Tracers. Chem. Rev. 107, 663–674. https://doi.org/10.1021/cr0503761

Swarzenski, P.W., Burnett, W.C., Greenwood, W.J., Herut, B., Peterson, R., Dimova, N., Shalem, Y., Yechieli, Y., Weinstein, Y., 2006. Combined time-series resistivity and geochemical tracer techniques to examine submarine groundwater discharge at Dor Beach, Israel. Geophys. Res. Lett. 33, 1–6. https://doi.org/10.1029/2006GL028282

Swarzenski, P.W., Dulai, H., Kroeger, K.D., Smith, C.G., Dimova, N., Storlazzi, C.D., Prouty, N.G., Gingerich, S.B., Glenn, C.R., 2017. Observations of nearshore groundwater discharge: Kahekili Beach Park submarine springs, Maui, Hawaii. J. Hydrol. Reg. Stud. 11, 147–165. https://doi.org/10.1016/j.ejrh.2015.12.056

Swarzenski, P.W., Reich, C., Kroeger, K.D., Baskaran, M., 2007. Ra and Rn isotopes as natural tracers of submarine groundwater

discharge in Tampa Bay, Florida. Mar. Chem. 104, 69–84. https://doi.org/10.1016/j.marchem.2006.08.001

Tachi, Y., Shibutani, T., Sato, H., Yui, M., 2001. Experimental and modeling studies on sorption and diffusion of radium in bentonite. J. Contam. Hydrol. 47, 171–186. https://doi.org/10.1016/S0169-7722(00)00147-9

Tait, D.R., Erler, D. V., Santos, I.R., Cyronak, T.J., Morgenstern, U., Eyre, B.D., 2014. The influence of groundwater inputs and age on nutrient dynamics in a coral reef lagoon. Mar. Chem. 166, 36–47. https://doi.org/10.1016/j.marchem.2014.08.004

Takeuchi, M., Tominaga, O., Sugimoto, R., Kitagawa, K., Yamanda, M., Honda, H., Shoki, J., Kobayashi, S., Ikuta, K., Taniguchi, M., 2017. Evaluation of the environmental condition of Submarine Groundwater Discharge (SGD) by using nitrate stable isotope ratio recorded in sea lettuce (Ulva sp.). JSFS 85th Anniv. Int. Symp. "Fisheries Sci. Futur. Gener. 5005.

Tamamura, S., Takada, T., Tomita, J., Nagao, S., Fukushi, K., Yamamoto, M., 2014. Salinity dependence of 226Ra adsorption on montmorillonite and kaolinite. J. Radioanal. Nucl. Chem. 299, 569–575. https://doi.org/10.1007/s10967-013-2740-3

Tamborski, J.J., Bejannin, S., Garcia-orellana, J., Souhaut, M., Charbonnier, C., Anschutz, P., Pujo-pay, M., Conan, P., Monnin, C., Stieglitz, T.C., Rodellas, V., Claude, C., van Beek, P., 2018. A comparison between water recirculation and terrestrially-driven dissolved silica fluxes to the Mediterranean Sea traced using radium isotopes. Geochim. Cosmochim. Acta. https://doi.org/10.1016/j.gca.2018.07.022

Tamborski, J.J., Cochran, J.K., Bokuniewicz, H.J., 2017a. Application of 224Ra and 222Rn for evaluating seawater residence times in a tidal subterranean estuary. Mar. Chem. 189, 32–45. https://doi.org/10.1016/j.marchem.2016.12.006

Tamborski, J.J., Cochran, J.K., Bokuniewicz, H.J., 2017b. Submarine groundwater discharge driven nitrogen fluxes to Long Island Sound, NY: Terrestrial vs. marine sources. Geochim. Cosmochim. Acta 218, 40–57. https://doi.org/10.1016/j.gca.2017.09.003

Tamborski, J.J., Rogers, A.D., Bokuniewicz, H.J., 2017c. Investigation of submarine groundwater discharge to tidal rivers: Evidence for regional and local scale seepage. Hydrol. Process. 31, 716–730. https://doi.org/10.1002/hyp.11079

Tamborski, J.J., Rogers, A.D., Bokuniewicz, H.J., Cochran, J.K., Young, C.R., 2015. Identification and quantification of diffuse fresh submarine groundwater discharge via airborne thermal infrared remote sensing. Remote Sens. Environ. 171, 202–217. https://doi.org/10.1016/j.rse.2015.10.010

Tamborski, J.J., van Beek, P., Rodellas, V., Monnin, C., Bergsma, E., Stieglitz, T.C., Heilbrun, C., Cochran, J.K., Charbonnier, C., Anschutz, P., Bejannin, S., Beck, A.J., 2019. Temporal variability of lagoon – sea water exchange and seawater circulation through a Mediterranean barrier beach. Limnol. Oceanogr. 00, 1–22. https://doi.org/10.1002/lno.11169

Taniguchi, M., 2006. Submarine groundwater discharge measured by seepage meters in sicilian coastal waters. Cont. Shelf Res. 26, 835–842. https://doi.org/10.1016/j.csr.2005.12.002

Taniguchi, M., Burnett, W.C., Cable, J.E., Turner, J. V., 2002. Investigation of submarine groundwater discharge. Hydrol. Process. 16, 2115–2129. https://doi.org/10.1002/hyp.1145

Taniguchi, M., Burnett, W.C., Smith, C.F., Paulsen, R.J., O'Rourke, D., Krupa, S.L., Christoff, J.L., 2003. Spatial and temporal distributions of submarine groundwater discharge rates obtained from various types of seepage meters at a site in the Northeastern Gulf of Mexico. Biogeochemistry 66, 35–53. https://doi.org/10.1023/B:BIOG.0000006090.25949.8d

Taniguchi, M., Dulai, H., Burnett, K.M., Santos, I.R., Sugimoto, R., Stieglitz, T.C., Kim, G., Moosdorf, N., Burnett, W.C., 2019. Submarine Groundwater Discharge: Updates on Its Measurement Techniques, Geophysical Drivers, Magnitudes, and Effects. Front. Environ. Sci. 7, 1–26. https://doi.org/10.3389/fenvs.2019.00141

Taniguchi, M., Ishitobi, T., Saeki, K.I., 2005. Evaluation of time-space distributions of submarine ground water discharge. Ground Water 43, 336–342. https://doi.org/10.1111/j.1745-6584.2005.0027.x

Taniguchi, M., Ishitobi, T., William Burnett, C., Shimada, J., 2007. Comprehensive evaluation of the groundwater-seawater interface and submarine groundwater discharge. IAHS-AISH Publ. 86–92.

Taniguchi, M., Iwakawa, H., 2004. Submarine groundwater discharge in Osaka Bay, Japan. Limnology 5, 25–32. https://doi.org/10.1007/s10201-003-0112-3

Taylor, R.G., Todd, M.C., Kongola, L., Maurice, L., Nahozya, E., Sanga, H., MacDonald, A.M., 2013. Evidence of the dependence of groundwater resources on extreme rainfall in East Africa. Nat. Clim. Chang. 3, 374–378. https://doi.org/10.1038/nclimate1731

Thibault, D.H., Sheppard, M.I., Smith, P.A., 1990. A critical compilation and review of default soil solid/liquid partition coefficients, Kd, for use in environmental assessments. At. Energy Canada Limited,.

Tovar-Sánchez, A., Basterretxea, G., Rodellas, V., Sánchez-Quiles, D., Garcia-Orellana, J., Masqué, P., Jordi, A., López, J.M., Garcia-Solsona, E., 2014. Contribution of groundwater discharge to the coastal dissolved nutrients and trace metal concentrations in Majorca Island: Karstic vs detrital systems. Environ. Sci. Technol. 48, 11819–11827. https://doi.org/10.1021/es502958t

Trezzi, G., Garcia-Orellana, J., Rodellas, V., Masqué, P., Garcia-Solsona, E., Andersson, P.S., 2017. Assessing the role of submarine groundwater discharge as a source of Sr to the Mediterranean Sea. Geochim. Cosmochim. Acta 200, 42–54. https://doi.org/10.1016/j.gca.2016.12.005

Trezzi, G., Garcia-Orellana, J., Rodellas, V., Santos-Echeandia, J., Tovar-Sánchez, A., Garcia-Solsona, E., Masqué, P., 2016. Submarine groundwater discharge: A significant source of dissolved trace metals to the North Western Mediterranean Sea. Mar. Chem. 186, 90–100. https://doi.org/10.1016/j.marchem.2016.08.004

Trier, R.M., Broecker, W.S., Feely, H.W., 1972. Radium-228 profile at the second Geosecs intercalibration station, 1970, in the North Atlantic. Earth Planet. Sci. Lett. 16, 141–145. https://doi.org/10.1016/0012-821X(72)90249-X

Uddameri, V., Singaraju, S., Hernandez, E.A., 2014. Temporal variability of freshwater and pore water recirculation components of submarine groundwater discharges at Baffin Bay, Texas. Environ. Earth Sci. 71, 2517–2533. https://doi.org/10.1007/s12665-013-2902-1

Utsunomiya, T., Hata, M., Sugimoto, R., Honda, H., Kobayashi, S., Miyata, Y., Yamada, M., Tominaga, O., Shoji, J., Taniguchi, M., 2017. Higher species richness and abundance of fish and benthic invertebrates around submarine groundwater discharge in Obama Bay, Japan. J. Hydrol. Reg. Stud. 11, 139–146. https://doi.org/10.1016/j.ejrh.2015.11.012

Valiela, I., Costa, J., Foreman, K., Teal, J.M., Howes, B., Aubrey, D., 1990. Transport of groundwater-borne nutrients from watersheds and their effects on coastal waters. Biogeochemistry 10, 177–197. https://doi.org/10.1007/BF00003143

Valiela, I., Foreman, K., LaMontagne, M., Hersh, D., Costa, J., Peckol, P., DeMeo-Andreson, B., D'Avanzo, C., Babione, M., Sham,

C.H., Brawley, J., Lajtha, K., 1992. Couplings of watersheds and coastal waters: Sources and consequences of nutrient enrichment in Waquoit Bay, Massachusetts. Estuaries 15, 443–457. https://doi.org/10.2307/1352389

Van Meter, K.J., Van Cappellen, P., Basu, N.B., 2018. Legacy nitrogen may prevent achievement of water quality goals in the Gulf of Mexico. Science (80-. ). 360, 427–430. https://doi.org/10.1126/science.aar4462

Vandenhove, H., Van Hees, M., 2007. Predicting radium availability and uptake from soil properties. Chemosphere 69, 664–674. https://doi.org/10.1016/j.chemosphere.2007.02.054

Veeh, H.H., Moore, W.S., Smith, S. V., 1995. The behaviour of uranium and radium in an inverse estuary. Cont. Shelf Res. 15, 1569–1583. https://doi.org/10.1016/0278-4343(95)00031-U

Vieira, L.H., Geibert, W., Stimac, I., Koehler, D., Rutgers van der Loeff, M.M., 2021. The analysis of 226Ra in 1-liter seawater by isotope dilution via single-collector sector-field ICP-MS. Limnol. Oceanogr. Methods 19, 356–367. https://doi.org/10.1002/lom3.10428

Vinson, D.S., Tagma, T., Bouchaou, L., Dwyer, G.S., Warner, N.R., Vengosh, A., 2013. Occurrence and mobilization of radium in fresh to saline coastal groundwater inferred from geochemical and isotopic tracers (Sr, S, O, H, Ra, Rn). Appl. Geochemistry 38, 161–175. https://doi.org/10.1016/j.apgeochem.2013.09.004

Vinson, D.S., Vengosh, A., Hirschfeld, D., Dwyer, G.S., 2009. Relationships between radium and radon occurrence and hydrochemistry in fresh groundwater from fractured crystalline rocks, North Carolina (USA). Chem. Geol. 260, 159–171. https://doi.org/10.1016/j.chemgeo.2008.10.022

Virtasalo, J.J., Schröder, J.F., Luoma, S., Majaniemi, J., Mursu, J., Scholten, J., 2019. Submarine groundwater discharge site in the First Salpausselkä ice-marginal formation, south Finland. Solid Earth 10, 405–423. https://doi.org/10.5194/se-10-405-2019

Wang, Q., Li, H., Zhang, Y., Wang, X., Zhang, C., Xiao, K., Qu, W., 2019. Evaluations of submarine groundwater discharge and associated heavy metal fluxes in Bohai Bay, China. Sci. Total Environ. 695, 133873. https://doi.org/10.1016/j.scitotenv.2019.133873

Wang, X., Chen, X., Liu, J., Zhang, F., Li, L., Du, J., 2021. Radon traced seasonal variations of water mixing and accompanying nutrient and carbon transport in the Yellow-Bohai Sea. Sci. Total Environ. 784, 147161. https://doi.org/10.1016/j.scitotenv.2021.147161

Waska, H., Kim, S., Kim, G., Peterson, R.N., Burnett, W.C., 2008. An efficient and simple method for measuring 226Ra using the scintillation cell in a delayed coincidence counting system (RaDeCC). J. Environ. Radioact. 99, 1859–1862. https://doi.org/10.1016/j.jenvrad.2008.08.008

Webster, I.T., Hancock, G.J., Murray, A.S., 1995. Modelling the effect of salinity on radium desorption from sediments. Geochim. Cosmochim. Acta 59, 2469–2476. https://doi.org/10.1016/0016-7037(95)00141-7

Welti, N., Gale, D., Hayes, M., Kumar, A., Gasparon, M., Gibbes, B., Lockington, D., 2015. Intertidal diatom communities reflect patchiness in groundwater discharge. Estuar. Coast. Shelf Sci. 163, 116–124. https://doi.org/10.1016/j.ecss.2015.06.006

Werner, A.D., Bakker, M., Post, V.E.A., Vandenbohede, A., Lu, C., Ataie-Ashtiani, B., Simmons, C.T., Barry, D.A., 2013. Seawater intrusion processes, investigation and management: Recent advances and future challenges. Adv. Water Resour. 51, 3–26.

https://doi.org/10.1016/j.advwatres.2012.03.004

WHO, 2011. Guidelines for Drinking-water Quality 4th Edtion.

Willett, I.R., Bond, W.J., 1995. Sorption of manganese, uranium, and radium by highly weathered soils. J. Environ. Qual. 24, 834–845. https://doi.org/10.2134/jeq1995.00472425002400050006x

Wilson, A.M., 2005. Fresh and saline groundwater discharge to the ocean: A regional perspective. Water Resour. Res. 41, 1–11. https://doi.org/10.1029/2004WR003399

Wilson, A.M., Evans, T.B., Moore, W.S., Schutte, C.A., Joye, S.B., 2015. What time scales are important for monitoring tidally influenced submarine groundwater discharge? Insights from a salt marsh. Water Resour. Res. 51, 4198–4207. https://doi.org/10.1002/2014WR015984

Wilson, A.M., Moore, W.S., Joye, S.B., Anderson, J.L., Schutte, C.A., 2011. Storm-driven groundwater flow in a salt marsh. Water Resour. Res. 47. https://doi.org/10.1029/2010WR009496

Young, K.S.R., Pradhanang, S.M., 2021. Small unmanned aircraft (sUAS)-deployed thermal infrared (TIR) imaging for environmental surveys with implications in submarine groundwater discharge (SGD): Methods, challenges, and novel opportunities. Remote Sens. 13. https://doi.org/10.3390/rs13071331

Yu, X., Xin, P., Lu, C., Robinson, C.E., Li, L., Barry, D.A., 2017. Effects of episodic rainfall on a subterranean estuary. Water Resour. Res. 53, 5774–5787. https://doi.org/10.1002/2017WR020809

Zarroca, M., Linares, R., Rodellas, V., Garcia-Orellana, J., Roqué, C., Bach, J., Masqué, P., 2014. Delineating coastal groundwater discharge processes in a wetland area by means of electrical resistivity imaging, 224 Ra and 222 Rn. Hydrol. Process. 28, 2382–2395. https://doi.org/10.1002/hyp.9793

Zektser, I.S., Loaiciga, H.A., 1993. Groundwater fluxes in the global hydrologic cycle: past, present and future. J. Hydrol. 144, 405–427. https://doi.org/10.1016/0022-1694(93)90182-9

Zektzer, I.S., Ivanov, V.A., Meskheteli, A. V., 1973. The problem of direct groundwater discharge to the seas. J. Hydrol. 20, 1–36. https://doi.org/10.1016/0022-1694(73)90042-5

Zhang, Y., Santos, I.R., Li, H., Wang, Q., Xiao, K., Guo, H., Wang, X., 2020. Submarine groundwater discharge drives coastal water quality and nutrient budgets at small and large scales. Geochim. Cosmochim. Acta 290, 201–215. https://doi.org/10.1016/j.gca.2020.08.026

Zhang, Y., Schaap, M.G., 2019. Estimation of saturated hydraulic conductivity with pedotransfer functions: A review. J. Hydrol. 575, 1011–1030. https://doi.org/10.1016/j.jhydrol.2019.05.058

Zhao, S., Xu, B., Yao, Q., Burnett, W.C., Charette, M.A., Su, R., Lian, E., Yu, Z., 2021. Nutrient-rich submarine groundwater discharge fuels the largest green tide in the world. Sci. Total Environ. 770, 144845. https://doi.org/10.1016/j.scitotenv.2020.144845

Zhou, Y.Q., Sawyer, A.H., David, C.H., Famiglietti, J.S., 2019. Fresh Submarine Groundwater Discharge to the Near-Global Coast. Geophys. Res. Lett. 46, 5855–5863. https://doi.org/10.1029/2019GL082749